METHODS FOR THE INTEGRATED DESIGN OF VISCOELASTIC MATERIALS AND STRUCTURAL GEOMETRY

BY

YONG HOON LEE

DISSERTATION

Submitted in partial fulfillment of the requirements
for the degree of Doctor of Philosophy in Mechanical Engineering
in the Graduate College of the
University of Illinois at Urbana-Champaign, 2020

Urbana, Illinois

Doctoral Committee:

Associate Professor Randy H. Ewoldt, Chair
Associate Professor James T. Allison, Director of Research
Associate Professor Pingfeng Wang
Assistant Professor Mattia Gazzola

Abstract

Design engineers have traditionally selected simple materials, including linear elastic solids and Newtonian fluids, for their designs, and optimize designed systems within the limitations of preselected materials. However, allowing complex materials (e.g., viscoelastic materials and soft solids) as options for system materials can eliminate some associated limitations on design freedom. Furthermore, designing material characteristics may open up avenues to unprecedented designs with optimal materials. This dissertation research presents integrated design methodologies for the system-level performance-driven design of structural geometry and viscoelastic material properties. By relaxing unnecessary assumptions and optimizing system-level performance by searching the rich spectrum of possible design options throughout the combined structural and material design space, the studies in this dissertation seek to obtain design improvements, which previously were inaccessible using conventional design paradigms and assumptions.

Achieving this integrated design of structural geometry and viscoelastic material properties has many underlying challenges. One of the main challenges is how to formulate design representations that can efficiently and effectively model the system behavior within the limits of physics, but are not restrictive with respect to other factors to allow full design exploration freedom. Another challenge comes from the numerical implementations and limits on computational resources available to design engineers. Higher-fidelity models or models with complex behavior (e.g., viscoelastic stress relaxation) are generally more expensive to solve. However, the computational cost of numerical models is a crucial factor in the success of integrated and multidisciplinary design optimization. Not all models are design-

appropriate. Specifically, quantities defining viscoelastic constitutive relations are interrelated to each other, and not all are independently controllable. Such challenges obstruct design with and of complex materials and integrated design associated with these material models. Thus, identifying underlying challenges and overcoming them are the main purposes of this dissertation research.

This dissertation is organized into two parts. The chapters in Part I present methodologies for designing surface texture geometries and other challenging design problems. Studies in this part present surface texture parameterizations for enhancing the lubricated frictional performance indices by eliminating unnecessary design constraints (Chapter 2), high-dimensional design optimization of surfaces texture using linearization, sequential linear programming, and trust-region methods (Chapter 3), and novel efficient sampling and implicit constraint generation methods for multiobjective surrogate-based optimization for challenging problems (Chapter 4). The chapters in Part II present integrated design studies and methodologies that apply to the design problems of viscoelastic material systems. Studies in this part present numerical methods for efficiently solving viscoelastic stress relaxation with convolution integrals (Chapter 5), a design-appropriate continuous stress relaxation spectra design representation and its use in the linear viscoelastic design problem (Chapter 6), and method for a simultaneous design of surface texture and non-Newtonian lubricant properties using nonlinear viscoelastic models to achieve better tribological performance beyond the results of the study presented in the earlier chapter that demonstrated surface texture design (Chapter 7).

The methodologies and design studies presented in this dissertation have an impact on exploring previously-unexplored design spaces from an integrated structural and material systems design perspective. The contributions presented in this dissertation open up new possibilities for design engineers to better use complex materials in the system-level performance-driven design studies incorporating a new material design paradigm.

To Seung Ae and Yonjin.

Acknowledgments

I would like to express my deepest gratitude and appreciation to my advisor, Professor James Allison, for his guidance and support. I could not have completed my dissertation without his constant care and valuable advice. I would also like to extend my most profound appreciation to my co-advisor, Professor Randy Ewoldt, for his thoughtful guidance and support. I must also thank my current and past collaborators, Dr. Jonathon Schuh, Dr. Rebecca Corman, Mr. Albert Patterson, and Mr. Chendi Lin, for their unparalleled knowledge and helpful contributions in my research projects. I learned a lot from all of my colleagues at the Engineering System Design Laboratory (ESDL) and the Ewoldt Research Group. Especially, I could not have been fabricated the experimental specimen without Mr. Albert Patterson's meticulous help. In addition, I learned a lot about numerical methods of control co-design from Dr. Daniel Herber, spacecraft attitude control systems from Mr. Vedant, rheometer techniques from Dr. Jonathon Schuh and Mr. Samya Sen, and various design-related insights from Dr. Danny Lohan and Mr. Satya Peddada. Much of my work has been inspired by and done with their help.

I have to sincerely thank my parents for their enormous love, sacrifice, and unlimited support throughout my life. Without their support and encouragement, I would not have even thought of starting this long academic journey. I would especially like to thank my wife, Seung Ae, for her countless support and encouragement with love. She has been with me for all these years, and I could not be any happier than I am with her. My son Yonjin continuously provided me with joy and relaxation that were very necessary during this challenging period of academic endeavor. I thank my sister Yeonjoo and her family for their

considerations and support while pursuing my doctorate abroad. I thank my family-in-laws for all their prayer and support. Especially, I am so grateful for my mother-in-law and her love. I could not have done this without the full support from all my family members. I also thank members of New Life Korean Church of Champaign County for their prayer and support. Finally, I would like to express my most enormous gratitude and honor to God, who has been my strength and ability in my whole life.

This study was supported in part under National Science Foundation Grant No. CMMI-1463203, Engineering Research Center for Compact and Efficient Fluid Power (supported by the National Science Foundation under Grant No. EEC-0540834), The Procter & Gamble Company, and National Science Foundation Grant No. CMMI-1653118. The findings and conclusions in this dissertation do not necessarily reflect the view of the funding agencies.

Table of Contents

List of Tables . . . . **xi**

List of Figures . . . . **xii**

List of Abbreviations . . . . **xvii**

List of Symbols . . . . **xix**

Chapter 1 Introduction **1**

I Methodologies for Surface Texture Design 6

Chapter 2 Arbitrary Surface Texture Design Enhances Full-Film Lubrication Performance **7**
- 2.1 Summary 7
- 2.2 Introduction 8
- 2.3 Problem Description 9
- 2.4 Surface Parameterization Method 11
  - 2.4.1 Cylindrical Textures 14
  - 2.4.2 Inclined plane spanning the full disk sector 14
  - 2.4.3 Other low-order design representations 15
  - 2.4.4 Two-dimensional cubic spline interpolation 15
- 2.5 Flow Simulation Method 17
  - 2.5.1 Reynolds Equation 17
  - 2.5.2 Boundary Conditions 18
- 2.6 Design Optimization Method 20
  - 2.6.1 Multiobjective Optimization 20
  - 2.6.2 Multiobjective Optimization Formulation 21
  - 2.6.3 ε-constraint method 23
- 2.7 Results and Discussion 24
  - 2.7.1 Cylindrical Textures 24
  - 2.7.2 Inclined plane spanning full sector area 30
  - 2.7.3 Arbitrary continuous texture designs 32
  - 2.7.4 Comparison of optimal designs 36
  - 2.7.5 Computational expense comparison 40

2.7.6 Limitations . . . 41
2.8 Conclusion . . . 43

Chapter 3 Efficient Design of Textured Surface Lubrication Using Linearization . . . 45
3.1 Summary . . . 45
3.2 Introduction . . . 46
3.3 Problem Formulation . . . 47
3.3.1 Problem Statement . . . 47
3.3.2 Numerical Model for Texture Surface Hydrodynamics . . . 48
3.3.3 Multiobjective Optimization . . . 55
3.3.4 Trust-Region and Step Size . . . 56
3.4 Verification . . . 59
3.5 Results and Discussion . . . 59
3.6 Conclusion . . . 62

Chapter 4 Efficient Sampling and Implicit Constraint Management Methods for Multiobjective Adaptive Surrogate-Based Optimization . . . 65
4.1 Summary . . . 65
4.2 Introduction . . . 66
4.2.1 Background and Related Work . . . 66
4.2.2 Challenges . . . 68
4.2.3 Summary of Contributions . . . 70
4.3 Methods . . . 71
4.3.1 The MO-ASMO Framework Structure . . . 71
4.3.2 Exploration Sampling (Initial and Update Stages) . . . 75
4.3.3 Exploitation Sampling (Update Stage) . . . 76
4.3.4 Selecting Validation Samples . . . 78
4.3.5 Modeling the Region of Invalid Inputs . . . 79
4.3.6 Stopping Criteria . . . 82
4.4 Test Problems . . . 84
4.4.1 P3: Valley-Shaped Constraint Function . . . 85
4.4.2 P5: Quarter-Car Suspension Design Using Viscoelastic Damper Problem . . . 86
4.5 Results and Discussions . . . 89
4.5.1 P1: Chakong and Haimes Function . . . 89
4.5.2 P2: Osyczka and Kundu Function . . . 91
4.5.3 P3: Valley-Shaped Constraint Function . . . 92
4.5.4 P4: DTLZ1 Function . . . 94
4.5.5 P5: Quarter-Car Suspension Design Using Viscoelasticity . . . 96
4.5.6 P6: Design of Viscoelastic Lubricant and Texture Geometry Using Giesekus Fluid . . . 98
4.5.7 Discussion on Sampling for Exploration and Exploitation . . . 100
4.6 Conclusions . . . 103

II Integrated Design With Viscoelasticity 106

Chapter 5 Numerical Design With Viscoelasticity: Survey, Efficient Strategies, and Outlook 107
5.1 Summary 107
5.2 Introduction 108
5.3 Linear Viscoelasticity 110
    5.3.1 Stress-Strain Relation for Linear Viscoelastic Materials 110
    5.3.2 Boltzmann Relaxation Modulus Function in Design 111
5.4 Survey and Analysis of Numerical Methods for Convolution Integrals 116
    5.4.1 Frequency-Domain Method 116
    5.4.2 Time-Domain Integration of Convolution Integral, Method 1 119
    5.4.3 Time-Domain Integration of Convolution Integral, Method 2 121
5.5 Efficient Time-Domain Methods for Convolution Integrals 122
    5.5.1 Time-Domain Truncation Technique for Efficient Computation 122
    5.5.2 Linear Time-Invariant State-Space Approximation 123
    5.5.3 Derivative Function Surrogate Model for Linear Time-Invariant State-Space Approximation 128
5.6 Practical Examples 131
    5.6.1 Simple Demonstration of State-Space Approximation of Linear Viscoelasticity 131
    5.6.2 Strain-Actuated Solar Arrays for Spacecraft Attitude Control Assisted By Viscoelastic Damping 132
5.7 Conclusions 134

Chapter 6 Continuous Relaxation Spectra Description for Design With Linear Viscoelasticity 137
6.1 Summary 137
6.2 Introduction 138
6.3 Methods 139
    6.3.1 Design-Appropriate Material Descriptions 139
    6.3.2 Relaxation Spectrum Representation 142
    6.3.3 Conversion Between Spectrum and Modulus 145
6.4 Reduced-Dimensionality Material Description 148
6.5 Viscoelastic Material Functions 149
6.6 Design Problem With Linear Viscoelasticity 151
6.7 Results 154
6.8 Conclusion 160

Chapter 7 Simultaneous Design of Non-Newtonian Lubricant and Surface Texture Using Surrogate-Based Multiobjective Optimization 162
7.1 Summary 162
7.2 Introduction 163
7.3 Formulation 168
    7.3.1 Non-Newtonian Fluid Models 168

7.3.2 Design Problem Formulation 173
7.4 Methodology 175
7.4.1 Solution Procedures for Fluid Flow 175
7.4.2 Design Procedures 178
7.5 Results and Discussion 181
7.5.1 Case 1: Lower-Fidelity Model With CEF Fluid 181
7.5.2 Case 2: Higher-Fidelity Model With Giesekus Fluid 185
7.5.3 Case 0: Newtonian Fluid Model Case Result 188
7.5.4 Comparisons and Discussion 190
7.6 Conclusion 197

Chapter 8 Conclusions and Outlook 199
8.1 Summary of Contributions 199
8.2 Extension of Dissertation Research 205
8.3 Outlook 207
8.4 Concluding Remarks 209

Appendices 211

Appendix A Viscoelastic Materials and Pipkin Space 212
A.1 Dimensionless Groups for Viscoelasticity 212
A.2 Pipkin Space 213

Appendix B Derivation of CEF-Reynolds Equation 214
B.1 Perturbation Solution 216
B.2 CEF-Reynolds Equation 220

Appendix C Experimental Validation and Sensitivity Analysis of Fluid and Texture Solvers 222
C.1 Experimental Validation Using Cone-and-Plate Rheometer 222
C.2 Solver Parameter Sensitivity Analysis 224

Appendix D Support Vector Domain Description 226

References 228

List of Tables

2.1 Cylindrical texture surface parameters 14
2.2 Spline interpolated textured surface parameters 16
2.3 Comparison of average computation cost per single scalarized optimization problem and system performance obtained from ε-constraint method and IP algorithm 40

3.1 Comparison of SLP to the full NLP result where the reference results from the NLP is used as the design fed into the SLP solution method 59
3.2 Computational Time to Find An Optimal Point (on Average) 62
3.3 Relative Computational Time Comparison 62

4.1 List of the test problems 84
4.2 Parameter values used in models of P5: Quarter-car design problem 86

6.1 Select list of continuous spectra model parameterizations 143

7.1 Fluid models used for design in this study and corresponding solver governing equations 164

C.1 Result of differential sensitivity analysis for the CEF-Reynolds solver parameters 225
C.2 Result of differential sensitivity analysis for the Giesekus-3D solver parameters 225

List of Figures

1.1 Diagram for representing the structure of the simultaneous analysis and design (SAND), an multidisciplinary design optimization (MDO) architecture 2

1.2 Performance indices are compared in the objective function space for texture designs with different parameterizations and constraints 3

2.1 Textured surface design problem setup adapted from experiments conducted by Schuh and Ewoldt 10

2.2 An example of texture height profile contours shown for a design domain sector and for a full disk 11

2.3 Mesh shapes and node point structure for design representation and flow simulation 12

2.4 Alternative texture shape design representations 13

2.5 The ε-constraint method converts a multiobjective optimization problem (MOP) to multiple single-objective optimization problems (SOPs) 23

2.6 Objective function contours based on a comprehensive sampling of the cylindrical texture design 25

2.7 Comparison between the Reynolds equation and the Navier-Stokes equation solutions 26

2.8 Geometry, shear stress, and pressure fields of optimized cylindrical texture designs in symmetric and asymmetric configurations 28

2.9 Geometric texture profile level-sets for asymmetric cylindrical textures with various angles (β) 29

2.10 Pressure field level-sets for asymmetric cylindrical textures with various angles (β) 30

2.11 Geometry, shear stress, and pressure field of the surface texture with inclined plane spanning the full sector area 31

2.12 Optimal designs for the cylindrical design exploration and the inclined plane spanning the full sector area studies. 32

2.13 Optimal texturing of an arbitrary but symmetric surface approaches a flat plate; symmetric texturing is unable to produce normal force 33
2.14 Geometric texture profile level-sets for optimized surface textures with spline design representation 34
2.15 Pressure field level-sets for optimized surface textures with spline design representation 35
2.16 Comparison of optimal designs in the objective function space for all design studies presented in this study 37
2.17 Comparison of geometric texture profile level-sets of optimal designs for N =3 to 7 at $F_N = 3$ [N] 38
2.18 Comparison of depth profiles: cross-sectional view of optimal designs, spline design representation cases with N =3, 5, 7, and $F_N = 3$ [N] 39

3.1 Benchmark design used as a starting design point for optimization studies . . 48
3.2 Schematic showing how the ε-constraint method is used for this problem . . 55
3.3 Optimal design results of two sample disk surfaces in a single sector view . . 60
3.4 Optimal design results of two sample texture shapes in the full-disk view . . 60
3.5 Comparison of the Pareto sets obtained using the nonlinear program (NLP) method and the sequential linear programming (SLP) method results obtained in this study 61

4.1 High-level flow chart of the proposed MO-ASMO framework 71
4.2 Implicit constraint generation based on the invalid input data using the support vector domain description (SVDD) method 81
4.3 Domain for computing hypervolume (HV) metric 84
4.4 Case P3: Valley-shaped constraint function 85
4.5 Case P5: Quarter-car suspension model with linear and viscoelastic dampers (VEDs) 87
4.6 Summary of results for case P1: Chakong and Haimes function 90
4.7 Summary of results for case P2: Osyczka and Kundu function 92
4.8 Summary of results for case P3: Valley-shaped constraint function 93
4.9 Comparison of results for case P3 with and without using the constrained sampling strategy 94
4.10 Summary of results for case P4: DTLZ1 function 95
4.11 Pareto-optimal solutions of P4: DTLZ1 function with 5 objective functions and 14 decision variables 96

4.12 Summary of results for case P5: quarter-car suspension design using viscoelastic damper problem 97
4.13 Solutions for case P5 visualized in parametric design space and material function space 98
4.14 Summary of results for case P6: design of viscoelastic lubricant and texture using the Giesekus fluid problem 99
4.15 Predicted Pareto-optimal solutions as the MO-ASMO algorithm refines the surrogate model 101
4.16 Convergence of MO-ASMO iterative refinement is presented for different exploitation and exploration sampling ratios, based on P2: the Osyczka and Kundu problem 102

5.1 Relaxation modulus functions (kernel function) originally created by the analytical equation and fitted using the LTISS are compared 130
5.2 Simple simulation to obtain the stress with the sinusoidal strain rate input to the viscoelastic element 130
5.3 Spacecraft numerical model and revolute damping joints with 2D shear stress-strain and 1D reduced-order models 133
5.4 Optimal designs based on the 1D reduced-order models with varying maximum control torque constraints 134

6.1 All linear viscoelastic (LVE) material functions are related to each other in the limit of LVE regime 140
6.2 A selection of commonly used continuous spectra models 144
6.3 An arbitrary continuous relaxation spectrum function in log-normal distribution is converted to the corresponding relaxation modulus 145
6.4 Various approximation methods for the relaxation spectrum using the relaxation modulus function is presented and compared 147
6.5 The quarter car suspension model representing dynamic model of one-fourth of a car suspension design 152
6.6 Sample input road profile used for designing the quarter car suspension . . . 153
6.7 The objective function space for the quarter car suspension design problem with VED 155
6.8 Optimal design results in the design space for the quarter car suspension with the multimode Maxwell models 156

6.9 Optimal design results in design space for the quarter car suspension with the log-normal and the BSW models 157
6.10 Viscoelastic material functions are reduced to three characteristic quantities and plotted in the Ashby-style cross-property plot 159

7.1 A lubricated periodic surface texture design problem in a rotational tribo-rheometer setting 165
7.2 Explored designs and optimal solutions (nondominated designs) for the CEF model case displayed in the objective function space 182
7.3 Sample textured sector and fluid designs in the Pareto set from the CEF model case 182
7.4 Viscoelastic material functions of corresponding sample optimal designs from the CEF model case 183
7.5 Explored designs and optimal solutions (nondominated designs) for the multi-mode Giesekus model case in the objective function space 185
7.6 Sample textured sector and fluid designs in the Pareto set from the multi-mode Giesekus model case 186
7.7 Viscoelastic material functions of corresponding sample optimal designs from the Giesekus model case 186
7.8 Explored designs and optimal solutions (nondominated designs) for the Newtonian fluid model case in the objective function space 188
7.9 Sample textured sector designs in the Pareto set from the Newtonian fluid model case 189
7.10 A comparison of the optimal solutions (Pareto set) of CEF, Giesekus, and Newtonian fluid models in the objective function space 190
7.11 Sample textured disk designs in the Pareto set from all three fluid model (CEF, Giesekus, and Newtonian) cases 194

8.1 Models used in design optimization can be conceptually presented in three-axis coordinate system 208
8.2 A comprehensive design framework that combines higher system-level design and lower microscopic mechanics of material-level design processes 209

A.1 Pipkin Space 213

B.1 Periodic cell of textured surface in cylindrical coordinates 214

C.1 Comparison of raw torque T and raw normal force F_N data from experiments using a cone-and-plate rheometer geometry and simulations using CEF-Reynolds and Giesekus-3D solvers 223

D.1 A test case showing how the SVDD algorithm describes boundaries of the data point clouds 227

List of Abbreviations

ACS attitude control system.
ASM adaptive surrogate modeling.
BSW Baumgaertel-Schausberger-Winter.
CCD central composite design.
CCD control co-design.
CEF Criminale-Ericksen-Filbey.
CFL Courant-Friedrichs-Lewy.
DAE differential algebraic equation.
DFSM derivative function surrogate modeling.
DO direct optimization.
DO-EC direct optimization using ε-constraint.
DOE design of experiments.
DT direct transcription.
ED Euclidean distance.
EIL experiment-in-the-loop.
FDL force-directed layout.
FF full factorial.
GA genetic algorithm.
GHM Gola-Huges-McTavish.
GLL Gauss-Lobatto-Legendre.
HDMR high-dimensional model representation.
HEB high-dimensional, expensive, and black-box.
HV hypervolume.
IDE integro-differential equation.
IRF impulse-response function.
LHD Latin hypercube design.
LP linear program.
LTISS linear time-invariant state-space.

LVE linear viscoelastic.

MBDO metamodel-based design optimization.

MBO metamodel-based optimization.

MDO multidisciplinary design optimization.

MO-ASMO multiobjective adaptive surrogate model-based optimization.

MOEA multiobjective evolutionary algorithm.

MOP multiobjective optimization problem.

MPS mode-pursuing sampling.

NLP nonlinear program.

NSGA-II nondominated sorting genetic algorithm II.

ODE ordinary differential equation.

PBF Prony basis function.

PDE partial differential equation.

PDI polydispersity index.

PIB polyisobutylene.

PSO particle swarm optimization.

PSP Pareto set pursuing.

RBF radial-basis function.

SAND simultaneous analysis and design.

SASA strain-actuated solar array.

SB-MOP surrogate-based multiobjective optimization problem.

SBO surrogate-based optimization.

SLA stereolithography.

SLP sequential linear programming.

SOP single-objective optimization problem.

SSS significant sampling space.

SVDD support vector domain description.

VE viscoelastic.

VED viscoelastic damper.

WRT weighted residual technique.

List of Symbols

$\mathbf{0}$ zero matrix.
$\mathbf{A}$ coefficient matrix of linear constraint.
β angle of asymmetry.
$\underline{\beta}$ Lagrange multiplier vector.
$\underline{b}$ constant vector of linear constraint.
$\mathbf{C}$ constraint function $n \times m_c$ matrix of n designs.
$\underline{c}$ vector of nonlinear constraints.
$\mathbf{De}$ Deborah number.
Δ residual of convergence metrics.
Δ_k trust region radius.
Δt time step size.
$\boldsymbol{D}$ differentiation matrix.
$\mathbf{F}$ objective function $n \times m_f$ matrix of n designs.
F_N normal force.
$\underline{f}$ constant vector of system of equations.
$\underline{f}$ vector of objective functions.
$\dot{\gamma}$ shear rate.
G', G'' dynamic modulus.
G stress relaxation modulus.
h gap height.
h_0 nominal gap height.
$\boldsymbol{H}$ gap height values in diagonal matrix.
H relaxation spectrum.
$\underline{h}$ gap height values in vector.
$\mathbb{I}$ surrogate model for region of invalid inputs.
$\boldsymbol{I}$ identity matrix.
$\underline{i}$ boolean vector that indicates which design points are of interest.
J creep compliance.

K_G Gaussian kernel.

$\boldsymbol{K}$ coefficient matrix of system of equations.

λ relaxation time.

L retardation spectrum.

m number of variables in a vector.

$\mathbb{M}$ surrogate model for expensive functions.

$\boldsymbol{M}$ quadrature weight values in diagonal matrix.

n number of design points in a matrix of variables.

$N_{\textbf{tex}}$ total number of periodic cells on the thrust bearing.

φ periodic spacing of the surface texture.

ϕ basis function.

ψ slope constraint for texture design.

R_c radius to the center of the texture.

Re Reynolds number.

R_i inner radius.

$\boldsymbol{R}$ radius values in diagonal matrix.

R_o outer radius.

R_t radius of the texture.

$\mathbf{S}$ displacement of force-directed dynamic sample relocation.

$\underline{s}$ magnitude of force-directed dynamic sample relocation.

τ^* nondimensional shear stress.

$\mathcal{V}$ hypervolume.

$\mathbf{Wi}$ Weissenberg number.

$\underline{\xi}$ state vector.

$\mathbf{X}$ design variable $n \times m_x$ matrix of n designs.

$\underline{x}$ vector of design variables.

Chapter 1

Introduction

Engineering design often involves comprehensive decision-making activities, including problem definition, formal representation, and optimization processes, spanning multiple interdisciplinary domains. Understanding interfaces between disciplinary areas opens opportunities for design improvement via a deep understanding of underlying mechanisms across the fields, and for the discovery of novel designs and concepts, leading toward unprecedented design innovations. Integrated design is a holistic approach that aims to solve design problems with many complications, including subproblems, multidisciplinary involvement, multiobjective optimization problems (MOPs) with conflicting design decisions, and many other design couplings all together. Figure 1.1 shows a multidisciplinary design optimization (MDO) architecture, referred to as simultaneous analysis and design (SAND) [1]. The integrated design approaches often utilize techniques, such as the SAND, to resolve design couplings associated with the problem in a holistic way [1, 2]. The integrated design approach is a powerful tool to enhance both design outcomes and design processes of problems with interdisciplinary design interactions.

Human activities in engineering design have played a significant role in building better designs with engineering knowledge. To achieve better performance and quality, engineers set design objectives for their system or product, while constraining the design space to meet various required conditions, such as laws of physics, budgets, dimensions, robustness, and other realistic barriers. However, these constraints significantly limit the freedom to explore design alternatives. Topics in design research include identifying more accurate, less restrictive constraints that enable an expanded design space to achieve unprecedented

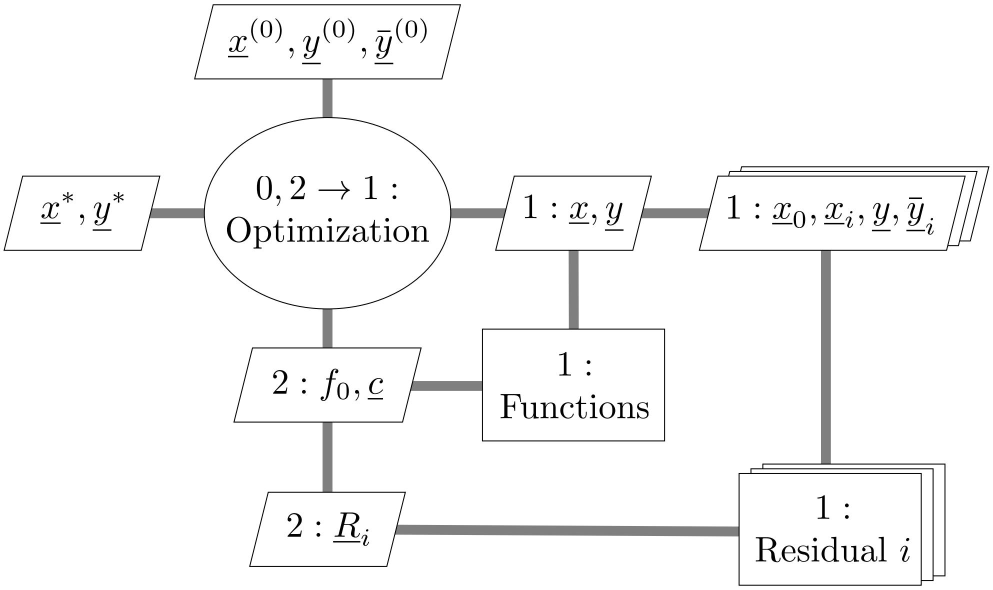

Figure 1.1: Diagram for representing the structure of the SAND, a MDO architecture [1, 2]. The figure adapted from Zhang et al. [3]. This method is utilized in studies presented in Chapters 3 and 5.

performance enhancement [4–6]. This effort can be made during all activities of design processes, and specifically by releasing unnecessary assumptions that limit the design to have specific geometrical shapes [4], topologies [7], architectures [8], manufacturing processes [6], and design processes [9]. Figure 1.2 demonstrates a significant performance increase by releasing geometric constraints that are widely used, but unnecessary. Starting from ‘circular’ symmetric and asymmetric texture profiles (which are shown as red circle and ✡ markers), releasing the area confining dimple shaped texture significantly reduced the friction (yellow + marker), and allowing free-form surface geometry simultaneously improved both frictional (apparent viscosity) and load-carrying capacity (normal force) metrics by over an order of magnitude (markers denoted as ‘spline’).

Along with conceptual, structural, architectural, and many other phases of design activities, engineering design processes often involve material selection, which influences the overall success of the design, but is overlooked in many cases. Engineers conventionally select simple materials, including linear elastic solids and Newtonian fluids, and optimize placement of the

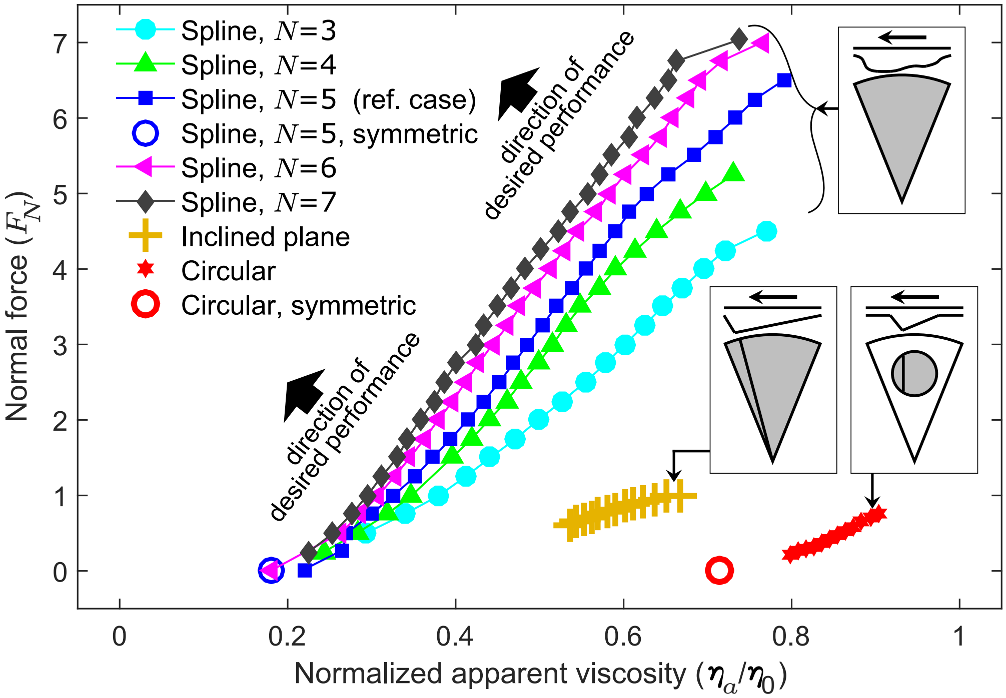

Figure 1.2: Performance indices are compared in the objective function space for texture designs with different parameterizations and constraints. Designs are improved significantly by increasing design flexibility via the texture surface representation and eliminating unnecessary design restrictions, interpreted as predefined shapes.

material and its geometry within the limitation of behaviors and responses of these simple materials. However, this intuitive selection of materials frequently limits the design freedom for seeking better performance, and mostly results in obtaining suboptimal designs. In such circumstances, allowing complex materials, particularly viscoelastic (VE) fluids and soft solids, as options for the material choice, will remove associated limitations on design freedom [10, 11]. Further, allowing more freedom via designing the complex materials may enable novel system performance [12–14].

This dissertation research presents methods for more fully utilizing design freedom by creating (1) more general geometric parameterizations, (2) design-appropriate fluid and structure representations, and (3) efficient design optimization algorithms and formulations to achieve better engineering designs. In addition, this dissertation presents analyses based on (4) design knowledge and interfacial mechanisms extracted from design solutions obtained through the activities presented in this research.

The dissertation is organized into two parts. The chapters in Part I present methodologies for designing surface texture geometries and other challenging design problems. Chapter 2 addresses different parameterizations that describe texture design in full-film lubricated sliding contact. The studies show a development of design representations that eliminates unnecessary design restrictions, and explores more general design spaces to achieve novel system performance beyond what was available with predefined texture shapes. Chapter 3 introduces a sequential linear programming (SLP) approach that can be used to handle high-dimensional design freedom beyond the parameterization approach used in Chapter 2. Due to nonlinearity associated with the coupling between formulations for design and physics, SAND was utilized to weakly couple these two domains. The final problem is linearized and solved sequentially using a trust-region method. Chapter 4 includes novel sampling strategies and an implicit constraint generation and management method for surrogate-based multiobjective optimization problems (SB-MOPs). The multiobjective adaptive surrogate model-based optimization (MO-ASMO) framework presented in this chapter is specifically developed for resolving design challenges that texture design problems exhibit. However, the study also demonstrated the capability of MO-ASMO framework for high-dimensional challenging problems, extending its impact beyond design studies presented in this dissertation.

The chapters in Part II present integrated design studies and methodologies that apply to the design problems of VE material systems. Chapter 5 addresses problem characteristics and challenges when designing *with* and *of* VE materials. This chapter then presents a survey and analyses of computational methods for solving convolution integral terms to calculate VE stress relaxation, with additional techniques that can further reduce computational effort. A time-domain truncation technique is introduced, and the use of derivative function surrogate modeling (DFSM) combined with a computationally-efficient linear time-invariant state-space (LTISS) system approximation for the convolution integral is proposed. Chapter 6 presents the use of design-appropriate models. The continuous relaxation spectra design representation is analyzed, relations and conversions between rheological quantities are discussed, and these concepts are demonstrated using a test problem. Chapter 7 presents the integrated design of surface textures and nonlinear VE lubricant materials using the surrogate-based multiobjective optimization approach to achieve both low friction and high load-carrying capacity, with the MO-ASMO framework introduced in Chapter 4. Two different non-Newtonian fluid models (the Criminale-Ericksen-Filbey (CEF) and multimode Giesekus models) are used in solving this simultaneous MOP. Due to computational complexity and observed solver instabilities to certain ranges of design inputs, the constraint boundary generation method based on support vector domain description (SVDD) is utilized to adaptively construct and refine estimates of implicit boundaries to prevent more samples from being created in the regions that are likely to lead to simulation failure.

Finally, Chapter 8 summarizes the studies presented in this dissertation and provides concluding remarks. As a whole, this dissertation presents a system-level performance-driven material design paradigm, and integrated structural geometry and complex materials (particularly VE fluids) design studies are found throughout the two parts and six main chapters (Chapters 2–7). The presented studies are interrelated to each other as part of a strategy to propose comprehensive design methodologies that may help advance engineering design with complex material systems. With the new paradigm of integrated material design in a system-level approach, we anticipate opening up more expansive possibilities for better designs by exploiting material properties and structures. The integrated design strategies presented in this dissertation are expected to enable exploitation of previously-unexplored design domains with truly new materials, new methodologies, and new design principles that potentially enable new products and systems with more efficient, cost-effective, and even life-changing possibilities that lead to opportunities for societal benefits, including more sustainable ways of development.

Part I

Methodologies for Surface Texture Design

Chapter 2

Arbitrary Surface Texture Design Enhances Full-Film Lubrication Performance[1]

2.1 Summary

Minimizing energy loss and improving system load capacity and compactness are important objectives for fluid power systems. Recent studies reveal that micro-textured surfaces can reduce friction in full-film lubrication and that asymmetric textures can reduce friction and increase normal force simultaneously. As an extension of these previous discoveries, we explore how enhanced texture design can maximize these objectives together. We design surface texture using a set of distinct parameterizations, ranging from simple to complex, to improve performance beyond what is possible for previously investigated texture geometries. Here we consider a rotational tribo-rheometer configuration with a fixed textured bottom disk and a rotating top flat disk with a controlled separation gap. To model Newtonian fluid flow, the Reynolds equation is formulated in cylindrical coordinates and solved using a pseudospectral method. Model assumptions include incompressibility, steady flow, constant viscosity, and a small gap height to disk radius ratio. Multiobjective optimization problems (MOPs) are solved using the epsilon-constraint method along with an interior-point nonlinear program (NLP) algorithm. The trade-off between competing objectives is quantified, revealing mechanisms of performance enhancement. Various geometries are explored and optimized, including symmetric, asymmetric circular dimples, and novel arbitrary continuous texture geometries represented using two-dimensional cubic spline interpolation, in this study. Shifting

---

[1] Reprinted by permission from ASME: Journal of Mechanical Design (Lee, Schuh, Ewoldt, and Allison. Enhancing full-film lubrication performance via arbitrary surface texture design. *J. Mech. Des.* 139(5): 053401), ©2017

from simple dimpled textures to more general texture geometries resulted in significant simultaneous improvement in both performance metrics for full-film lubrication texture design. An important qualitative result is that textures resembling a spiral blade tend to improve performance for rotating contacts.

2.2 Introduction

Friction is a significant source of energy loss in mechanical components. The influence of surface roughness within lubricated hydrodynamic contacts has been well-studied in the tribology community. Creating micro-dimples at frictional contact interfaces is known to be effective in reducing frictional losses [15–17]. Furthermore, recent studies proposed a possibility that textured surfaces for sliding hydraulic interfaces can reduce effective friction, improve sealing, and increase the load capacity simultaneously by creating texture in favorable shapes and dimensions [18–20]. However, the roughened or dimpled surfaces in previous studies were restricted to relatively simple shapes, such as predefined shapes, randomly roughened surfaces, and macroscopic sinusoidal textures [17, 21–29]. Although most existing studies in the literature include either symmetric texture profiles or asymmetry only for the top profile of texture rim perimeters, Refs. [26, 27, 30] showed that generating normal force with asymmetric depth profiles is more effective than with symmetric depth profiles. Due to recent manufacturing advancements, such as additive manufacturing and electric/electrochemical micromachining, textures with more general geometries and scales are realizable for hydrodynamic lubrication surfaces [18, 31, 32]. Here more general texture geometries are investigated.

Film lubrication involves lubricant flow, which is often modeled using the fluid flow governing equations (e.g., Navier-Stokes equations). Solving general forms of these equations is computationally expensive, limiting the utility of such models for design studies [19, 33]. In hydrodynamic lubrication, however, the distance between sliding surfaces is much smaller than other length scales in the system; this allows the governing equations for flow to be simplified to the Reynolds equation, which is more favorable for computation [34]. In a recent study, the Reynolds equation was solved for the full-film lubrication problem with circular dimples using the pseudospectral method [35]. This numerical method exhibits exponential convergence with increasing order of polynomial basis function, is computationally efficient, and has been validated against experiments [35, 36].

Here we are building upon this pseudospectral solution method for the Reynolds equation to explore a much wider range of surface texture designs with the primary objective of friction reduction. Arbitrary continuous texture shapes are optimized using effective parameterization techniques. Important existing options for describing curved shape designs include analytical approaches, basis vectors, domain elements, Fourier descriptors, polynomial functions, response surfaces, and splines [37, 38]. These methods are often used in aeronautical system design (e.g., airfoil shape optimization [37]) and other applications (e.g., photo-voltaic internal reflection texture design [39]). The specific parameterization used in this study involves spline functions defined in two orthogonal directions to represent arbitrary texture shapes in three-dimensional space.

2.3 Problem Description

The objective of the design problem in this study is to maximize the film lubrication efficiency and effectiveness by designing the shape of the textured surface using systematic methods. The experimental setup in Schuh and Ewoldt [30] revealed that asymmetric-depth-profile dimpled surface textures decrease frictional loss. Figure 2.1a illustrates the problem setup used for the previous experimental research. Based upon this configuration, we perform a more comprehensive computational study here enabled by more flexible texture surface design representation and exploration. A pair of gap-controlled disks are aligned axially and are separated by a Newtonian fluid. The rotating upper disk is flat, while the stationary bottom

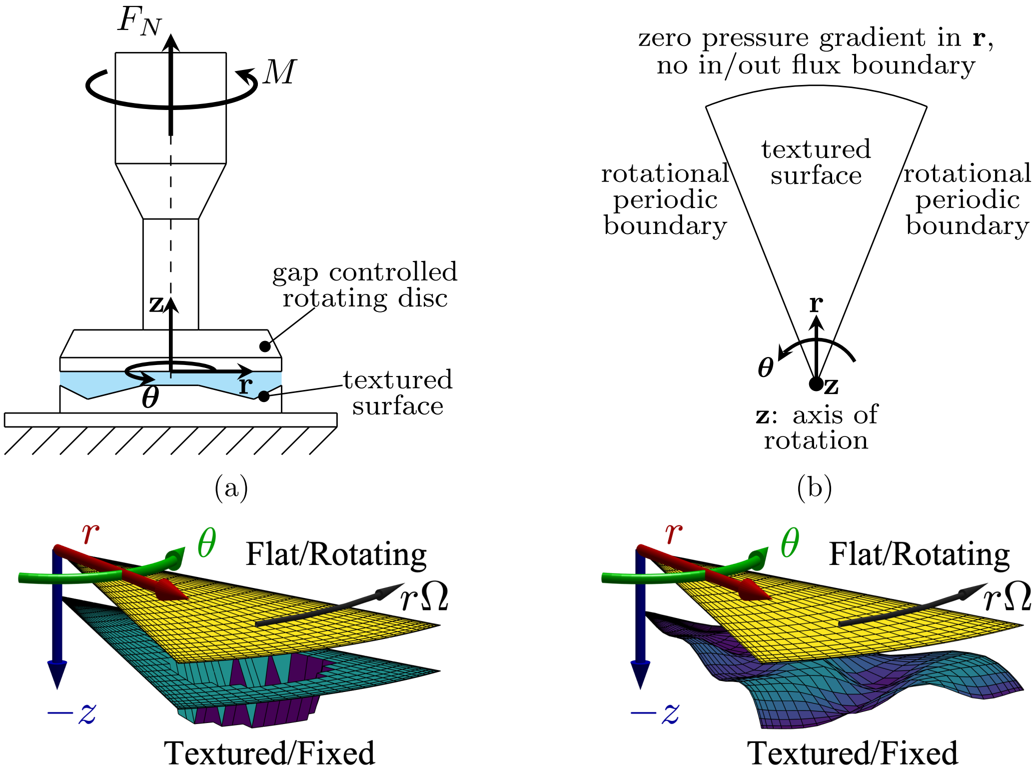

(a) (b)

(c) (d)

Figure 2.1: Textured surface design problem setup adapted from experiments conducted by Schuh and Ewoldt [30]. The periodic asymmetric dimpled textures used in the previous study are replaced here with arbitrary continuous texture shapes. (a) Front view of the experimental setup. (b) Top view of one textured surface periodic sector. (c) 3D view of circular symmetric dimpled periodic sector. (d) 3D view of arbitrary textured periodic sector.

disk is textured. All points of the surface in the design domain—illustrated in Fig. 2.1b—are defined using a moderate-dimension spline representation. The design domain is a periodic sector of the bottom disk instead of the entire disk. The full disk is divided into N_{tex} sectors. The number N_{tex} is an arbitrary choice, and $N_{\text{tex}} = 10$ is selected for the studies presented here. Future work may involve adjusting N_{tex}, or alternate domain representations, but is outside the scope of this study. Simulation results are equivalent to the behavior of a full disk with repeated sectors. This simplification reduces the computational expense and is assumed to be reasonable due to the rotational nature of the setup. The sector surface design is assumed to be periodic, i.e., the texture repeats and the boundaries of each sector match to preserve texture continuity. This is consistent with the $N_{\text{tex}} = 10$ repeating dimples in the

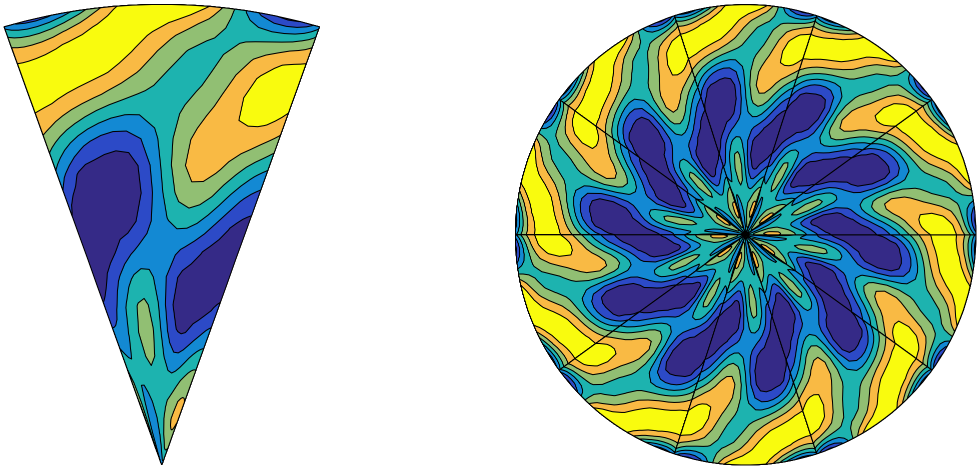
(a) (b)

Figure 2.2: An example of texture height profile contours shown for a design domain sector and for a full disk. Darker color corresponds to a lower surface level (larger gap height) (a) Design domain periodic sector. (b) Full disk shape.

experiments [30]. Figure 2.2 presents a visualization of how a repeated sector represents a periodic texture design for a full disk surface. While the design optimization process and the flow simulation are computed using the single-sector design domain given in Fig. 2.2a, the results correspond to physical behavior for a full disk shown in Fig. 2.2b due to periodic boundary conditions.

2.4 Surface Parameterization Method

In previous related work, surface textures have been described using very simple parameterizations. For example, one strategy assumes that surface texture features consist only of cylindrical dimples, either with flat or angled lower surfaces, and are parameterized using dimple diameter, depth, and lower surface angle [19, 30]. Another strategy prescribes a set of allowable surface textures (e.g., circle, ellipse, triangle) and selects among them by comparing performance [21, 25, 26]. Another study designed texture with respect to its top profile view, but maintained the gap height inside the texture at a fixed value [40]. This approach provides a general outline shape as a texture boundary, but still does not represent

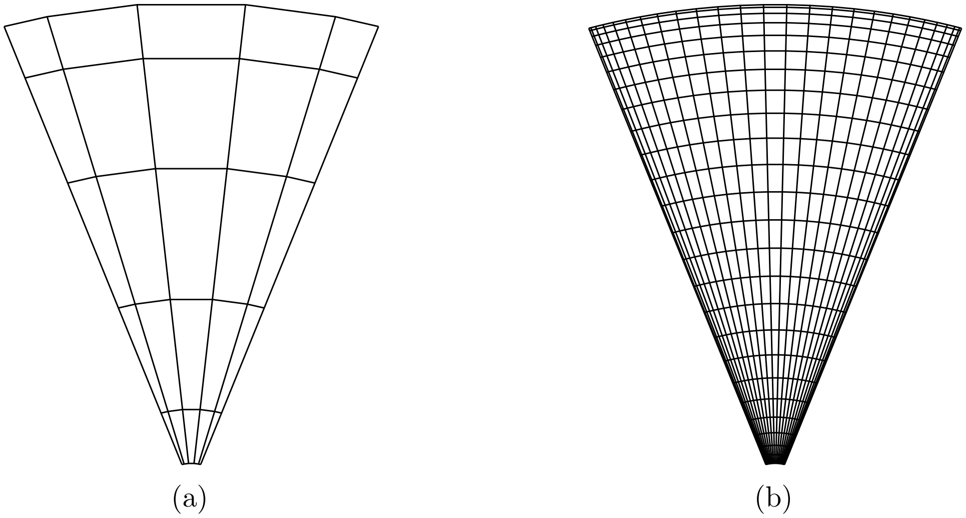
(a) (b)

Figure 2.3: Mesh shapes and node point structure for design representation and flow simulation. The mesh for a reduced-dimension cubic spline texture shape design representation is shown on the left. This design mesh is much more coarse than the mesh on the right that is required for accurate simulation. The surface geometry defined by the cubic spline is interpolated to determine all the height values at the fine mesh points required for simulation. (a) Coarse mesh (6×6 nodes) for design representation. (b) Fine mesh (26×26 nodes) for flow simulation.

a general height profile for texture design.

A core objective of the present study is to perform a design exploration of much more general texture designs as a means to gain greater insight into surface texture design for enhanced efficiency. One strategy is to simply use h_{ij}, the surface height at computational mesh nodes, as the surface design description. While this provides high accuracy and a high-resolution design description, it results in a large-dimension nonlinear optimization problem. Our current implementation of the optimization problem solution requires treating the simulation (i.e., in this study, lubricant flow computation) as a black box, necessitating finite difference calculations. While ongoing work is focused on investigating alternative implementations that leverage problem structure, such a large-dimension design representation is impractical for the present study. In previous work, it was determined for this system configuration that the coarsest accurate mesh for simulation involves 26×26 nodes (polynomial order $N = 25$, see Sec. 2.5.1 for detail) [35]. Using h_{ij} directly, accounting for periodic

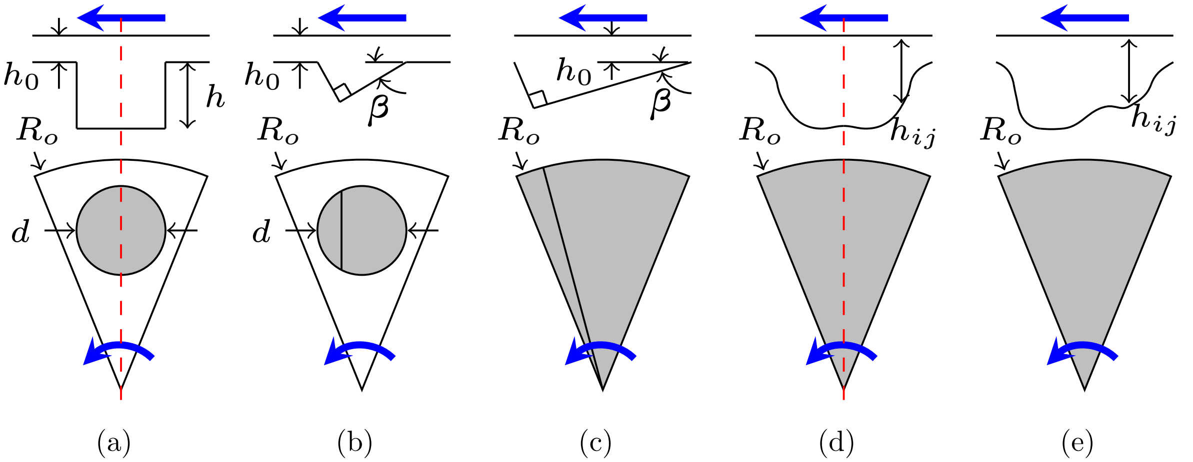

Figure 2.4: Alternative texture shape design representations. A cross-sectional view of each representation is shown in the top row, while a top view of each textured sector is shown in the bottom row. The gray area denotes the textured region (non-gray regions indicate unchanged flat surfaces). The top flat plates are rotating in the direction of the thick blue arrows, while the bottom textured surfaces are fixed. (a) Symmetric cylindrical texture. (b) Asymmetric cylindrical texture. (c) Asymmetric planar texture spanning the full sector area. (d) Arbitrary continuous texture with symmetry constraint. (e) Arbitrary continuous texture.

boundary constraints, would therefore require $(25 + 1) \times 25 = 650$ optimization variables. Therefore, a reduced-dimension design representation is needed[2]. As detailed below in Sec. 2.4.4, we use a two-dimensional cubic spline on a coarse mesh (Fig. 2.3a) for design representation and interpolate to a finer mesh for simulation (Fig. 2.3b).

We consider several types of textures, of varying design freedom, shown in Fig. 2.4. The simple angled cylindrical dimple textures from previous work are illustrated in Figs. 2.4a-2.4b. The aim here is to support the exploration of more general texture design shapes, as shown in Figs. 2.4c-2.4e, with reduced dimension, and to evaluate performance improvements available through these more general texture designs. The simplified cylindrical texture parameterization is reviewed first, followed by a description of a more general two-dimensional spline representation.

---

[2] Chapter 3 presents the solution of full-dimensional large scale version of the same design problem using the sequential linear programming (SLP) method [41].

Table 2.1: Cylindrical texture surface parameters

Item			symmetric cylinder	asymmetric cylinder
Disk radius	R_o	[mm]	20	20
Texture location	R_c	[mm]	14.3	14.3
Sector division	N_{tex}	[–]	10	10
Nominal gap	h_0	[mm]	0.269	0.269
Texture radius	R_t	[mm]	$1 \leq x_1 \leq 4$	$1 \leq x_1 \leq 4$
Texture depth	h	[mm]	$0 \leq x_2 \leq 2.5$	–
Inclination	β	[°]	0	$0 \leq x_3 \leq 20$

2.4.1 Cylindrical Textures

The previous experimental setup involved a single cylindrical dimple with a fixed location in each sector. The asymmetric texture angle was varied in those previous studies to gain an initial understanding of this behavior [19, 30]. Here we build upon these initial studies by optimizing this dimpled texture design. The complete set of cylindrical dimple parameters is listed in Table 2.1. Design variables include the radius and the depth (x_1, x_2) for symmetric textures or the radius and the angle (x_1, x_3) for asymmetric textures. Geometric configurations of these textures are illustrated in Figs. 2.4a–2.4b, along with the shape parameters. We used a nominal gap h_0 of 0.269 [mm] to compare to experiments; this value of h_0 is fixed and used as lower bound of the gap distance. Also, see Fig. 2.4b for a visualization of how the inclination β in Table 2.1 is defined in the cylindrical texture with an asymmetric height profile.

2.4.2 Inclined plane spanning the full disk sector

We will see that larger radius textures improve performance. With this observation, we can predict that if the texture area spans the full sector area, it may be possible to further improve performance. A new geometric parameterization is defined to demonstrate the effect of expanded texture area, where an entire sector is an inclined plane tilted at angle β, as shown in Fig. 2.4c. Note that this geometry is continuous but nonsmooth.

2.4.3 Other low-order design representations

Polynomial Texture

A few additional low-order design representations were investigated in addition to the cylindrical and inclined plane texture parameterizations. First, a unimodal polynomial function was used to generate the height profile by specifying the location of the peak function value. Height values at both periodic sides and the inner/outer boundaries were fixed to the nominal gap height (h_0). Numerical experiments indicated that this class of texture performed poorly, possibly because large local slopes could not be achieved. Detailed results for this case are omitted for brevity.

Radial Basis Function Texture

Radial-basis functions (RBFs) are used widely in approximating or interpolating functions. RBFs were tested as a texture geometry representation where the height and location of a number of thin-spline RBFs were used as design variables. Several challenges were discovered. Changing texture design in significant ways requires changing the number of RBFs used, which cannot be done during the optimization solution using continuous algorithms. In addition, the number of parameters required is large relative to the range of texture geometries that are accessible. Each RBF requires at least three parameters. RBFs do not provide a low-dimension representation, and do not support efficient design space exploration for this problem compared to the spline representation discussed next. Detailed results for this case are also omitted for brevity.

2.4.4 Two-dimensional cubic spline interpolation

Here we introduce a low-dimension texture design representation that supports the description of arbitrary continuous geometries. This provides enhanced design flexibility and the possibility of capitalizing on new mechanisms for improving fluid system performance. To describe

Table 2.2: Spline interpolated textured surface parameters

Item			symmetric sector	asymmetric sector
Disk radius	R_o	[mm]	20	20
Sector division	N_{tex}	[#]	10	10
Nominal gap	h_0	[mm]	0.269	0.269
Texture depth	h_{ij}	[mm]	$h_0 \leq x_{ij} \leq 1.5$	$h_0 \leq x_{ij} \leq 1.5$
Slope constraint	ψ	[°]	30	30

the full-sector texture design using a limited number of design variables, the height profile is specified at nodes of the coarse mesh shown in Fig. 2.3a. As a manufacturability constraint, the inclination angle between coarse mesh nodes is limited to a maximum of 30°. Detailed parameters used in this representation are given in Table 2.2. After specifying a low-resolution height profile, the two-dimensional spline representation is used to map this profile onto the fine computational mesh shown in Fig. 2.3b. This allows the surface texture design to be specified using a limited number of design variables, while still supporting high-resolution simulation. Coarse mesh node heights are the only design variables in this parameterization. Because of the periodic constraint at the left and right sector sides, the design variables include the height profile of only one of two sides. Thus, for $(N+1) \times (N+1)$ nodes, the number of design variables is $(N+1) \times N$. Alternatively, a texture symmetry constraint can be imposed. With symmetry, the number of design variables for $(N+1) \times (N+1)$ nodes is $\lceil (N+1)^2 / 2 \rceil$, where $\lceil \cdot \rceil$ is the ceiling function. Symmetric designs are investigated first, as shown in Fig. 2.4d, followed by studies of asymmetric designs, shown in Fig. 2.4e, that further improves system performance.

2.5 Flow Simulation Method

2.5.1 Reynolds Equation

The gap-controlled full-film shear flow is modeled following the study presented by Schuh et al. [36]. This model was based on physical experiments with surface textures and Newtonian fluids, where cavitation effects were not observed [30]. Therefore, the model chosen does not include cavitation, and any use of cavitation is outside the scope of this study. The Reynolds equation, given in Eq. (2.1), satisfies both mass and momentum conservation for an incompressible Newtonian fluid under the assumptions that (1) inertia terms are negligible, and (2) the gap is small compared to other length scales in the geometry [42].

$$\frac{1}{r}\frac{\partial}{\partial r}\left(rh^3\frac{\partial p}{\partial r}\right)+\frac{1}{r}\frac{\partial}{\partial \theta}\left(\frac{h^3}{r}\frac{\partial p}{\partial \theta}\right)=6\eta_0\Omega\frac{\partial h}{\partial \theta} \tag{2.1}$$

The pressure field $p\left(r,\theta\right)$ from Eq. (2.1) is used to calculate the velocity field $\underline{u}\left(r,\theta,z\right)$ in Eq. (2.2).

$$u_r = \frac{1}{2\eta_0}\frac{\partial p}{\partial r}\left(z^2-zh\right) \tag{2.2a}$$

$$u_\theta = \frac{1}{2\eta_0 r}\frac{\partial p}{\partial \theta}\left(z^2-zh\right)+r\Omega\left(\frac{h-z}{h}\right) \tag{2.2b}$$

Boundary conditions for velocity are $u_\theta = r\Omega$ and $u_r = u_z = 0$ at $z = 0$, and $u_\theta = u_r = u_z = 0$ at $z = h$. We use steady-state conditions with fixed angular velocity $\Omega = 10$ [rad/s] and constant viscosity $\eta_0 = 1.4$ [Pa s]. The Reynolds number, based on the nominal gap, is $\mathrm{Re} = \rho\Omega R_o h_0/\eta_0 = 0.033$, and this value can be applied to the predefined dimple shape texture cases. For the arbitrary continuous texture cases, the Reynolds number is instead computed based on the range of the gap, and can vary from 0.033 to 0.186. These values correspond to the experimental conditions of Schuh and Ewoldt [30], but the approach is general, and results can be made nondimensional by scaling with respect to viscous effects ($p \sim \eta_0 R\Omega/h_0$) [18].

The details of simulating the partial differential equation (PDE) in Eq. (2.1) are described in Ref. [36]. Briefly, the equation is discretized using the pseudospectral method, which is a variation of the weighted residual technique (WRT), where the PDE is solved in its variational form [43]. The resulting integrals for the variational form of the PDE are solved using Gauss-Lobatto-Legendre (GLL) quadrature, where the function evaluations occur at the GLL points and the quadrature weights are chosen optimally such that integrals of the solution are exact for polynomials of degree $2N-1$, where N is the number of evaluation points (shown as nodes in Fig. 2.3b). For all case studies presented here, a fixed number of computational mesh points, as illustrated in Fig. 2.3b, was used for the Reynolds equation solver. This computational mesh density is validated to be sufficient for accurate objective function prediction [35]. Since the Reynolds equation model is solved using the same mesh for the entire set of studies, its computational cost and prediction accuracy are independent of design representation fidelity. Full details of this methodology are given in Refs. [35, 36, 43, 44], where the model predictions have been validated against experiments from Refs. [30, 35].

A previous study emphasized that the dimensionless parameters are important for interpreting the physics of lubricated sliding contacts [18]. However, we do not use dimensionless parameters in flow simulation or in the optimization formulation. Analyses with dimensional variables in this study are still meaningful because similarity is maintained for the flow within the range of Reynolds numbers we are modeling. Results could be made dimensionless by scaling with respect to viscous effects [18].

2.5.2 Boundary Conditions

The Reynolds equation model for this study predicts the pressure field with assumptions that recirculation is not present in the velocity field, that the r and θ direction velocity field is a linear combination of simple shear and pressure-driven flow, and that the pressure is invariant in the z-direction. In the experiments, the outer edge of the textured domain was an oil-air interface with the air at atmospheric pressure. Boundary conditions on the pressure and the velocity at the outer edge can be derived using the conservation of normal and tangential stress. However, it is not possible to directly implement the boundary conditions on the velocity field, because the Reynolds equation only defines and manipulates the pressure field (unlike the Navier-Stokes equations). However, we have explicit equations for velocity fields in terms of pressure as given in Eq. (2.2). Therefore, boundary conditions on velocity need to be converted to pressure conditions.

In the design studies presented here, it is assumed that texture variations extend all the way to the outermost boundary of the sector. The boundary condition at the outer edge can be a choice between $p = 0$ (Dirichlet boundary condition) or $\frac{\partial p}{\partial r} = 0$ (Neumann boundary condition). The choice has consequences for the r-velocity u_r boundary conditions [36]. If $p = 0$ at the outer edge, then $\frac{\partial p}{\partial \theta} = 0$, and this eliminates the pressure-driven flow in the θ direction (first term in Eq. (2.2b)). Then, if $\frac{\partial h}{\partial \theta} \neq 0$, i.e., texturing, at the outer edge, we have $\frac{\partial u_\theta}{\partial \theta} \neq 0$, and thus by mass conservation $\frac{\partial u_r}{\partial r} \neq 0$. This means the r velocity component can be nonzero at the outer edge for the condition $p = 0$. This nonzero r velocity would cause fluid to leave the disk-shaped textured domain (which was not observed experimentally), and would also result in a nonzero shear stress component ($\tau_{rz} = \eta \left(\frac{\partial u_r}{\partial z} \right)$) on the outer free surface. To enforce $u_r = 0$ at the outer edge (no flux), the gradient of pressure in the r direction at the outer edge must be zero (Eq. (2.2a)), i.e., $\frac{\partial p}{\partial r} = 0$, the Neumann boundary condition, and $\frac{\partial p}{\partial \theta}$ is unspecified. The use of periodic and Neumann boundary conditions results in a pressure field distribution quantified in terms of relative pressure with respect to an arbitrarily fixed pressure at a certain location. We eliminated this arbitrary shift in the pressure profile by constraining the *average* value of the pressure to be zero at the outer edge of the texture. This effectively assumes no net pressure drop across the liquid-air interface, e.g., due to surface tension at a curved interface (Laplace pressure drop). This was also eliminated experimentally by calibrating and subtracting this effect [30].

2.6 Design Optimization Method

2.6.1 Multiobjective Optimization

Multiobjective optimization involves minimization or maximization of a set of multiple conflicting objective functions. The solution of such a problem is a set of nondominated (Pareto-optimal) solutions, as opposed to a single optimum point as with single-objective optimization. A design point is nondominated if one objective cannot be improved without degrading at least one other objective [45].

Two primary classes of methods are used to solve multiobjective optimization problems (MOPs): population-based or scalarization-based methods. Population-based methods, such as nondominated sorting genetic algorithm II (NSGA-II) [46], solve the optimization problem once, and generate a set of solutions that form the Pareto set (approximately). These methods often improve the probability of finding global instead of local optima, but may be computationally expensive due to a large number of function evaluations typically being required [47].

The second class of methods converts a single MOP into a set of 'scalarized' single-objective optimization problems (SOPs). These scalarization-based methods are often used in design optimization studies due to their computational efficiency and simplicity [48]. The weighted-sum method is the simplest scalarization approach, but cannot identify nondominated solutions in nonconvex regions of a Pareto front. In addition, resulting nondominated points are often clustered instead of uniformly distributed across the Pareto surface. These limitations can be overcome through more sophisticated scalarization approaches, such as the ε-constraint method [49], which is illustrated in Fig. 2.5 and described in Section 2.6.3. We used the ε-constraint method in this study to enable the identification of nonconvex Pareto fronts while supporting the use of computationally-efficient gradient-based optimization methods.

2.6.2 Multiobjective Optimization Formulation

The conflicting objectives of the full-film lubrication problem considered here are to (1) minimize the shear load, represented as normalized apparent shear viscosity η_a/η_0, and (2) to maximize the normal force load F_N. Friction is a significant source of energy loss for systems involving lubricated hydrodynamic contacts. Friction can be reduced by increasing the gap between the sliding contact surfaces. Increasing this gap, however, degrades load capacity and sealing performance.

Fluid and pressure losses due to poor sealing are very undesirable outcomes, e.g., for hydraulic power systems. Improved sealing requires increased normal force, but increased normal force may increase frictional losses (e.g., fluid squeeze-out, higher contact friction, etc.) [50]. Therefore, these two objective functions conflict, and the solution to this multiobjective design problem will be a set of nondominated points that quantify trade-off options. Adding certain types of textures to the full-film lubrication problem was found in previous studies to simultaneously improve both of these objective functions. In other words, transitioning to more effective texture classes shifts the Pareto surface toward more desirable objective function values. These previous studies were limited to very simple uniform dimpled textures [17–19, 21, 35, 36]. Here we aim to shift the attainable Pareto set even more by considering more general texture designs. We also aim to gain fundamental insights about how best to design surface textures for full-film lubrication applications.

The MOP formulation used here is:

$$\begin{aligned} \underset{\mathbf{x}}{\text{minimize}} \quad & \left\{ \frac{\eta_a(\mathbf{x})}{\eta_0}, -F_N(\mathbf{x}) \right\} && \text{(2.3a)} \\ \text{subject to} \quad & \mathbf{x}_{\min} \leq \mathbf{x} \leq \mathbf{x}_{\max}, && \text{(2.3b)} \\ & h_{\min} \leq h_{ij}(\mathbf{x}) \leq h_{\max},\ \forall \{i,j\} \in \mathbb{D}, && \text{(2.3c)} \end{aligned}$$

where $\mathbf{x}$ is a vector of design variables that represents texture geometry (e.g., spline, etc.)

and fluid properties are fixed. In this study, geometric parameterizations are formulated to implicitly satisfy the periodic boundary conditions for the surface shape. For a given value of $\mathbf{x}$, the resulting geometric surface description is then used to determine high-resolution surface height values: $h_{ij}(\mathbf{x})$, $\forall \{i, j\} \in \mathbb{D}$. The height values $h_{ij}(\cdot)$ quantify the surface shape at mesh points needed for the pseudospectral method, $\mathbb{D}$ is the set of indices for all mesh points in the design domain, and $\{i, j\}$ are node indices in the two-dimensional mapped mesh space. The objective functions ultimately depend on $\mathbf{x}$. The height values, obtained from $\mathbf{x}$, are used within the simulation to obtain intermediate quantities needed to compute the objective function values. The simulation solves for the pressure distribution $p(r, \theta)$ and velocity field $u_r\,(r, \theta, z)$, $u_\theta\,(r, \theta, z)$.

The first objective function, normalized apparent viscosity $\eta_a(\mathbf{x})/\eta_0$, is calculated by a ratio of apparent viscosity ($\eta_a(\mathbf{x})$, depends on design) to actual fluid viscosity (η_0, fixed, depends on fluid selection) [51]. The apparent viscosity is defined from the torque M on the rotating disk (integrated shear stress). For the rotating disk configuration, apparent viscosity can be written as a function of disk torque M.

$$\eta_a = \eta_a\,(M) = \frac{2h_0}{\pi R_o^4}\frac{M}{\Omega} \tag{2.4a}$$

$$\text{where,} \quad M = N_{\text{tex}} \int_{-\varphi/2}^{\varphi/2} \int_{R_i}^{R_o} \tau_{\theta z}\big|_{z=0}\, r^2 \; dr \; d\theta \tag{2.4b}$$

$$\text{and} \quad \tau_{\theta z}\big|_{z=0} = -\frac{1}{2}\frac{1}{r}\frac{\partial p}{\partial \theta}h - \eta_0 \frac{r\Omega}{h} \tag{2.4c}$$

R_o is the outer radius of the textured disk; h_0 is a controlled minimum gap height between the fixed and rotating disks; Ω is the rotating disk angular velocity. Equation (2.4b) defines how disk torque is calculated, which requires evaluation of the θ-direction (tangential) shear stress ($\tau_{\theta z}(r, \theta)$, where z is the vertical coordinate) at the rotating surface across the complete domain. The shear stress calculation requires knowledge of the velocity field, which for the Reynolds equation depends on gradients of the pressure field ($\nabla p(r, \theta)$) across the entire

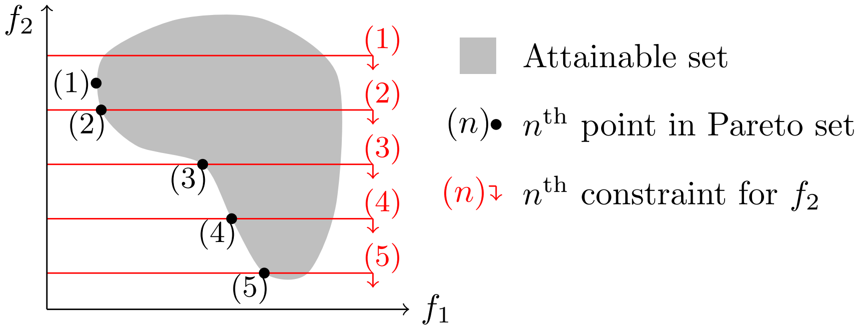

Figure 2.5: The ε-constraint method converts a MOP to multiple SOPs. For each scalarized problem, one objective is minimized while satisfying bound constraints on the other objectives.

computational domain of the flow field. For example, the shear stress in the theta direction can be calculated as a function of $\partial p\left(r,\theta\right)/\partial\theta$ as given in Eq. (2.4c). The second objective function, the negative normal force ($-F_N$), is calculated by integrating pressure over the domain, and then multiplying this value by the total number of disk sectors (N_{tex}) as shown in Eq. (2.5).

$$F_N = F_N\left(p\right) = N_{\text{tex}} \int_{-\varphi/2}^{\varphi/2} \int_{R_i}^{R_o} p \; r \; dr \; d\theta \tag{2.5}$$

2.6.3 ε-constraint method

The ε-constraint method is a type of scalarization technique for multiobjective optimization. A MOP is transformed into a set of SOPs by retaining just one of the original objective functions, and the remaining objective functions are converted to constraints that bound these other objective function values [49]. Figure 2.5 illustrates how the ε-constraint method minimizes the first objective function ($f_1(\cdot)$), while a constraint prevents the second objective function ($f_2(\cdot)$) from exceeding a bound denoted by red horizontal lines in the objective function space. The objective function space is a multidimensional space $\mathbf{f} \in R^m$, where R is the real number space, and m is the number of objective functions. This procedure is repeated, each time with a different bound on $f_2(\cdot)$. In the example shown in Fig. 2.5 the optimization problem is solved five times to generate five Pareto-optimal solutions. This strategy supports the use of existing single-objective optimization algorithms in solving

MOPs, including the ability to resolve nonconvex portions of the Pareto frontier hypersurface (a curved line for two objectives) and to generate well-distributed Pareto-optimal points. The multiobjective formulation in Prob. (2.3) can be reformulated for the ε-constraint solution as:

$$
\begin{aligned}
\underset{\mathbf{x}}{\text{minimize}} \quad & \frac{\eta_a(\mathbf{x})}{\eta_0} && \text{(2.6a)}\\
\text{subject to} \quad & -F_N \leq \varepsilon_k && \text{(2.6b)}\\
& \mathbf{x}_{\min} \leq \mathbf{x} \leq \mathbf{x}_{\max} && \text{(2.6c)}\\
& h_{\min} \leq h_{ij}(\mathbf{x}) \leq h_{\max},\ \forall \{i,j\} \in \mathfrak{D} && \text{(2.6d)}\\
& \forall k \in \{1, 2, \ldots, n_p\}, && \text{(2.6e)}
\end{aligned}
$$

where n_p is the number of Pareto-optimal points to solve for. One possible strategy, which is used in this study, is to increment ε_i uniformly, i.e., $\varepsilon_{i+1} = \varepsilon_i + \delta$, where $\varepsilon_1 = (-F_N)_{\min}$ and $\delta = ((-F_N)_{\max} - (-F_N)_{\min})/(n_p - 1)$.

2.7 Results and Discussion

2.7.1 Cylindrical Textures

A full factorial set of cylindrical texture designs, both in symmetric and asymmetric configurations, was generated and evaluated to provide insight into how design variables influence objective functions, and to assess trade-offs. Texture radius (R_t) and depth (h) are the design variables used for the symmetric cylindrical texture study, and texture radius (R_t) and angle (β) are the design variables used for the asymmetric cylindrical texture study. Figure 2.6 illustrates the contours of the two objective functions for both cases. Figures 2.6a-2.6b corresponds to the symmetric texture, and Figs. 2.6c-2.6d correspond to the asymmetric texture.

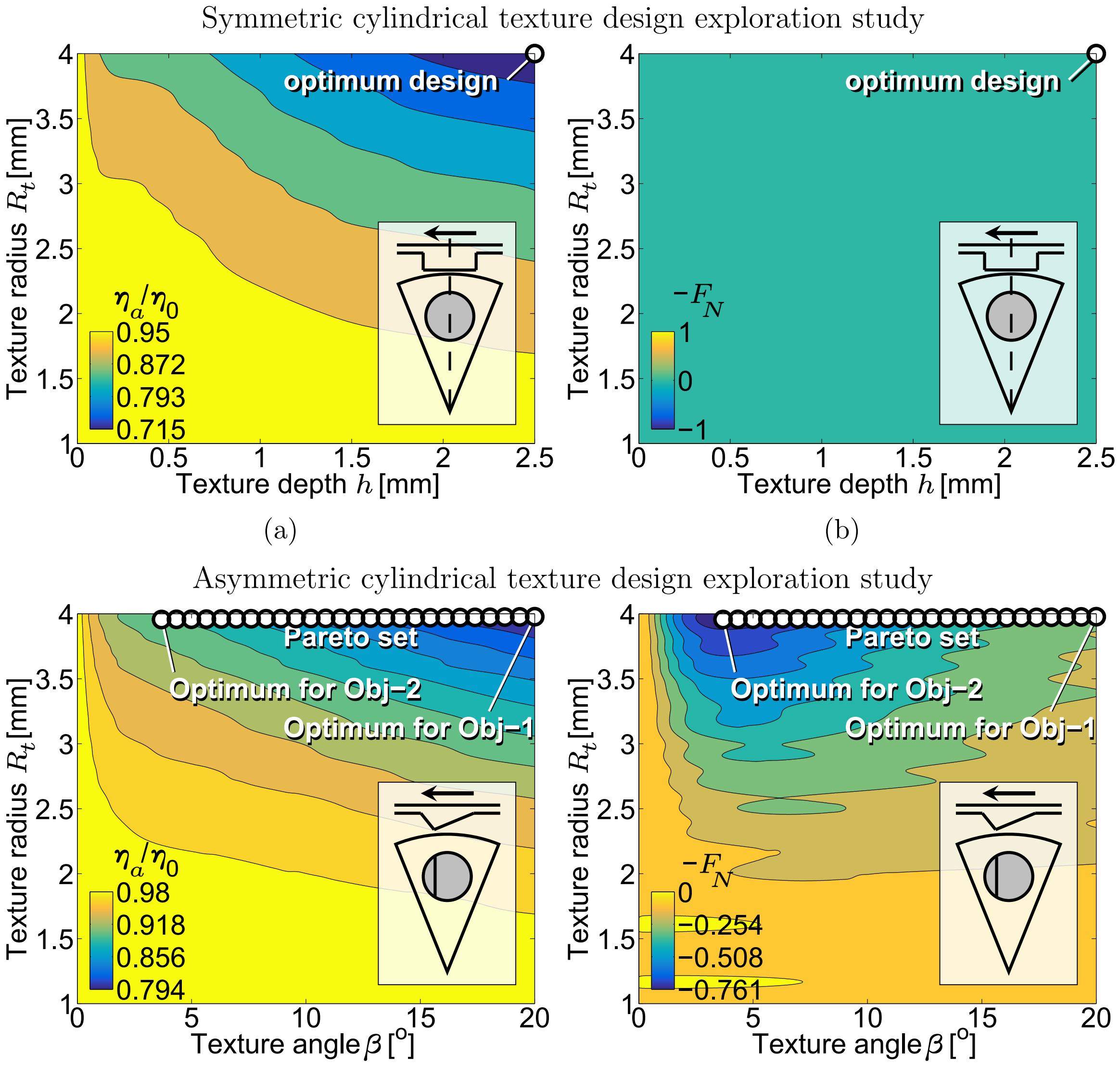

(a) (b)

(c) (d)

Figure 2.6: Objective function contours based on a comprehensive sampling of the cylindrical texture design (symmetric and asymmetric textures). Trade-offs are apparent, and the Pareto sets are illustrated in the figures. Asymmetry improves performance capability, especially in terms of the normal force. Symmetric texture result of (a) normalized apparent viscosity η_a/η_0 [–] and (b) negative normal force $-F_N$ [N]. Asymmetric texture results of (c) normalized apparent viscosity η_a/η_0 [–] and (d) negative normal force $-F_N$ [N].

For the symmetric textures, shear load (normalized apparent viscosity) decreases with "big" textures (i.e., larger radius and deeper depth) down to $\eta_a/\eta_0 = 0.714$, while no normal force is observed. Thus, the lowest shear load determines the optimal design (circles in Fig. 2.7). For asymmetric textures, the angle β determines texture depth ($\beta = 0$ is a flat

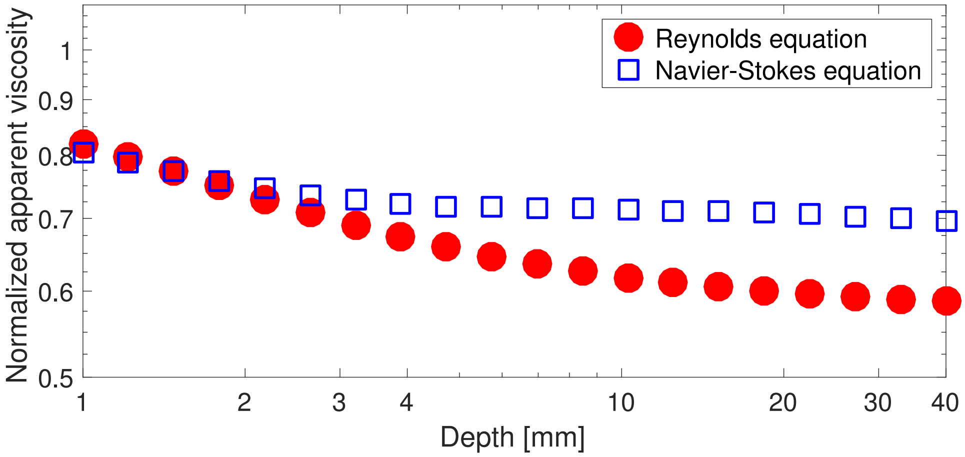

Figure 2.7: Comparison between the Reynolds equation and the Navier-Stokes equation solutions in terms of the normalized apparent viscosity for the symmetric cylindrical textures as a function of depth.

surface). The shear load is still minimized for “big” textures (i.e., a large radius and a large β). The normal force is expected to be maximized at an intermediate angle β [30, 36], and here this occurs at $\beta = 3.6°$. Normalized shear load ranges from 0.794 to 0.902, and normal force ranges from 0.212 to 0.762 [N]. Asymmetry is required to generate normal force.

Design variable bounds are chosen such that the Reynolds equation simulation results reasonably agree with results based on the full Navier-Stokes equation. Figure 2.7 shows both the Reynolds equation and the Navier-Stokes equation solutions using ANSYS Fluent in terms of the normalized apparent viscosity for the symmetric cylindrical texture problem. When the texture depth is 2 [mm] and 4 [mm], the solution of the Reynolds equation deviates 1.65% and 6.93%, respectively, from the solution of the full Navier-Stokes equation. Due to this limitation in the Reynolds equation model, the depth variable should be constrained to preserve accuracy. Furthermore, the full Navier-Stokes predictions indicate that the normalized apparent viscosity plateaus beyond a certain depth (note that the plot is log-scale). This means that the frictional performance cannot be enhanced more through increases in depth beyond a certain value.

For both symmetric and asymmetric textures, the first objective function (minimizing normalized apparent viscosity) has monotonic dependence on texture depth and radius, as shown in Figs. 2.6a and 2.6c (the objective decreases with increasing depth and radius). In the asymmetric configuration study, the angle was varied between 0–20°. Within this range, increasing the angle corresponds to increased average texture depth, and increased lubricant volume. This observation, along with the results presented here, indicates that the total volume removed for a texture is important for reducing friction.

The behavior of the second objective function (maximizing normal force) is different for the symmetric and asymmetric configurations. Symmetric cylindrical design variables do not influence normal force because geometric symmetry in the sliding direction results in negative and positive pressure distributions that countervail each other through the expanding-contracting channel gap height. This matches the results reported in previous experimental and theoretical studies that measurable normal forces were not detected in symmetric cylindrical surface textures [30, 34].

The second objective function widely varies when changing the asymmetric configuration design variables. Figure 2.6d shows that the normal force depends on both the texture angle β and the radius R_t. In particular, the best normal force value occurred at a specific texture angle value, $\beta = 3.6^\circ$, with the texture radius R_t at the upper bound, 4.0 [mm]. Moving away from this point improves the normalized apparent viscosity, but degrades normal force. Therefore, the result of this optimization study is a set of nondominated designs that express the trade-off between these two objective functions. We can improve normal force through asymmetric textures, but at the cost of degraded apparent viscosity.

Detailed insight into the flow physics (shear stress and pressure fields) are shown in Figs. 2.8, 2.9, and 2.10. Figure 2.8 compares symmetric and asymmetric optimal designs (minimum η_a/η_0 for symmetric cylinder and maximum F_N for asymmetric cylinder). The pressure field results in Fig. 2.8c show that the pressure is counterbalanced across the vertical line of symmetry. Thus, the overall pressure acting in the direction normal to sliding is canceled, resulting in no normal force. This numerical result explains why design variables for symmetrical textures do not affect the normal force, as shown in Fig. 2.6b.

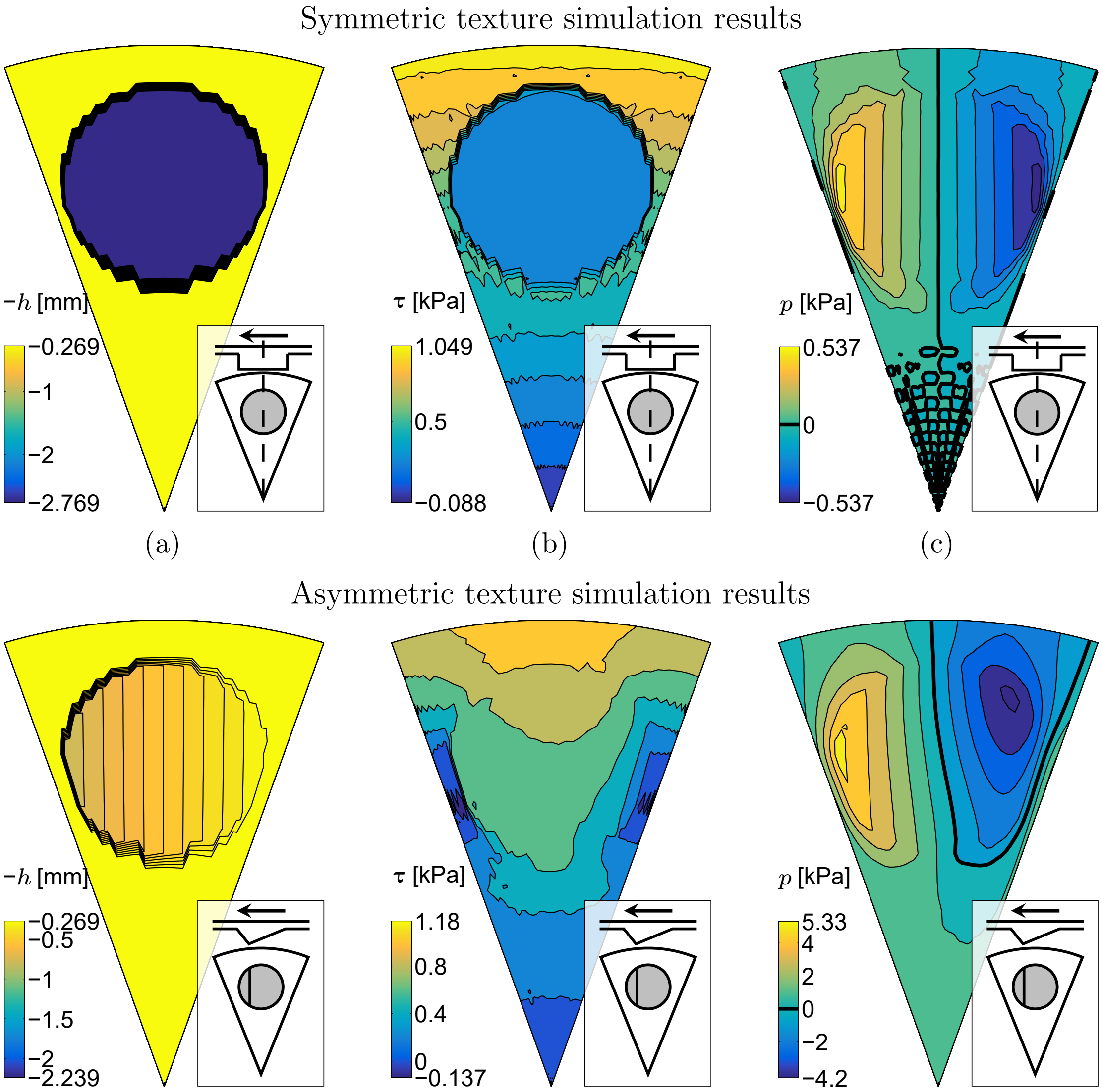

(a) (b) (c)

(d) (e) (f)

Figure 2.8: Geometry, shear stress, and pressure fields of optimized cylindrical texture designs in symmetric and asymmetric configurations. Symmetric texture results of (a) texture depth profile $-h$ [mm], (b) shear stress τ [kPa], and (c) pressure p [kPa] with $R_t = 4$ [mm], $h = 2.5$ [mm]. Asymmetric texture results of (d) texture depth profile $-h$ [mm], (e) shear stress τ [kPa], and (f) pressure p [kPa] with $R_t = 4$ [mm], $\beta = 3.6°$.

For the asymmetric configuration, the pressure distribution is not counterbalanced and can produce a net normal force. Here the positive overall pressure generates a positive normal force. Figure 2.10 shows how the pressure distribution changes with angle β. Corresponding surface texture shapes are given in Fig. 2.9. At the angle of maximum normal force ($\beta = 3.6°$), the range of pressures is at its maximum. The maximum normal force increases with β up to

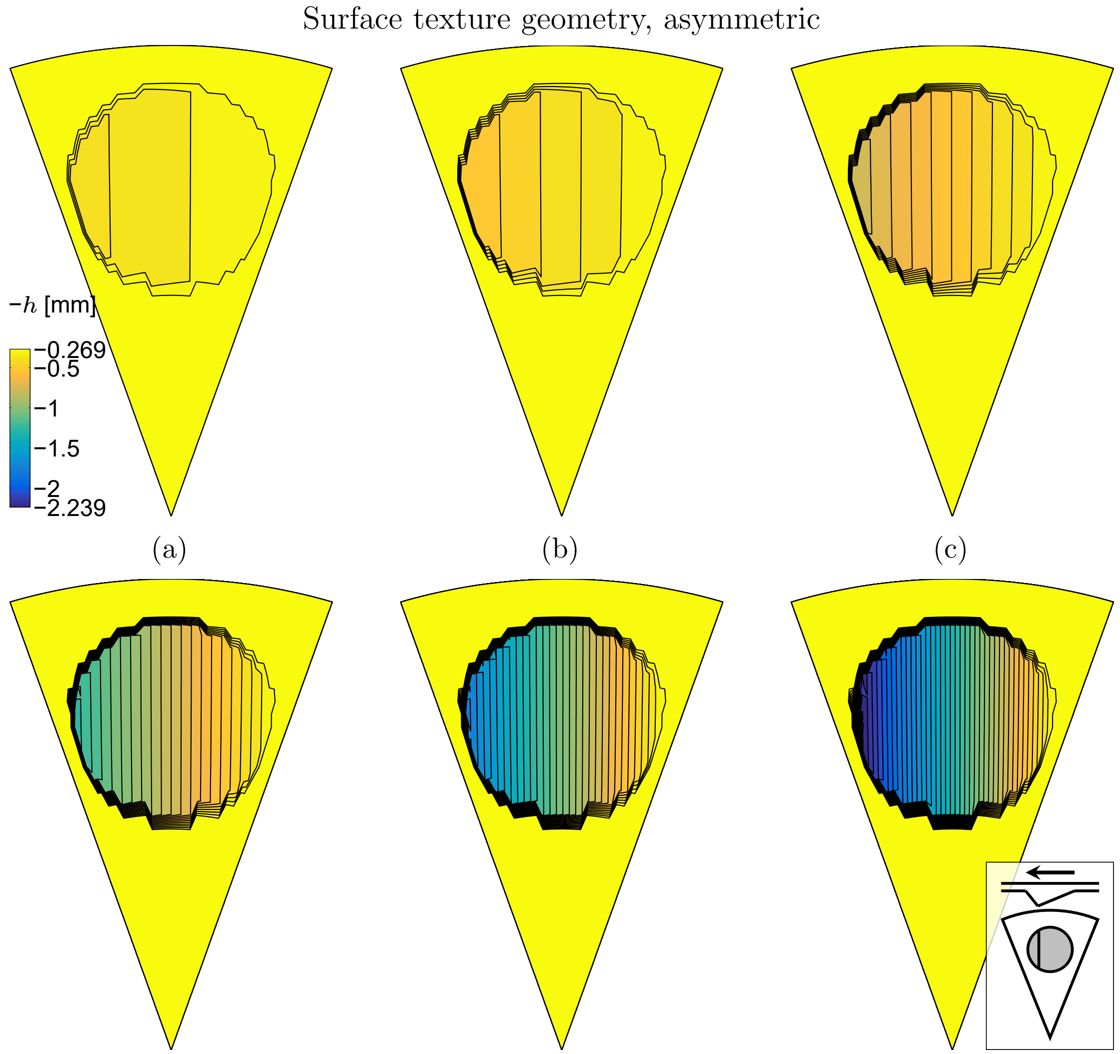

(a) (b) (c)

(d) (e) (f)

Figure 2.9: Geometric texture profile level-sets for asymmetric cylindrical textures with various angles (β). Six β angles are sampled within the range of inclination limits. (a) $\beta = 0.9°$, (b) $\beta = 1.8°$, (c) $\beta = 3.6°$, (d) $\beta = 7.2°$, (e) $\beta = 10.8°$, (f) $\beta = 14.4°$. Corresponding pressure contours for the surface textures are given in Fig. 2.10.

$\beta = 3.6°$, but then decreases with angle beyond $\beta = 3.6°$. The interface between positive and negative pressure consistently moves from left to right with increasing angle. This is because when the angle of asymmetry is greater than 45°, the resulting surface texture is geometrically similar to a texture with an angle of $(90° - \beta)$ with the flow in the opposite direction, and it has been previously shown that when the direction of motion changes for asymmetric surface textures, the sign of the normal force also changes [30, 35].

Computed pressure fields for above surface textures

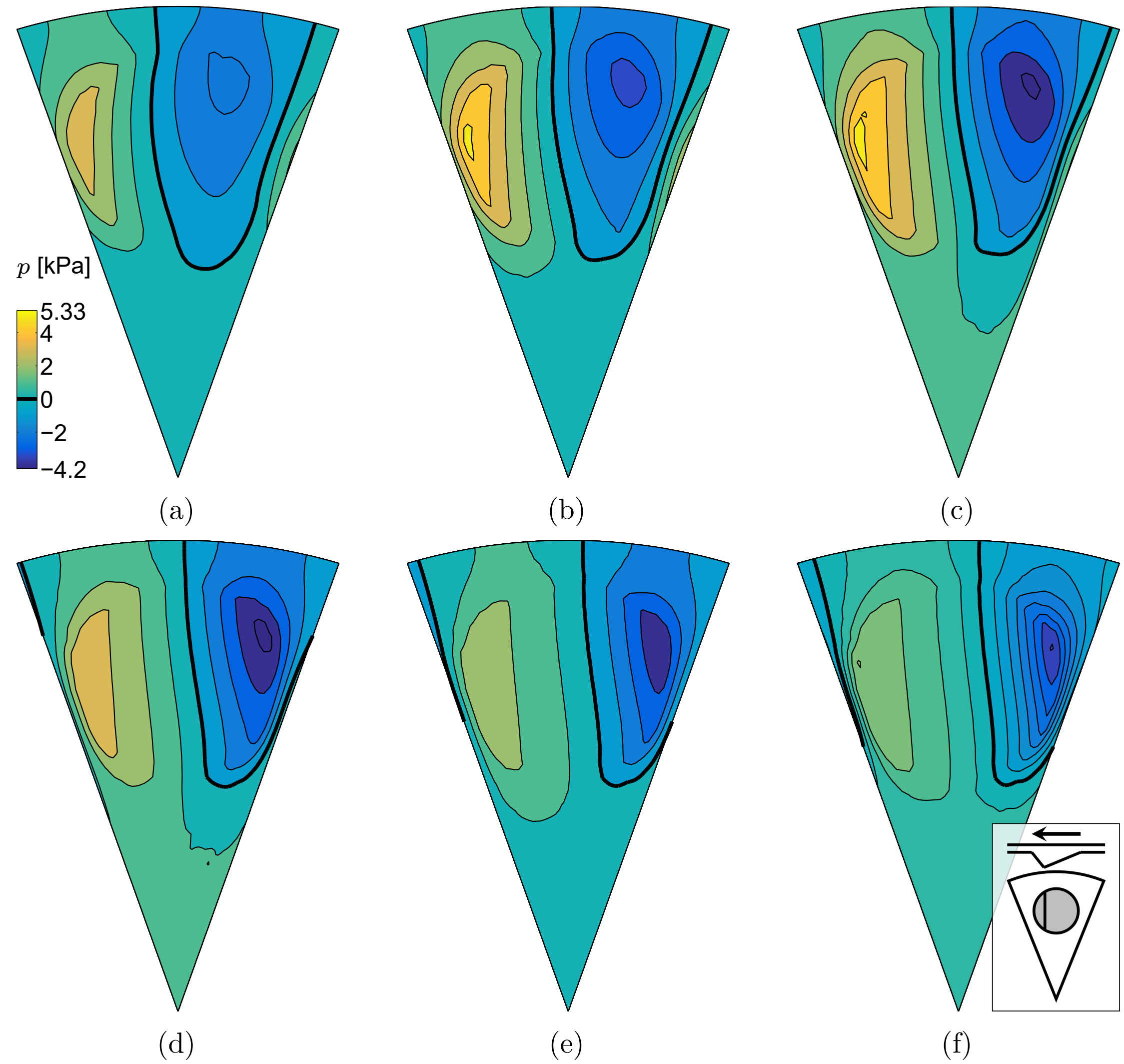

(a) (b) (c) (d) (e) (f)

Figure 2.10: Pressure field level-sets for asymmetric cylindrical textures with various angles (β). Six β angles are sampled within the range of inclination limits. (a) $\eta_a/\eta_0 = 0.942$, $F_N = 0.281$ [N] for $\beta = 0.9°$, (b) $\eta_a/\eta_0 = 0.920$, $F_N = 0.573$ [N] for $\beta = 1.8°$, (c) $\eta_a/\eta_0 = 0.904$, $F_N = 0.755$ [N] for $\beta = 3.6°$, (d) $\eta_a/\eta_0 = 0.880$, $F_N = 0.614$ [N] for $\beta = 7.2°$, (e) $\eta_a/\eta_0 = 0.854$, $F_N = 0.449$ [N] for $\beta = 10.8°$, (f) $\eta_a/\eta_0 = 0.829$, $F_N = 0.333$ [N] for $\beta = 14.4°$. Corresponding surface texture geometry shapes are given in Fig. 2.9.

2.7.2 Inclined plane spanning full sector area

Figure 2.11 shows a result of an inclined plane texture design that involves a slow expansion followed by rapid contraction. In the pressure distribution contour plot (Fig. 2.11c), a thick contour line (zero-pressure line) highlights the boundary between positive and negative

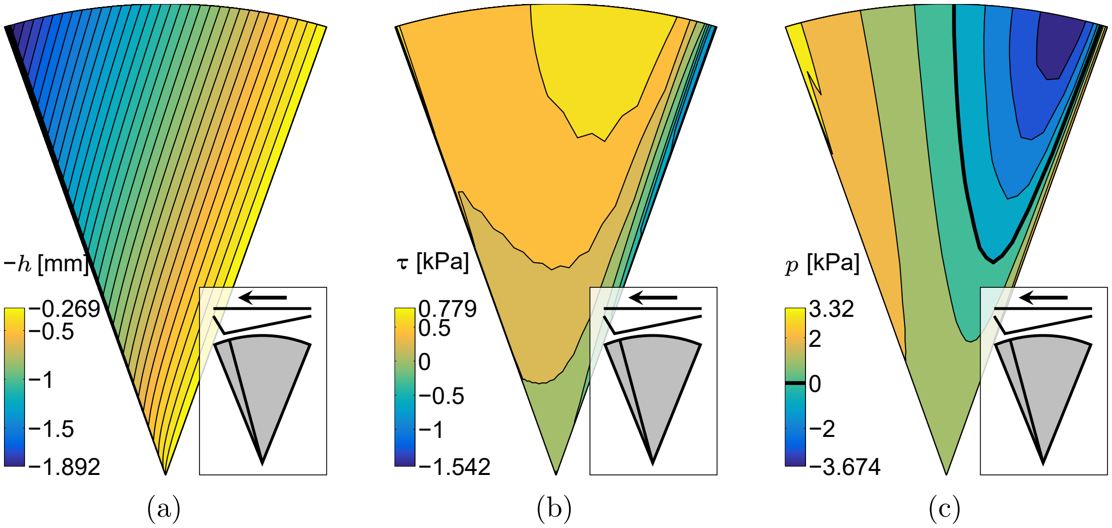

Figure 2.11: Geometry, shear stress, and pressure field of the surface texture with inclined plane spanning the full sector area. Asymmetric inclined plane texture result of (a) texture depth profile $-h$ [mm], (b) shear stress τ [kPa], and (c) pressure p [kPa].

normal force regions. The positive normal force region has a larger area than the negative normal force region. Integrating this pressure distribution over the sector area results in a positive net normal force. This is the general observation for cases where slow expansion is followed by rapid contraction.

Figure 2.12a shows the Pareto fronts for the inclined plane and cylindrical textures. It compares design solutions in the objective function space, including both symmetric and asymmetric configurations for cylindrical textures. By expanding the inclined region of the texture, both objectives can be improved simultaneously. It is clear that normalized apparent viscosity is significantly reduced when shifting to the full inclined plane geometry. Since this design representation has only a single design variable β, it is possible to visualize the response of both objectives with respect to β, as shown in Fig. 2.12b. This plot shows a clear conflict between the two objective functions. Negatively inclined angle β creates flow in rapid expansion followed by slow contraction, while positively inclined angle β creates flow in slow expansion followed by fast contraction. The sign of the inclined plane angle β determines the sign of normal force F_N, but the magnitude of the normal force is symmetric between positive and negative inclined angle β. Furthermore, apparent viscosity η_a/η_0 has

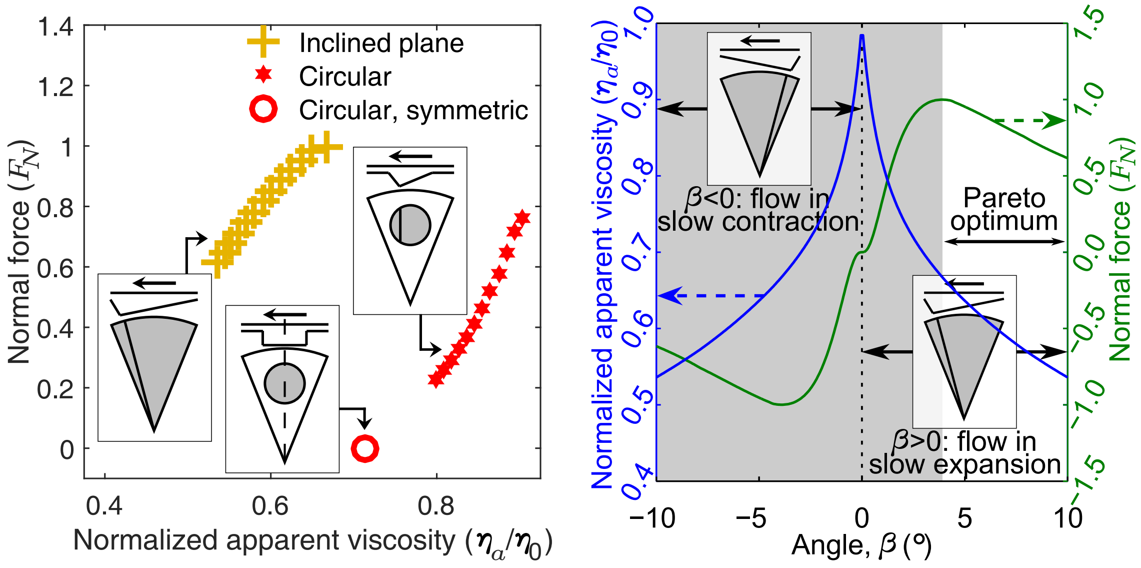

(a) (b)

Figure 2.12: Optimal designs for the cylindrical design exploration and the inclined plane spanning the full sector area studies. (a) Optimal designs comparison. (b) $\beta - \eta_a/\eta_0$ and $\beta - F_N$ plots. The solid red stars in (a) is the Pareto set for the cylindrical texture identified from the contours of Figs. 2.6c-2.6d. In (b), the two objectives (blue: η_a/η_0, green: F_N) are plotted together as a function of β for the inclined plane design. The gray area indicates the region of suboptimal designs.

even symmetry with respect to β. The region corresponding to Pareto-optimal designs is identified by the white area in Fig. 2.12b. The gray area in this plot indicates the set of suboptimal designs that are dominated by the Pareto-optimal designs.

2.7.3 Arbitrary continuous texture designs

The study is now extended to arbitrary continuous surface elevation changes parameterized using spline interpolation. The objectives of this investigation include understanding how to improve performance further through more sophisticated texture designs, and what physical mechanisms make any improvements possible.

Using the coarse mesh described in Section 2.4 and Fig. 2.3a, designs are represented using a $(N+1) \times N$ matrix of surface elevation values, accounting for periodic boundary constraints. For the reference case this matrix has dimension 6×5, with a resulting design

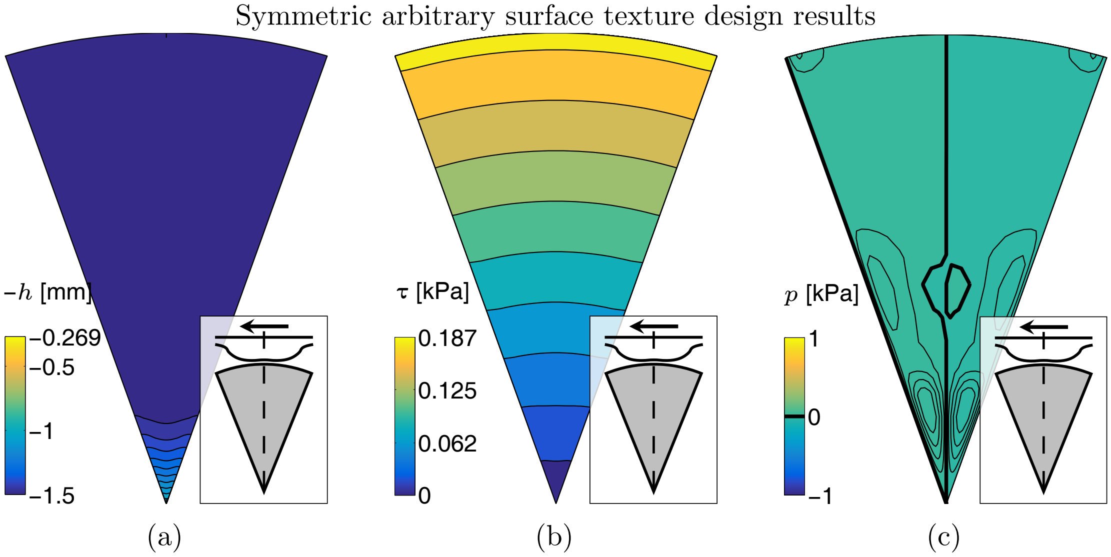

Figure 2.13: Optimal texturing of an arbitrary but symmetric surface approaches a flat plate; symmetric texturing is unable to produce normal force. The optimal solution maximizes the gap everywhere to decrease the viscous shear load. Arbitrary but symmetric texture results of (a) texture depth profile $-h$ [mm], (b) shear stress τ [kPa], and (c) pressure p [kPa].

representation dimension of 30 for asymmetric arbitrary continuous surface texturing. We first consider symmetric designs (Fig. 2.4d), which have a lower design representation dimension due to the symmetry constraint ($\lceil (5+1)^2/2 \rceil = 18$). Then, we allow asymmetric designs by removing the symmetry constraint (Fig. 2.4e). We also vary the design space resolution from $N = 3$ to $N = 7$ to examine the dependence of optimal performance on resolution.

Figure 2.13 shows the optimal design with the symmetry constraint. It is nearly a flat plate that maximizes the allowable gap height. As with the symmetric cylindrical texture result, the pressure distribution is balanced, and the normal force is zero. As before, the problem reduces to a single-objective function problem due to symmetry and insensitivity of normal force to texture design. This is a significant result. Even with arbitrary surface topography, symmetry must be broken to generate a normal force from textured surfaces. Gap reduction has no benefit in terms of normal force, so the optimization algorithm is free to minimize shear by setting the surface elevation to the maximum gap at all locations, resulting in the flat surface shown in Fig. 2.13. Near $r = 0$ the surface elevation does increase

Surface texture geometry, asymmetric

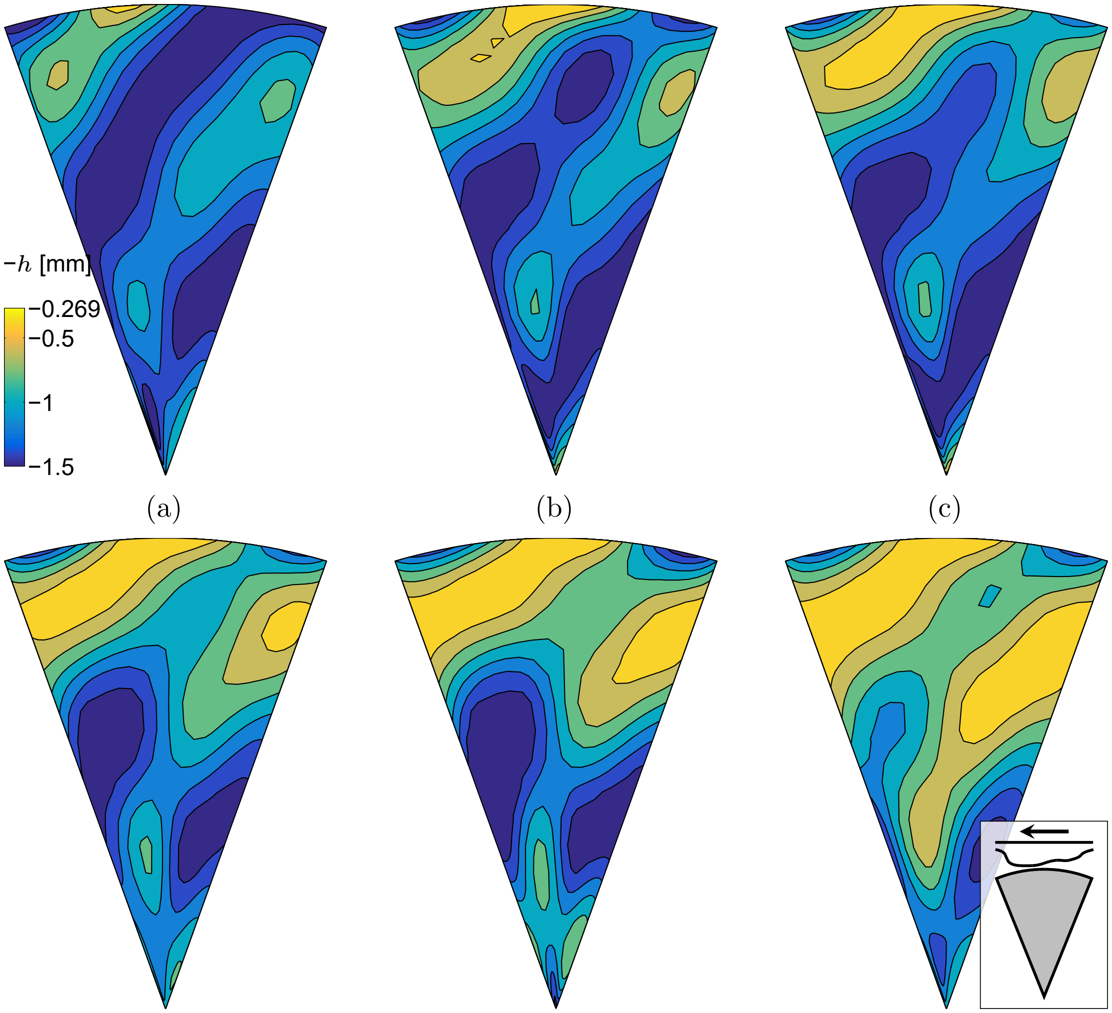

(a) (b) (c)

(d) (e) (f)

Figure 2.14: Geometric texture profile level-sets for optimized surface textures with spline design representation (spline resolution $N = 5$). Asymmetry is permitted. Six designs are uniformly sampled from 27 designs in the Pareto set to illustrate trends. These Pareto-optimal designs are denoted as blue squares in Fig. 2.16. (a) Design #4, $F_N > 0.75$ [N], (b) Design #8, $F_N > 1.75$ [N], (c) Design #12, $F_N > 2.75$ [N], (d) Design #16, $F_N > 3.75$ [N], (e) Design #20, $F_N > 4.75$ [N], (f) Design #24, $F_N > 5.75$ [N]. Corresponding pressure contours for the surface textures are given in Fig. 2.15.

slightly. This is because the sensitivity of the normalized apparent viscosity with respect to gap height is negligible in this region. We found that a completely flat surface enhances the objective value by only 0.016% compared to the optimization solution.

When the symmetry constraint is removed, the sliding surface textures can generate

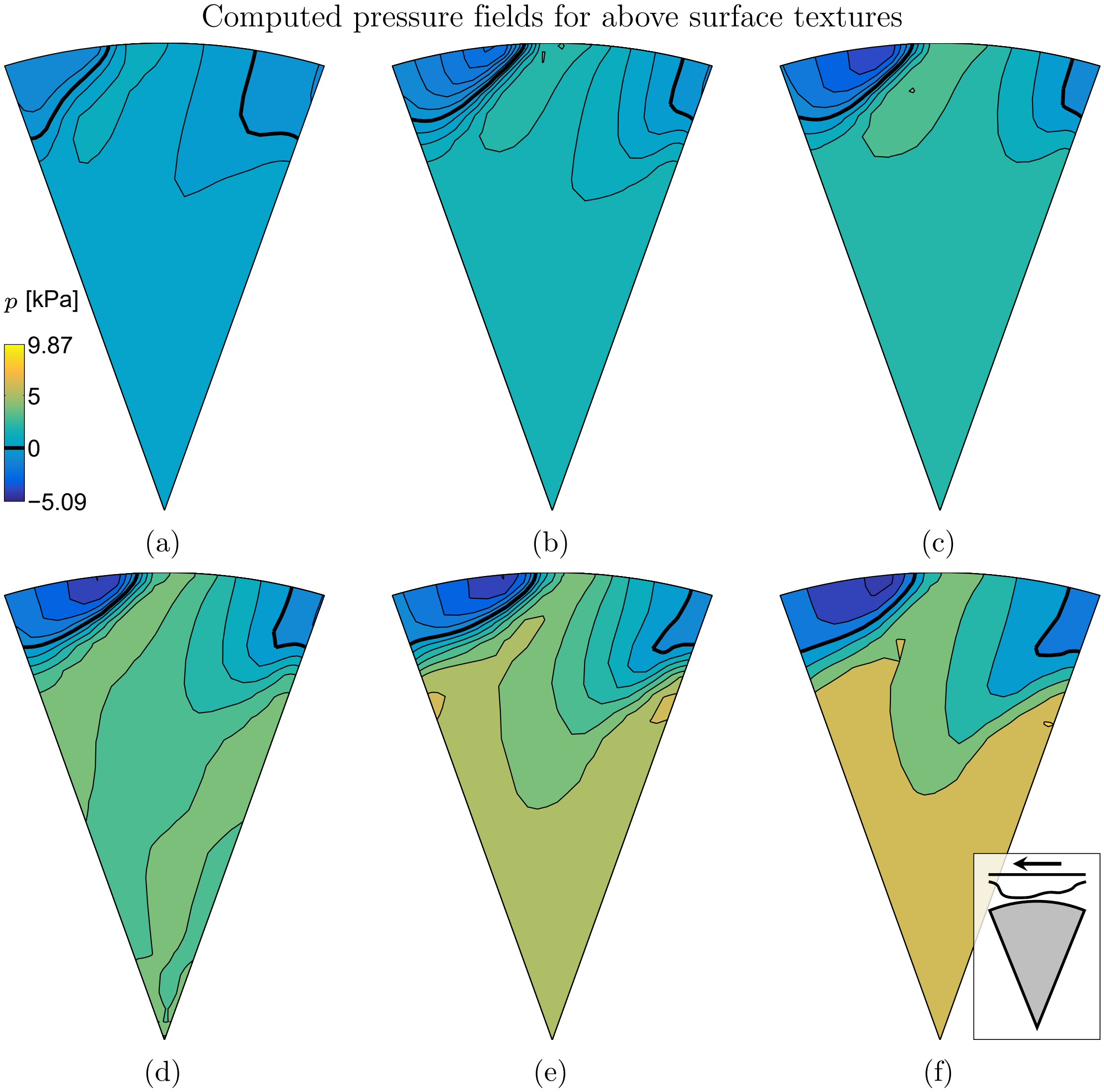

Figure 2.15: Pressure field level-sets for optimized surface textures with spline design representation (spline resolution $N = 5$). Asymmetry is permitted. Thick contour lines denote zero pressure (boundaries between negative and positive pressures) locations. These Pareto-optimal designs are denoted as blue squares in Fig. 2.16. (a) Design #4, $\eta_a/\eta_0 = 0.299$, $F_N = 0.750$ [N], (b) Design #8, $\eta_a/\eta_0 = 0.394$, $F_N = 1.750$ [N], (c) Design #12, $\eta_a/\eta_0 = 0.469$, $F_N = 2.750$ [N], (d) Design #16, $\eta_a/\eta_0 = 0.538$, $F_N = 3.753$ [N], (e) Design #20, $\eta_a/\eta_0 = 0.607$, $F_N = 4.750$ [N], (f) Design #24, $\eta_a/\eta_0 = 0.709$, $F_N = 5.752$ [N]. Corresponding surface texture geometry shapes are given in Fig. 2.14.

nonzero normal forces as with the asymmetric cylindrical texture designs. Figures 2.14 and 2.15 show asymmetric texture geometries and the corresponding pressure fields for six different Pareto-optimal designs. Designs are displayed in order of increasing normalized apparent viscosity value (and also increasing normal force). The designs shown in Fig. 2.14

are sampled uniformly from the Pareto set obtained by solving Eq. (2.6) with splines $N = 5$. The corresponding Pareto set is shown as blue squares (the reference case) in Fig. 2.16, which is observed to be nonconvex in the objective-function space. Using an approach such as the ε-constraint method was essential for resolving nonconvex portions of the Pareto set.

In some portions of the design domain, the texture slope limitation has a significant impact on results. It may be helpful (e.g., for manufacturability) to add constraints to limit texture slope in further design studies. This could be implemented approximately using linear constraints on design variables. With the 30-variable spline representation, this slope constraint strategy requires $2 \times (6-1)^2 = 50$ linear constraints. All spline interpolated studies presented here use these linear constraints to limit the inclined angle of the textured profile.

The geometric result shown in Fig. 2.14a-2.14f converged to a shape that is similar to a spiral blade. The spiral blade-like texture profile has a portion colored in yellow (higher heights, Figs. 2.14a-2.14f) that acts as a converging channel directing flow radially inward. This increases pressure near the disk center and generates a positive net normal force, as shown in Fig. 2.15. This mechanism helps explain how the asymmetric spiral blade-like surface design can help increase normal force in this rotational configuration. The directed flow toward the disk center may also help reduce leakage, an important practical consideration for fluid power systems. This increased pressure at the center helps support axial loads and load applied on the sealing components, while the low hydraulic pressure near the outer rim of the disks helps to contain the fluid within the gap between sliding disks. These design results match the known previous experimental observation that a spiral groove enhances load-capacity for a parallel flat surface bearing configuration [22].

2.7.4 Comparison of optimal designs

Pareto-optimal designs shown in Fig. 2.16 show how the objective functions can be improved significantly by transitioning from simple dimpled textures to arbitrary continuous texture

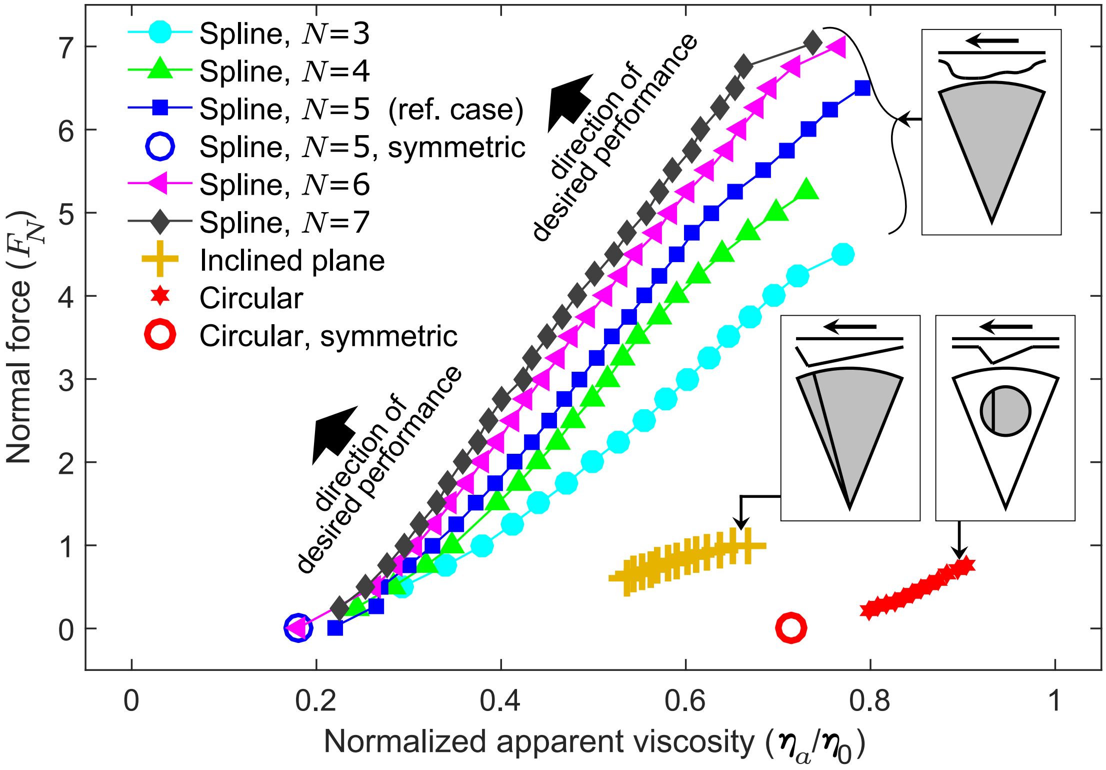

Figure 2.16: Comparison of optimal designs in the objective function space for all design studies presented in this study. Performance indices are improved significantly by increasing design flexibility via the texture surface representation.

geometries. Note that the vertical axis is F_N as opposed to $-F_N$, to be more intuitive, so points closer to the upper left are more desirable. Only normalized apparent viscosity (η_a/η_0) changes in the symmetric cases; the optimal solution maximizes the operating gap to the greatest extent possible. For the asymmetric case, switching from dimpled cylindrical to arbitrary spline-based textures shifts the Pareto sets significantly toward the upper left, indicating roughly an order of magnitude performance improvement while enforcing the manufacturability constraint. Enhanced normal force generation is observed as more spline control points are added as design variables (increasing texture design resolution). However, in the region of nearly zero normal force, increasing the number of spline control points, $(N+1)\times N$, does not provide a meaningful improvement in reducing the normalized apparent viscosity, because the optimal surfaces are flat with a maximum gap height value.

Figure 2.17 compares texture profile level-sets for full-disk geometries at $F_N = 3$ [N]. For

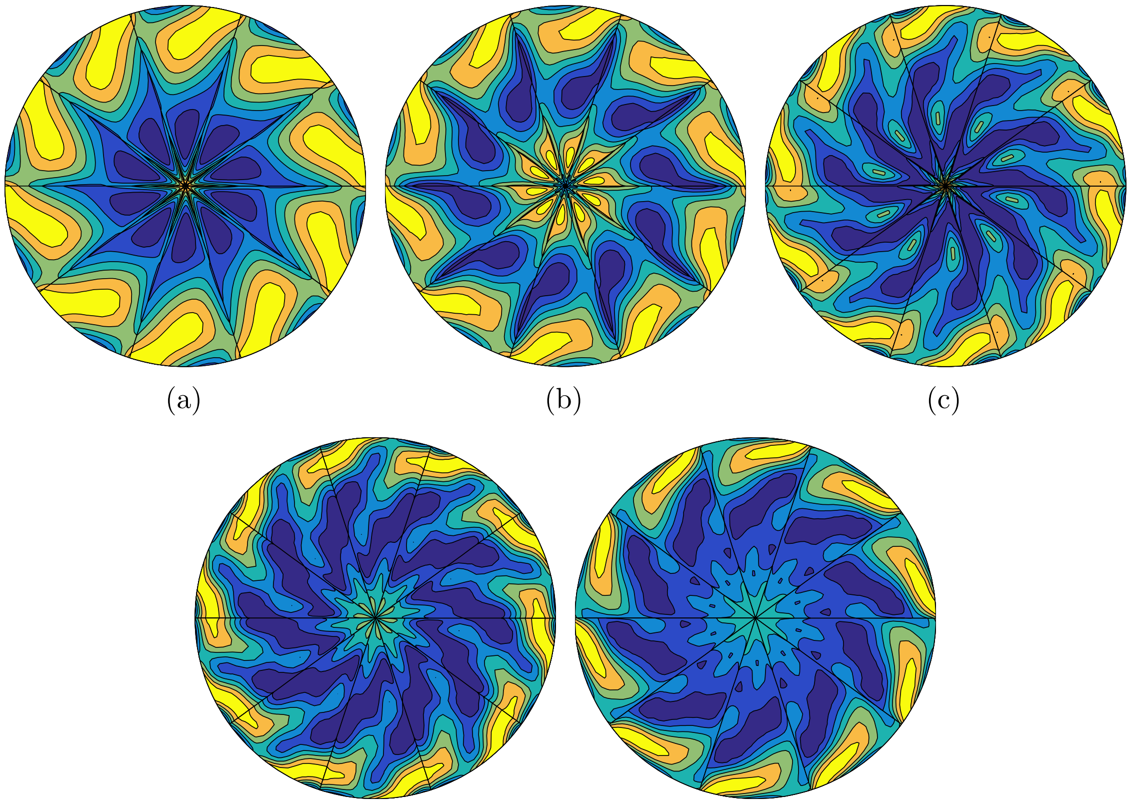

(a) (b) (c) (d) (e)

Figure 2.17: Comparison of geometric texture profile level-sets of optimal designs for $N = 3$ to 7 at $F_N = 3$ [N]. As design resolution increases, the thickness of the blade-like feature becomes sharper, and a lower normalized apparent viscosity value can be achieved. (a) $N = 3$, $\eta_a/\eta_0 = 0.6015$. (b) $N = 4$, $\eta_a/\eta_0 = 0.5160$. (c) $N = 5$, $\eta_a/\eta_0 = 0.4857$. (d) $N = 6$, $\eta_a/\eta_0 = 0.4439$. (e) $N = 7$, $\eta_a/\eta_0 = 0.4237$.

each disk level-set, the corresponding value of normalized apparent viscosity is given. As Fig. 2.16 illustrated previously, increased design mesh resolution results in optimal designs with lower normalized apparent viscosity values. While the same level of the normal force is generated ($F_N = 3$ [N]) by these five designs, the blade shape becomes sharper, and the landscape profile becomes more detailed as the design mesh becomes finer. Figure 2.18 illustrates comparisons of optimal cross-sectional depth profiles for spline-based designs across a range of texture resolutions ($N = 3, 5, 7$) for four different radial positions r. Among solutions in the Pareto set, the optimal design point generating the normal force of $F_N = 3$ [N] is chosen for this comparison. At all three resolutions, the same trend is observed. Namely,

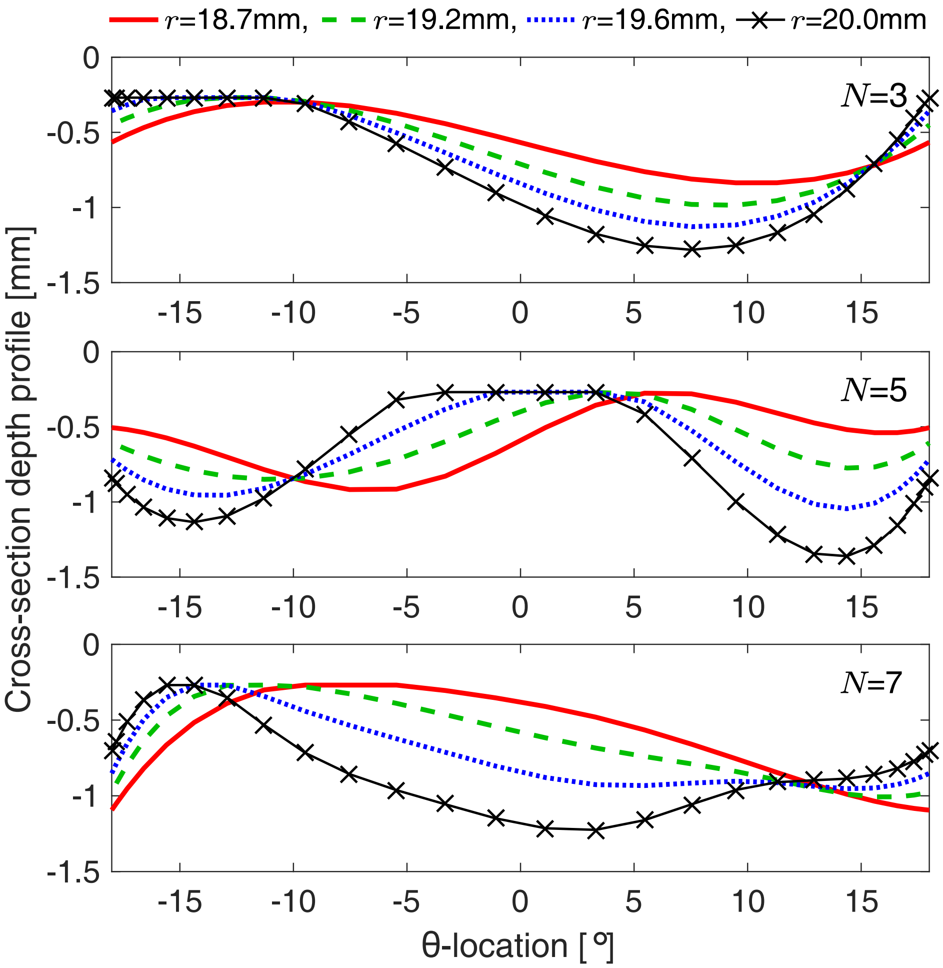

Figure 2.18: Comparison of depth profiles: cross-sectional view of optimal designs, spline design representation cases with N =3, 5, 7, and $F_N = 3$ [N]. The horizontal axis indicates the angular (θ) location within a sector, and vertical axes correspond to texture elevation. Each subfigure corresponds to a different spline N. Positive thrust occurs when the opposing upper flat surface moves in the positive θ-direction.

texture profiles consist of asymmetric expansion-contraction channels. In addition, these periodic asymmetric profiles shift to the right with decreasing radial position, resulting in spiral texture geometries. While low-dimension spline representations ($N = 3$) produce texture geometries that can capitalize on the physical effects discussed above, increasing N results in complex waviness in designs and improved performance. Higher-resolution representations, however, increase computational expense (discussed next).

Table 2.3: Comparison of average computation cost per single scalarized optimization problem and system performance obtained from ε-constraint method and interior-point (IP) algorithm

Order of design mesh (number of variables)		$N = 3$ (4×3)	$N = 4$ (5×4)	$N = 5$ (6×5)	$N = 6$ (7×6)	$N = 7$ (8×7)
Computation time per single IP run [min]		3.7	7.3	12.2	17.5	25.1
Normal force F_N [N]	at $\eta_a/\eta_0 = 0.3$	0.54	0.62	0.76	0.91	1.08
	at $\eta_a/\eta_0 = 0.5$	2.02	2.78	3.21	3.84	4.23
	at $\eta_a/\eta_0 = 0.7$	4.05	5.02	5.67	6.59	6.89
Apparent viscosity η_a/η_0 [–]	at $F_N = 1$	0.38	0.35	0.33	0.31	0.29
	at $F_N = 3$	0.60	0.52	0.49	0.44	0.42
	at $F_N = 5$	0.86	0.70	0.63	0.58	0.56

2.7.5 Computational expense comparison

All problems were solved using dual Intel® Xeon® X5650 CPUs with a total of 12 physical cores. Gradient evaluation within the interior-point algorithm [52] is computed in parallel to utilize all CPU cores. All cases converged to solutions with a function value tolerance of 10^{-8}. A summary of the average computation time for single scalarized problems is given in Table 2.3. Computation time for the complete MOP is approximately the number of Pareto-optimal points for a given curve in Fig. 2.16, multiplied by the average computation time for each interior-point (IP) solution reported in Table 2.3.

To compare the computational cost across the range of spline design resolutions, Table 2.3 lists the cost per single IP run (i.e., the time to find one point in the Pareto set). The computation time required to calculate both objective functions for a single design was typically less than 0.1 seconds. This is independent of N, because the computational domain (Fig. 2.3b) is the same for all design resolutions N. The solution time for a single IP run, however, increases significantly with N. For higher-resolution cases (e.g., $N = 5, 6, 7$), functional performance increases as shown in Fig. 2.16, but this must be weighed against the increase in computational expense quantified in Table 2.3. An appropriate choice may depend on a number of factors, including application and whether the studies are supporting early- or late-stage design decisions.

2.7.6 Limitations

The design studies here are performed under certain assumptions and simplifications described in Sections 2.3, 2.4, and 2.5, which place inherent limitations on the results of this design study. These limitations are due to the simplification of governing equations, properties of certain texture design representations, and limited design representation resolution.

First, the Reynolds equation model is valid only when the aspect ratio of the confined flow is sufficiently wide (Fig. 2.7), but is favorable for design optimization studies due to the associated computational efficiency. Thus, design study results are limited by the approximate simulation model, which may dominate true physical limitations. In addition, cavitation is not considered in our Reynolds equation model. Although some previous studies accounted for cavitation effects [21, 22, 25, 40, 53], it was not observed in our experiments [30]. Cavitation effects could be included in future work using the same optimization framework presented here with an appropriate system model.

Second, our study did not look at the coefficient of friction μ^*, which is one popular way to identify an optimal design. The coefficient of friction is defined as the shear stress divided by the normal force. This measure is equivalent to the value of our first objective η_a/η_0 divided by our second objective F_N. The resulting optimal design using μ^* as the objective function would produce a single point on the Pareto front generated here. In more general design problems, design utility may not be represented accurately by the coefficient of friction. For example, if small F_N is needed but reducing η_a/η_0 is more important, this is not captured by minimizing the coefficient of friction.

Third, design studies are limited to a sector (one-tenth of a full disk) with a rotational-periodic boundary repeated in every $\phi = 2\pi/10$ [rad]. Although periodic boundary conditions approximate accurately full disk behavior, the assumption of periodicity implicitly constrains the designs explored. In addition, different sector sizes (e.g., $\{2\pi/6, 2\pi/8, 2\pi/12\}$ [rad], etc.) may produce different results and new insights. Future studies should investigate different sector sizes, as well as the elimination of the periodic sector assumption and design the full disk texture directly. Furthermore, different kinematics (e.g., linear sliding motion) other than the rotating disk configuration will have different optimal designs since pressure cannot be built up near a center-of-rotation region. Future studies should address different practical configurations.

Fourth, while performance was improved by moving to a free-form texture design representation, spline parameterization still requires at least tens of design variables. Optimization studies were performed using efficient gradient-based methods with limited multi-start to balance computational expense and the improving probability of finding global optima. More effective global methods may be impractical due to the problem dimension, and because the simulation is utilized here as a black-box model.

Increasing design resolution using the current optimization strategy may be impractical, but the increased resolution is required to investigate true performance limits accessible via texture design. Several limitations were observed when using the current low-dimension texture design representation, including a generation of very sharp edges or sudden nonsmooth slope changes. Alternative optimization strategies that support higher-resolution design representation should be investigated. One possible strategy is to use design abstraction techniques, such as generative design algorithms [54], image warping methods [55], or other surface representation techniques [56]. A G', G'' using the simulation mesh values h_{ij} may be another promising strategy, but a practical solution will require novel large-scale optimization formulations that capitalize on problem structure to manage the significantly increased problem dimension (e.g., thousands of optimization variables). Ongoing work is exploring the possibility of using convex programming techniques to support significant increases in design resolution while maintaining computational tractability (e.g., [57]). One such strategy, based on SLP, was investigated and is presented in the next chapter.

2.8 Conclusion

Full-film lubrication problems have been studied extensively in the tribology community, often with the objective of improving normal load capacity and decreasing shear load resistance. Using textured contact surfaces is known to be effective for reducing frictional energy loss. More recently, an experimental study has revealed that asymmetric depth profile texture patterns can improve performance further by generating net normal forces to carry higher loads [30]. Based on these previous discoveries pertaining to full-film lubrication, this study presented an investigation of how the transition to more sophisticated texture designs can improve performance in exceptional ways, and has offered insights into the underlying mechanisms that enable these improvements. The studies presented here focused on the simultaneous improvement of apparent viscosity and normal force.

Predefined texture shapes, such as cylindrical dimples, limit potential performance improvements that are achievable with more general surface texture design. A general design pattern was clearly present among the Pareto-optimal results for the asymmetric spline-based design study. The resulting designs resemble a spiral blade, and observations of the flow and pressure fields provide insight into the mechanisms leveraged by these designs to improve performance.

The ultimate objective of these and other related efforts is to realize new levels of performance and efficiency for fluid power systems and to reveal physical and design principles that support these improvements. Ongoing efforts complement the results presented here, including the development of new models and solution techniques that will enable the computationally-efficient design of very high-resolution texture geometries by capitalizing on problem structure. The next steps include investigation of full-film lubrication problems in configurations that are more representative of practical engineering systems, investigating texture design representations based on generative algorithms, incorporating manufacturability and cost considerations, and transitioning from Newtonian to non-Newtonian fluid system models. For example, a linear sliding motion can be another configuration to represent practical reciprocating contact surfaces [58]. Different targets for normal load or sliding speed may affect optimal solutions [59]. Optimization results have provided a rich set of design data from which qualitative design insights can be extracted. Future work will iteratively deepen, validate, and enhance this qualitative understanding, leading to valuable design knowledge that may impact technologies, such as bearing systems, reciprocating mechanisms (e.g., automotive engines), energy systems, and fluid power systems.

Chapter 3

Efficient Design of Textured Surface Lubrication Using Linearization[1,2]

3.1 Summary

Surface textures reduce friction in lubricated sliding contact. This behavior can be modeled using the Reynolds equation, a single partial differential equation (PDE) that relates the hydrodynamic pressure to the gap height. In a previous study, a free-form texture design optimization problem was solved based on this model and two competing design objectives. A pseudospectral method was used for the PDE solution, which was treated as a black box in the optimization problem. This optimization implementation did not exploit model structure to improve numerical efficiency, so design representation fidelity was limited. Here a new strategy is introduced where design representation resolution and computational efficiency are simultaneously enhanced. This is achieved by introducing a new optimization variable involving both the pressure gradient and the cube of gap height at each mesh node location, and it solves the flow and texture design problems simultaneously. This transformation supports the linearization of the governing equations and design objectives. The sequential linear programming (SLP) is used with the ε-constraint method to generate Pareto-optimal texture designs with high resolution and low computational expense. An adaptive trust-region is used along with the linear program (LP) to manage linearization error based on quantified

---

[1] Part of the content reported in this chapter is presented in (Lin, Lee, Schuh, Ewoldt, and Allison. Efficient optimal surface texture design using linearization. In Schumacher et al. (ed.) *Advances in Structural and Multidisciplinary Optimization: Proc. WCSMO-12*:632-647, Springer), ©2018 by the authors.

[2] Mr. Yong Hoon Lee, Mr. Chendi Lin, and Dr. Jonathon Schuh collaboratively derived the formulation based on Dr. Jonathon Schuh's Reynolds equation solver. Mr. Yong Hoon Lee also contributed with the numerical optimization techniques.

solution improvement. Comparing to the nonlinear program (NLP) implementation, the solutions converged to a set of Pareto-optimal points that is similar to the results of the NLP. Still, some solutions are slightly suboptimal in a few regions. The SLP method does not meaningfully enhance the performance of the design, but improves the computational speed significantly, up to 8.4 times faster than the NLP method.

3.2 Introduction

Surface textures reduce friction in lubricated sliding contact [16]. In many practical engineering applications with a lubricated sliding contact, reducing energy loss, wear, friction-induced noise, and improving compactness are important design objectives [4, 60]. Since the roughness of a sliding surface primarily affects friction performance, a comprehensive set of studies has been conducted to understand how changes in surface roughness can reduce friction. Many existing studies focus on creating an array of dimples with circular or other shapes. It has been demonstrated that circular micro dimples fabricated using abrasive jet machining and laser beam machining with different sizes can help reduce lubrication friction [15]. A theoretical model of micro-dimple hydrodynamics has been introduced and verified experimentally, showing that surface microstructures enhance frictional performance [16]. Previous studies have not been limited to only circular dimple shapes. More recent studies show that other specific surface texture top profile shapes can further improve frictional and load-carrying performance [20, 22, 61], while other studies also investigated the effect of depth profile changes as well [21, 30].

A series of recent studies tried to further enhance the frictional performance and load-carrying capacity by expanding the surface texture to the free-form design of the full interface surface and led to the improvement of both objectives by an order of magnitude [4, 62]. These studies involved a reduced-dimension texture design parameterization as a strategy to improve computational efficiency for optimization studies, at the expense of reduced texture design resolution. The optimization studies were based on a Reynolds equation model, which is the simplest option for predicting the frictional performance of lubricated sliding contacts. Several earlier numerical studies have been performed using the Reynolds equation to examine the effects of surface textures on friction reduction [53, 63, 64]. However, solving a fluid flow requires a computationally expensive solution of a nonlinear system of equations (even when based on a simplified governing equation, such as the Reynolds equation). Here a more efficient method for solving the texture optimization problem for lubricated sliding contact is proposed by linearizing the Reynolds equation and sequentially updating the approximated linearization.

3.3 Problem Formulation

3.3.1 Problem Statement

Using the rotational tribo-rheometer setup presented in Chapter 2, Fig. 2.1a, we are designing a two-dimensional texture profile for the fixed bottom plate. The nominal gap height between the top and bottom plates is fixed, and the torque and normal force on the moving flat surface is measured [30]. This study aims to decrease friction within the system while simultaneously increasing the normal force produced by the surface texture. Recent studies demonstrated that these two objectives could be achieved with asymmetric depth profile surface textures [4, 30, 36]. In this study, we optimize the height profile of the surface texture using a computationally-efficient linearization technique applied to the Reynolds equation. The design variable (gap height) has the same dimensions as the computational mesh, i.e., we are designing the gap height at each mesh point instead of using the reduced-dimension design representation of Chapter 2. Figure 2.1a shows the front view of the experimental setup of this study. Two disks are separated by Newtonian fluid, with the flat disk rotating on the top, and the textured surface fixed at the bottom. To reduce the computing complexity, we divide the full disk into N_{tex} periodic sectors. In this study, the choice of N_{tex} will affect our

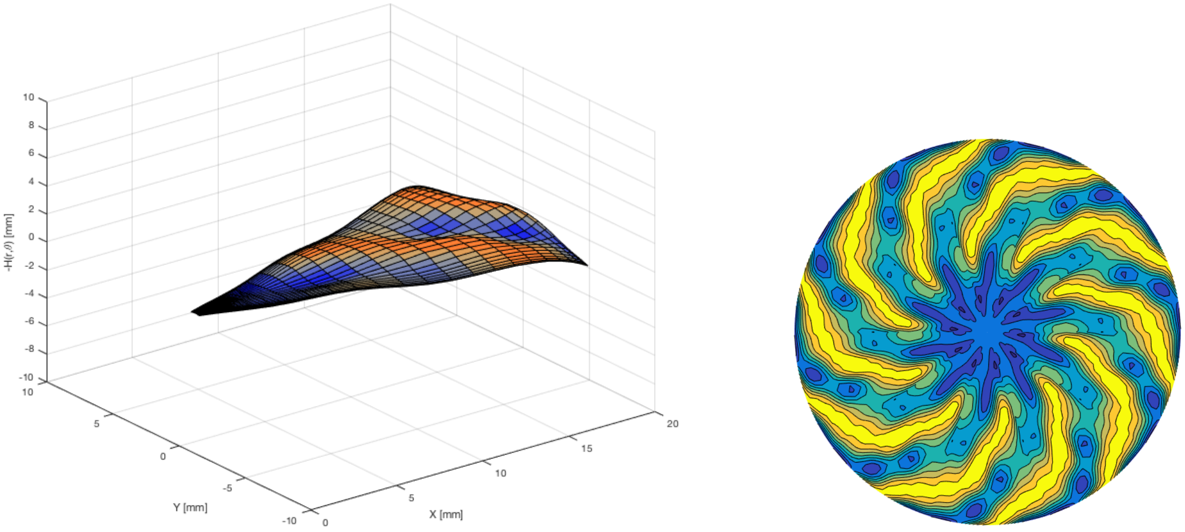

(a) (b)

Figure 3.1: Benchmark design used as a starting design point for optimization studies presented in this chapter. This benchmark design is the optimal surface texture profile obtained in the study presented in Chapter 2 [4]. The corresponding normal force is $F_N = 7.03$ N, and the normalized apparent shear viscosity is $\tau = 0.737$ (normalized). (a) Surface for a single disk sector of the benchmark design. (b) Full disk image of the benchmark design.

results, and we chose $N_{\text{tex}} = 10$. Figure 2.1b is a closer view of the design domain. The top plate is flat, rotating in the θ-direction, while an arbitrary textured surface is fixed at the bottom. Eventually, the texture surface design will be mapped into a full disk by applying the periodic boundary condition.

The surface texture profile when $F_N = 7.03$ and $\tau = 0.737$ from Lee et al. [4] is used as the starting design point for all optimization studies presented here. This benchmark design is shown in Fig. 3.1. By applying different upper bounds on apparent shear viscosity, we can obtain a set of optimal points. This procedure will be discussed in more detail in Sections 3.3.3, 3.3.4, and 3.5.

3.3.2 Numerical Model for Texture Surface Hydrodynamics

Here we assume that (1) the operating lubricant can be modeled as an incompressible Newtonian fluid with constant viscosity, (2) the flow occurs at low Reynolds numbers so that inertial terms can be neglected, and (3) the gap height is small compared to other length scales in the problem so that gradients in the flow direction can be neglected. Based on these assumptions, the system may be modeled using the Reynolds equation [42] in cylindrical coordinates, given as:

$$\frac{1}{r}\frac{\partial}{\partial r}\left(rh^3\frac{\partial p}{\partial r}\right)+\frac{1}{r}\frac{\partial}{\partial \theta}\left(\frac{h^3}{r}\frac{\partial p}{\partial \theta}\right)=6\eta\Omega\frac{\partial h}{\partial \theta} \tag{3.1}$$

where p is the pressure, h is the gap height, η is the fluid viscosity, and Ω is the angular velocity. The Reynolds equation is a linear, second-order partial differential equation with a non-constant coefficient for pressure that satisfies both conservation of mass and momentum equations. The velocity boundary conditions used to derive Eq. (3.1) are given as:

$$\text{at } z=0: \; v_\theta = r\Omega \text{ , and } v_r = v_z = 0 \tag{3.2a}$$

$$\text{at } z=h: \; v_\theta = v_r = v_z = 0. \tag{3.2b}$$

Integrating conservation of momentum and applying boundary conditions produces the velocity field, given as:

$$v_r = \frac{1}{2\eta}\frac{\partial p}{\partial r}\left(z^2 - zh\right) \tag{3.3a}$$

$$v_\theta = \frac{1}{2\eta}\frac{1}{r}\frac{\partial p}{\partial \theta}\left(z^2 - zh\right) + r\Omega\left(1-\frac{z}{h}\right). \tag{3.3b}$$

Schuh et al. [36] developed the MATLAB™ code for solving Eq. (3.1) using the pseudospectral method, which transforms the partial differential equation (PDE) into an approximate system of algebraic equations, given as:

$$\boldsymbol{K}\underline{p} = \underline{f}, \tag{3.4}$$

where:

$$\begin{aligned}\boldsymbol{K} =& \frac{-\varphi}{R_o - R_i} \left(\boldsymbol{I} \otimes \boldsymbol{D}\right)^T \left(\boldsymbol{M} \otimes \boldsymbol{M}\right) \left(\boldsymbol{I} \otimes \boldsymbol{R}\right) H^3 \left(\boldsymbol{I} \otimes \boldsymbol{D}\right) \\ & - \frac{\left(R_o - R_i\right)}{\varphi} \left(\boldsymbol{D} \otimes \boldsymbol{I}\right)^T \left(\boldsymbol{M} \otimes \boldsymbol{M}\right) \left(\boldsymbol{I} \otimes \boldsymbol{R}^{-1}\right) \boldsymbol{H}^3 \left(\boldsymbol{D} \otimes \boldsymbol{I}\right) \qquad (3.5a)\end{aligned}$$

$$\underline{f} = 3\eta\Omega \left(R_o - R_i\right) \left(\boldsymbol{M} \otimes \boldsymbol{M}\right) \left(\boldsymbol{I} \otimes \boldsymbol{R}\right) \left(\boldsymbol{D} \otimes \boldsymbol{I}\right) \underline{h}. \qquad (3.5b)$$

Here, φ is the total angle for a periodic sector, R_o is the outer radius, R_i is the inner radius, $\boldsymbol{I}$ is the identity matrix, $\boldsymbol{D}$ is a full matrix containing coefficients for approximating the required derivatives, $\boldsymbol{M}$ is a diagonal matrix of Gauss-Lobatto-Legendre (GLL) quadrature weights, $\boldsymbol{R}$ is a diagonal matrix of radius values from R_i to R_o, $\underline{h}$ is a vector, reshaped from the matrix containing the gap height values at each grid point, $\boldsymbol{H}$ is a matrix with diagonal elements from the vector h, and $\otimes$ is the Kronecker product. It was assumed in this derivation that the gap height is periodic in the θ-direction.

A previous design optimization study, presented in Chapter 2, used h as an input to Eq. (3.4), which was then solved to obtain the pressure field, and the velocity field is computed using this pressure field [4]. These fields were then used to determine the objective functions for a given gap height profile (load capacity and a friction metric). In the previous strategy, the Reynolds equation solver was treated as a *black-box* simulation. Each new design candidate tested by the optimization algorithm required simulation, contributing to significant computational expense as the Reynolds equation structure was not leveraged for a more efficient solution. However, if we examine Eq. (3.4) carefully, observations reveal an opportunity to capitalize on problem structure, utilizing both the simultaneous analysis and design (SAND) method [1, 2] and linearization. The SAND formulation involves simultaneous Reynolds equation solution and gap height (texture design) determination. The first step is to rewrite Eq. (3.4) in the following form, given as:

$$\begin{bmatrix} \boldsymbol{K}_r & \boldsymbol{K}_\theta \end{bmatrix} \begin{bmatrix} \underline{h}^3 \odot \underline{p_r} \\ \underline{h}^3 \odot \underline{p_\theta} \end{bmatrix} = \boldsymbol{A}\underline{h}, \tag{3.6}$$

where p_r is the gradient of the pressure in the r-direction, p_θ is the gradient of pressure in the θ-direction, $\odot$ is element-wise multiplication (Hadamard product), and:

$$\boldsymbol{K}_r = \frac{-\varphi}{R_o - R_i} \left(\boldsymbol{I} \otimes \boldsymbol{D}\right)^T \left(\boldsymbol{M} \otimes \boldsymbol{M}\right) \left(\boldsymbol{I} \otimes \boldsymbol{R}\right) \tag{3.7a}$$

$$\boldsymbol{K}_\theta = \frac{-\left(R_o - R_i\right)}{\varphi} \left(\boldsymbol{D} \otimes \boldsymbol{I}\right)^T \left(\boldsymbol{M} \otimes \boldsymbol{M}\right) \left(\boldsymbol{I} \otimes \boldsymbol{R}^{-1}\right) \tag{3.7b}$$

$$\boldsymbol{A} = 3\eta\Omega \left(R_o - R_i\right) \left(\boldsymbol{M} \otimes \boldsymbol{M}\right) \left(\boldsymbol{I} \otimes \boldsymbol{R}\right) \left(\boldsymbol{D} \otimes \boldsymbol{I}\right). \tag{3.7c}$$

In Eq. (3.6), the design variable h appears on both the left- and the right-hand side of the equation, and the equation depends nonlinearly on the gap height. Using a SAND strategy, we combine our design and analysis variables into a new independent optimization variable, denoted $\underline{x}$ here, given as:

$$\underline{x} = \begin{bmatrix} \underline{h}, & \underline{p_r}, & \underline{p_\theta} \end{bmatrix}^\mathsf{T}. \tag{3.8}$$

To make Eq. (3.6) linear in our design variable, we linearize $\underline{h}^3 \odot \underline{p_r}$ and $\underline{h}^3 \odot \underline{p_\theta}$ near their tangent planes using a multivariate Taylor series expansion, given as:

$$\underline{h}^3 \odot \underline{p_r} \approx \underline{h_0}^3 \odot \underline{p_{r_0}} + 3\underline{h_0}^2 \odot \underline{p_{r_0}} \odot \left(\underline{h} - \underline{h_0}\right) + \underline{h_0}^3 \odot \left(\underline{p_r} - \underline{p_{r_0}}\right) \tag{3.9a}$$

$$\underline{h}^3 \odot \underline{p_\theta} \approx \underline{h_0}^3 \odot \underline{p_{\theta_0}} + 3\underline{h_0}^2 \odot \underline{p_{\theta_0}} \odot \left(\underline{h} - \underline{h_0}\right) + \underline{h_0}^3 \odot \left(\underline{p_\theta} - \underline{p_{\theta_0}}\right), \tag{3.9b}$$

where $\underline{h_0}$ is a nominal gap height vector, and $\underline{p_{r_0}}$ is the pressure gradient in the r-direction, and $\underline{p_{\theta_0}}$ is the pressure gradient in the θ-direction for the nominal gap height. Substituting Eqs. (3.9a) and (3.9b) into Eq. (3.6) using our new design variable $\underline{x}$, produces the following formulation, after simplification, given as:

$$\left(\begin{bmatrix}\boldsymbol{K}_r & \boldsymbol{K}_\theta\end{bmatrix}\begin{bmatrix}3\boldsymbol{H}_0^2\boldsymbol{P}_{r_0} & \boldsymbol{H}_0^3 & \boldsymbol{0}\\ 3\boldsymbol{H}_0^2\boldsymbol{P}_{\theta_0} & \boldsymbol{0} & \boldsymbol{H}_0^3\end{bmatrix} - \begin{bmatrix}\boldsymbol{A} & \boldsymbol{0} & \boldsymbol{0}\end{bmatrix}\right)\underline{x} = \begin{bmatrix}\boldsymbol{K}_r & \boldsymbol{K}_\theta\end{bmatrix}\begin{bmatrix}3\underline{h_0}^3 \odot \underline{p_{r_0}}\\ 3\underline{h_0}^3 \odot \underline{p_{\theta_0}}\end{bmatrix} \tag{3.10}$$

where $\boldsymbol{H}_0^2\boldsymbol{P}_{r_0}$ is a diagonal matrix with the elements $\underline{h_0}^2 \odot \underline{p_{r_0}}$, the diagonal matrix $\boldsymbol{H}_0^2\boldsymbol{P}_{\theta_0}$ is composed of elements $\underline{h_0}^2 \odot \underline{p_{\theta_0}}$, $\boldsymbol{H}_0^3$ is a diagonal matrix with the elements $\underline{h_0}^3$, and $\boldsymbol{0}$ is the zero-matrix with appropriate dimensions. Equation (3.10) can be rewritten in the following compact form, given as:

$$\hat{\boldsymbol{K}}\underline{x} = \underline{\hat{f}}. \tag{3.11}$$

All of the design variables appear only on the left-hand side of Eq. (3.11), and the right-hand side is known after the nominal gap height profile is given. Therefore, solving Eq. (3.11) (with appropriate pressure boundary conditions [36]) produces the associated pressure field gradients for a given gap height design.

Our two objective functions are the normal force F_N and the nondimensional shear stress τ^*, which is equivalent to the apparent viscosity normalized by the fluid viscosity (η_a/η_0). The normal force is obtained by integrating the pressure field. Solving Eq. (3.11), however, produces pressure field gradients. The pressure field can be obtained from its gradient using:

$$\begin{bmatrix}\boldsymbol{I}\otimes\boldsymbol{D}\\ \boldsymbol{D}\otimes\boldsymbol{I}\end{bmatrix}\underline{p} = \begin{bmatrix}\underline{p_r}\\ \underline{p_\theta}\end{bmatrix}. \tag{3.12}$$

Once the pressure has been obtained, the normal force on the flat plate is calculated using:

$$F_N \equiv \int_0^{2\pi}\int_{R_i}^{R_o} prdrd\theta = N_{\text{tex}}\int_{-\varphi/2}^{\varphi/2}\int_{R_i}^{R_o} pr\ drd\theta, \tag{3.13}$$

where the total number of periodic cells on the thrust bearing is:

$$N_{\text{tex}} = \frac{2\pi}{\varphi}. \tag{3.14}$$

This is calculated numerically using:

$$F_N = N_{\text{tex}} \left(\frac{\varphi \left(R_o - R_i \right)}{4} \right) \left(\underline{w} \otimes \underline{w} \right)^T \left(\boldsymbol{I} \otimes \boldsymbol{R} \right) \underline{p}, \tag{3.15}$$

where $\underline{w}$ is the vector of GLL quadrature weights.

Pressure derivatives are used to determine the velocity using Eqs. (3.3a) and (3.3b), and derivatives of the velocity components are used to determine the shear stress on the top plate, given as:

$$\left.\tau_{z\theta}\right|_{z=0} = \eta \left(\frac{\partial v_\theta}{\partial z} + \frac{1}{r} \frac{\partial v_z}{\partial \theta} \right) \Bigg|_{z=0}. \tag{3.16}$$

Substituting Eq. (3.3b) into this equation produces:

$$\left.\tau_{z\theta}\right|_{z=0} = - \left(\frac{1}{2r} \frac{\partial p}{\partial \theta} h + \eta \frac{r\Omega}{h} \right). \tag{3.17}$$

The torque M on the flat plate is calculated from the shear stress, given as:

$$M \equiv \int_0^{2\pi} \int_{R_i}^{R_o} \left(\left.\tau_{z\theta}\right|_{z=0} \right) r^2 dr d\theta = N_{\text{tex}} \int_{-\varphi/2}^{\varphi/2} \int_{R_i}^{R_o} \left(\left.\tau_{z\theta}\right|_{z=0} \right) r^2 \, dr d\theta, \tag{3.18}$$

which is calculated numerically as:

$$M = N_{\text{tex}} \left(\frac{\varphi \left(R_o - R_i \right)}{4} \right) \left(\underline{w} \otimes \underline{w} \right)^T \left(\boldsymbol{I} \otimes \boldsymbol{R}^2 \right) \underline{\tau_{z\theta}}. \tag{3.19}$$

The torque can then be used to determine the nondimensional shear stress (objective function) as follows:

$$\tau^* \equiv \frac{\dfrac{2}{\pi R_o^3} M}{\dfrac{\eta R_o \Omega}{h_0}} = \frac{2h_0}{\eta \pi R_o^4} \frac{M}{\Omega}. \tag{3.20}$$

Using the parameters defined in the design variable vector $\underline{x}$, we can rewrite Eq. (3.17) to obtain:

$$\tau_{z\theta}\big|_{z=0} = -\left(\frac{1}{\varphi r} p_\theta h + \eta \frac{r\Omega}{h}\right), \tag{3.21}$$

where we have used:

$$\frac{\partial p}{\partial \theta} = \frac{2}{\varphi} p_\theta. \tag{3.22}$$

Equation (3.21) is nonlinear in h and p_θ. Since we previously linearized our problem about h_0 and p_{θ_0}, we must also linearize $\tau_{z\theta}$ about h_0 and p_{θ_0} for our analysis to be consistent. Performing Taylor series expansions for the nonlinear terms produces:

$$p_\theta h = p_{\theta_0} h_0 + p_{\theta_0}(h - h_0) + (p_\theta - p_{\theta_0}) h = -p_{\theta_0} h_0 + p_{\theta_0} h + p_\theta h_0, \tag{3.23a}$$

$$\frac{1}{h} = \frac{1}{h_0} - \frac{1}{h_0^2}(h - h_0) = \frac{2}{h_0} - \frac{1}{h_0^2} h, \tag{3.23b}$$

which when substituted back into Eq. (3.21) yields:

$$\tau_{z\theta}\big|_{z=0} = -\left(\left(\frac{p_{\theta_0}}{r\varphi} - \eta \frac{r\Omega}{h_0^2}\right) h + \frac{h_0}{r\varphi} p_\theta - \frac{p_{\theta_0} h_0}{r\varphi} + 2\eta \frac{r\Omega}{h_0}\right). \tag{3.24}$$

This is calculated numerically using:

$$\underline{\tau_{z\theta}} = -\begin{bmatrix} \boldsymbol{B}_h & \boldsymbol{0} & \boldsymbol{B}_{p_\theta} \end{bmatrix} \underline{x} - \underline{c}, \tag{3.25}$$

where:

$$\boldsymbol{B}_h = \frac{1}{\varphi} P_{\theta_0} \left(\boldsymbol{I} \otimes \boldsymbol{R}^{-1}\right) - \eta \Omega \left(\boldsymbol{I} \otimes \boldsymbol{R}\right) \left(\boldsymbol{H}_0^2\right)^{-1} \tag{3.26a}$$

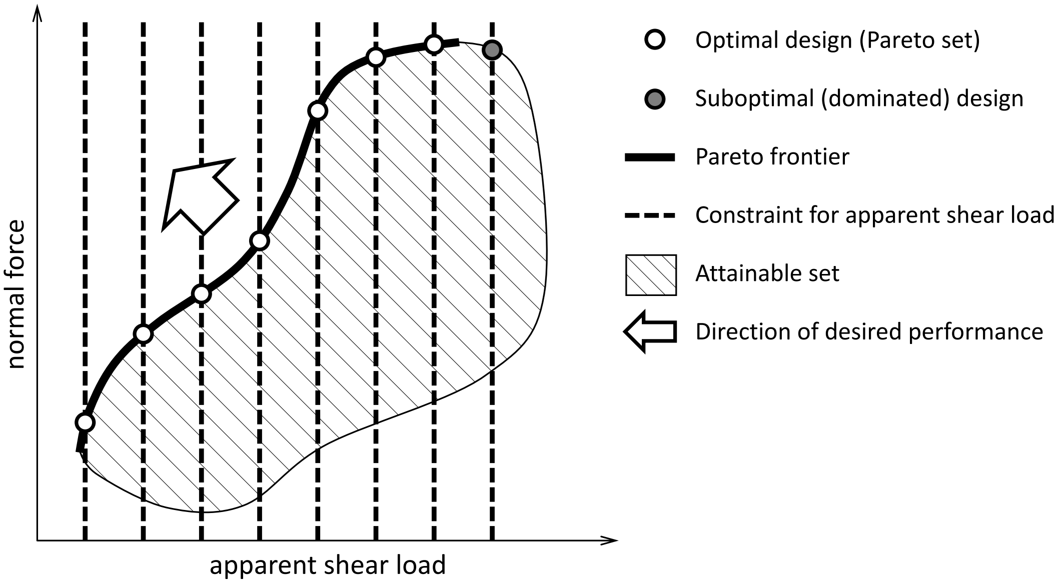

Figure 3.2: Schematic showing how the ε-constraint method is used for this problem. We optimize one objective function (here, maximizing normal force) while constraining the other metric using an inequality constraint (here, constraining apparent shear viscosity to be less than a certain value). The incrementally varied maximum bound on shear load is shown as a dashed line. Open circles are the optimal design points obtained from each of the optimization subproblems. The gray circle is an example of a dominated (suboptimal) design point. These optimal designs are on the Pareto frontier, shown with a thick solid black line.

$$\boldsymbol{B}_{p_\theta} = \frac{1}{\varphi}\boldsymbol{H}_0\left(\boldsymbol{I}\otimes\boldsymbol{R}^{-1}\right) \tag{3.26b}$$

$$\underline{c} = -\frac{1}{\varphi}\boldsymbol{P}_{\theta_0}\left(\boldsymbol{I}\otimes\boldsymbol{R}^{-1}\right)\underline{h_0} + 2\eta\Omega\left(\boldsymbol{I}\otimes\boldsymbol{R}\right)\underline{h_0}^{-1}, \tag{3.26c}$$

and $\boldsymbol{P}_{\theta_0}$ is a diagonal matrix of elements $\underline{p_{\theta_0}}$, $\boldsymbol{H}_0^2$ is a diagonal matrix of elements $\underline{h_0}^2$, and $\underline{h_0}^{-1}$ is an element-wise inversion of $\underline{h_0}$. Equation (3.25) can be used with Eqs. (3.19) and (3.20) to calculate the nondimensional shear stress.

3.3.3 Multiobjective Optimization

Since we are solving a multiobjective problem with two competing objective functions, the solution sought is a Pareto frontier that expresses the tradeoff between these two objectives [48]. The ε-constraint method [49] is a commonly used technique to convert a multiobjective problem into a set of optimization problems with single objective functions. This is done by optimizing a single objective function while using the other objectives functions as inequality constraints with bounds. By adjusting these bounds for the objective functions posed as inequality constraints, we generate a set of problems. The solution of each of these problems produces a single point on the Pareto frontier.

Figure 3.2 demonstrates the conflict between our two objectives, (1) minimizing the shear load, which is represented by the apparent shear viscosity normalized by the fluid viscosity (expressed as η_a/η_0), and (2) maximizing the normal force. Both these objectives help reduce friction in this lubrication problem, which is the main source of energy loss. From the Pareto frontier, we can tell that, as normal force F_N increases, the apparent shear stress increases inevitably. The feasible region for our design objectives is shaded; all optimal designs lie within this region. We optimized the normal force with respect to a given shear load, which was used as our inequality constraint. The dashed black lines are different shear load values, and the white circles are the optimal normal force values obtained for each given shear load bound. The open circles lie on the boundary of the attainable set. Connecting the white circles gives our Pareto front of optimal solutions, which is shown with the solid black line. The gray circle at the top right is an example of a *dominated point*; it is dominated because feasible solutions exist where both objectives can be improved simultaneously, as evident in Fig. 3.2. The texture designs that give this Pareto front are the optimal texture designs.

3.3.4 Trust-Region and Step Size

An adaptive trust-region method is essential to control linearization error and helps improve solution convergence [65, pp. 303–308]. Here we implement a trust-region method that involves the following steps described below to obtain the solution iteratively.

Step 1. Initialize Parameters

- Specify initial starting point $\underline{x}_0$ and initial trust-region radius Δ_0.

For gap height $\underline{h}$, the initial trust-region radius is set to be 10% of the size of gap height bounds at each grid point, and for the gradient of pressure values $\underline{p}_r$ and $\underline{p}_\theta$, the initial trust-region radius is set to be 100 [Pa].

- Set the trust-region constants, $0 < \eta_1 < \eta_2 < 1$ and $0 < \gamma_1 < 1 < \gamma_2$.

  In this study, we set $\eta_1 = 0.01$, $\eta_2 = 0.9$, $\gamma_1 = 0.5$ and $\gamma_2 = 1.5$. However, the algorithm is not sensitive to the choice of parameter values [65].

- $k = 0$.

- Compute $f(\underline{x}_k)$ at the initial point $\underline{x}_0$, set $m_0(\underline{x}_0) \leftarrow f(\underline{x}_0)$.

Step 2. Linear program (LP) Solution

- Solve the LP problem $\min\{m_k(\underline{x}^*)\}$ to get $s_k = \underline{x}^* - \underline{x}_k$.

  Based on the linearized problem, a linear program with a trust-region constraint is solved for s_k to determine a new design $x_k + s_k$ (trial point) that is inside the trust-region.

  We use $f(\underline{x}_k)$ to indicate the objective function based on the original nonlinear equations, and $m(\underline{x}_k)$ to represent the approximation of the objective function.

Step 3. Acceptance of Trial Point

- Compute $f(\underline{x}_k + \underline{s}_k)$ and ρ_k, where:

$$\rho_k = \frac{f(\underline{x}_k) - f(\underline{x}_k + \underline{s}_k)}{m_k(\underline{x}_k) - m_k(\underline{x}_k + \underline{s}_k)} \tag{3.27}$$

- Update trial point for the next step $\underline{x}_{k+1}$, where:

$$\underline{x}_{k+1} = \begin{cases} \underline{x}_k + \alpha \underline{s}_k & \text{if } \rho_k \geq \eta_1, \\ \underline{x}_k & \text{if } \rho_k < \eta_1. \end{cases} \tag{3.28}$$

Generally, α is set to 1. However, for robustness, α can be much smaller value to move slowly toward the solution. Here in this study, we set $\alpha = 0.01$.

If the acceptance criteria ρ_k is larger than the parameter η_1, the iteration is successful and $\underline{x}_{k+1}$ is used as the next point for the next iteration. On the other hand, the acceptance criteria is smaller than η_1, the iteration is unsuccessful, and we linearize the model at the same location $\underline{x}_k$ for the next iteration.

Step 4. Trust-Region Radius Update

- Update trust-region radius Δ_{k+1}, where:

$$\Delta_{k+1} \in \begin{cases} [\Delta_k,\ \min(\gamma_2 \Delta_k,\ \Delta_{\max})] & \text{if } \rho_k \geq \eta_2, \\ [\gamma_1 \Delta_k,\ \Delta_k] & \text{if } \rho_k \in (\eta_1,\ \eta_2], \\ (0,\ \gamma_1 \Delta_k] & \text{if } \rho_k < \eta_1. \end{cases} \tag{3.29}$$

By comparing ρ_k with η_1 and η_2, the trust-region can be adjusted to approach the solution in an appropriate manner. If the linear approximation is very accurate (i.e., the acceptance ρ_k is larger than η_2), the trust-region will be expanded. On the contrary, if ρ_k is small, the trust-region will be shrunk accordingly.

Step 5. Step Toward Next Iteration

- $k \leftarrow k + 1$.
- If the gradient is larger than the stopping criteria, return to Step 2 for the next iteration.

With this method, the trust-region size is adjusted adaptively to maintain acceptable linearization accuracy. When the algorithm uses a good search direction, and the estimate is accurate, the trust-region is expanded. If the LP algorithm does not converge, produces a poor search direction, or does not estimate function values accurately, then we shrink the

Table 3.1: Comparison of sequential linear programming (SLP) to the full nonlinear program (NLP) result where the reference results from the NLP is used as the design fed into the SLP solution method. The SLP results match the nonlinear optimization results exactly, validating the fluid analysis part of the SLP formulation.

Shear Load	0.76	0.73	0.71	0.69	0.63	0.57	0.50
Normal Force (NLP)	6.25	6.00	5.75	5.50	5.00	4.25	3.25
Normal Force (SLP)	6.25	6.00	5.75	5.50	5.00	4.25	3.25

trust-region to compensate. Inspired by the move limit method used in the truss design method from John et al. [66], we choose a new design point with α as the move limit if no improvement is observed. Instead of adaptively updating α as the literature suggested, we use a constant value, 0.01, in this study. Studying strategies for adaptively updating alpha is a topic left for future work.

3.4 Verification

We compare our results to those reported in Chapter 2 for the same problem that utilized an NLP solution method with a spline texture design representation [4]. Here, we use previous optimal designs from the NLP solution as starting points for the SLP strategy introduced here.

The results of the SLP and NLP solution strategies are compared in Table 3.1. SLP obtains the same optimal normal force values as NLP, validating our method. However, the LP cannot produce an improvement over the NLP results as the LP can only identify locally optimal points.

3.5 Results and Discussion

Using the results from the previous NLP study as our starting points (where $F_N = 7.37$ [N]), we generated the Pareto set by using different values for the apparent shear viscosity bound

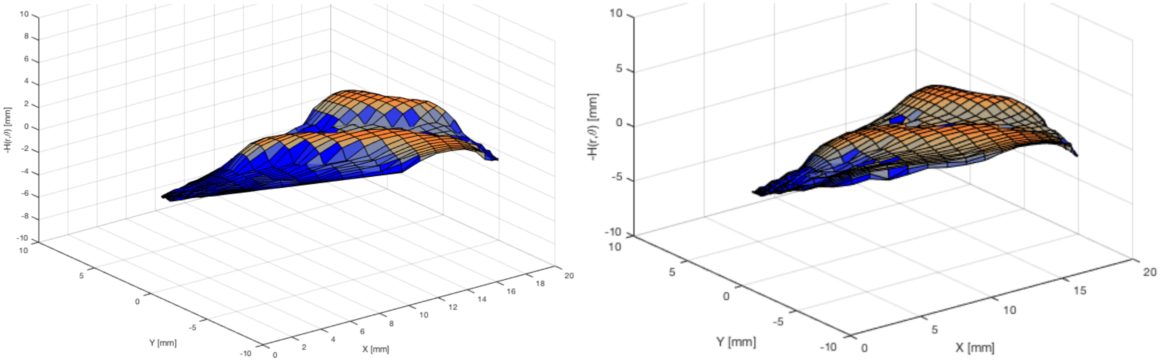

(a) (b)

Figure 3.3: Optimal design results of two sample disk surfaces in a single sector view. Each surface texture design corresponds to a different point on the Pareto frontier, as shown in Fig. 3.5. (a) Sample surfaces, $\tau^* = 0.481$, $F = 2.91$. (b) Sample surfaces, $\tau^* = 0.632$, $F = 5.20$.

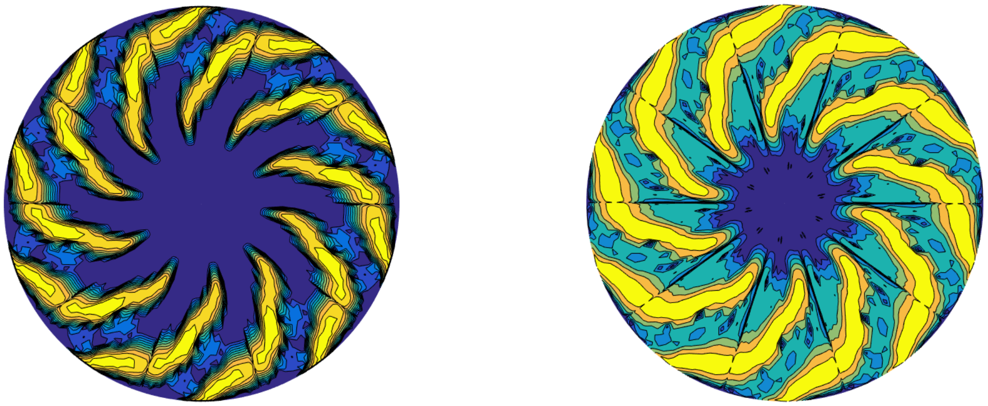

(a) (b)

Figure 3.4: Optimal design results of two sample texture shapes in the full-disk view. Each disk image corresponds to a different point on the Pareto frontier, as shown in Fig. 3.5. (a) Sample full-disk plot, $\tau^* = 0.481$, $F = 2.91$. (b) Sample full-disk plot, $\tau^* = 0.632$, $F = 5.20$.

(as shown in Section 4.2). Sample surface texture designs from the Pareto set are shown in Figs. 3.3a and 3.3b. The Pareto set was obtained using the LP optimizer included in MOSEK™ with a single start method coupled with our trust-region strategy. This improves the ability to find optimal points that may be far away from the initial design point.

Figure 3.5 compares the Pareto fronts obtained using the SLP solution to those obtained using NLP with varying spline representation orders ($N \in \{3,\ 5,\ 7\}$), where $N = 5$ is used as a reference solution. The SLP solution performs similar to the reference NLP solution

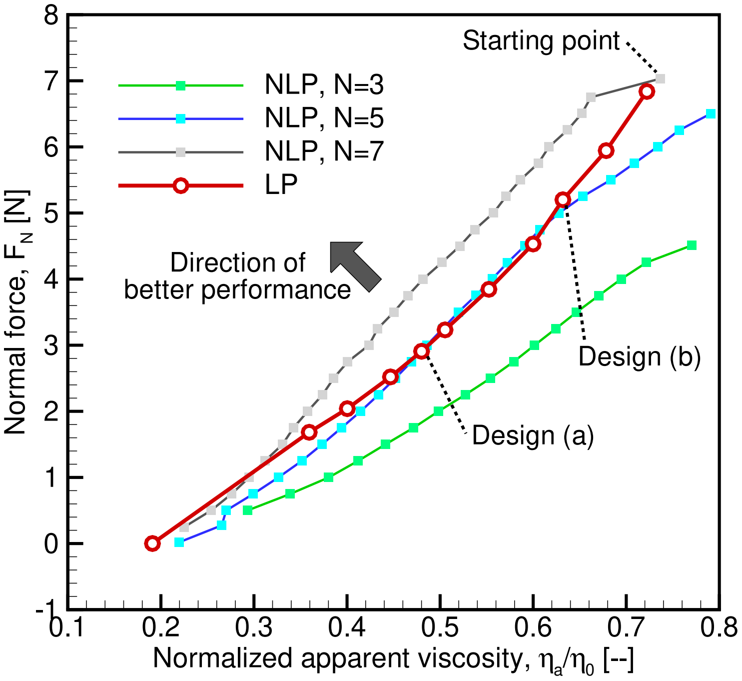

Figure 3.5: Comparison of the Pareto sets obtained using the NLP method [4] and the SLP method results obtained in this study. Design (a) corresponds to the results given in Fig. 3.3a and 3.4a. Design (b) corresponds to the results given in Fig. 3.3b and 3.4b. SLP produces better results than NLP when compared to spline surface representations of order $N = 3$, and 5 in a certain range of operating performance. The NLP solution with spline order $N = 5$ was chosen as the reference case. The SLP solution performs similar to the reference case in the region $0.469 < \tau_* < 0.628$, but performs better than the reference case at both high and low τ^*. The NLP solutions with spline order $N = 7$ (improved resolution) perform better than the SLP solution.

in the region $0.469 < \tau^* < 0.628$, but performs better than the reference case at both high and low τ^* values. In the region where $0.469 < \tau^* < 0.628$, there are points where the SLP method performs worse than the NLP method (maximum 25% deviation in normal force value between the two methods at $\tau^* = 0.5$). This may be due to the choice of trust-region and step size. Another factor may be the existence of multiple distinct surface texture designs with the same normal force value for a give shear load, as shown in Fig. 3.1.

The greatest advantage of using the SLP strategy is realized when comparing computational expense for the solution. Table 3.2 compares the total computation time required

Table 3.2: Computational Time to Find An Optimal Point (on Average)

$N = 3$ (NLP)	$N = 4$ (NLP)	$N = 5$ (NLP)	$N = 6$ (NLP)	$N = 7$ (NLP)	SLP
3.7 min	7.3 min	12.2 min	17.5 min	25.1 min	1.3 min

Table 3.3: Relative Computational Time Comparison

NLP with reduced design representation	$N = 3$	$N = 4$	$N = 5$	$N = 6$	$N = 7$
Time improvement using SLP [%]	185	462	838	1,246	1,831

(on average) to find an optimal point when using different N values for both the NLP and SLP methods. The reported computation time was obtained using a dual-core Intel Core™ i5-4250U processor for all studies. As with many numerical optimization problems, we see that there is a tradeoff here between solution quality and computational expense. Introducing the SLP strategy allows us to reduce computational expense significantly while achieving solution quality comparable to many of the NLP results. Table 3.3 shows how much faster the SLP solution is compared to the different NLP solutions. Even for the lowest-order spline design representation, the NLP method is almost twice as slow as SLP. When comparing the highest-order NLP solution time to SLP, we find that SLP is approximately 20 times faster.

3.6 Conclusion

Several numerical studies have been performed based on a Reynolds equation model to examine the effects of surface texture design variation on friction reduction and normal force generation. The previous optimization studies [4, 62] achieved an efficient solution by reducing the design representation dimension using spline texture representation and solving the NLP optimization problem. During these previous studies, the simulation was treated as a black box. Here, the model structure was leveraged to formulate an SLP strategy to improve design representation fidelity and computational efficiency simultaneously. Improved design fidelity may support the identification of new types of designs and physical mechanisms to further improve system performance over the previous NLP results. However, this consideration is a topic of ongoing work and not within the scope of this study.

Numerical studies presented here indicate significant improvements in computational efficiency while maintaining reasonable solution quality. While NLP solutions using high-order spline representations produced higher-performance designs than SLP, the SLP solution was at least an order of magnitude faster. Another improvement is robustness to the starting point. The previous NLP strategy required a multi-start approach to converge to a reasonable solution reliably. This study showed that a single well-selected starting point was sufficient for generating all Pareto-optimal points. This method was demonstrated using a sector of the sliding surface, but it could be extended to other models based on a semi-circle, or even the full rotating disk.

The SLP method, however, has several clear limitations. As SLP cannot explore outside the trust-region; once the trial point drops inside the feasible region, it can only find a local optimum. Thus, it cannot improve the solution beyond the best results from the previous NLP studies. In addition, because of linearization error, the SLP method produces a design with reduced performance when τ^* values are between 0.469 and 0.628.

Another limitation of the current implementation relevant to moving trust-regions should be highlighted. When using the ε-constraint method, a multiobjective optimization problem is decomposed into a set of single-objective subproblems. A typical strategy in the solution of these subproblems is to use the result of one subproblem as a starting point for a neighboring subproblem. This typically helps reduce solution expenses. In this particular implementation, however, if we use the solution of a subproblem with a larger shear load bound as a starting point for a subproblem with a smaller shear load bound, the initial point will violate the shear load constraint. When the LP solver detects a constraint violation, it attempts to satisfy the constraint by moving the solution far from the current design. A large single step is taken, reducing iterations. Conversely, when solving a subproblem using a starting point obtained from a lower shear load subproblem, the trust-region limits progress. Even if the trust-region radius is adapted, effective design exploration is hampered. To address this issue, first, we began the process by solving the largest shear load subproblem, and decremented the shear load constraint. Thus, in this study, we solve this problem beginning with the largest shear load case, and using the result of this subproblem, lower shear load subproblems are solved. An improvement of this trust-region updating issue is a topic of ongoing work.

Several SLP method improvements and research questions have been identified for future work. A more sophisticated step size update strategy may help accelerate convergence and improve the exploration of a wider range of designs. SLP method robustness should be improved, including the ability to start from arbitrary design points (such as a flat plane) and converge to high-performance solutions. Finally, alternative formulations may better capture the underlying physical mechanisms that lead to improved performance. For example, a quadratic approximation may be a better approximation for the governing equations and objective functions. While this may help drive the solution method to better designs, an LP can no longer be formulated. A problem with quadratic constraints will not be as easy to solve as an LP, but may still support the use of problem structure for solution efficiency better than previous general NLP studies.

Chapter 4

Efficient Sampling and Implicit Constraint Management Methods for Multiobjective Adaptive Surrogate-Based Optimization[1]

4.1 Summary

Surrogate-based optimization (SBO) techniques are extensively used in engineering design. However, using this techniques with multiobjective optimization introduces significant challenges beyond the SBO methods focus on single-objective optimization problems (SOPs). This study focuses specifically on resolving difficulties arise with the surrogate-based multiobjective optimization problems (SB-MOPs). Efficient exploitation and exploration sampling methods for adaptive SB-MOPs are proposed in this study. Also, a technique for adaptively generating and managing implicit constraints using support vector domain description (SVDD) is presented and demonstrated with practical engineering design problems. Combining these novel sampling methods, constraint management methods, and SBO algorithms that are capable of solving multiobjective optimization problems (MOPs), we developed the multiobjective adaptive surrogate model-based optimization (MO-ASMO) framework, a comprehensive approach for solving challenging MOPs. The sampling methods enforce all sample points to be feasible regarding any inexpensive constraint to minimize waste of computational effort. This is done before any expensive model evaluations using a small optimization subproblem that adjusts sample points. If the full model fails multiple times with certain ranges of inputs due to numerical instability, or due to implicit constraints that are unknown a priori, an implicit constraint generation and management technique, based

---

[1] Part of the content reported in this chapter is reprinted by permission from ASME (Lee, Corman, Ewoldt, and Allison. A multiobjective adaptive surrogate modeling-based optimization framework using efficient sampling strategies. In *Proc. ASME IDETC/CIE*, DETC2017-67541, Cleveland, OH), ©2017

on SVDD, adaptively creates and refines constraints as more data are collected throughout the MO-ASMO outer-loop iterations. To obtain enhanced solutions with adaptive surrogate model refinement, the sampling for the exploitation of the predicted solution neighborhood utilizes a force-directed layout (FDL)-inspired sample placement technique. This method ensures the created samples located near, but not on, the hypersurface of the Pareto set predicted in the current iteration to enhance approximation model accuracy in the regions where solutions are likely to exist. A total of six test problems (four mathematical problems and two practical engineering design problems) are solved using the MO-ASMO framework to analyzed advantages of the proposed methods' capability and efficiency.

4.2 Introduction

4.2.1 Background and Related Work

Engineering design and other optimization problems often have multiple design objectives, where two or more objectives are competing with each other, and the decision problem involves a trade-off between these competing objectives. The solution to such a problem is generally expressed as a set of nondominated (Pareto-optimal) design alternatives and is referred to as a Pareto set; non-dominated points are designs for which no objective function can be improved without degrading any other objective functions through design changes [45, 68]. Many strategies exist for addressing multiobjective optimization problems (MOPs), classified into multiobjective evolutionary algorithms (MOEAs) [46, 69, 70], scalarization techniques [48, 49, 71–73], or set-based algorithms [74]. An important drawback of all these approaches for solving MOPs is the potential for a large required number of function evaluations. This is particularly concerning for high-dimensional, expensive, and black-box (HEB) optimization problems.

Surrogate-based optimization (SBO), also known as metamodel-based optimization (MBO) or metamodel-based design optimization (MBDO), is often used to mitigate the computational burden for solving HEB optimization problems. Results of full model responses are approximated with a limited set of design points (training samples) and their full model function values [75–77]. This approximation is realized using interpolation, regression, or machine-learning methods [75, 78–81]. Optimization is then performed using this approximated inexpensive surrogate model-fidelity function evaluations. Surveys of surrogate modeling methods and strategies for design optimization are presented in Refs. [82–84]. Please note that the scope of the study presented here does not include investigation pertaining to selection of and a comparison between surrogate modeling methods or classes of multiobjective optimization strategies.

Training samples are obtained using static and/or adaptive sampling methods for the exploration of design space and the exploitation of the predicted solution region. Static or sequential space-filling techniques, such as random, full factorial (FF), Latin hypercube design (LHD), minimax/maximin distances, and entropy-based sampling methods, are commonly used sampling techniques in existing SBO methods [85, 86]. These traditional sampling approaches are useful for the exploration (global search) stage of the surrogate model refinement, especially when the design space is not thoroughly explored. However, these simple space-filling techniques are often not efficient for the exploitation (precise solution finding) stage, because training a surrogate model that is accurate across the entire design domain is computationally expensive and not necessary for optimization purposes [67].

An important strategy for limiting the number of expensive full model evaluations is beginning with a coarse initial sample and then adaptively select new sample points to update the surrogate model for strategic accuracy improvement [19, 87–89]. Considering sampling efficiency in refining a surrogate model with additional samples, the model only needs to be accurate in the neighborhood of the solution for design optimization problems. New samples often are either chosen in regions near the predicted optimum, or in sparsely sampled regions to improve the probability of finding a global optimum. Adaptive refinement strategies can be classified based on types of update sequences and other characteristics. Some previous studies presented efficient ways to adaptively sample training points. Peng et al. [90] used a significant sampling space (SSS) approach that shrinks the sampling region as the predicted solution converges (but uses the same traditional sampling methods for the shrunk region), and Cheng et al. [91] used a mode-pursuing sampling (MPS) approach that incorporates dynamically-adjusted trust-regions.

4.2.2 Challenges

Considering decades of demand and applications for efficient SBO for HEB solution methods, not many studies have tackled all challenges faced during practical engineering design optimization efforts, such as constraint management that can handle failures in function evaluations, or multiobjective problem considerations in the sampling stages. Some previous studies address multiobjective problems using surrogate models. However, their usage is coupled with a certain type of optimizer, e.g., particle swarm optimization (PSO) [92], limited to a very small number of design variables [93], or their sampling methods are not distinctively different to those for single-objective optimization problems (SOPs).

Managing constraints is challenging in SBOs. Eldred and Dunlavy [94] considered constraints only during the optimization phase; the surrogate model is not constructed with constraints in consideration. Hussein and Deb [95] allowed infeasible training points, but used a convexifying term involving a sum of constraint violations. However, these strategies are less effective for problems where constraints are coupled densely with design variables (e.g., a multidimensional geometric mesh with gradient limiter appeared in Lee et al. [4]). In addition, many engineering simulation models may fail when attempting to evaluate infeasible design points. For these cases, methods should prevent expensive full model function evaluation of infeasible points. This avoidance of computational resource waste could be accomplished by filtering. However, in problems with narrow, non-convex feasible domains, this may require discarding a large portion of sample points generated using conventional strategies (e.g., LHD or central composite design (CCD)). Processing and filtering a large number of infeasible sample points to obtain a few feasible points may dominate computational effort, and is an inefficient strategy. Here we seek strategies that, by nature, generate only feasible sample points.

For some design problems, it is possible that a particular design input corresponds to a feasible design in terms of the constraints, but is not solvable using the model functions (functions that evaluate objectives and/or constraints, e.g., simulations) due to a number of reasons, such as numerical instability or physical impossibility. In this case, it may not be known what values of design input variables cause the failure of function evaluation until attempting execution of the expensive full model function, preventing the definition of constraints in advance [13]. In this study, we use a novel strategy using the support vector domain description (SVDD) [96, 97] to adaptively define constraint boundaries to avoid the optimization algorithm exploring regions where failures of full model function evaluations are observed. To distinguish this type of constraints from typical preformulated infeasible regions, we refer to these regions as "invalid" input, or "invalid regions", for simplicity.

Another sampling challenge touched on above is efficient sampling for updating surrogate models, balancing exploration (global search), and exploitation (precise solution) of the design space [98–100]. Previous studies aimed to achieve the following goals simultaneously: 1) finding a global solution, 2) finding an accurate local solution, and 3) limiting the number of expensive full model function evaluations. Many efforts in adaptive surrogate modeling (ASM) have been successful in achieving these objectives for SOPs. Extension to MOPs, however, gives rise to new challenges that have not been addressed thoroughly. For example, regarding the exploitation goal, an accurate local solution requires that the surrogate model is accurate in the neighborhood of the estimated Pareto set (often an $(m_x - 1)$-dimensional hypersurface in the design space, where the design space dimension is m_x), as opposed to just being accurate in the neighborhood of the estimated optimal design (a single design point). Quantifying this local accuracy and validating the surrogate model is much more complicated for MOPs compared to SOPs. This motivates new efficient sampling strategies for model validation.

4.2.3 Summary of Contributions

This study presents advancements of ASM for MOPs that aim to effectively reduce the number of required expensive full model evaluations to obtain optimal solutions (a Pareto set). These advancements aim to cope with challenging problem characteristics, such as tightly-constrained design spaces (small, complex feasible domains) and the need to evaluate only feasible sample points. This study's contributions include: (1) a novel global sampling strategy for tightly-constrained design spaces, (2) a novel adaptive sampling strategy, and (3) avoidance of regions where full model function failures are observed. The proposed global sampling algorithm can generate globally-distributed feasible training points. This advantage is especially useful when the feasible design space is extremely small relative to the full design space, which often makes standard sampling strategies impractical. The new adaptive sampling algorithm utilizes a novel force-directed point locating strategy for generating sample points near the estimated Pareto set. This approach is inspired by the force-directed layout (FDL) algorithms often used for graph visualizations [101, 102]. In addition, when full model function failure repeatedly occurs in a specific range of design spaces, whether constraints are satisfied or not, the input validity management subroutine can identify these regions using SVDD and block it from further exploration. This strategy is also advantageous when the feasibility of design space regions is unknown a priori, and helping to prevent failure of the optimization solution method when function failure occurs.

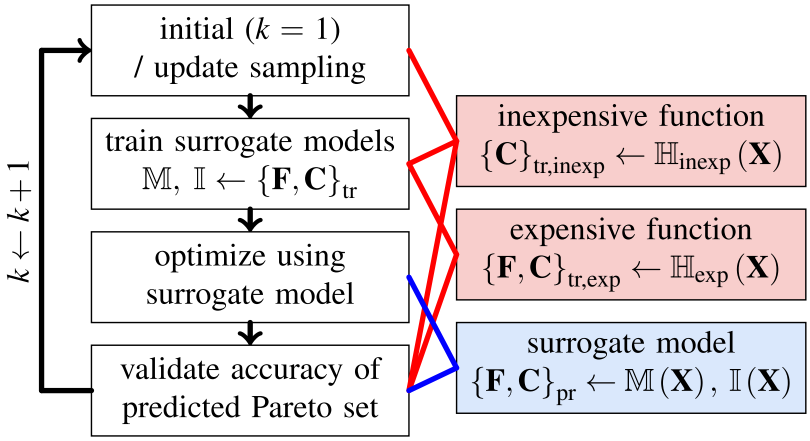

Figure 4.1: High-level flow chart of proposed MO-ASMO framework. A direct sampling strategy is used for updating the surrogate model, meaning that the surrogate model is validated and updated only after the target optimization problem is solved on the model. There is no inner loop that updates the surrogate model, and the update sampling is only performed at the outermost iterative loop. The algorithm is described in detail in the following sections.

4.3 Methods

4.3.1 The MO-ASMO Framework Structure

The multiobjective adaptive surrogate model-based optimization (MO-ASMO) algorithm we developed (readers may obtain the code from Refs. [103, 104]) solves MOPs given in Eq. (4.1) on a constructed surrogate model, which is updated iteratively using new training sample points. The full model may include combinations of expensive objective functions, expensive nonlinear constraint functions, and inexpensive linear and nonlinear constraint functions. The nonlinear constraints are classified into expensive ($\underline{c}_{\text{exp}}$) and inexpensive ($\underline{c}_{\text{inexp}}$) groups and enforced in different steps.

$$
\begin{aligned}
\underset{\underline{x}=[x_1,\cdots,x_{m_x}]}{\text{minimize}} \quad & \underline{f}\left(\underline{x}^{\mathrm{T}}\right) = \left[f_1,\cdots,f_{m_f}\right] \\
\text{subject to} \quad & \mathbf{A}_{\text{ineq}}\underline{x}^{\mathrm{T}} - \underline{b}_{\text{ineq}} \leq \underline{0},\ \mathbf{A}_{\text{eq}}\underline{x}^{\mathrm{T}} - \underline{b}_{\text{eq}} = \underline{0}, \\
& \underline{c}_{\text{ineq,exp}}\left(\underline{x}^{\mathrm{T}}\right) \leq \underline{0},\ \underline{c}_{\text{eq,exp}}\left(\underline{x}^{\mathrm{T}}\right) = \underline{0}, \\
& \underline{c}_{\text{ineq,inexp}}\left(\underline{x}^{\mathrm{T}}\right) \leq \underline{0},\ \underline{c}_{\text{eq,inexp}}\left(\underline{x}^{\mathrm{T}}\right) = \underline{0}, \\
& \underline{x}_{\text{lb}} \leq \underline{x} \leq \underline{x}_{\text{ub}}, \\
\text{where} \quad & \left[\underline{f},\underline{c}_{\text{ineq}},\underline{c}_{\text{eq}}\right]_{\text{exp}} \leftarrow \text{full model (expensive) func.}\left(\underline{x}\right), \\
& \left[\underline{c}_{\text{ineq}},\underline{c}_{\text{eq}}\right]_{\text{inexp}} \leftarrow \text{full model (inexpensive) func.}\left(\underline{x}\right),
\end{aligned}
\tag{4.1}
$$

where $\underline{x}$ is the vector of design variables, $\underline{f}$ is the vector of objective functions, $\mathbf{A}$ is the coefficient matrix, $\underline{b}$ is the constant vector of linear constraints, and $\underline{c}$ is the nonlinear constraints vector. Subscripts 'exp' and 'inexp' correspond to the *expensive* and *inexpensive* groups of full model functions. The flow chart in Fig. 4.1 illustrates the high-level algorithm strategy. Many parts of the algorithm are implemented from our previous version of the MO-ASMO framework [67, 103], but the overall structure of the algorithm has been re-written to accommodate more general problem-solving capability. According to Wang and Shan [82], the algorithm can be classified as a *direct sampling approach*, meaning that samples are directly generated toward the optimum in support of the surrogate model. The direct sampling can be described in following sequences: (1) initial training samples are generated; (2) design points of training samples are evaluated with the full model to obtain training data; (3) surrogate models for **F** and **C** are constructed: $\mathbb{M}$ is to model expensive function responses and $\mathbb{I}$ is to encapsulate invalid regions, by using all existing results. The framework is independent of multiobjective optimization algorithm choice. Thus, users can choose from any type of MOEAs (e.g., nondominated sorting genetic algorithm II (NSGA-II) [46]) or gradient-based (e.g., scalarization methods [48, 71]) algorithms. Here we used ε-constraint and NSGA-II algorithms for our test problems. We assume that computational costs for the optimization

Algorithm 1: Main loop of the MO-ASMO code

```
while *stopping criteria not met* do
    $\mathbf{X}_T \leftarrow$ initial or update sampling
    $\{\mathbf{F}, \mathbf{C}\}_{T,\mathrm{tr}} \leftarrow$ expensive function evaluations for $\mathbf{X}_T$
    $\{\mathbf{F}, \mathbf{C}\}_{T,\mathrm{tr,v}}$ , $\{\mathbf{F}, \mathbf{C}\}_{T,\mathrm{tr,i}} \leftarrow$ separate valid/invalid points from $\{\mathbf{F}, \mathbf{C}\}_{T,\mathrm{tr}}$
    $\{\mathbf{F}, \mathbf{C}\}_{T,\mathrm{tr,v},p}$ , $\{\mathbf{F}, \mathbf{C}\}_{T,\mathrm{tr,i},p} \leftarrow$ append $\{\mathbf{F}, \mathbf{C}\}_{T,\mathrm{tr,v}}$ , $\{\mathbf{F}, \mathbf{C}\}_{T,\mathrm{tr,i}}$
    $\mathbb{M} \leftarrow$ train surrogate model using $\{\mathbf{X}, \mathbf{F}, \mathbf{C}\}_{T,\mathrm{tr,v},p}$
    $\mathbb{I} \leftarrow$ train invalid region model using $\{\mathbf{X}, \mathbf{F}, \mathbf{C}\}_{T,\mathrm{tr,i},p}$
    $\mathbf{X}_0 \leftarrow$ choose staring points for optimization
    $\{\mathbf{X}, \mathbf{F}, \mathbf{C}\}_{P,\mathrm{pr}} \leftarrow$ surrogate-based optimization
    $\mathbf{X}_V \leftarrow$ choose validation points from $\mathbf{X}_{P,\mathrm{pr}}$
    $\{\mathbf{F}, \mathbf{C}\}_{V,\mathrm{tr}} \leftarrow$ expensive function evaluations for $\mathbf{X}_V$
    $\{\mathbf{F}, \mathbf{C}\}_{V,\mathrm{tr,v}}$ , $\{\mathbf{F}, \mathbf{C}\}_{V,\mathrm{tr,i}} \leftarrow$ separate valid/invalid points from $\{\mathbf{F}, \mathbf{C}\}_{V,\mathrm{tr}}$
    $\varepsilon \leftarrow$ compute Euclidean distance error ($||\Delta\mathbf{F}||$)
    $\Delta \leftarrow$ compute residuals of convergence metrics
    evaluate stopping criteria using $\varepsilon$ and $\Delta$
    $k \leftarrow k + 1$
```

using the surrogate model is very low compared to the cost of the full model evaluations when using the MOEAs, e.g., NSGA-II. Even if millions of function evaluations are required to obtain a good Pareto set estimate based on the surrogate model, this computational expense is still a fraction of the expense for evaluating the full model multiple times. This framework is capable of handling up to a hundred design variables stably (and likely even more), as well as more than two objective functions. To avoid excessive memory consumption in these multidimensional problems, we refrained from using full-factorial type loops in the algorithm, and users can choose from either vectorization or parallelization for their problem. Details of each step in the main loop algorithm are explained in later sections.

The main loop of the MO-ASMO strategy is given in Algorithm 1. Unlike gradient-based or trajectory-based optimization algorithms, population-based and surrogate-based algorithms need to handle multiple design points at once. Thus, the variables **X**, **F**, **C** are the matrices that contain vectors of design variables, objective functions, and constraint functions of multiple design points. For example, design variables of single design point can be expressed as a row vector $\underline{x} = [x_1, \cdots, x_{m_x}]$ and the matrix that contains multiple design points can be expressed as a matrix $\mathbf{X} = [\underline{x}_1, \cdots, \underline{x}_n]^{\mathrm{T}}$ of size $n \times m_x$, where m_x is the number of design variables and n is the number of design points. Subscripts T, P, V, and p correspond to *training*, *Pareto-optimal*, *validation*, and *pool*, respectively; subscripts 'tr' and 'pr' corresponds to *true* and *predicted*; subscripts 'v' and 'i' corresponds to *valid* and *invalid* inputs. The algorithm begins with the loop number index $k = 1$. Initial samples (when $k = 1$) are generated by users' choice of design of experiments (DOE) method. Update samples (when $k > 1$) consist of both exploration samples and exploitation samples. Sampling methods are explained in later sections. After evaluating the full model on the samples, the algorithm distinguishes a valid set of input and output from an invalid set. Using the pool of valid input and output data, the algorithm trains surrogate models for objective functions ($\mathbb{M} : \mathbf{X} \to \mathbf{F}$) and constraint functions ($\mathbb{M} : \mathbf{X} \to \mathbf{C}$); trains invalid region model using invalid data set ($\mathbb{I} : \mathbf{X} \to \mathbf{C}_{\mathrm{v/i}}$). The *pool* (subscript p) contains all the sets of values compiled throughout the history of main-loop iterations of k.

Multiobjective optimization is performed on the surrogate models created in the prior steps, using the starting points selected for a particular optimization algorithm of choice. For example, if a population-based method, such as NSGA-II, is the algorithm of choice for the surrogate-based multiobjective optimization problem (SB-MOP), the number of starting points are the same as the population size and selected from the previous main loop iteration results (plus randomly generated points, if more points are needed). If the ε-constraint method is the algorithm of choice for the SB-MOP, the starting points are chosen from the previously-predicted Pareto-optimal points, based on the distance between each ε-constraint value and the location of the target point.

After the predicted Pareto set is obtained from the surrogate-based optimization, validation samples are chosen among the solution. The full model results of the validation samples are compared to the surrogate model results to compute error metrics, such as Euclidean distance and residual of various convergence metrics, to evaluate a stopping condition. If the errors are larger than the stopping criteria, the MO-ASMO algorithm loops again with

Algorithm 2: Sampling algorithm for exploration

```
1 $\mathbf{X}_T \leftarrow$ sampling in $(0,1)^{m_x \times n}$ space
2 $\mathbf{X}_T \leftarrow$ scale $\mathbf{X}_T$ from $(0,1)^{m_x \times n}$ space to $(\underline{x}_{\text{lb}}, \underline{x}_{\text{ub}})$ space
3 $\mathbf{X}_0 \leftarrow \mathbf{X}_T$
4 for $j \leftarrow 1, \cdots, n$ do
5     solve: minimize $d\left(\underline{x}_j\right) = w_1 d_1 + w_2 d_2$, subject to:
      $d_1 = \left|\left|\underline{x}_j - \underline{x}_{0,j}\right|\right|$, $d_2 = \sum_{l=1}^{n_{T,p}} - \ln\left(\left|\left|\underline{x}_j - \underline{x}_{T,p,l}\right|\right| \neq 0\right)$,
      $\mathbf{A}_{\text{ineq}}\underline{x}_j^{\text{T}} - \underline{b}_{\text{ineq}} \leq \underline{0}$, $\mathbf{A}_{\text{eq}}\underline{x}_j^{\text{T}} - \underline{b}_{\text{eq}} = \underline{0}$, $\mathbf{C}_{\text{ineq}} \leq \underline{0}$, $\mathbf{C}_{\text{eq}} = \underline{0}$, $\mathbb{I}\left(\underline{x}_j\right) \leq 0$
6 for $j \leftarrow 1, \cdots, n$ do
7     $\mathbf{X}_T(j) \leftarrow \underline{x}_j$ (concatenate).
```

updated samples for refining the surrogate models.

4.3.2 Exploration Sampling (Initial and Update Stages)

The sampling stage aims to determine the region in the design space where we would like to gain more information, helping to place new samples efficiently during the iterative SBO process. Combinations of exploration of global response and exploitation of the predicted solution neighborhood are utilized throughout the optimization process. Exploration sampling helps to provide a more comprehensive knowledge of the entire design domain to the optimizer, and this is specifically important in the early stages of adaptive refinement of the surrogate model to improve the likelihood of identifying globally nondominated solutions.

Here, a novel sampling strategy is created for generating exploration samples, and is described in detail in Algorithm 2. The objective d_2 and the constraint model $\mathbb{I}$ apply only to the update sampling stage, since d_2 utilizes the pool of previous design points; the invalid region model $\mathbb{I}$ can be defined after at least one main loop iteration. In the sampling stage, the LHD method is a typical choice, but any other DOE methods, such as CCD or random sampling, can be used instead. After the samples are scaled to the design variable bounds, the optimization subproblem given in Line 5 is solved for each sample point to enforce linear, nonlinear constraints, and a constraint defined by the invalid region model given in Section 4.3.5, while minimizing relocation distance (d_1) and maximizing distances from

Algorithm 3: Sampling algorithm for exploitation

```
$\left(\underline{x}_{P,\text{lb}}, \underline{x}_{P,\text{ub}}\right) \leftarrow$ hypercube encapsulating $\mathbf{X}_{P,\text{pr}}$ with added margin
$\mathbf{X}_{P,\text{pr}} \leftarrow$ scale $\mathbf{X}_{P,\text{pr}}$ from $\left(\underline{x}_{P,\text{lb}}, \underline{x}_{P,\text{ub}}\right)$ space to $(0,1)^{m_x \times n}$ space
$\mathbf{X}_{\text{B}} \leftarrow$ get $n_{\text{exploitation}}$ numbers of cluster centers of $\mathbf{X}_{P,\text{pr}}$
for $j \leftarrow 1, \cdots,$ predefined maximum number of steps do
    $\mathbf{S} \leftarrow \mathbf{0}$, $\mathbf{X}_{\text{diff}} \leftarrow \mathbf{X}_M - \mathbf{X}_B$, $\underline{r}_{\text{diff}} \leftarrow ||\mathbf{X}_{\text{diff}}||$
    $\mathbf{S} \leftarrow \mathbf{S} - (\mathbf{X}_{\text{diff}} / \underline{r}_{\text{diff}}) \log\left(C_1 \underline{r}_{\text{diff}}\right)$
    for $l \leftarrow 1, \cdots, n_{P,pr}$ do
        $\mathbf{X}_{\text{diff}} \leftarrow \mathbf{X}_M - \underline{x}_{P,\text{pr},l}$, $\underline{r}_{\text{diff}} \leftarrow ||\mathbf{X}_{\text{diff}}||$
        $\mathbf{S} \leftarrow \mathbf{S} + (\mathbf{X}_{\text{diff}} / \underline{r}_{\text{diff}}) \left(1/n_B^2\right) \left(C_2 / \underline{r}_{\text{diff}}^2\right)$
    $\underline{s} \leftarrow ||\mathbf{S}||$, $\underline{s}_{\max}$ diminishes as $j$ increases
    $\mathbf{S} \leftarrow (\mathbf{S}/\underline{s}) \min\left(\underline{s}, \underline{s}_{\max}\right)$
    $\mathbf{X}_M \leftarrow \mathbf{X}_M + \mathbf{S}$
$\mathbf{X}_T \leftarrow$ combine (concatenate) $\mathbf{X}_T$ and $\mathbf{X}_M$
```

previously existing points (d_2). The expensive constraints must be excluded from being enforced in this stage. Linear constraints only require design variable values to be evaluated. Nonlinear constraints that do not require expensive function evaluation are enforced to generate samples in tentatively-feasible regions in the design space.

4.3.3 Exploitation Sampling (Update Stage)

In the update stage, another novel sampling method was developed for the exploitation of the predicted solution neighborhood, inspired by the FDL algorithm that is often used in graph visualization [101, 102]. In this sampling stage, sampling points must be placed not on, but near the Pareto set *hypersurface* (in $m_x - 1$ dimensional space, when design space dimension is m_x) to improve surrogate model accuracy in the vicinity of the estimated solution (Pareto set). The exploitation sampling strategy is described in Algorithm 3. $\mathbf{X}_B$ represents a matrix of the centers of previously-predicted Pareto-optimal design point clusters, also called *base points*; $\mathbf{X}_M$ represents a matrix that contains points created nearby each cluster center included in $\mathbf{X}_B$, also called as *moving points*; $\mathbf{S}$ is a matrix that contains the displacement vectors of sample points for each step of the force-directed dynamic sample relocation algorithm; $\underline{s}$ is a vector that contains the magnitudes of the displacement vectors of sample points included in **S**.

Sample points are subjected to two types of predefined forces and move dynamically toward equilibrium. For simplicity, the force is directly interpreted as a displacement, following Fruchterman and Reingold [102]. One type of force is a combined attractive-repulsive force (but in a quantity of displacement) using a log-spring law between each new sample point and a corresponding base point, as quantified in Eq. (4.2):

$$\underline{s}_{B,i} = -\frac{\underline{x}_{M,i} - \underline{x}_{B,i}}{\left|\left|\underline{x}_{M,i} - \underline{x}_{B,i}\right|\right|} \log\left(C_1 \left|\left|\underline{x}_{M,i} - \underline{x}_{B,i}\right|\right|\right), \tag{4.2}$$

where $\underline{s}_i$ is the displacement vector of i-th design point that is included in the displacement matrix **S**, and $\underline{s}_{B,i}$ represents the *log-spring* portion (a force acting between a new sample point and the corresponding base point) of the total computed displacement $\underline{s}_i$.

The other type of force considered in this study is a repulsive force using an inverse-square law between each of a new sample point and all points in the Pareto set, as quantified in Eq. (4.3):

$$\underline{s}_{P,i} = \sum_{l=1}^{n_P} \frac{\underline{x}_{M,i} - \underline{x}_{P,l}}{\left|\left|\underline{x}_{M,i} - \underline{x}_{P,l}\right|\right|} \frac{1}{n_B^2} \frac{C_2}{\left|\left|\underline{x}_{M,i} - \underline{x}_{P,l}\right|\right|^2} = \sum_{l=1}^{n_P} \frac{\underline{x}_{M,i} - \underline{x}_{P,l}}{\left|\left|\underline{x}_{M,i} - \underline{x}_{P,l}\right|\right|^3} \frac{C_2}{n_B^2} = \sum_{l=1}^{n_P} \underline{s}_{P,i,l} \tag{4.3}$$

where:

$$\underline{s}_{P,i,l} = \frac{\underline{x}_{M,i} - \underline{x}_{P,l}}{\left|\left|\underline{x}_{M,i} - \underline{x}_{P,l}\right|\right|^3} \frac{C_2}{n_B^2}. \tag{4.4}$$

Here, $\underline{x}_{P,l}$ is the l-th point in the Pareto set, and n_P is the number of points in the Pareto set. The term $\underline{s}_{P,i}$ represents the *inverse-square* portion (forces acting between a new sample point and all points in the previously-predicted Pareto set) of the total computed displacement $\underline{s}_i$, which now can be represented as:

$$\underline{s}_i = \underline{s}_{B,i} + \underline{s}_{P,i} = \underline{s}_{B,i} + \sum_{l=1}^{n_P} \underline{s}_{P,i,l}. \tag{4.5}$$

Algorithm 4: Algorithm for selecting validation samples

```
$\underline{i} \leftarrow$ initialize with $(\mathsf{false})^{n_P \times 1}$
for $j \leftarrow 1, \cdots, m_f$ do
    $\{\mathbf{X}, \mathbf{F}\}_{P,\mathrm{pr}} \leftarrow \mathsf{row\text{-}sort}\left(\{\mathbf{X}, \mathbf{F}\}_{P,\mathrm{pr}}, \mathsf{column}{:}f_j\right)$
    $\underline{i}^l \leftarrow (\mathsf{true})$ where $l \leftarrow$ index of $\underline{x}_{P,\mathrm{pr}}$ for $\underline{x} \leftarrow \mathsf{argmin}\,(f_{j,P,\mathrm{pr}})$
    for $l \leftarrow 1, \cdots, (n_P - 1)$ do
        $d_l \leftarrow \left|\left|\underline{x}_{P,\mathrm{pr},(l+1)} - \underline{x}_{P,\mathrm{pr},l}\right|\right|$
        if $d_l \gg \mathit{mean}\,(\forall d_l)$ then
            $\underline{i}^l \leftarrow (\mathsf{true}), \underline{i}^{(l+1)} \leftarrow (\mathsf{true})$
while $\mathit{count}\,(\underline{i} = (\mathit{true})) < n_V$ do
    $\underline{d}_{\min} \leftarrow \underline{0}^{n_P \times 1}$
    for $l \leftarrow 1, \cdots, n_P$ do
        $\underline{d}_{\min,l} \leftarrow$ minimum distance from any of $\underline{x}_{P,\mathrm{pr},q}$ for all $q$ with $\underline{i}^q = (\mathsf{true})$
    $\underline{i}^l \leftarrow (\mathsf{true})$ where $l \leftarrow$ index of $\underline{x}_{P,\mathrm{pr}}$ that has maximum value in $\underline{d}_{\min}$
$\mathbf{X}_V \leftarrow \mathbf{X}_{P,\mathrm{pr}}^{\underline{i}=(\mathsf{true})}$
```

After the forces (in the form of displacement $\underline{s}_i$) are computed, the sample point ($\underline{x}_M$) is moved to a new position toward the force equilibrium. However, to produce a smooth and convergent behavior, a maximum displacement limit is applied in each step, the magnitude of which diminishes over steps. Updates for the position of the new sample point is given as:

$$\underline{x}_{M,i}^{r+1} = \underline{x}_{M,i}^{r} + \min\left(\left(\underline{s}_{B,i} + \underline{s}_{P,i}\right), \underline{s}_{\max}\right), \tag{4.6}$$

where maximum displacement $\underline{s}_{\max}$ diminishes as the step r increases. C_1 and C_2 are arbitrary values, and optimal choices for these parameters are unknown. For this study, we perform 20 point-moving steps, and specify $C_1 = 100$, $C_2 = 10$ for the force-directed sampling method.

4.3.4 Selecting Validation Samples

The strategy for selecting validation samples is given in Algorithm 4. Here, $\underline{i}$ is a boolean vector that indicates which design points are selected as validation samples. In the direct sampling method we used in the MO-ASMO framework, optimization is performed before the constructed surrogate model is validated. Thus, the predicted solution obtained by the optimizer of choice can be utilized directly for validating the surrogate model accuracy. These sample points are used to check the Euclidean distance error between the values predicted by the surrogate model and the values computed by the full model. When validating the solution accuracy (and this is locally equivalent to the surrogate model accuracy in the neighborhood of the predicted solution), it is important to determine (approximately) whether the surrogate model is accurate enough across the entire predicted Pareto set. Thus, the algorithm for selecting validation samples among many points in the Pareto set should select points strategically. Several assumptions are made here regarding how validation samples should be specified. First, the selected samples for validation need to be uniformly distributed among obtained Pareto-optimal solutions; and second, the selected samples for validation also need to include extreme locations, such as anchor points and segment ends of discontinuous Pareto sets (if discontinuities exist). In the selection procedure, extreme samples are chosen first (anchor points in Line 4 and discontinuous solution points in Line 8 in Algorithm 4). The rest of the samples are selected uniformly using a distance-based bisection method, defined in Line 13 of Algorithm 4.

4.3.5 Modeling the Region of Invalid Inputs

When the full model response is not easily predictable and simulation failure occurs with specific ranges of design input values, a model for defining invalid input regions can be useful to avoid wasting computational resources. Examples of simulation failures may include numerical instabilities, physically irrational inputs not easily formulated as formal a priori constraints, or simulation model limits.

The model proposed here for approximately defining the invalid region(s) model utilizes the SVDD method [96, 97] to train virtual hyper-boundaries between *valid* and *invalid* design spaces [13]. The SVDD virtual hyper-boundaries are trained and updated during each MO-ASMO iteration to provide up-to-date constraint information to the sampling and optimization algorithms. Training the SVDD model requires a solution of an optimization subproblem, given as:

$$\begin{aligned} \text{maximize} \quad & W\left(\underline{\beta}\right)=\sum_i \beta_i K_G\left(\underline{x}_i,\underline{x}_i\right)-\sum_{i,j}\beta_i\beta_j K_G\left(\underline{x}_i,\underline{x}_j\right) \\ \text{subject to} \quad & \sum_i \beta_i = 1,\ \forall i:\ 0\le\beta_i\le C, \end{aligned} \tag{4.7}$$

where Lagrange multipliers $\underline{\beta}=[\beta_1,\cdots,\beta_{n_x}]$ are bounded by an arbitrary constant C, and the Gaussian kernel K_G is defined as:

$$K_G\left(\underline{x},\underline{y}\right)\equiv\exp\left(-q\left|\left|\underline{x}-\underline{y}\right|\right|^2\right). \tag{4.8}$$

The Gaussian kernel K_G used here implicitly maps invalid design points $\underline{x}$ to some higher-dimensional feature space, which allows us to define a hypersphere tightly encapsulating the region of the invalid design point clouds. Varying C can help detect the outliers in the dataset that describes the domain. Parameter q also determines the tightness of the domain description around the training data.

If any arbitrary point $\underline{z}$ in the design space is inside the encapsulated boundary, the radius from the center of the hypersphere to the point $\underline{z}$ in the featured space is smaller than the radius to the boundary points $\underline{x}_{\text{sv}}$, which is called a *support vector*. The arbitrary point $\underline{z}$ is inside the hypersphere boundary if:

$$R^2\left(\underline{x}_{\text{sv}}\right)-R^2\left(\underline{z}\right)\ge 0, \tag{4.9}$$

where:

$$R^2\left(\underline{z}\right)=K_G\left(\underline{z},\underline{z}\right)-2\sum_i\beta_i K_G\left(\underline{z},\underline{x}_i\right)+\sum_{i,j}\beta_i\beta_j K_G\left(\underline{x}_i,\underline{x}_j\right). \tag{4.10}$$

The support vectors ($\underline{x}_{\text{sv}}$) are the points with positive (non-zero) Lagrangian multipliers (β_i) smaller than the C value among the training points. Note that the points inside the boundary are indicated by $\beta_i=0$. Figure 4.2 shows a two-dimensional demonstration of the

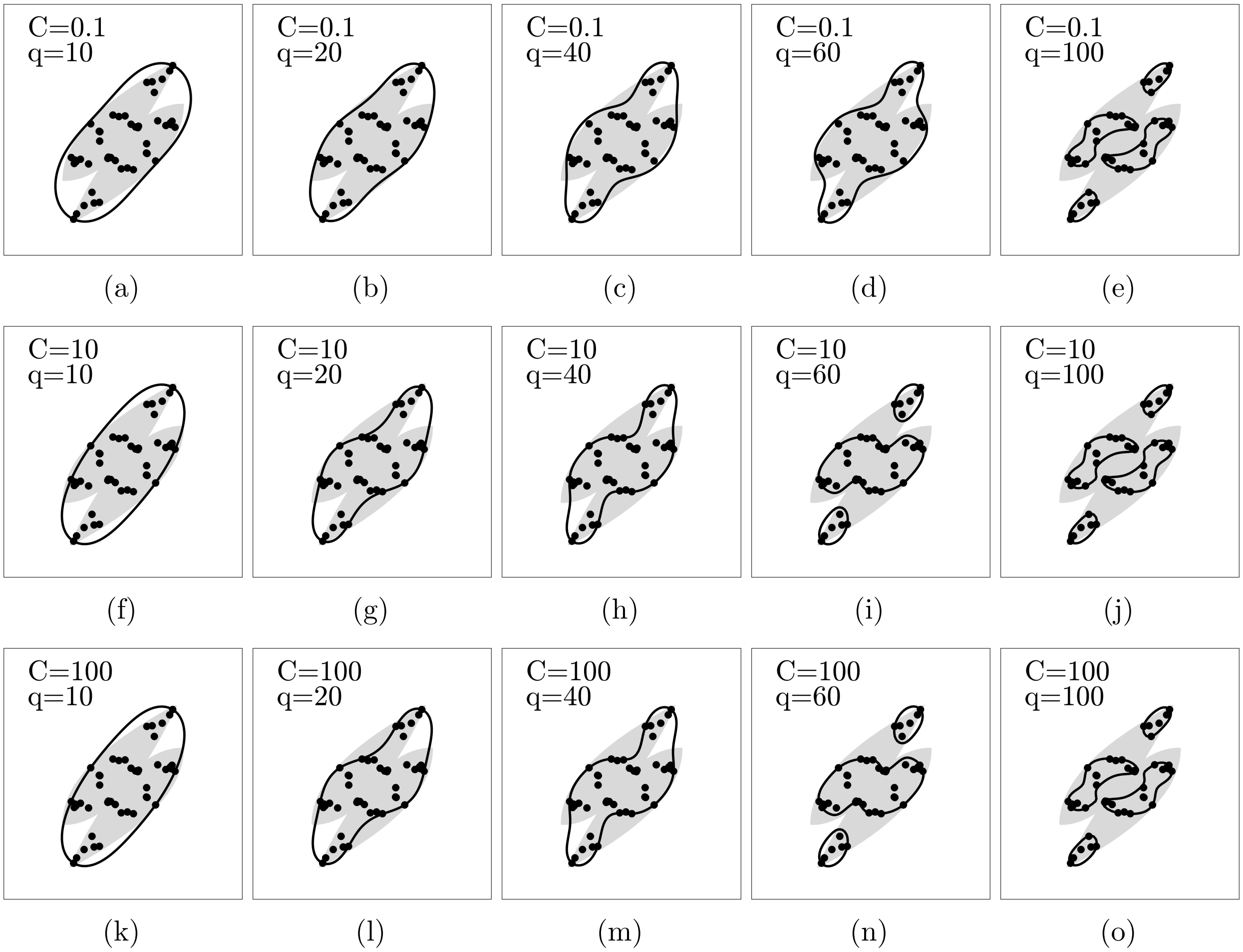

Figure 4.2: Implicit constraint generation based on the invalid input data using the SVDD method. Shaded area is the actual invalid input domain. Black lines encapsulate the invalid data points to construct implicit boundaries with continuous feasibility contours. Parametric studies are illustrated for $0.1 \leq C \leq 100$ and $10 \leq q \leq 100$.

implicit constraint generation for encapsulating invalid regions based on invalid input data. Constraint tightness is especially sensitive to the value of q. Regardless of the values of the C and q parameters, the invalid input domain (shaded region) is well-bounded by the SVDD constraint generation method.

In earlier design work utilizing the SVDD [97, 105], valid design input data are encapsulated. With this earlier strategy, the boundary encapsulating valid design inputs may help the optimization algorithm find solutions efficiently within valid design input regions. However, from the perspective of the exploration of unknown design spaces, it does not provide useful information. This previous approach is effective when the sample data to train the SVDD boundary are already distributed over a wide range of a design space without leaving an unexplored region. Thus, to aid the exploration algorithm in navigating unexplored regions freely while avoiding regions of invalid input data, we used the SVDD method to encapsulate invalid data set to approximates the boundary of regions that cannot be simulated. One of our earlier studies demonstrated that this "converse" approach is effective in the context of particular simulation-based MOP [13].

4.3.6 Stopping Criteria

Checking hard convergence, such as first- and second-order optimality conditions (and especially for SB-MOPs), is not always straightforward for SBO problems when the algorithm does not aim to achieve high accuracy over the entire surrogate model. Soft convergence metrics, such as relative improvement in the objective function, can be an alternative to hard convergence when they are not available for specific SBO problems [94]. In addition, determining convergence for SB-MOPs has additional difficulties. Since the solution of MOPs is not a single design point, even checking the zero-order condition ($||\mathbb{M}(\underline{x}) - \mathbb{H}(\underline{x})|| \to 0$) for each solution point in the Pareto set ($\underline{x}_P$) can be cost-prohibitive. This study uses soft convergence metrics, including hypervolume (HV)-related metrics of the Pareto frontier, as well as the Euclidean distance error to check the zero-order condition for select points in the objective function space. The algorithm for determining the stopping condition terminates the main loop when one or all criteria of users' choice are consecutively satisfied for a specified number of occurrences (or just once) during the main iterations.

Euclidean Distance Error

Checking the zeroth-order condition for select points (selected in the validation stage) is one of the most primitive but important metrics for determining the convergence of SB-MOP solution algorithms. In m-dimensional Euclidean space, the zeroth-order condition can be

Algorithm 5: Algorithm for computing hypervolume residual metric

```
if $k = 1$ (initial iteration) then
    return $\mathcal{R} \leftarrow 1$
$\mathcal{V}^{r=k} \leftarrow$ compute hypervolume
$\Delta\mathcal{V}_{\max} \leftarrow \max\left(\mathcal{V}^{r=1,\cdots,k}\right) - \min\left(\mathcal{V}^{r=1,\cdots,k}\right)$
return $\Delta\mathcal{V} \leftarrow \left|\mathcal{V}^{r=k} - \mathcal{V}^{r=k-1}\right| / \Delta\mathcal{V}_{\max}$
```

expressed as a Euclidean norm (distance) between predicted and true (result of the full model) points in the objective function space. Thus, we refer to this convergence metric as a Euclidean distance (ED) error between predicted and true objective function values, and it is given as:

$$\varepsilon_{\text{ED}} = \left|\left|\mathbb{M}\left(\underline{x}\right) - \mathbb{H}\left(\underline{x}\right)\right|\right| . \tag{4.11}$$

The ED error (ε_{ED}) is computed for each sample point selected for validation during the stopping condition evaluation stage, and the maximum, mean, or median values can be used as stopping criteria.

Residual of Hypervolume (HV)

The HV is one of the most popular soft convergence metrics that indicate the convergence of the Pareto frontier as well as the diversity of the solution in a combined sense [69]. To accurately monitor the HV, it is important to set a consistent bound for a domain in the objective function space, which is often unknown a priori. Also, if the bounds are adaptively adjusted using all explored design points, a new point that is far from the solution drastically affects the value of the HV metric. Thus, we adaptively adjust the bounds by setting a utopia point, an anti-utopia point, and the predicted nondominated points. Within the hypercube defined with these aforementioned points, the HV is computed as the volume shaded by the hypersurface of the nondominated points, as illustrated in Fig. 4.3. As denoted in this figure, the domain of interest for computing the HV metric is the hypercube tightly containing the Pareto set using utopia and anti-utopia points, defined using the Pareto set. A Monte-Carlo

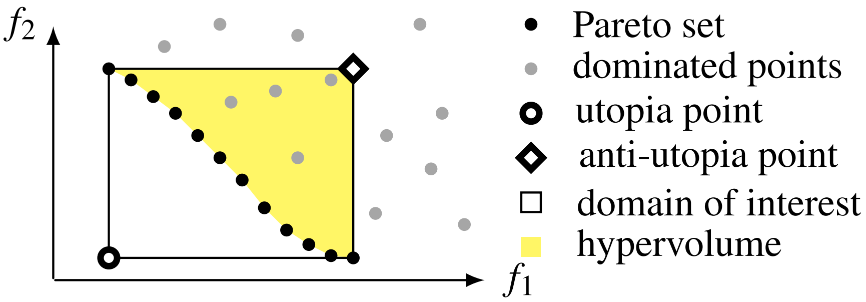

Figure 4.3: Domain for computing hypervolume (HV) metric. In m-dimensional objective function space, the HV metric is calculated as a hypervolume that is bound by utopia and anti-utopia points and dominated by the Pareto frontier. Drawing shows an example of HV as a shaded area for 2D objective function space.

Table 4.1: List of the test problems

ID	Case Name and Reference	m_x	m_f	m_c
P1	Chakong and Haimes [68]	2	2	2
P2	Osyczka and Kundu [106]	6	2	6
P3	Valley-shaped constraint	2	2	1
P4	Deb et al. (DTLZ1) [107]	12	3	0
P4	Deb et al. (DTLZ1)	14	5	0
P5	Q-car suspension design	6	2	5
P6	Lee et al. (III.A.2) [13]	36	2	107

method was used to acquire an approximated value of the HV metric. Both or either the absolute HV size ($\mathcal{V}$), and the ratio of HV size to the domain used for computing the HV, can be used for computing residuals (Δ) for determining the stopping condition. The algorithm for computing HV residual is given in Algorithm 5, where $\mathcal{V}^r$ is the HV at r-th iteration of the adaptive refinement procedure of the MO-ASMO method.

4.4 Test Problems

The MO-ASMO framework developed here is tested using several benchmark problems, which are listed in Table 4.1. Benchmark problems P1 through P4 are mathematical benchmark problems, whereas problems P5 through P6 are practical engineering design optimization problems. Readers are referred to the original works for the problem definitions of the

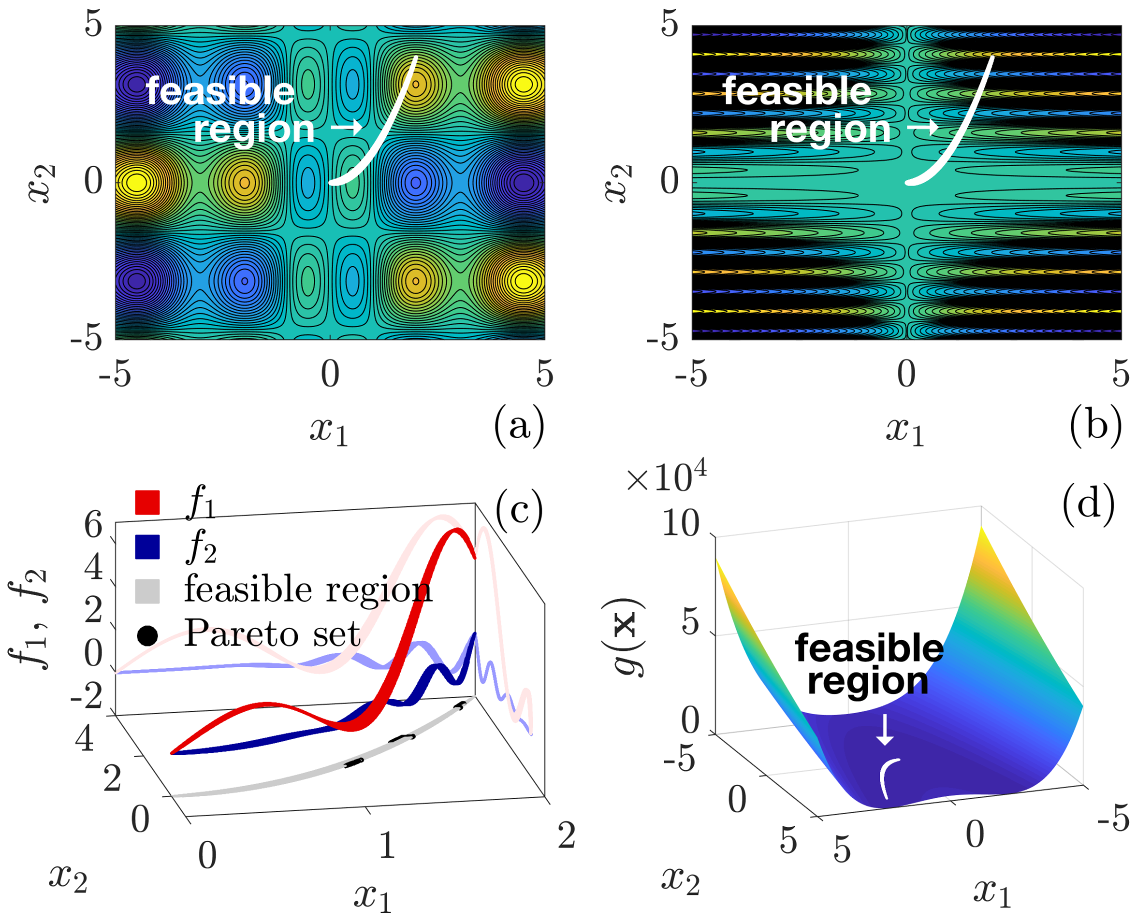

Figure 4.4: Case P3: Valley-shaped constraint function. (a) and (b) Responses of objective function 1, 2 (contours) and feasible region (white). (c) Objective function responses and Pareto set within feasible region. (d) Constraint function and feasible region.

problems listed as P1 [68], P2 [106], P4 [107, Problem DTLZ1], and P6 [13, Section III.A.2]. Definitions of the problems introduced in this chapter (P3 and P5) are described in the following sections.

4.4.1 P3: Valley-Shaped Constraint Function

We developed a new test problem, defined in Eq. (4.12) and illustrated in Fig. 4.4, to test the proposed framework more thoroughly with respect to the ability to manage tightly-constrained feasible domains [67, 108]. This problem combines sinusoidal and exponential objective functions with a shifted Rosenbrock valley function [109] as a constraint, and is

Table 4.2: Parameter values used in models of P5: Quarter-car design problem

Variable	Value	Unit	Variable	Value	Unit
m_1	466.5	[kg]	m_2	49.8	[kg]
k_1	5,700	[kg/s^2]	k_2	135,000	[kg/s^2]
c_2	1,400	[kg/s]	ζ_R	0.1	[m]

defined as:

$$\begin{aligned}
\underset{\underline{x}=[x_1,x_2]^{\mathrm{T}}}{\text{minimize}} \quad & \underline{f}\left(\underline{x}\right) = [f_1, f_2] \\
\text{subject to} \quad & g \leq 0 \\
\text{where} \quad & f_1 = \left(3\sin\left(\tfrac{5x_1}{2}\right) - 2x_1\right)\left(\cos\left(x_2\right)\exp\left(\tfrac{-x_2^2}{1000}\right)\right), \\
& f_2 = 3\left(\tfrac{3|x_1|}{10}\right)^{19/25}\left(\tfrac{1}{8}x_2\sin\left(5x_2\right)\right), \\
& g = \left(100\left(x_2 - x_1^2\right)^2 + \left(x_1 - 1\right)^2\right) - 1, \\
& -5 \leq x_1 \leq 5,\ -5 \leq x_2 \leq 5.
\end{aligned} \tag{4.12}$$

The feasible region in the design space is shown as a white colored region in Figs. 4.4a, 4.4b, and 4.4d, and is shaded with light gray in Fig. 4.4c. The Rosenbrock valley function is already a poorly-scaled function, so exploring the region of interest (the narrow feasible region in this case) is challenging for many optimization algorithms.

4.4.2 P5: Quarter-Car Suspension Design Using Viscoelastic Damper Problem

Another problem we developed for testing the MO-ASMO method is an optimization of a quarter-car automotive suspension using a viscoelastic damper (VED), which is illustrated in Fig. 4.5b [67]. The quarter-car suspension model, shown in Fig. 4.5a, is a common simplification for analyzing and designing vehicle dynamics [110, 111]. We replaced the linear damper c_1 between sprung and unsprung mass in Fig. 4.5a with a linear VED "VE" in Fig. 4.5b. This VED is parameterized using the multimode Maxwell model [112]. In this problem, design variables are parameters defining the VE element. Other parameters are

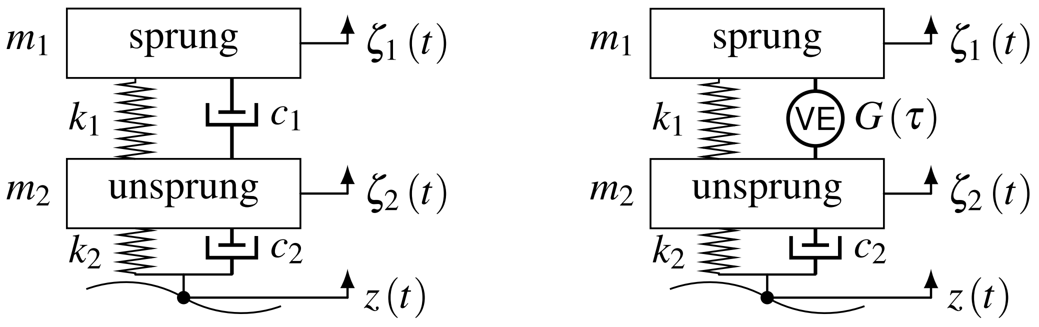

(a) (b)

Figure 4.5: Case P5: Quarter-car suspension model with linear and VEDs. (a) Standard quarter-car suspension model with linear dashpot as a dampling mechanism. (b) Quarter-car suspension model with viscoelastic element as a dampling mechanism.

fixed constants, given in Table. 4.2, and the road profile $z(t)$ is predefined after Allison [113].

The design objectives are (1) enhancing the comfort by minimizing amplitude of acceleration and (2) enhancing the handling by minimizing wheel deflection, given as:

$$\underline{f} = [f_1,\ f_2], \tag{4.13}$$

where:

$$\begin{aligned} f_1 &= \frac{1}{t_f - t_0}\int_{t_0}^{t_f}\left(\ddot{\zeta}_1(t)\right)^2 dt, \\ f_2 &= \frac{1}{t_f - t_0}\int_{t_0}^{t_f}\left(\zeta_2(t) - z(t)\right)^2 dt. \end{aligned} \tag{4.14}$$

Reducing the comfort metric corresponds to enhancing a surveyed human comfort level [114], and reducing the handling metric corresponds to less variance in tire contact force, helping to enhance cornering and traction performance [115].

The linear VE behavior is described using a time-dependent function, the relaxation kernel, $G(\tau)$. The time-dependent force through a one-dimensional VE element, F_{VE}, can be represented as a convolution integral using this relaxation kernel, given as:

$$F_{\mathrm{VE},\dot{\zeta}} = \int_{-\infty}^{t} G(t-t')\,\dot{\zeta}(t')\,dt' = \int_{0}^{\infty} G(s)\,\dot{\zeta}(t-s)\,ds, \tag{4.15}$$

where $s = t - t'$, and $\dot{\zeta}$ is the deformation velocity of the VE element. In general, the relaxation kernel G does not require a structure of linear springs and dashpots. Here, however, we utilize the Maxwell model, which utilizes this specific structure, for our parameterization to simplify design representation. An M-mode Maxwell model for the relaxation function can be described by:

$$G\left(t\right) = \sum_{m=1}^{M} G_m \exp\left(-\frac{t}{\lambda_m}\right), \tag{4.16}$$

where G_m is the m-th Maxwell spring constant, and λ_m is the m-th relaxation time. A Maxwell element consists of a linear spring and a linear dashpot connected in series. Since this parameterization can have the same (or similar) relaxation kernel function with many different sets of parameters, we limited λ_m to have monotonically decreasing values using the constraints $\lambda_i > \lambda_{i+1}$. We also limited the sum of G_m terms to be 300 or less ($\sum G_m \leq 300$). Since the model is scaled in log space, it is impossible to model these constraints using linear constraints. However, they can be evaluated without running an expensive simulation; thus, the MO-ASMO algorithm may take advantage of this by shrinking the exploring design region significantly, which is a challenge that this MO-ASMO algorithm was developed specifically for. We also have two additional constraints defining the rattle space of the suspension ($\zeta_1 - \zeta_2 \leq \zeta_R$, $\zeta_2 - \zeta_1 \leq \zeta_R$), which could be evaluated after the simulation is performed. These constraints are enforced by the optimization algorithm.

A dynamic simulation model of this quarter-car suspension system is given as:

$$\dot{\underline{\xi}} = \mathbf{A}\underline{\xi} + \mathbf{B}\dot{z} + \mathbf{C}, \tag{4.17}$$

where:

$$\mathbf{A} = \begin{bmatrix} 0 & 1 & 0 & 0 \\ -k_2/m_2 & -c_2/m_2 & k_1/m_2 & 0 \\ 0 & -1 & 0 & 1 \\ 0 & 0 & -k_1/m_1 & 0 \end{bmatrix},\ \mathbf{B} = \begin{bmatrix} -1 \\ c_2/m_2 \\ 0 \\ 0 \end{bmatrix},\ \mathbf{C} = \begin{bmatrix} 0 \\ F_{\mathrm{VE},\left(\dot{\zeta}_1 - \dot{\zeta}_2\right)}/m_2 \\ 0 \\ -F_{\mathrm{VE},\left(\dot{\zeta}_1 - \dot{\zeta}_2\right)}/m_1 \end{bmatrix}, \tag{4.18}$$

and the state vector is given as:

$$\underline{\xi} = \begin{bmatrix} \zeta_2 - z \\ \dot{\zeta}_2 \\ \zeta_1 - \zeta_2 \\ \dot{\zeta}_1 \end{bmatrix}. \tag{4.19}$$

This state-space model is solved using the forward predictor-corrector method with numerical evaluation of the nested convolution integral given in Eq. (4.15) for each time derivative function evaluation. This solution approach is a type of single-shooting method for dynamic system optimization, and with the numerous required convolution integral evaluations, the computational cost is very high compared to the other test problems. As a result, the MO-ASMO solution method is beneficial not only in terms of total function evaluations, but also in terms of computational time.

4.5 Results and Discussions

4.5.1 P1: Chakong and Haimes Function

The Chakong and Haimes problem (case P1) is formulated assuming that the constraints are all nonlinear and expensive, which means that no constraints are enforced during the sampling stage. The results are shown in Fig. 4.6. Pareto-optimal solutions obtained by the MO-ASMO and direct optimization (DO) methods are compared in Fig. 4.6a, where DO-EC

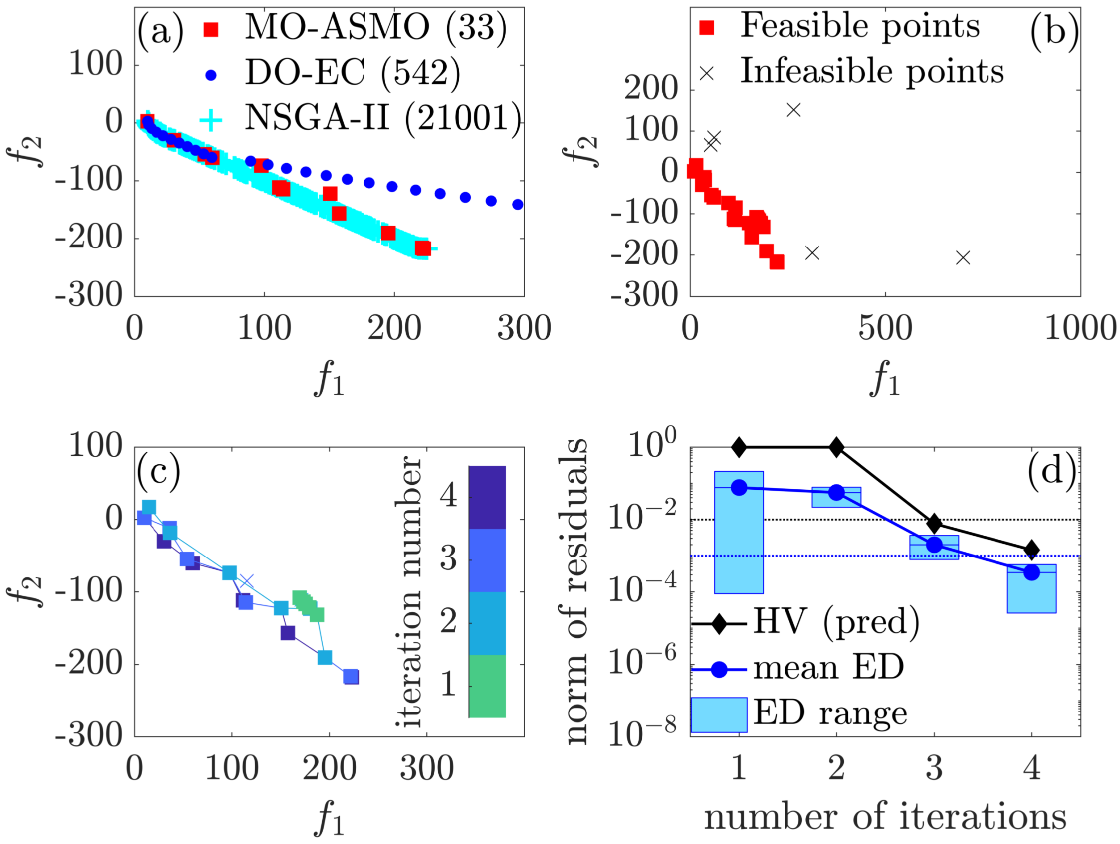

Figure 4.6: Summary of results for case P1: Chakong and Haimes function. (a) Comparison of solutions using different methods. (b) Full model results during the MO-ASMO run. (c) Solution points obtained during each MO-ASMO refinement. (d) Convergence in Euclidean distance (ED) and hypervolume (HV) metrics.

stands for the direct optimization using ε-constraint (DO-EC) method and numbers in the parentheses are the numbers of (hypothetically-expensive) full model evaluations required to obtain the solutions. Figure 4.6b shows feasible and infeasible points evaluated using the full model in the objective function space. Figure 4.6c describes how the Pareto frontier evolved during the MO-ASMO iterations using the full model results in the objective function space. Square markers are nondominated points, and cross (×) markers are dominated points at each MO-ASMO iteration. Figure 4.6(d) shows the convergence based on ED and HV metrics. The HV metric is computed using the predicted solutions at each iteration.

The MO-ASMO algorithm evaluated the full model 33 times (25 feasible and 8 infeasible points) to obtain a set of solutions comparable to the result of NSGA-II algorithm, which required 21,001 full model evaluations. The DO-EC method could only provide a suboptimal solution even with a 16 times more full model evaluations (total: 542 evaluations), compared to the MO-ASMO algorithm. When the constraints are enforced before the optimization, the convergence of the MO-ASMO algorithm is slower (46 feasible and 10 infeasible points, total 56 full model evaluations) because there is no objective function response information in the infeasible region provided to the surrogate model. Infeasible points are often evaluated in the validation stage in the early stage of the MO-ASMO iterations because of inaccurate surrogate models trained using limited samples, and this is unavoidable. Thus, enforcing the constraints during the sampling stage is not helpful for this problem.

4.5.2 P2: Osyczka and Kundu Function

The Osyczka and Kundu problem (case P2) is formulated, assuming that the constraints are all nonlinear and expensive, as we assumed for case P1. The results are shown in Fig. 4.7. Pareto-optimal solutions of different methods are compared in Fig. 4.7a. Direct optimization using NSGA-II required a very large number of generations and over 200,000 full model evaluations for obtaining solutions near the left-most edge in the plot (where f_2 values are above 40). In contrast, the MO-ASMO algorithm easily obtained the solutions for the same region within a few iterations with fewer than 100 full model evaluations. The DO-EC method easily obtained the left-most anchor point, but suffered difficulty in the middle regions of the Pareto frontier, and near the other anchor point where f_1 values are between -250 and -40. Feasible and infeasible points explored by MO-ASMO are given in Fig. 4.7b. An evolution of the solution in the objective function space is given in Fig. 4.7c, and the convergence metrics are given in Fig. 4.7d. The solution converged at 114 full model evaluations, resulting in 63 feasible and 51 infeasible training points, and the MO-ASMO algorithm captured the shape of the Pareto-frontier accurately. Also, as we see in case P1, enforcing the constraints during the sampling stage does not help accelerate solution convergence for this problem.

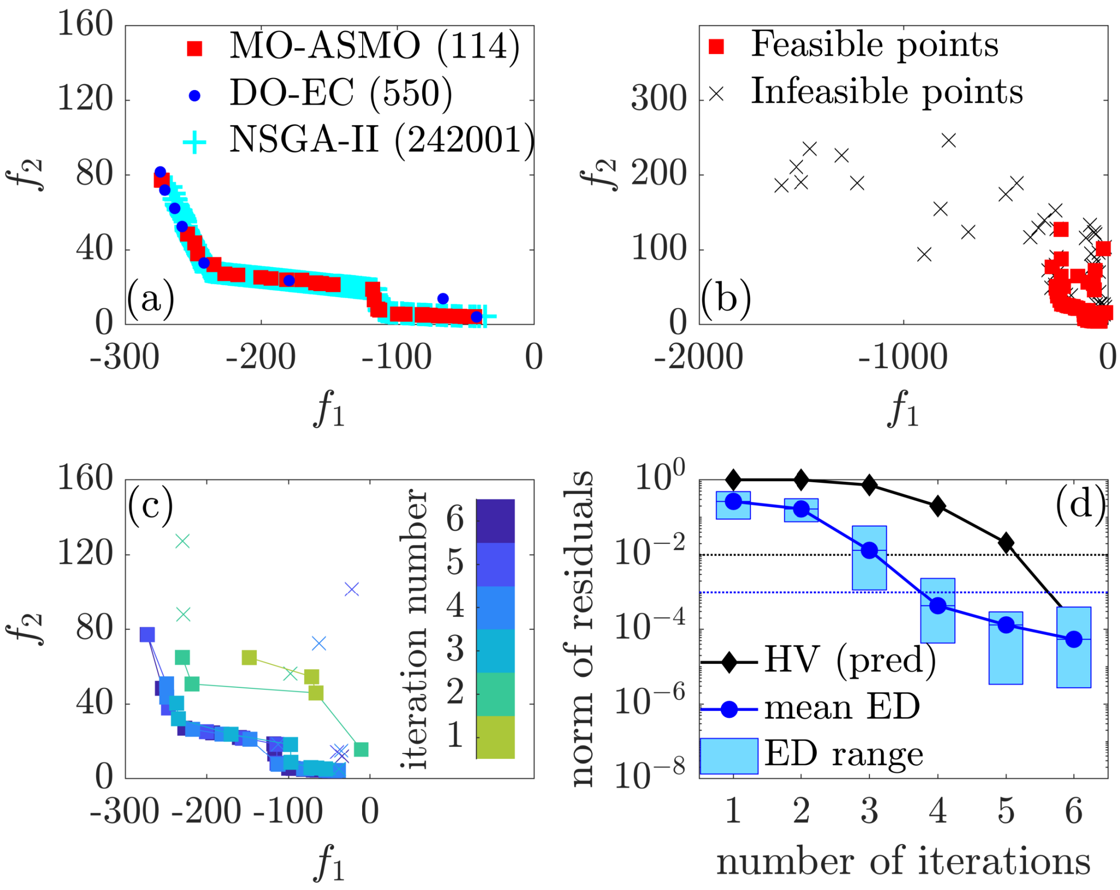

Figure 4.7: Summary of results for case P2: Osyczka and Kundu function. (a) Comparison of solutions using different methods. (b) Full model results during the MO-ASMO run. (c) Solution points obtained during each MO-ASMO refinement. (d) Convergence in Euclidean distance (ED) and hypervolume (HV) metrics.

4.5.3 P3: Valley-Shaped Constraint Function

The valley-shaped constraint problem is formulated assuming that the constraint function is inexpensive and independent of the objective function; thus, we can enforce the constraint during the sampling stage. For the constraint function in this problem, the feasible region is long, narrow, non-convex, and nearly flat in terms of the constraint function value (see Fig. 4.4d). Thus, it is not efficient to generate samples for training the surrogate model using standard sampling strategies. Also, the Pareto frontier of this problem is neither continuous in the objective function space, nor in the design space, which increases design exploration difficulty. Thus, enforcing the constraint function directly prior to the SBO stage has a

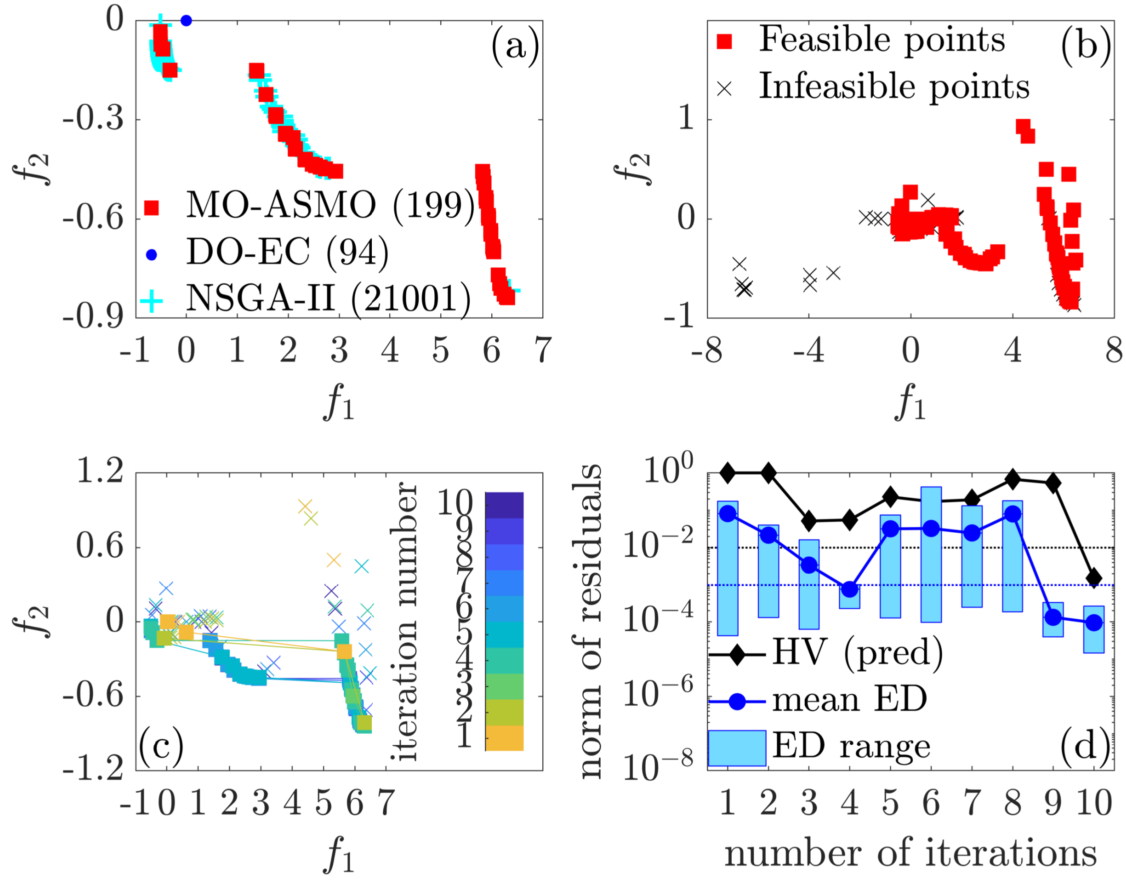

Figure 4.8: Summary of results for case P3: Valley-shaped constraint function. Initial and update samples for training the surrogate models comply the constraint function prior to run the SBO. (a) Comparison of solutions using different methods. (b) Full model results during the MO-ASMO run. (c) Solution points obtained during each MO-ASMO refinement. (d) Convergence in Euclidean distance (ED) and hypervolume (HV) metrics.

comparative advantage over standard SBO procedures, which first fit the surrogate model to the constraint function and then run the optimization.

The results of case P3 using the constrained sampling technique are shown in Fig. 4.8. As shown in Fig. 4.8a, the Pareto-optimal solutions obtained by the MO-ASMO algorithm with 199 expensive full model evaluations are significantly superior to the solutions obtained by other direct optimization methods. Even with 21,001 function evaluations, the NSGA-II algorithm failed to obtain solutions where f_2 values are in between -0.82 and -0.45, while the MO-ASMO algorithm quickly obtained the solution of the same region within 5 iterations (see Fig. 4.8c). The DO-EC method could not even properly explore the feasible region. Only

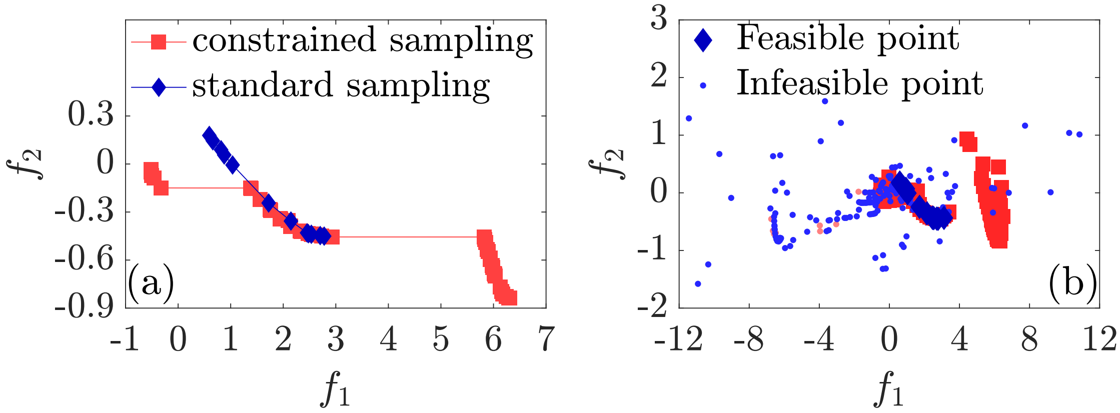

Figure 4.9: Comparison of results for case P3 with and without using the constrained sampling strategy. (a) Comparison of Pareto-optimal solutions. (b) Comparison of full model results during the MO-ASMO run.

one suboptimal solution point was obtained, shown as a circle in Fig. 4.8a.

In this problem, the proposed MO-ASMO algorithm demonstrates an advantage that stems from utilizing the sampling method that enforces inexpensive constraints during the sampling stage. Figure 4.9a shows a comparison of Pareto sets obtained with and without using this sampling technique. The MO-ASMO algorithm converged with 199 expensive full model evaluations (144 feasible and 55 infeasible points) using this sampling technique. However, without using this technique, the algorithm could not obtain an acceptable set of solutions throughout the entire objective function space even after 232 expensive full model evaluations (14 feasible and 218 infeasible points, see Fig. 4.9b). The advantage of enforcing the inexpensive constraints during the sampling stage could be utilized in other problems when the range or shape of constraint functions is unknown or challenging to be modeled by standard surrogate modeling techniques.

4.5.4 P4: DTLZ1 Function

DTLZ1 function [107] is an unconstrained MOP that has flexibility both in number of decision variables and objective functions. As was demonstrated in the original introduction of this test problem in Deb et al. [107], we started solving this problem with 3 objective functions

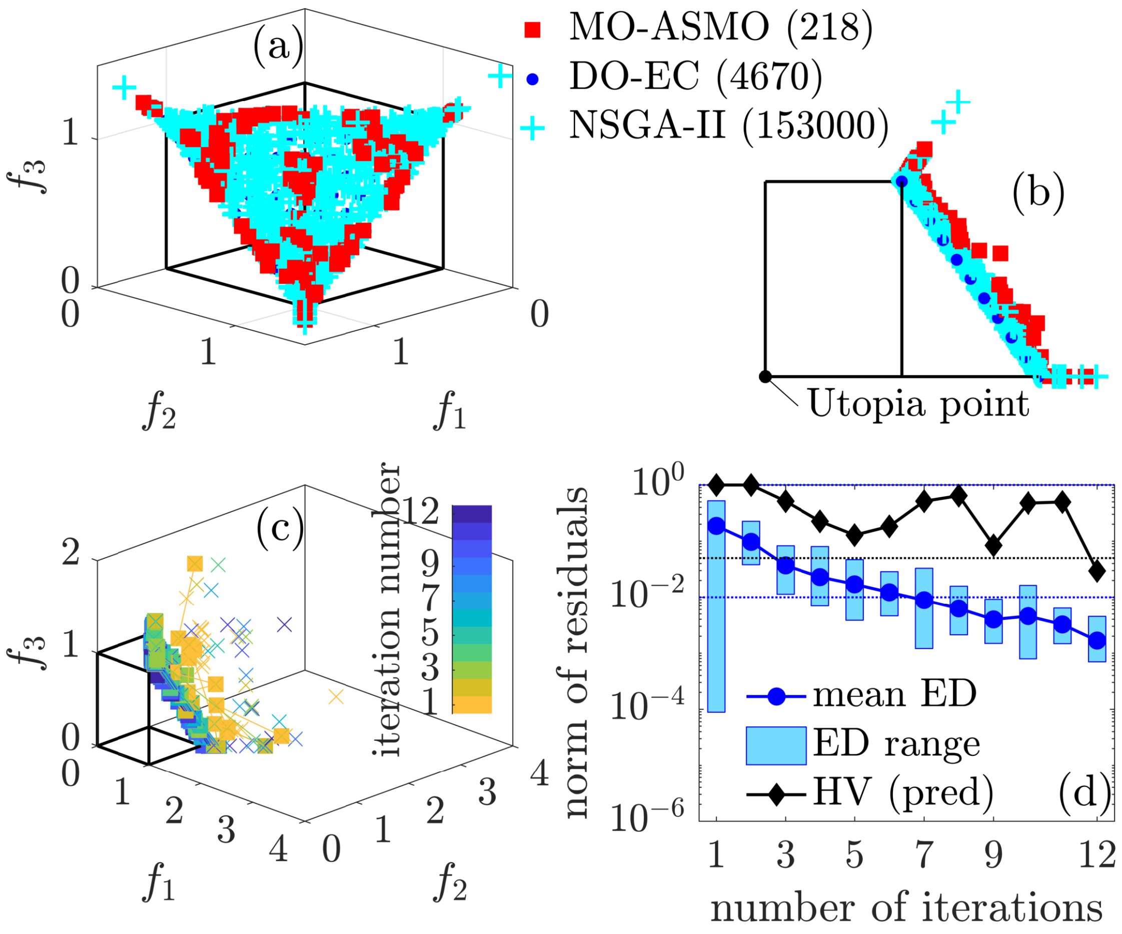

Figure 4.10: Summary of results for case P4: DTLZ1 function. (a) Comparison of solutions using different methods. (b) Solutions viewing at a direction parallel to the plane of true Pareto frontier. (c) Solution points obtained during each MO-ASMO refinement. (d) Convergence in Euclidean distance (ED) and hypervolume (HV) metrics.

and 12 design variables by setting $M = 3$ and $k = 10$. Figure 4.10 shows the results of case P4. As shown in Figs. 4.10a and 4.10b, the solutions obtained by the MO-ASMO algorithm are close to those obtained by other DO methods, but with significantly fewer full model evaluations (MO-ASMO: 218, DO-EC: 4,670, NSGA-II: 153,000). Solutions obtained by DO-EC are closest to the utopia point and are uniformly distributed, while those obtained by the MO-ASMO method are clustered and slightly dominated by the solutions of other methods. The MO-ASMO and the NSGA-II algorithms suffered difficulty in obtaining exact anchor points, while the DO-EC method directly obtained the exact anchor points (although a large number of the full model evaluations were required). An evolution of the solution

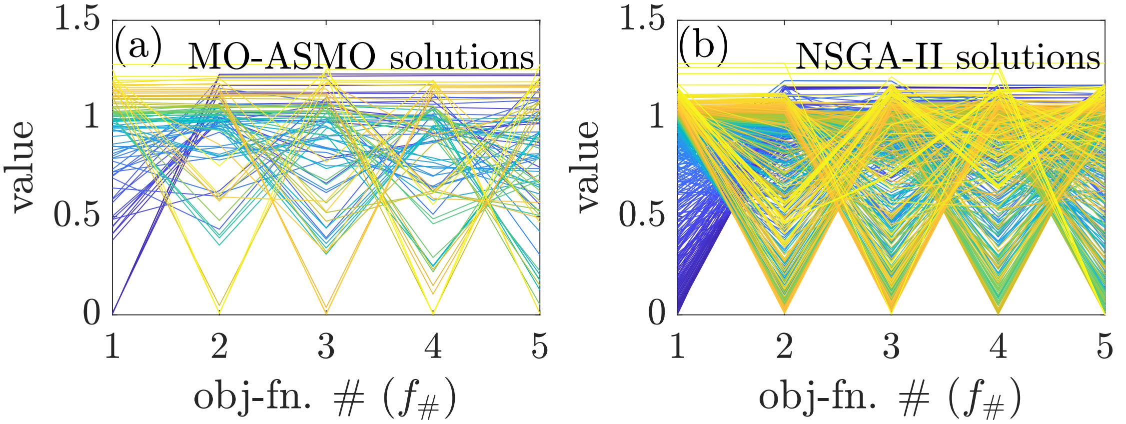

Figure 4.11: Pareto-optimal solutions of P4: DTLZ1 function with 5 objective functions and 14 decision variables. (a) Solutions obtained using the MO-ASMO algorithm. (b) Solutions obtained using the NSGA-II algorithm.

in the objective function space is illustrated in Fig. 4.10c, and the convergence metrics are shown in Fig. 4.10d.

Since this problem is scalable, we also tested the MO-ASMO algorithm using $M = 5$ and $k = 10$. Solutions obtained by the MO-ASMO and NSGA-II are compared in Fig. 4.11. The MO-ASMO algorithm evaluated the full model 218 times, while DO using NSGA-II needed 303,000 evaluations to achieve solutions with a similar distribution range. This demonstrates that the MO-ASMO algorithm is highly efficient for problems with a small to a moderate number of objective functions (5 for this problem), and a moderate number of decision variables (14 for this problem).

4.5.5 P5: Quarter-Car Suspension Design Using Viscoelasticity

Quarter-car suspension design using the VED problem is a simulation-based practical engineering design optimization problem. The problem has 3 inexpensive and 2 expensive inequality constraints. The inexpensive inequality constraints are functions of the decision variables, while the expensive inequality constraints are functions of the objective function values. Figure. 4.12 shows the results of case P5. Computational cost for each simulation is relatively high compared to the mathematical test problems; thus, it is impractical to solve

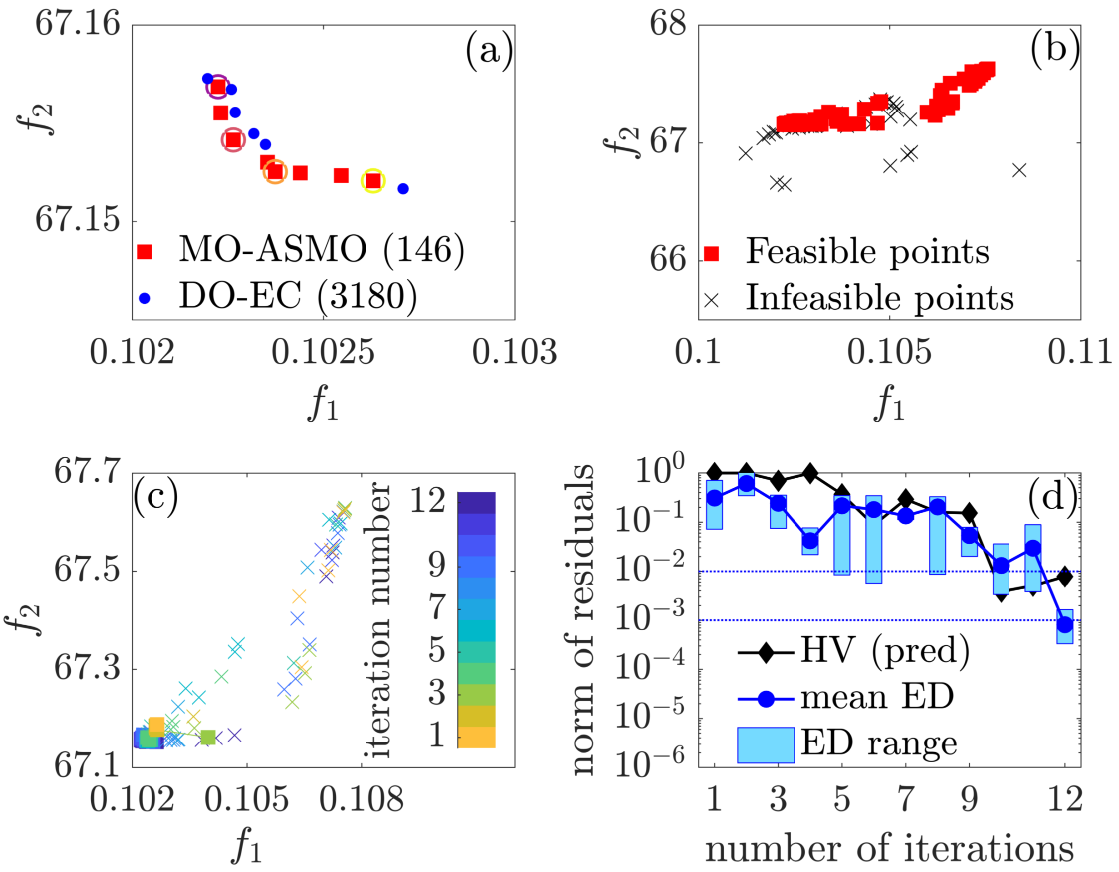

Figure 4.12: Summary of results for case P5: quarter-car suspension design using viscoelastic damper problem. An inexpensive subset of constraint functions is enforced during the sampling stages. (a) Comparison of solutions using different methods. (b) Full model results during the MO-ASMO run. (c) Solution points obtained during each MO-ASMO refinement. (d) Convergence in Euclidean distance (ED) and hypervolume (HV) metrics.

this problem using exhaustive MOEAs.

Pareto-optimal solutions of the MO-ASMO and DO-EC in the objective function space are compared in Fig. 4.12a. The MO-ASMO performed 146 full model evaluations (92 feasible and 54 infeasible, see Fig. 4.12b) to obtain the Pareto set requiring 43 minutes of computation time using all 8 threads of an Intel™ i7-6700HQ™ CPU. However, even using 20 times more evaluations of the full model (3,180 times total, requiring over 12 hours using the same CPU), the DO-EC method could only obtain solutions that were suboptimal and dominated by those obtained by MO-ASMO. DO using a gradient-based optimization algorithm is only effective for obtaining anchor points for this problem. As we see in Fig. 4.12c, the range

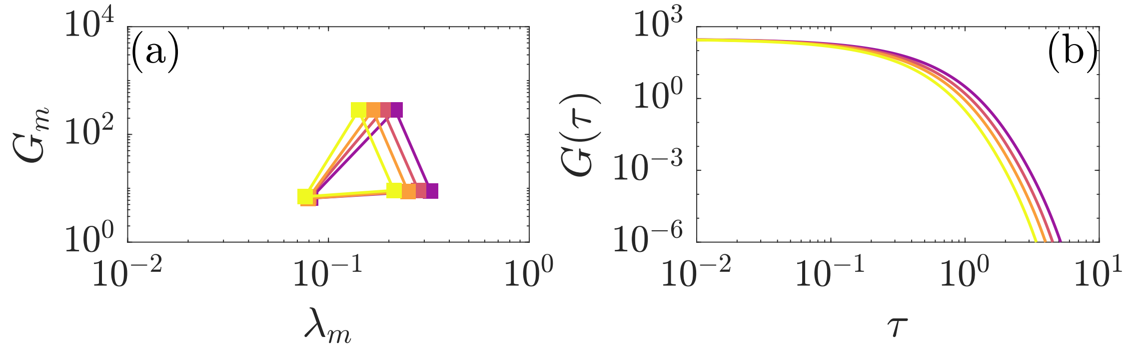

Figure 4.13: Solutions for case P5 visualized in parametric design space and material function space. (a) Solution visualized in Maxwell model parameter space. (b) Solution visualized in viscoelastic relaxation kernel function space. Plot line intensity corresponds to circle intensity in Fig. 4.12a marking the MO-ASMO solutions in the objective function space.

of performance metrics in the objective function space is larger than the range over which the Pareto set is located. We see continuous enhancement of solutions as the number of MO-ASMO iterations increases, which is also shown in the convergence plot in Fig. 4.12d.

Select solutions are visualized in G_m–λ_m and $G(\tau)$–τ spaces, as shown in Fig. 4.13. Line color intensity used in these plots corresponds to the line intensity of circle markers in Fig. 4.12a, indicating the corresponding solutions in the objective function space. These rheological characteristics presented in Fig. 4.13 could be used to fabricate materials for designing the VEDs for automotive suspensions optimally.

4.5.6 P6: Design of Viscoelastic Lubricant and Texture Geometry Using Giesekus Fluid

We have formulated the simultaneous design problem of viscoelastic lubricant and texture using the Giesekus fluid model in Chapter 7; the problem was solved in the previous literature using an earlier version of the MO-ASMO algorithm [13]. This problem has a relatively large number of constraints that make the design space very complicated. In addition, the physics solver exhibits numerical instabilities under certain conditions, resulting in frequent function evaluation failures during the optimization process. Here, we present the MO-ASMO features

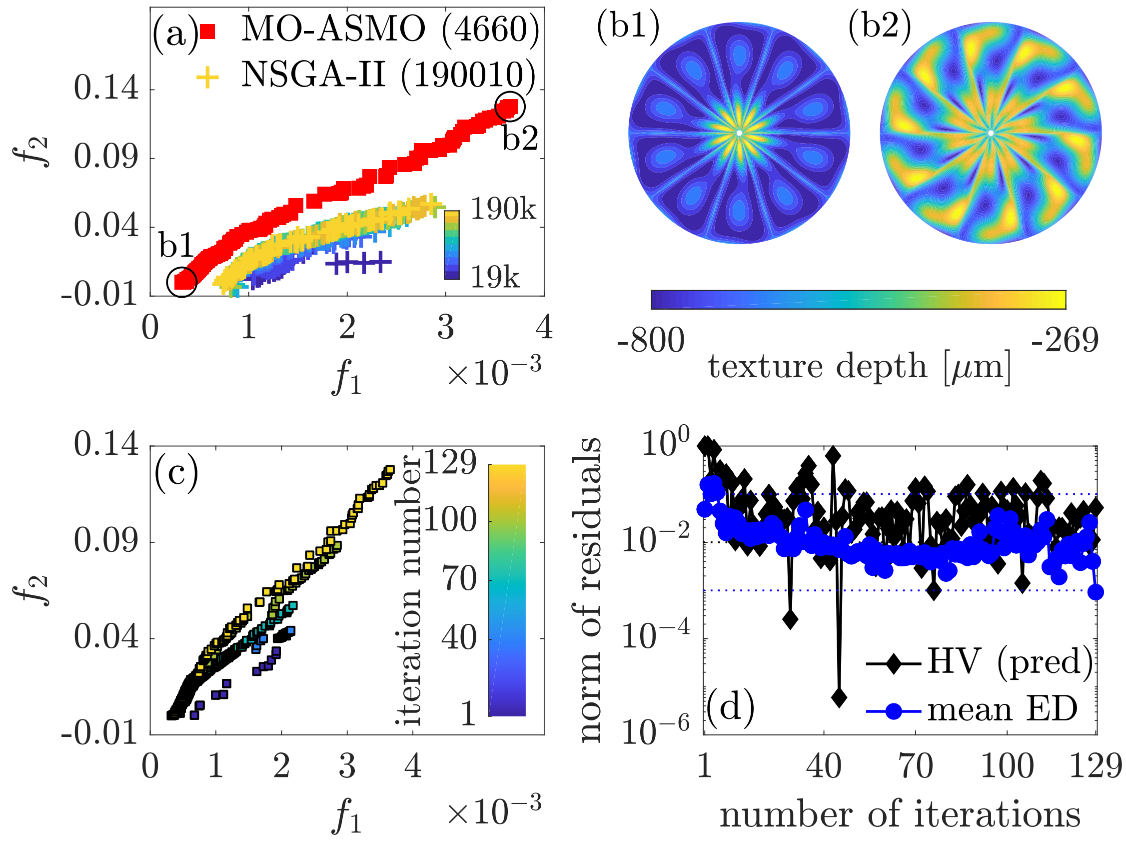

Figure 4.14: Summary of results for case P6: design of viscoelastic lubricant and texture using the Giesekus fluid problem. An inexpensive subset of constraint functions is enforced during the sampling stages. (a) Comparison of solutions using different methods. (b) Obtained designs located at the anchor points in the objective function space. (c) Solution points obtained during each MO-ASMO refinement. (d) Convergence in Euclidean distance (ED) and hypervolume (HV) metrics.

that enabled this problem to be solved efficiently by introducing an in-depth analysis of the corresponding results.

The MO-ASMO algorithm evaluated the full model 4,660 times. All the designs explored by the MO-ASMO algorithm were feasible in terms of predefined constraints. However, due to the numerical solver's instabilities, it was unable to obtain full model solutions for 986 design points. These failed design points are incrementally provided at each iteration to the optimization algorithm to reduce exploration of design space regions that are likely to result in solver failure. This reduction is achieved through iterative refinement of design space boundaries constructed via SVDD.

Since arbitrary design points have very low (nearly zero) probability of satisfying all the constraints for this problem, the NSGA-II algorithm, which does not utilize constraint information when obtaining populations for the next iteration, struggles to push the Pareto frontier to the actual solution range, as shown in Fig. 4.14a. The MO-ASMO algorithm also required many iterations and a significant number of full model evaluations to converge to a good solution set, but this is not abnormal considering the well-known *curse of dimensionality* issue with respect to the number of design variables and constraints. The obtained texture shapes (at the anchor points) align with the results presented in the previous literature, where the design with lower friction shows deeper flat texture, and the design with higher load-carrying capacity exhibits spiral blade-like texture that converges fluid pressure toward the center of the disk, as illustrated in Fig. 4.14b.

4.5.7 Discussion on Sampling for Exploration and Exploitation

The purpose of adaptively refining the surrogate model is to obtain an accurate solution across the regions where Pareto-optimal designs are located. Sampling for the exploration of the entire design space has the purpose of finding better possible solutions in the unknown design space in a global manner. To complement global exploratory sampling, sampling for the exploitation of the predicted solution region has the purpose of obtaining more accurate and improved-performance solutions. A balance between these two sampling strategies is crucial to further reduce the number of expensive full model evaluations, while improving the probability of finding a global and accurate solution. This balance also should evolve over iterative refinement, since the exploration is critical for early iterations, but not in the later stage of surrogate model refinement.

However, this balance cannot be easily determined a priori by the specifications of the problem, such as the number of design variables, objective functions, or constraint functions associated with the problem. The optimal balance depends highly on the characteristics of

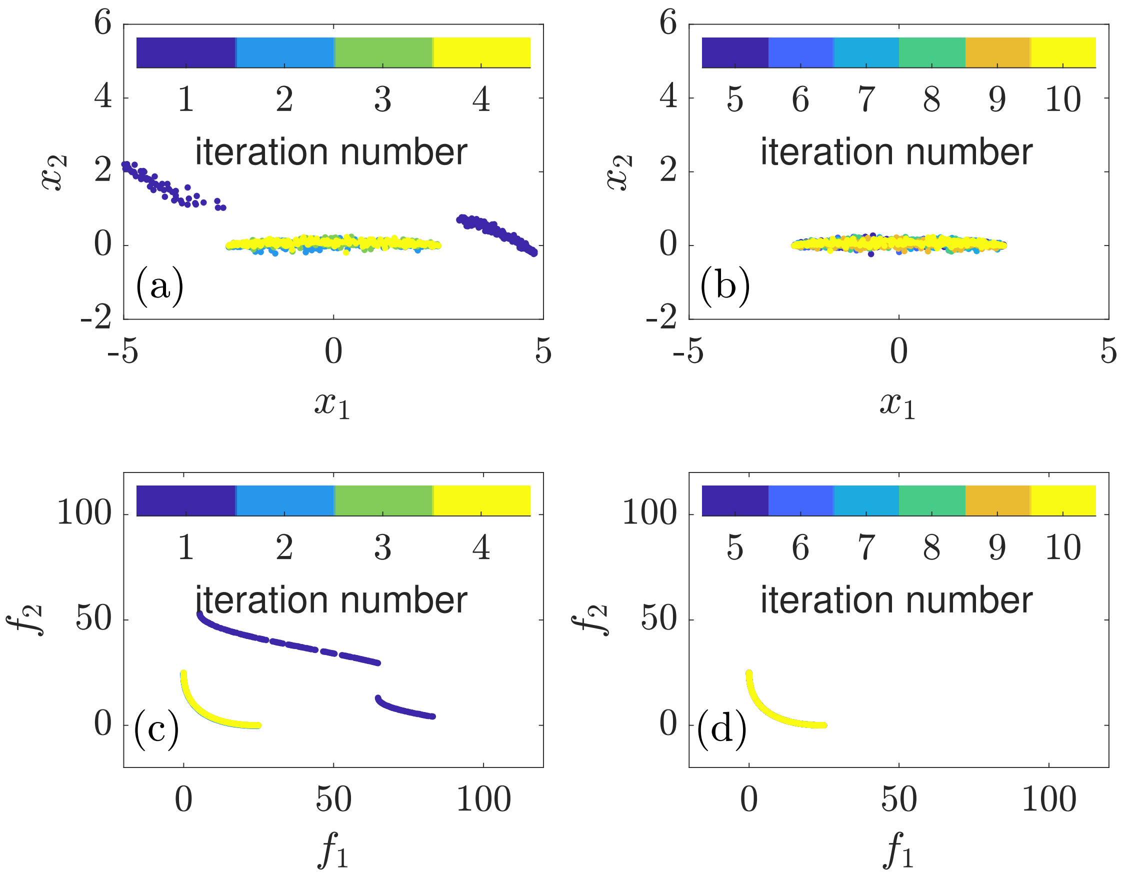

Figure 4.15: Predicted Pareto-optimal solutions as the MO-ASMO algorithm refines the surrogate model. Numbers of initial and update (including validation) samples are 4 and 8 per each iteration. The solution was globally accurate as early as at the second iteration. (a) and (b) Locations of Pareto set in the design space for iteration #1–4 and #5–10. (c) and (d) Locations of Pareto set in the objective function space for iteration #1–4 and #5–10.

each problem. For example, the multiobjective sphere function, presented as:

$$\underline{f} = \left[\sum_{i=1}^{2} (x_i - 2.5)^2 \, , \; \sum_{i=1}^{2} (x_i + 2.5)^2 \right] \tag{4.20}$$

has two independent unimodal function shapes, and the optimal solution is a straight line connecting the points $(-2.5,\ 0)$ and $(2.5,\ 0)$. Unlike the more challenging problems presented in the earlier sections, the Pareto-optimal solutions' location can be identified easily with very few samples. As shown in Fig. 4.15, the MO-ASMO algorithm found the Pareto-optimal solution at the second iteration with a coarse level of accuracy.

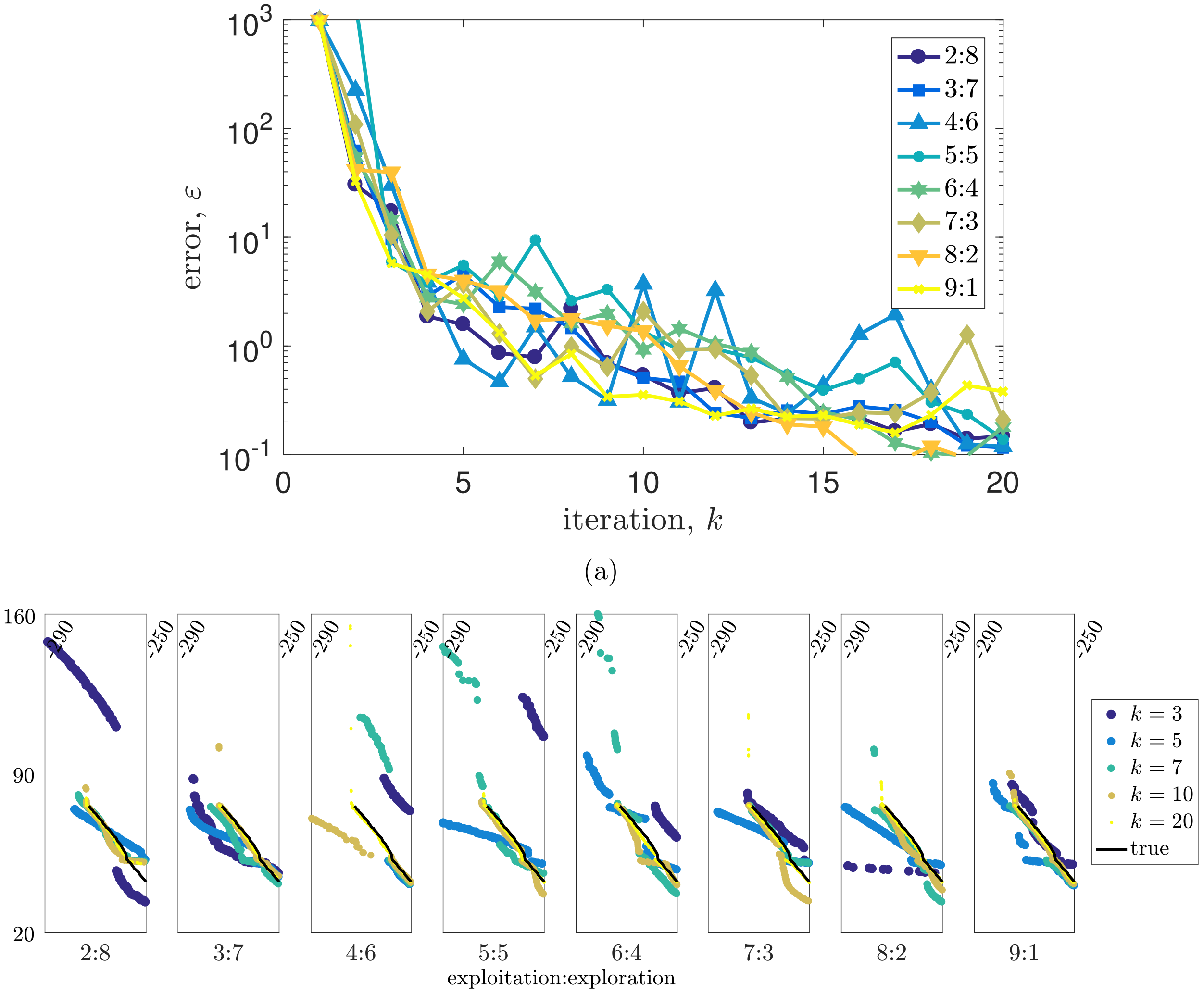

(a)

(b)

Figure 4.16: Convergence of MO-ASMO iterative refinement is presented for different exploitation and exploration sampling ratios, based on P2: the Osyczka and Kundu problem. (a) Convergence is compared using the ED error ε metric for different sampling ratios. (b) Pareto sets obtained via MO-ASMO for a varied number of iterations ($k = 3, 5, 7, 10, 20$) and different sampling ratios are compared.

Although the framework we developed currently does not include a mechanism for adaptively adjusting the balance between exploitation and exploration, we tested and compared the error, and the Pareto set convergence for different balance ratios, based on the P2: the Osyczka and Kundu problem. Figure 4.16 compares the ED error and the shape of the Pareto set in a magnified region in the objective function space for a varied number of iterations and various ratios between the exploitation and the exploration samplings. The balance between the exploitation and the exploration is defined as the ratio of new sample points at each MO-ASMO iteration, placed according to the sampling purposes. Since the exploration sampling is based on semi-randomized LHD, it is very difficult to characterize convergence using only a few tests. However, in Fig. 4.16a, errors for all different ratios have a decreasing trend as the iteration number increases. A few cases, such as 4:6 (4 samples for exploitation and 6 samples for exploration), exhibit oscillatory convergence characteristics. Also, we find that an extremely large ratio for exploitation helps the solution to converge faster compared to other cases, such as the 8:2 and 9:1 cases. Problems with low dimensionality typically do not require a large number of exploration samples to obtain a rough approximation of where the optimal solutions are likely located in.

Figure 4.16b shows a magnified view of the Pareto set for selected iterations ($k = 3, 5, 7, 10, 20$) for each distinct balance ratio. At iteration 20 (yellow), most cases have converged to the true solution, which is taken to be the result obtained after a large number of generations using the NSGA-II. However, intermediate solutions differ across distinct cases. As we pointed out in the analysis of Fig. 4.16a, MO-ASMO exhibits some convergence difficulties when sample points are allocated equally to exploitation and exploration. One possible approach for resolving this problem is the observation that the number of sample points for these two categories may vary concerning how well the surrogate model represents the trend of global responses, such as inflections, convexity, modal characteristics, and monotonicity. Here, MO-ASMO has the potential to be improved by utilizing adaptive balance adjustment during the surrogate model refinement iterations, and ongoing study will address this potential improvement mechanism.

4.6 Conclusions

We developed MO-ASMO, an SB-MOP solver framework, with novel efficient sampling strategies for challenging MOPs. The developed sampling strategies address shortcomings of methods often used in conventional SBO algorithms, specifically for HEB simulations with tightly-constrained feasible domains.

The sampling method developed for design space exploration is utilized both in the initial and the update sampling stages. When constraints exist that are functions of the design variables and solved separately from the expensive functions, enforcing these constraints in the sampling stage saves a significant amount of computational effort by avoiding expensive function evaluations that would not be valuable for finding solutions. Thus, solving an optimization subproblem that moves the samples toward the feasible domain before running any expensive functions is effective specifically for tightly-constrained problems, which is demonstrated with the test problems P3 and P6 in Section 4.5.

Also, the sampling method developed for exploitation of predicted solution regions is utilized in the update sampling stage to further enhance the solution accuracy, and to move the approximate Pareto frontier toward better solutions. An FDL-inspired sample placement technique is presented to help place new samples near, but not on, the predicted solution set to enhance better prediction of the Pareto frontier in the next iterative surrogate model refinement. This strategy ensures that new samples are not just duplicates of already-predicted Pareto set points, but improves the knowledge in the predicted Pareto frontier's vicinity, helping faster convergence. As demonstrated with the P2 and as shown in Fig. 4.16, the convergence rate was faster at around iteration number of 10 to 15 when we use more samples for exploitation than exploration. However, this result also suggests that the balance between exploration and exploitation should be adaptively adjusted throughout the iterative refinement procedure.

For problems with frequent simulation failures, or that have implicit constraints that cannot be known in a priori, an adaptive constraint generation and management strategy using the SVDD technique is proposed in this study. Without this technique, the authors could only obtain significantly suboptimal solutions for the combined texture and fluid design problem given in P6. Regardless of methods, including SBOs and MOEAs, the best possible solution obtained without this novel constraint management technique was similar to the solution indicated by the 'NSGA-II' markers (+) in Fig. 4.14a, since the optimizer wasted a significant amount of computational effort on invalid inputs that led to simulation failures, and these solution strategies could not learn from those failed simulations. However, with the SVDD technique encapsulating the regions with many invalid inputs for sampling methods and optimizers to avoid, we observed significant improvement over the Pareto frontier, while limiting the number of expensive full model evaluations to a reasonable level.

The developed MO-ASMO framework has demonstrated the effectiveness of two novel sampling strategies and a novel constraint management strategy in a combined way using a total of 6 test problems. This solution framework is expected to support solution of a wide range of practical simulation-based design optimization problems, extending its impact beyond the test problems presented in this study. Using the MO-ASMO framework, we expect to explore new types of designs with previously unexploited mechanisms to achieve new performance levels or functionalities in many other engineering design problems. However, there are many gaps beyond the scope of this study that could improve the SB-MOP solvers. Ongoing work is addressing the application of this framework to higher-dimensional problems. Beyond heuristic sampling strategies, mathematical frameworks, such as the high-dimensional model representation (HDMR), could be utilized to further alleviate difficulties arising from the *curse of dimensionality* [116]. Also, a hybrid SBO-DO approach may further enhance the efficiency of the MO-ASMO without relying solely on sampling strategies that involve stochastic elements. Finally, a deeper investigation of balancing exploitation and exploration should be conducted to enhance our understanding of how best to use the MO-ASMO framework for challenging HEB MOPs, aiming to reduce the required number of full model evaluations, while still improving the likelihood of identifying globally optimal solutions.

Part II

Integrated Design With Viscoelasticity

Chapter 5

Numerical Design With Viscoelasticity: Survey, Efficient Strategies, and Outlook

5.1 Summary

Design with and of viscoelastic (VE) materials exhibits various challenges. These challenges often come from function-valued material properties, denoted as material functions. This study explores the stress-strain relation of linear viscoelastic (LVE) materials, their models based on Boltzmann relaxation modulus functions and its design implications. Also, various numerical methods are surveyed and analyzed, which solve the stress-strain relation that contains the 'fading memory' concept of the Boltzmann relaxation modulus function. The Boltzmann stress relaxation concept introduces a convolution integral term in the stress-strain relation, which is often a term that is included in differential equations, making overall system governing equation an integro-differential equation (IDE). In this study, a frequency-domain method and various time-domain methods are compared. Also, several efficient numerical methods, including the time-domain truncation method and the linear time-invariant state-space (LTISS) system approximation of the convolution integral, and the derivative function surrogate modeling (DFSM) implementation, along with the LTISS system approximation of the convolution integral, to further mitigate computational effort for expensive dynamic system design problems. Two numerical cases are demonstrated. Prony basis functions are utilized to fit the relaxation modulus function to obtain the LTISS system that approximates the true response of the convolution integral. Also, the time-domain truncation method is demonstrated using a spacecraft attitude control design problem where the system is assisted by a passive viscoelastic damper (VED).

5.2 Introduction

Engineering design *with* [117–120] and *of* [12–14, 121, 122] viscoelasticity exhibits unique difficulties regarding the materials' characteristics and their responses to the external input. Conventional materials, such as linear elastic solids and Newtonian fluids, are well described by simple constitutive equations with constant-valued material properties. Although these material properties can depend on operating conditions (e.g., temperature or external pressure), these values remain constant throughout analysis if the operating conditions are controlled. However, the viscoelastic (VE) materials or other class of complex materials, including soft solids, fluids with polymers, suspensions of particles or droplets, or solutions exhibit ranges of different behaviors at the same time, and those behaviors can be functions of timescale, frequency, stress amplitude, or many other quantities [112, 123]. The material constitutive models and analysis framework should consider these function-valued material properties and their mechanical relationships.

Function-valued material properties (or material functions, hereafter) govern the behaviors of these complex materials. Select examples of material functions include (1) shear-rate dependent viscosity ($\eta\left(\dot{\gamma}\right)$) that describes shear thinning and shear thickening, (2) shear-rate dependent normal stress coefficients ($\Psi_1 = N_1\left(\dot{\gamma}\right)/\dot{\gamma}^2$, $\Psi_2 = N_2\left(\dot{\gamma}\right)/\dot{\gamma}^2$), (3) frequency-dependent storage and loss moduli ($G'\left(\omega\right)$, $G''\left(\omega\right)$), and (4) time-dependent relaxation modulus and creep compliance ($G\left(t\right)$, $J\left(t\right)$) [112]. Many rheological constitutive models utilize these material functions to connect the materials' characteristics to the mechanical equations to express continuum-level system behaviors. Examples of these constitutive equations are the Criminale-Ericksen-Filbey (CEF) model and the Giesekus model utilized in Chapter 7. Rheological materials can be characterized using various visco-rheometric techniques (e.g., cone and plate rheometry with a shear-rate sweep or small-amplitude oscillation frequency sweep) to obtain tabular values of appropriate material functions. Rheological constitutive models can be fitted with the obtained material functions, providing required physical quantities (e.g., shear stress tensor $\underline{\underline{\tau}}$) to analyze the continuum-level or system-level governing equations.

However, the use of rheological material functions or constitutive models is not straightforward in material design problems; in particular, the material design problem is the inverse process of the analysis problem described above. Arbitrary function shapes do not guarantee physically-realizable materials. Furthermore, many constitutive models also do not provide material constraints that limit the parameters to remain in the realizable design space. Thus, constraining the material design within a realizable material domain range is a challenging problem.

In addition, due to certain material characteristics, some classes of materials require a past transient history of states (e.g., stress, strain, strain rate) to predict future material states, meaning that the current state is not enough to compute the future state of the material behavior. An example of such a class is the set of VE materials. In the time-domain analysis of the VE materials, a convolution integral is required to describe the mechanical behavior of the material's memory effect, unless the analysis can be converted to frequency-domain analysis with periodic external input. These convolution integral equations are generally computationally expensive to solve, and in many cases, they need to be approximated in a less expensive form for practical solution requirements.

In this study, we review and compare available methods that could be applied to solve design problems with VE materials that exhibit the difficulties described above. We also present demonstrations of several different approaches for designing material systems with viscoelasticity to discuss and compare their advantages and disadvantages. Also, we limit our focus to linear viscoelastic (LVE) materials. Extending the methods discussed here toward nonlinear viscoelasticity is beyond the scope of this study.

5.3 Linear Viscoelasticity

5.3.1 Stress-Strain Relation for Linear Viscoelastic Materials

Rheological materials and their responses can be classified regarding their characteristic scales. With two dimensionless groups, the Deborah number ($\mathrm{De} = \lambda / t_{\mathrm{char}}$) and the Weissenberg number ($\mathrm{Wi} = \lambda \dot{\gamma}$), the classification of rheologically-complex materials can be mapped into a distorted two-dimensional space, called a Pipkin space [124]. λ is the relaxation time, t_{char} is the characteristic time or the observation time, and $\dot{\gamma}$ is the shear-rate. Detailed explanations of the dimensionless groups and the Pipkins space are given in Sections A.1 and A.2 of Appendix A, respectively. The VE materials respond to an external force or displacement over time with a memory effect, where the De number characterizes this behavior. Specifically, LVE materials exhibit this memory effect in their stress-strain relation within the limit of small amplitudes ($\mathrm{Wi} \ll 1$).

A one-dimensional stress-strain relationship of LVE materials can be described in the Riemann-Stieltjes integral, with the concept of a *fading memory* that Boltzmann [125] proposed, given as:

$$\sigma\left(t\right) = \int_{-\infty}^{t} G\left(t - t'\right) d\gamma\left(t'\right), \tag{5.1}$$

where σ is the stress (we use σ in this chapter in replace of ς for convenience), G is the relaxation modulus (also named Boltzmann function or memory kernel), and γ is the shear strain. For continuously-differentiable $\gamma\left(t\right)$, the above Riemann-Stieltjes integral can be represented with the standard Riemann integral, given as:

$$\sigma\left(t\right) = \int_{-\infty}^{t} G\left(t - t'\right) d\gamma\left(t'\right) = \int_{-\infty}^{t} G\left(t - t'\right) \dot{\gamma}\left(t'\right) dt', \tag{5.2}$$

where $\dot{\gamma}$ is the shear-rate. Note that this one-dimensional equation can be expanded to a three-dimensional version of the equation, given as:

$$\underline{\underline{\sigma}}\left(t\right) = \int_{-\infty}^{t} G\left(t - t'\right) \underline{\underline{\dot{\gamma}}}\left(t'\right) dt', \tag{5.3}$$

where $\underline{\underline{\sigma}}$ is the stress tensor, and $\underline{\underline{\dot{\gamma}}}$ is the rate of the strain tensor. Within the LVE assumption, a component of $\underline{\underline{\sigma}}$ is only coupled with the same component of $\underline{\underline{\dot{\gamma}}}$; thus, we can safely use the one-dimensional equation given in Eqs. (5.1) and (5.2) to generally represent the behavior of the LVE materials. With a change of variable $s = t - t'$, the convolution integral becomes:

$$\sigma\left(t\right) = \int_{0}^{\infty} G\left(s\right) \dot{\gamma}\left(t - s\right) ds. \tag{5.4}$$

In the case where no strain history exists (e.g., the material is relaxed for enough time before testing), then the integration range of Eq. (5.4) reduces to $(0, t)$ in place of $(0, \infty)$.

As we see in Eq. (5.3), the stress σ at time t requires the entire history of the shear-rate $\dot{\gamma}$ from time 0 to t, or if there is a strain history before the initial time, the required history of the shear-rate is the time range from $-\infty$ to the current time t. Thus, in time-marching dynamic simulations with the LVE materials or elements, the entire history of at least a subset of appropriate states is required for current step computations. This property of VE materials significantly increases the simulation problem computational expense, which is amplified when used in conjunction with design optimization.

5.3.2 Boltzmann Relaxation Modulus Function in Design

The Boltzmann [125] relaxation modulus function (or memory kernel function) $G(t)$ represents the material's stress relaxation strength over time after strain is applied. Equation 5.4 and $G(t)$ do not intrinsically characterize specific classes of materials, so this model can be considered as a material-agnostic material description. Since the material function shape or values can be completely arbitrary, directly designing the material function demands additional constraints that externally provide additional information guides the designed function to exhibit real material behaviors.

The direct design of the relaxation modulus function shape opens the full set of possibilities for finding optimal material designs, and can be thought of as a highly-flexible VE material design representation. However, this approach may generate relaxation modulus functions that are not physically realizable via mechanisms that give rise to real VE materials. This direct design representations has been used in a few previous studies. Rao and Allison [122] use direct optimal control methods, including a single-shooting method and a direct transcription (DT) method to directly manipulate the function shape of the relaxation modulus to find an optimal LVE material design solution. An additional set of constraints was added to guide the designed relaxation modulus function $G(t)$ to be monotonically-decreasing [126]. This set of constraints prevents the design solution from violating physics and helps to ensure 'fading memory' behavior, although this constraint does not always guarantee that the relaxation modulus function is realizable.

A more common design technique is to utilize parametric models that have physical meanings. The LVE material models have their own mechanical analogs using combinations of linear springs and dashpots [123]. The Maxwell model is the simplest material model that describes the LVE fluids, and this model's mechanical analog is a series connection of one linear spring and one linear dashpot. The Kelvin-Voigt model is another simplest material model that describes LVE solids. Again, this model can be described in the mechanical analog as a parallel combination of the linear spring and the linear dashpot. These material models can be used for parameterizing the relaxation modulus function. For a linear dashpot, the relaxation modulus function can be represented as:

$$G(t) = \eta \delta(t), \tag{5.5}$$

where η is the dashpot damping coefficient, and $\delta(t)$ is the Dirac delta function. Interestingly, Eq. (5.5) applies exactly to Newtonian fluids. Designing Newtonian fluids within the framework of the Boltzmann relaxation modulus function is equivalent to obtaining a single design variable η to minimize a cost function or maximize the system performance. Moving to the Maxwell fluid model, the relaxation modulus function can be represented as:

$$G\left(t\right) = Ge^{-t/\lambda}, \tag{5.6}$$

where G is the Maxwell relaxation modulus constant or the Maxwell spring constant, and λ is the relaxation time. However, this single-mode Maxwell model is limited to approximation of materials without dispersed relaxation times, limiting the material's polydispersity index (PDI) of the relaxation times to 1 [127]. For materials with multiple relaxation timescales, this model can be extended to the multimode formulation, given as:

$$G\left(t\right) = \sum_{i=1}^{n} G_i e^{-t/\lambda_i}. \tag{5.7}$$

Corman et al. [12] presented a design framework incorporating LVE using the discrete Prony-series VE material model, also known as the multimode Maxwell model, as well as the critical gel model. The study presented possibility that a parameterized material function could be utilized as a design target for engineering design. Similarly, Lee et al. [67] presented a quarter car suspension design with a viscoelastic damping element using the multimode Maxwell model; this was used as a test problem for a new design optimization algorithm. The study utilized different numbers of modes to compare computational time and differences in results when used in conjunction with optimization. As the number of modes was increased, the computational expense increased significantly, limiting the allowable number of modes in design studies not by material characteristics, but by available computing resources. Here, a parameterization of the material function does not significantly increase the number of parameters, but increases the capability of representing a wide range of the dispersed nature of the relaxation characteristics.

As discussed in Section 6.3.2 of Chapter 6, the relaxation strength can be a continuous spectrum with a range of relaxation timescales, given as:

$$G\left(t\right)=\int_{0}^{\infty}\frac{H\left(\lambda\right)}{\lambda}e^{-t/\lambda}d\lambda=\int_{0}^{\infty}H\left(\lambda\right)e^{-t/\lambda}d\ln\lambda, \tag{5.8}$$

which is a more general form that describes materials with ranges of relaxation times. Distributed relaxation times and strengths that exist in real viscoelastic materials can be described more naturally using this continuously-distributed spectrum $H(\lambda)$, with various models that parameterize the spectrum using a handful number of variables. See Table 6.1 of Chapter 6 for a select list of continuous relaxation spectra models and their parameters. Some models have statistical distribution parameters that are not closely related to the physics of material microstructural mechanics, e.g., the log-normal distribution model [128–130]. However, many other models have parameters that connect the material model shapes to the physically-meaningful quantities more closely, such as peak relaxation strength and its timescale, changes of relaxation strength and timescale boundaries of different regimes, or molecular weight-based relaxation times, e.g., the modified Baumgaertel-Schausberger-Winter (BSW) model [131]. Although many studies utilize the continuous relaxation spectra representation to fit certain materials of interest, designing the material properties with this concept is in a very early-stage of investigation, and few relevant publications are currently available. Corman and Ewoldt [132] proposed the use of a continuous relaxation spectrum for designing LVE materials, and presented an Ashby-style plot for designers to intuitively access and compare characteristics of LVE materials. Based on this work, Lee et al. [121] presented the use of the continuous relaxation spectra and the Ashby-style plot within the larger top-down systems design framework, beginning from the system-level objectives, mapping down to the desired material rheology, and ultimately connecting toward the material microstructure design with a bi-directional exchange of information between different design levels.

Although many parameterized material models and spectrum models utilize physically-meaningful parameters to constrain the material functions to have characteristics of existing materials, these parameters are still not enough to constrain the design space to be confined within the physically achievable material options. There are a few possible approaches that can help resolve this issue. One of them is the use of data-driven algorithms with experiment-in-the-loop (EIL) design optimization. While designing the systems and materials simultaneously, data-driven algorithms can check if the obtained design candidates are physically feasible using the automated (or human-assisted) experiments to perform (1) material synthesis, (2) material characterization, and using the data obtained from the experiment (3) provide design space boundaries. In different contexts, a few studies addressed similar approaches. Lee et al. [13] utilized a support vector domain description (SVDD)-based data-driven approach to adaptively generate and manage implicit constraints to avoid numerically-instable design spaces. Deodhar et al. [133] proposed a theoretical framework for the EIL plant and controller optimization for optimally-designing a system with highly-nonlinear dynamics. Similarly, the materials design could take advantage of this adaptive constraint generation and management scheme to find the feasible design space, and this work is left for future exploration.

A selection of the right material model is also an important topic for designing with material systems. Design-appropriate material models and their general criteria are addressed in Corman et al. [12], Schuh et al. [36], and Corman and Ewoldt [132]. However, these studies are limited to their own material model choice and do not cover a comprehensive model comparison and selection framework. Outside of the design context, a wide range of previous literature exists that discusses fitting parameters, selecting, and comparing rheological models with, especially, experimentally-obtained data. However, the majority of these previous studies are only done in the context of accurately simulating the existing and already-characterized materials. Jansen [134] worked on fitting the material relaxation modulus function with different material models and compared to the experimental data. Kimanzi [135] worked on selecting viscoelastic materials for impact absorption. Freund and

Ewoldt [136] discussed a model selection strategy using Bayesian inference, addressing the decision-making between a more robust model and a more accurate model. Considering the gap between the analysis and the design with material systems, a study needs to be performed for the rheological material model selection and decision-making regarding not only robustness and accuracy, but also design-appropriateness and feasibility of the material models.

5.4 Survey and Analysis of Numerical Methods for Convolution Integrals

5.4.1 Frequency-Domain Method

Computing stress-strain relations with LVE materials is costly due to its convolution integral term in Eq. (5.4). Many previous studies transformed the convolution integral term from the time-domain to the frequency-domain to mitigate the computational cost, and to efficiently solve the response spectrum of the system [12, 112, 123, 137, 138]. Consider an oscillatory shear flow between two parallel plates with gap height h, and the top plate is sinusoidally oscillating with small amplitude $\delta \sin \omega t$, where $\delta \ll h$. Then the shear strain and shear-rate are defined as:

$$\gamma(t) = \frac{\delta}{h} \sin \omega t = \gamma_0 \sin \omega t, \text{ and} \tag{5.9a}$$

$$\dot{\gamma}(t) = \frac{\delta}{h} \omega \cos \omega t = \dot{\gamma}_0 \cos \omega t, \tag{5.9b}$$

where $\gamma_0 = \delta / h \ll 1$ and $\dot{\gamma} = \omega \gamma_0$. The shear stress-strain relation then becomes:

$$\sigma(t) = \int_0^\infty G(s)\, \dot{\gamma}(t-s)\, ds \tag{5.10}$$

$$= \int_0^\infty G(s)\, \dot{\gamma}_0 \cos \omega (t-s)\, ds \tag{5.11}$$

$$= \int_0^\infty G(s)\,\dot{\gamma}_0\left[\cos\omega t\cos\omega s + \sin\omega t\sin\omega s\right]ds. \tag{5.12}$$

The dynamic storage and loss moduli are defined with the relaxation modulus function, given as:

$$G'(\omega) = \omega\eta''(\omega) = \omega\int_0^\infty G(s)\sin(\omega s)\,ds, \tag{5.13a}$$

$$G''(\omega) = \omega\eta'(\omega) = \omega\int_0^\infty G(s)\cos(\omega s)\,ds, \tag{5.13b}$$

and combining these dynamic moduli into the stress-strain relation, Eq. (5.12) becomes:

$$\sigma(t) = G'(\omega)\,\gamma_0\sin\omega t + \eta'(\omega)\,\dot{\gamma}_0\cos\omega t. \tag{5.14}$$

The interrelation between the above dynamic storage and loss moduli are constrained by the Kramers-Kronig relations [112], given as:

$$G'(\omega) - G'_\infty = \frac{2}{\pi}\int_0^\infty \frac{sG''(s)}{\omega^2 - s^2}ds, \text{ and} \tag{5.15a}$$

$$G''(\omega) = \frac{2\omega}{\pi}\int_0^\infty \frac{G'(s)}{s^2 - \omega^2}ds, \tag{5.15b}$$

where:

$$G'_\infty = \lim_{\omega\to\infty} G'(\omega). \tag{5.16}$$

For some material models, including Newtonian fluid model, single- and multimode Maxwell models, critical gel model, and continuous version of the Maxwell spectrum models, the dynamic storage and loss moduli can be analytically derived from their material model equations [112, 123]. The Prony series representing the M-mode Maxwell model can be represented in frequency-domain, given as:

$$G'\left(\omega\right) = \sum_{m=1}^{M} G_m \frac{\left(\lambda_m \omega\right)^2}{1+\left(\lambda_m \omega\right)^2}, \text{ and} \tag{5.17a}$$

$$G''\left(\omega\right) = \sum_{m=1}^{M} G_m \frac{\lambda_m \omega}{1+\left(\lambda_m \omega\right)^2}. \tag{5.17b}$$

The relaxation modulus function $G(t)$ with the continuous relaxation spectrum $H(\lambda)$ can also be represented in frequency-domain [123], given as:

$$\begin{aligned} G'\left(\omega\right) &= \int_0^\infty \omega \sin \omega s \left[\int_0^\infty H\left(\lambda\right) e^{-s/\lambda} \frac{d\lambda}{\lambda}\right] ds && (5.18a)\\ &= \int_0^\infty \omega H\left(\lambda\right) \frac{d\lambda}{\lambda} \int_0^\infty e^{-s/\lambda} \sin \omega s \, ds && (5.18b)\\ &= \int_{-\infty}^\infty \frac{\left(\lambda\omega\right)^2}{1+\left(\lambda\omega\right)^2} H\left(\lambda\right) d \ln \lambda && (5.18c)\\ G''\left(\omega\right) &= \int_0^\infty \frac{\omega}{1+\left(\lambda\omega\right)^2} H\left(\lambda\right) d\lambda. && (5.18d) \end{aligned}$$

Integrating over the spectrum range $(0, \infty)$ can be computationally expensive with the continuous relaxation spectrum $H\left(\lambda\right)$, especially when the dynamic system needs to be analyzed over a wide frequency range. In the frequency-domain, discrete spectrum models with a limited number of modes (e.g., Eq. (5.17)) are significantly less expensive to compute than the continuous spectrum model given in Eq. (5.18).

Despite its popularity in the rheology community, where the sinusoidal oscillatory loading condition is widely used for characterizing the VE materials, this approach has a significant drawback for use in the design of dynamic systems. Although periodic sinusoidal loading conditions can be utilized to obtain frequency responses of the system, realistic dynamics do not generally have this overly-simplified input profile. These time-dependent dynamic systems require time-dependent VE computation, and will be discussed in the following subsections.

5.4.2 Time-Domain Integration of Convolution Integral, Method 1

The most primitive, but computationally-expensive method is the direct integration of convolution integral in the simulation. A dynamic system is generally represented in the form of an ordinary differential equation (ODE), which can be conveniently converted to standard state-space equation form, and the stress-strain (or force-displacement) relation of the VE material incorporates the convolution integral. Combining the VE stress-strain relation into the dynamic equation yields an integro-differential equation (IDE). For example, when a dynamic system is represented as a simple ODE, given as:

$$m\ddot{x}\left(t\right)+F_{\mathrm{VE}}\left(t\right)+kx\left(t\right)=0, \tag{5.19}$$

and the VE force-displacement relationship is represented as a convolution integral, given as:

$$F_{\mathrm{VE}}\left(t\right)=\frac{\alpha_F}{\alpha_x}\int_0^t G\left(\tau\right)\dot{x}\left(t-\tau\right)d\tau, \tag{5.20}$$

where α_F is a geometric mapping parameter between force and stress ($F=\alpha_F\sigma$), and α_x is a geometric mapping parameter between displacement and shear strain ($x=\alpha_x\gamma$). Combining Eqs. (5.19) and (5.20) yields:

$$m\ddot{x}\left(t\right)+\frac{\alpha_F}{\alpha_x}\int_0^t G\left(\tau\right)\dot{x}\left(t-\tau\right)d\tau+kx\left(t\right)=0, \tag{5.21}$$

which contains both integral and differential terms, making an IDE. When this equation is discretized for numerical solution, the first and third terms in the left-hand side at discrete time step k depend only on the single previous step $k-1$. This is called a single-step dependency. However, the second term in the left-hand side depends on the entire step histories of previous states, demanding k number of previous trajectory data for each required state. When the current step k is moving forward, the size of the required previous trajectory data increases proportionally. Assuming that we solve the integral term using a simple quadrature method, the number of required numerical quadratures n_{q} for the total number of simulation time steps n_t is:

$$n_{\mathrm{q}} = \frac{n_t \left(n_t + 1\right)}{2} \sim O\left(n_t^2\right), \tag{5.22}$$

which is a quadratic time algorithm ($O\left(n^2\right)$) with respect to time complexity [139]. Since this method is the most straightforward approach, many dynamic simulation studies [140–142] and a handful of design studies [14, 67, 121, 122] of VE materials utilized this direct integration method, despite its large computational cost.

A discretized form of direct integration can be derived using the following steps. In the single-step formulation, state values at the current time step $(k+1)$ only depend on quantities computed by state values at the previous time step (k), given as:

$$\underline{\xi}^{k+1} = \underline{\xi}^{k} + \frac{\Delta t}{1!}\dot{\underline{\xi}}^{k} + \frac{\left(\Delta t\right)^2}{2!}\ddot{\underline{\xi}}^{k} + \cdots + \frac{\left(\Delta t\right)^n}{n!}\underline{\xi}^{(n)k} + R_n, \tag{5.23}$$

where $\underline{\xi}$ is a state vector, Δt is the time step size, k is the time step number, and $R_n \sim \left(\Delta t\right)^{n+1}$. This assumes that time steps are uniform. In practical implementation, the first-order term is generally sufficient for dynamic simulation, although rarely some time-marching schemes use the second-order term for more accurate time-domain integration. The direct integration of the convolution integral term can be represented using a first-order time integration approximation, given as:

$$\underline{\xi}^{k+1} = \underline{\xi}^{k} + \left(\Delta t\right)\dot{\underline{\xi}}^{k} \tag{5.24a}$$

$$= \underline{\xi}^{k} + \Delta t \int_0^{t^k} G\left(s\right)\xi\left(t^k - s\right) ds \tag{5.24b}$$

$$= \underline{\xi}^{k} + \Delta t \sum_{i=1}^{k-1} \int_{t^{i}}^{t^{i+1}} G\left(s\right) \xi \left(t^{k} - s\right) ds, \tag{5.24c}$$

where the integral term can be discretized with any suitable single-step quadrature method. For example, the Euler method is applied to Eq. (5.24c), given as:

$$\underline{\xi}^{k+1} = \underline{\xi}^{k} + \Delta t \sum_{i=1}^{k-1} \left[\left(\Delta t\right) G\left(t^{i}\right) \underline{\xi}\left(t^{k-i}\right)\right] \tag{5.25a}$$

$$= \underline{\xi}^{k} + \left(\Delta t\right)^{2} \sum_{i=1}^{k-1} \left[G^{i} \underline{\xi}^{k-i}\right]. \tag{5.25b}$$

5.4.3 Time-Domain Integration of Convolution Integral, Method 2

Diethelm and Freed [143] proposed that the computation of this convolution integral can be enhanced using the property that the relaxation modulus function $G(t)$ is always monotonically decreasing and asymptotically approaching zero. When the convolution integral is decomposed to isolate the steady-state modulus, specifically:

$$\sigma\left(t\right) = \int_{0}^{t} G\left(\tau\right) \dot{x}\left(t-\tau\right) d\tau = tG_{\infty} + \int_{0}^{t} \widehat{G}\left(\tau\right) \dot{x}\left(t-\tau\right) d\tau, \tag{5.26}$$

where:

$$G_{\infty} = \lim_{\tau \to \infty} G\left(\tau\right) \quad \text{and} \quad \widehat{G}\left(\tau\right) = G\left(\tau\right) - G_{\infty}, \tag{5.27}$$

the convolution integral $\widehat{G}$ satisfies the conditions required by the method proposed by Diethelm and Freed [143]. The convolution integral part of Eq. (5.26) can be decomposed into a sequence of integrals, given as:

$$\int_{0}^{t} \widehat{G}\left(\tau\right) \dot{x}\left(t-\tau\right) d\tau = \left(\int_{0}^{QT} + \int_{QT}^{Q^{2}T} + \cdots + \int_{Q^{\mu-1}T}^{Q^{\mu}T}\right) \widehat{G}\left(\tau\right) \dot{x}\left(t-\tau\right) d\tau, \tag{5.28}$$

where $t = Q^{\mu}T$ with $T > 0$, $Q \in \{3, 5, 7, \cdots\}$ is a quality parameter, and $\mu = \log_{Q}\left(t_{f}/T\right)$

designates the subintervals in the integration. To reduce the number of required numerical quadratures, the algorithm uses a different interval size for each interval of the convolution integration given in Eq. (5.28), where a mesh size for each interval increases as the sequence of interval increases. The numerical quadrature is performed with a mesh of $h = TQ^{n-1}/S$ for the n-th interval, where $S \geq 4$ is the number of integration steps in each integration interval. This variable interval scheme reduces the complexity of direct integration of the convolution integral from the quadratic time to a linearithmic time ($O(n \log n)$) with respect to time complexity; this still is not highly efficient, but does produce a large decrease in computational cost [139]. Readers are referred to Diethelm and Freed [143] and Freed [144] for detailed algorithm and numerical method implementation descriptions.

5.5 Efficient Time-Domain Methods for Convolution Integrals

5.5.1 Time-Domain Truncation Technique for Efficient Computation

Theoretically, the stress relaxation modulus function needs to be computed for the interval $(0, \infty)$ in Eq. (5.4). In many cases with time-domain analysis, the dynamic response of the system is abrupt compared to the change in the relaxation modulus function. With these fast-moving dynamics, the numerical integration needs to have a fine mesh for the time-domain, which increases the computational cost (time and memory) significantly, and becomes impractical in many cases. To resolve this issue, a time-domain truncation technique is used in our previous work [14].

Depending on the rate of strength decay in the relaxation modulus function, a cutoff time t^{α} is defined with the following procedure:

1. define parameters: $\alpha = 10^{-3}$: cutoff factor, $t^{\alpha} = 10^{-6}$: initial guess of the cutoff time.

2. numerically solve $\log\left(G\left(t^{\alpha}\right)\right)-\log\left(\alpha G\left(0\right)\right)=0$ for t^{α}.

Then, solve the VE convolution integral in Eq. (5.4) only for the integration range of $(0, t^{\alpha})$, which is an approximation of Eq. (5.4), but truncates very small memory effects that come from the distant past (specifically, more than t^{α} seconds prior), given as:

$$\sigma\left(t\right)=\int_{0}^{t^{\alpha}} G\left(s\right)\dot{\gamma}\left(t-s\right)ds. \tag{5.29}$$

The computation time depends directly on the decay rate of the relaxation modulus function. The time complexity still remains the same, but depending on how the integration is performed, the actual integration time can be significantly reduced using this technique, e.g., $O\left(n^{2}\right)$ can be reduced to $O\left(n^{2}/a\right)$, where the factor $a \gg 1$ is passively determined by the value of α and the decay rate of $G\left(t\right)$.

5.5.2 Linear Time-Invariant State-Space Approximation

Dynamic systems can be represented as a single or a set of differential equations, which can also be generally transformed into a first-order derivative function using input, output, and state vectors. In this case, the derivative function model can be represented in state-space form, and once a dynamic system is represented in a state-space form, then there exist many numerical integration techniques that can efficiently handle and solve linear and nonlinear dynamic system simulation and design optimization problems [44, 145, 146].

The direct integration methods described in Sections 5.4.2, 5.4.3, and 5.5.1 add a significant computational burden at each time step in the dynamic system simulation, because the inner convolution integral term needs to be computed separately at each time step during the integration of the dynamic system. This is even worse when used with the DT method, since each time-domain nodal point has its own defect constraint that needs to be evaluated multiple times before it reaches the converged solution. The DT method is highly efficient only when the dynamics can be directly converted to the defect constraint, but, in this case, the VE stress-strain relation needs to be solved separately to provide information to the defect constraint enforcement, and therefore, the numerical structure of the DT method cannot be leveraged.

One strategy is to convert the convolution integral term in the single-step formulation using a linear time-invariant state-space (LTISS) model that approximately follows the response of the true convolution integral response [147–149]. This strategy is well-described in Herber and Allison [148]. This approach also has been widely utilized in simulating dynamics with ocean waves energy [150]. The Cummins equation [151], in the context of ocean wave energy, parallels the VE convolution integral given in Eq. (5.4), where the radiation impulse-response function (IRF) $K_r(t)$ in the wave energy equation has exactly the same characteristics as the relaxation modulus function $G(t)$ has in the viscoelastic materials model.

Consider a convolution integral equation, given as:

$$y(t) = \int_{-\infty}^{t} G(t-\tau)\dot{\gamma}(\tau)d\tau, \tag{5.30}$$

where $y(t)$ is the output, $k(t)$ is the IRF, which can be an arbitrary kernel function (stress relaxation modulus $G(t)$, creep compliance $J(t)$, or others in different contexts), $u(t)$ is the input, and $\tilde{\cdot}$ represents an approximation of corresponding variables. An LTISS model for approximating the convolution integral in Eq. (5.30) can be represented as [149, pp. 64–66]:

$$y(t) \approx \tilde{y}(t) = \int_{-\infty}^{t} \tilde{G}(t-\tau)\dot{\gamma}(\tau)d\tau = \mathbf{C}\underline{\xi}(t) \tag{5.31}$$

where:

$$\dot{\underline{\xi}}(t) = \mathbf{A}\underline{\xi}(t) + \mathbf{B}\dot{\gamma}(t). \tag{5.32}$$

Here, $\underline{\xi}$ is a vector of the n additional states, with matrices $\mathbf{A}_{n\times n}$, $\mathbf{B}_{n\times 1}$, and $\mathbf{C}_{1\times n}$ that comprise the LTISS system and is exact with $\tilde{G}(t)$.

To ensure the similarity between the original $y(t)$ and the approximated $\tilde{y}(t)$ responses, the response values at the initial time point need to be enforced with an equivalence condition, given as:

$$y\left(t_0\right) = \tilde{y}\left(t_0\right) = \mathbf{C}\underline{\xi}\left(t_0\right). \tag{5.33}$$

Solving the linear system described in Eq. (5.32), the general solution to the LTISS system is given as:

$$\underline{\xi}\left(t\right) = e^{\mathbf{A}(t-t_0)}\underline{\xi}\left(t_0\right) + \int_{t_0}^{t} e^{\mathbf{A}(t-\tau)}\mathbf{B}\dot{\gamma}\left(\tau\right)d\tau, \tag{5.34}$$

where $e^{\mathbf{A}}$ is the matrix exponential, given as:

$$e^{\mathbf{A}t} = \sum_{i=0}^{\infty}\frac{\mathbf{A}^i t^i}{i!}. \tag{5.35}$$

The approximated IRF and the LTISS model are interrelated by the impulse response, given as:

$$\tilde{G}\left(t\right) = \mathbf{C}e^{\mathbf{A}t}\mathbf{B}. \tag{5.36}$$

For a specified system, there are infinite possible LTISS models that approximate the original convolution integral. However, there are certain useful standardized methods to find appropriate matrices **A**, **B**, and **C**, and these methods are referred to as canonical forms [149, p. 25, p. 159]. The companion form is one of these canonical forms, and given as:

$$\mathbf{A} = \begin{bmatrix} 0 & 0 & \cdots & 0 & -a_0 \\ 1 & 0 & \cdots & 0 & -a_1 \\ 0 & 1 & \cdots & 0 & -a_2 \\ \vdots & \vdots & \ddots & \vdots & \vdots \\ 0 & 0 & \cdots & 1 & -a_{n-1} \end{bmatrix}, \mathbf{B} = \begin{bmatrix} b_0 \\ b_1 \\ b_2 \\ \vdots \\ b_{n-1} \end{bmatrix}, \mathbf{C} = \begin{bmatrix} 0 & 0 & \cdots & 0 & 1 \end{bmatrix}. \tag{5.37}$$

This form still maintains the generality of representing any arbitrary IRF, but with an advantage that the required number of parameters is reduced compared to the most general form, given in Eqs. (5.31) and (5.32).

The dynamic system (denoted as a subscript 'd') with the LTISS system approximation (denoted as a subscript 'c') can be combined into single state vector $\underline{\xi} = \left[\underline{\xi}_{\mathrm{d}}, \underline{\xi}_{\mathrm{c}}\right]^{\mathrm{T}}$. Then, the discretized dynamic formulation is:

$$\begin{bmatrix} \underline{\xi}_{\mathrm{d}} \\ \underline{\xi}_{\mathrm{c}} \end{bmatrix}^{k+1} = \begin{bmatrix} \underline{\xi}_{\mathrm{d}} \\ \underline{\xi}_{\mathrm{c}} \end{bmatrix}^{k} + \int_{t^k}^{t^{k+1}} \begin{bmatrix} \dot{\underline{\xi}}_{\mathrm{d}} \left(\underline{\xi}_{\mathrm{d}}(\tau), \underline{\xi}_{\mathrm{c}}(\tau), \underline{u}_{\mathrm{d}}(\tau), \underline{x}_p\right) \\ \dot{\underline{\xi}}_{\mathrm{c}} \left(\underline{\xi}_{\mathrm{c}}(\tau), \dot{\gamma}_{\mathrm{d}}(\tau)\right) \end{bmatrix} d\tau \tag{5.38a}$$

$$= \begin{bmatrix} \underline{\xi}_{\mathrm{d}} \\ \underline{\xi}_{\mathrm{c}} \end{bmatrix}^{k} + \int_{t^k}^{t^{k+1}} \begin{bmatrix} \mathbf{A}_{\mathrm{d}}\underline{\xi}_{\mathrm{d}}(\tau) + \mathbf{B}_{\mathrm{d}}\underline{u}_{\mathrm{d}}(\tau) + \mathbf{C}_{\mathrm{c}}\underline{\xi}_{\mathrm{c}}(\tau) \\ \mathbf{A}_{\mathrm{c}}\underline{\xi}_{\mathrm{c}}(\tau) + \mathbf{B}_{\mathrm{c}}\dot{\gamma}_{\mathrm{d}}(\tau) \end{bmatrix} d\tau. \tag{5.38b}$$

Since $\dot{\gamma}_{\mathrm{d}}$ is a scalar included in the state of the dynamic model, this variable can be considered as a part of $\underline{\xi}$. Then the discretized dynamic system formulation can be expressed as:

$$\underline{\xi}^{k+1} = \underline{\xi}^{k} + \int_{t^k}^{t^{k+1}} \hat{\mathbf{A}}\underline{\xi}(\tau) + \hat{\mathbf{B}}\underline{u}(\tau)\, d\tau, \tag{5.39}$$

where:

$$\hat{\mathbf{A}} = \begin{bmatrix} \mathbf{A}_{\mathrm{d}} & \mathbf{C}_{\mathrm{c}} \\ \mathbf{B}_{\mathrm{c}} & \mathbf{A}_{\mathrm{c}} \end{bmatrix}, \ \hat{\mathbf{B}} = \begin{bmatrix} \mathbf{B}_{\mathrm{d}} & \mathbf{0} \\ \mathbf{0} & \mathbf{0} \end{bmatrix}, \ \underline{u} = \begin{bmatrix} \underline{u}_{\mathrm{d}} \\ \underline{0} \end{bmatrix}, \tag{5.40}$$

and some components of the matrices should be rearranged appropriately.

The LTISS system approximation can be utilized with some basis functions. One particular useful type of basis functions is the Prony basis function (PBF) that appears in Prony's method, a signal fitting method for damped exponentials or sinusoids [152]. Consider a particular basis function $\phi(t)$, used to construct both approximated IRF $\tilde{G}$ and the LTISS system. The approximated IRF is constructed using the sum of N basis functions, given as $\tilde{G}(t) = \sum_{i=1}^{N} \phi_i$. A single PBF has four parameters, and is given as:

$$\phi(t, \theta) = \theta_1 e^{-\theta_2 t} \cos(\theta_3 t + \theta_4), \tag{5.41}$$

where the basis function has an exponentially-decaying cosine wave with phase delay and variable amplitude. Without loss of generality, we assume $\theta_1 > 0$, $\theta_2 > 0$, $\theta_3 > 0$, and $0 \leq \theta_4 \leq 2\pi$. Specifically, θ_2 is set positive to ensure that $\lim_{t\to\infty} \tilde{G}(t) = 0$. The LTISS system approximation using the PBF requires two states for each mode, given as:

$$\mathbf{A}_\phi = \begin{bmatrix} -\theta_2 & \theta_3 \\ -\theta_3 & -\theta_2 \end{bmatrix}, \ \mathbf{B}_\phi = \begin{bmatrix} \sin\theta_4 \\ \cos\theta_4 \end{bmatrix}, \ \mathbf{C}_\phi = \begin{bmatrix} 0 & 1 \end{bmatrix}, \tag{5.42}$$

and can be superposed with multiple basis function parameters. The PBF can be reduced to constrained submodels, including the Gola-Huges-McTavish (GHM) model, and the Prony series function, which is also known as the generalized Maxwell model. These reduced models are presented and described in Herber and Allison [148].

Unlike the direct integration methods presented in Sections 5.4.2, 5.4.3, and 5.5.1, the LTISS system approximation has the Markovian characteristic that the current value of the state depends only on the state of one previous step, meaning that the storage of state history is unnecessary. Although fitting the LTISS model may require additional computational effort, this characteristic of the method significantly reduces overall computational cost for VE simulation and design optimization.

One large drawback of this method, from the perspective of application to VE material design optimization, is that the matrices in the approximated LTISS system cannot be designed directly. The matrices **A**, **B**, and **C** includes elements that are tuned to approximate the original convolution integral, but directly manipulating values of these elements may lead the model to exhibit arbitrary nonphysical behaviors, and even the stability of the model is not guaranteed. Instead, the material function parameters should be designed, and the LTISS system approximation can only be fitted after obtaining the relaxation modulus function $G(t)$. The LTISS system approximation may especially useful for design optimization problems where the VE material properties are held fixed, but the dynamic interaction between the VE material and other system elements must be modeled accurately and efficiently.

5.5.3 Derivative Function Surrogate Model for Linear Time-Invariant State-Space Approximation

With the LTISS system approximation explained above, the convolution integral equation can be converted to a single-step method (also can be referred to as a Markov process). This property enables the application of a wide range of solution methods based on efficient numerical techniques. One challenge with LTISS system approximations is the addition of a large number of auxiliary states. Novel strategies may exist to reduce approximation order, while maintaining accuracy. Here, we suggest extending the derivative function surrogate modeling (DFSM) method, introduced by Deshmukh and Allison [153], to solve design optimization problems with dynamic systems with LVE materials to even further mitigate the computational cost.

The DFSM approach is particularly useful when the dynamic system is complex, and the derivative function evaluation consumes significant computational time. Examples of these systems include nonlinear physics, such as flexible members, structural contact, fluid-structure interactions, or systems with many components numerically interrelated with ODEs and differential algebraic equations (DAEs). A practical example demonstrated that the DFSM is particularly useful was the control co-design (CCD) of a wind turbine system [153]. Since the LTISS system approximation presented in Section 5.5.2 and the LTISS system can also be directly applied to the ocean wave systems, the DFSM strategy has a potential to provide a computational benefit when utilized in the floating offshore wind turbine systems, where the dynamics of the system is a result of many interactions between various components, including a convolution integral term in the floating platform dynamics [154].

The surrogate model can be constructed with sample training points distributed in the model input domain. Since the surrogate model is utilized for approximating the dynamics, a large number of uniformly-distributed global samples is preferred for the initial sampling stage, to provide good approximation over the entire range, and to reduce the number of refinement during the surrogate-assisted dynamic simulations. Training of the surrogate model could be performed with possibly any surrogate modeling techniques. As we used the Gaussian process surrogate model (Kriging) in the study presented in Chapter 4, it is convenient to utilize the same technique for the DFSM for the LTISS approximation study.

Suppose we have a nonlinear dynamic system that has a vector function of system derivative $\dot{\underline{\xi}}_{\mathrm{d}}\left(\underline{\xi}\left(t\right), \underline{x}_p\right)$, and the surrogate model that approximates this derivative function is denoted as $\tilde{\dot{\underline{\xi}}}_{\mathrm{d}}\left(\underline{\xi}\left(t\right), \underline{x}_p\right)$. Since the dynamic system is nonlinear, Eq. (5.38a) cannot be expressed in the form of Eq. (5.38b); instead, we need to use the derivative function in the dynamic system formulation, given as:

$$\begin{bmatrix} \underline{\xi}_{\mathrm{d}} \\ \underline{\xi}_{\mathrm{c}} \end{bmatrix}^{k+1} = \begin{bmatrix} \underline{\xi}_{\mathrm{d}} \\ \underline{\xi}_{\mathrm{c}} \end{bmatrix}^{k} + \int_{t^k}^{t^{k+1}} \begin{bmatrix} \dot{\underline{\xi}}_{\mathrm{d}}\left(\underline{\xi}_{\mathrm{d}}\left(\tau\right), \mathbf{C}_{\mathrm{c}}\underline{\xi}_{\mathrm{c}}\left(\tau\right), \underline{u}_{\mathrm{d}}\left(\tau\right), \underline{x}_p\right) \\ \mathbf{A}_{\mathrm{c}}\underline{\xi}_{\mathrm{c}}\left(\tau\right) + \mathbf{B}_{\mathrm{c}}\dot{\gamma}_{\mathrm{d}}\left(\tau\right) \end{bmatrix} d\tau. \tag{5.43}$$

Since the convolution integral part (denoted as subscript ‘c’) became linear and cheap to solve, the derivative function of the dynamic part (denoted as subscript ‘d’) needs to be approximated with the surrogate model $\underline{\xi}_{\mathrm{d}} \approx \tilde{\underline{\xi}}_{\mathrm{d}}\left(\underline{\xi}_{\mathrm{d}}, \underline{\xi}_{\mathrm{c}}, \underline{u}_{\mathrm{d}}, \underline{x}_p\right)$.

One observation here is that the surrogate model input dimension could be very high if the numbers of states and control input are high. The surrogate model needs to be trained by a significantly large number of training sample points due to the ‘curse of dimensionality’. Therefore, this method can only be efficient for a problem with the expensive derivative function, rather than a large-scale dynamic system.

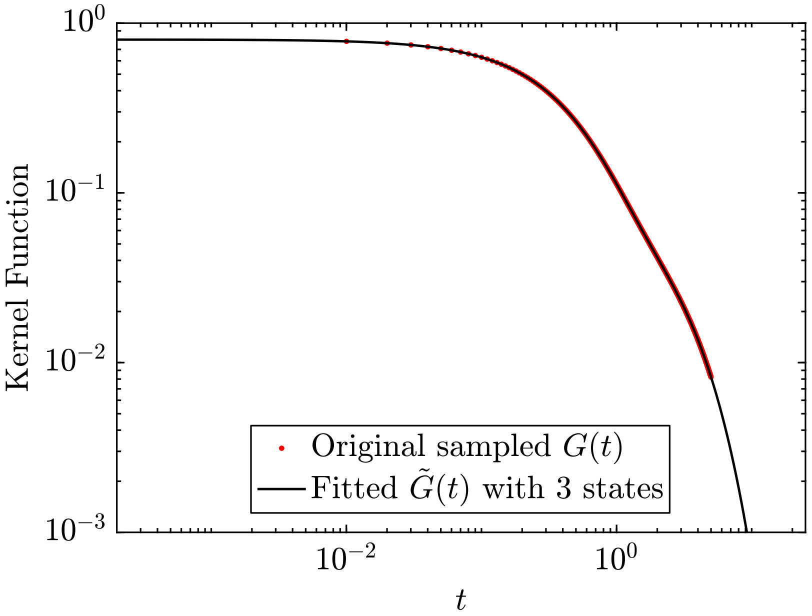

Figure 5.1: Relaxation modulus functions (kernel function) originally created by the analytical equation and fitted using the LTISS are compared.

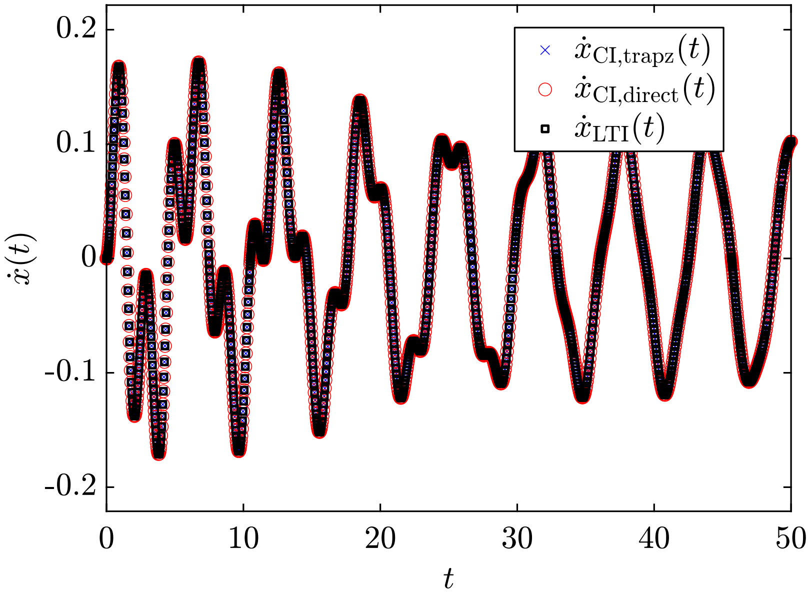

Figure 5.2: Simple simulation to obtain the stress with the sinusoidal strain rate input to the viscoelastic element. Since simulation started from a rest state, the initial transient shows unsteady behavior before it reaches steady periodic response.

5.6 Practical Examples

5.6.1 Simple Demonstration of State-Space Approximation of Linear Viscoelasticity

The study presented in this section aims to demonstrate an LTISS system approximation of the VE relaxation modulus function, and to utilize the obtained approximated system for simulation. First, a three-mode Maxwell model with following parameter values is fitted using the LTISS system approximation method with Prony basis functions: $G_1 = 0.5$, $\lambda_1 = 1/3$, $G_2 = 0.2$, $\lambda_2 = 1/2$, $G_3 = 0.1$, $\lambda_3 = 2$. The obtained LTISS is:

$$\mathbf{A} = \begin{bmatrix} -0.5 & 0.0 & 0.0 \\ 0.0 & -3.0 & 0.0 \\ 0.0 & 0.0 & -2.0 \end{bmatrix}, \mathbf{B} = \begin{bmatrix} -0.3162 \\ 0.7071 \\ -0.4472 \end{bmatrix}, \mathbf{C} = \begin{bmatrix} -0.3162 & 0.7071 & -0.4472 \end{bmatrix}. \quad (5.44)$$

With these three additional states, the computational time required for obtaining this LTISS result was 4.24 [s], and this is the most time-consuming part in the LTISS system approximation for the linear viscoelasticity. Once the fitting is completed, the use of the obtained LTISS system approximation is a computationally efficient part. Figure 5.1 shows the original material function $G(t)$ and the fitted function $\tilde{G}\,(t)$ in the logarithmic scale plot. The pattern search method was used for fitting the function by minimizing the sum of least square errors until the optimality condition reached nearly machine precision.

Figure 5.2 illustrates the simulation results obtained from three different methods: (1) trapezoidal quadrature using the direct integration, (2) more sophisticated adaptive numerical quadrature performed with absolute tolerance criteria of 10^{-6} level using the MATLAB `integral` function, and (3) linear system of equations with three additional states fitted using the LTISS system approximation. Although fitting takes some time, the simulation using the LTI system is computationally very efficient. The LTISS system required only 0.16 [s] to solve the entire simulation, while the trapezoidal quadrature required 5.72 [s] with the direct integration of the convolution integral. The most accurate, sophisticated numerical quadrature method required 72.3 [s] for computing the same simulation. However, all numerical methods exhibited essentially identical simulation results. Notably, the LTISS system approximation produces an accurate solution with only three additional states.

5.6.2 Strain-Actuated Solar Arrays for Spacecraft Attitude Control Assisted By Viscoelastic Damping

The study presented in this section aims to utilize passive viscoelastic damping to reduce control system complexity for strain-actuated solar array (SASA) spacecraft attitude control systems (ACSs). SASA utilizes high-frequency distributed actuation to actively control jitter reduction. Relying on active damping alone, however, requires significant control system complexity, which has so far limited adoption of intelligent structures in spacecraft control systems. Here, we seek to understand how to modify passive system design in strategic ways to reduce control system complexity using the LVE elements. A detailed problem definition with a comprehensive explanation can be found in Lee et al. [14].

In this study, we use direct integration method 1 with the time-domain truncation technique for more efficient computation. Rotational viscoelastic damping joints are modeled with (1) two-dimensional shear stress-strain model (high-fidelity) and (2) one-dimensional reduced-order model (low-fidelity). The high-fidelity model computes a transient rotational shear flow equation derived from a full 3D Cauchy momentum equation. Because of the numerical stability governed by the Courant-Friedrichs-Lewy (CFL) condition, the time step size we used in this study was significantly small, resulting in the optimal control problem being computationally expensive. Thus, we tested the time-domain truncation technique here to solve the problem in a practical amount of time with limited computing resources.

Optimal Maxwell model material function parameters for the two-dimensional axisymmet-

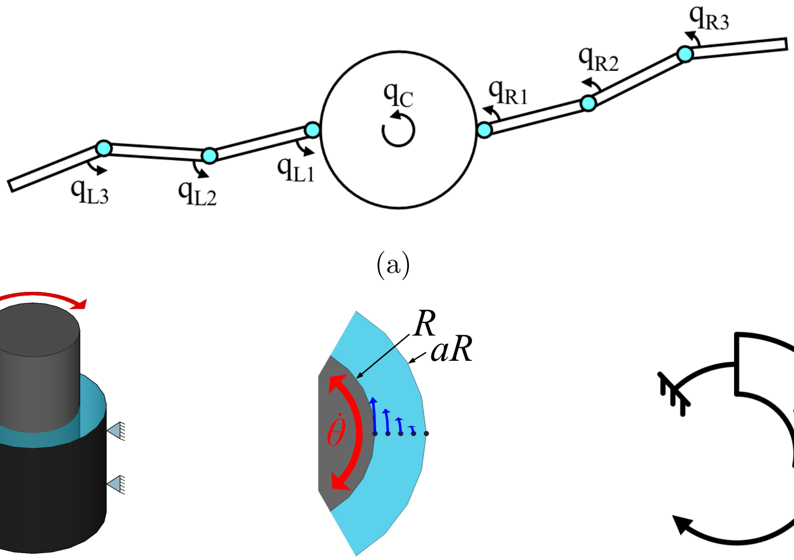

(a)

(b) (c) (d)

Figure 5.3: Spacecraft numerical model and revolute damping joints with 2D shear stress-strain and 1D reduced-order models. (a) Full 2D spacecraft model with two solar panels using a n-revolute-joint pseudo-rigid-body dynamic model (nR-PRBDM). (b) Conceptual design of viscoelastic revolute joint damper. (c) 2D shear stress-strain fluid model of viscoelastic revolute joint damper. (d) 1D reduced-order model of viscoelastic revolute joint damper.

ric model case are $G_0^* = 0.943$ [MPa] and $\lambda_0^* = 1.36 \times 10^{-3}$ [s]. We anticipate these results to be close to planned experimental data due to the fairly realistic model. The optimal control design exhibits some higher-frequency oscillations to mitigate vibrations due to viscoelastic material memory effects.

Optimal Maxwell model material function parameters for one-dimensional reduced-order model case are $G_0^* = 1.09$ [MPa] and $\lambda_0^* = 8.69 \times 10^{-4}$ [s], corresponding to a larger initial stress and smaller relaxation time compared to the 2D axisymmetric model results. Control trajectories do resemble those from the 2D model study, but with less pronounced oscillations. The computational time required to solve for this model is significantly smaller (13 minutes compared to 4 hours) with an Intel Xeon Gold 32-core CPU. This reduction in computational expense would enable more extensive design studies, such as a longer time horizons for multi-stage maneuvers. While control trajectories are sufficiently close to inform later design activities, the difference between Maxwell model parameters is not small, corresponding to

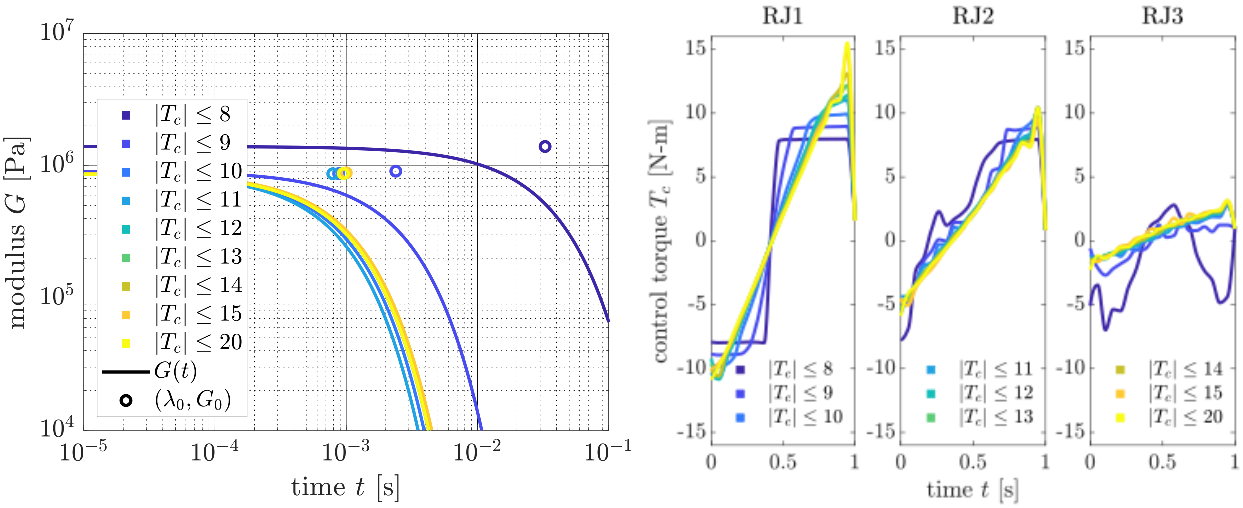

(a)

(b)

Figure 5.4: Optimal designs based on the 1D reduced-order models with varying maximum control torque constraints. (a) Material function designs. (b) Corresponding control torque designs.

distinct materials.

In both models, displacement trajectories satisfy the final time boundary condition with a maximum constraint violation in the order of 10^{-8} or smaller. Using these results, the original paper studied how the control system limits affect the viscoelastic damping design changes, as shown in Fig. 5.4. When control system capability is limited, the optimal material functions change to incorporate longer and stronger relaxation characteristics. Readers are referred to Lee et al. [14] for detailed optimal solution data with discussions.

5.7 Conclusions

Various numerical methods are explored for simulating viscoelasticity, and potentially for the use with integrated material system design. One-dimensional stress-strain relation with the Boltzmann relaxation modulus function was analyzed. Then we evaluated the rheological concepts that appeared in the context of LVE materials, and most importantly, evaluated regarding the IDE with convolution integral terms, from the perspective of simulation-based material system design.

Several different numerical approaches for integrating the convolution term were discussed. The most popular frequency-based method is briefly explained. This method is especially useful with material characterization, since many rheological measurements are performed using a frequency sweep of oscillatory loading conditions. However, from an integrated material and dynamic system design perspective, frequency-based methods cannot predict actual system behavior with the non-periodic transient inputs. Thus, we continue exploring time-domain integration methods.

A direct time-domain numerical solution of convolution integral is very costly. Since the material behavior depends on the entire previous stress-strain history, using this direct integration in the simulation is expensive, and sometimes impractical to use in design optimization. However, several variant integration methods are widely used. The most primitive numerical integration of the convolution term exhibits $O\left(n^2\right)$ computational time complexity. An improved direct integration method is also explained, which exhibits $O\left(n \log n\right)$ time complexity. A time-domain truncation method was also introduced to further reduce the computational time for direct integration methods.

Most importantly, the LTISS system approximation is introduced and demonstrated to approximate the response of the convolution integral with a few additional state variables. Construction of an appropriate LTISS for solving LVE in the time-domain significantly reduces the computational time of dynamic simulation, which had been a critical barrier for the use of LVE materials in engineering design. While maintaining or controlling the model accuracy by determining the optimal number of added states, the LTISS representation gives the LVE behavior in time-domain without directly computing the costly convolution integral term. Also, this advantage is not limited to LVE material models. LTISS could also be implemented for a wider range of material models that have intrinsic hereditary effects, which are expressed by a convolution integral term.

Possible applicability of the DFSM is also discussed. With dynamic systems that have expensive derivative functions, DFSM could be applied along with the LTISS system approximation. The integrated DFSM and LTISS system approximation utilize the Markov characteristic of the approximated convolution integral term, and could provide a benefit to specific types of design problems.

From the design perspective, none of the LTISS parameters, except for material function parameters of a few models, can be directly designed. For example, manipulating material function shape, manipulating matrix elements of the LTISS approximated model, or even manipulating parameters of the material functions do not guarantee that the resultant material characteristics are physically-realizable. Future study needs to address this issue for design engineers to freely explore and utilize the largely untapped potential of rheologically-complex materials in design of dynamic engineering systems.

Chapter 6

Continuous Relaxation Spectra Description for Design With Linear Viscoelasticity[1,2,3]

6.1 Summary

Designing *with* and *of* rheologically-complex materials introduces an added difficulty due to its complex nature. These difficulties include (1) material system parameters that are not independently controllable but correlated to each other, (2) computationally expensive nature in the numerical analysis of material behaviors with hysteresis, and (3) non-trivial design parameterizations for function-valued material characteristics, which depend on a timescale (linear viscoelasticity), an amplitude (nonlinear material behavior) or often both (nonlinear viscoelasticity). This study focuses on material descriptions and representations that are conveniently used for engineering design, especially for linear viscoelastic (LVE) materials, which involve function-valued material properties that can depend on a timescale.

Engineering system design with LVE materials requires a material description with parameters that are simple and uniquely represent material characteristics. Here, a mathematical framework for the continuous relaxation spectra representation is introduced. The continuous relaxation spectrum $H(\tau)$ is demonstrated to be a design-appropriate and independently-controllable material representation for linear viscoelasticity. Using continuous relaxation

---

[1] Part of the content reported in this chapter is reprinted by permission from ASME (Lee, Corman, Ewoldt, and Allison. A multiobjective adaptive surrogate modeling-based optimization framework using efficient sampling strategies. In *Proc. ASME IDETC/CIE*, DETC2017-67541, Cleveland, OH), ©2017.

[2] Part of the content reported in this chapter is presented in (Lee, Corman, Ewoldt, and Allison. Continuous relaxation spectra and its reduced-dimensionality descriptions for engineering design with linear viscoelasticity. In *ASME IMECE*, IMECE2019-13370, Salt Lake City, UT), ©2019 by the authors.

[3] Mr. Yong Hoon Lee focused on numerical modeling of material models, mathematical conversion between design representations, and design optimization aspects, while Dr. Rebecca E. Corman focused on developing material descriptions and representations.

spectra in design offers the benefit of intrinsically limiting material design candidates to physically meaningful options. Next, we use a reduced-dimensionality description of the continuous relaxation spectra representation based on the integral moments. This representation helps designers interpret material design results, providing valuable information for the material selection problem.

To demonstrate how these concepts can be used in engineering system design, we solve simple test cases of design optimization problems using the continuous relaxation spectra representation and the quarter car suspension design problem. Also, we analyze the design results using the reduced-dimensionality material description. The design-appropriate material description and the reduced-dimensionality LVE material interpretation supports enhanced intuition for designing with LVE materials, which has an advantage on drawing physical interpretations from the results and may help expand the appropriate use of these materials in engineering design.

6.2 Introduction

Designing materials (and possibly the synthesis of new materials as a result of the design) opens an avenue to unprecedented design innovations. Rheologically-complex materials, including soft solids and viscoelastic (VE) fluids, offer a material behavior beyond the capabilities of simple hard materials and Newtonian fluids widely used in general engineering systems design. However, we see that designing with these complex materials has various associated challenges, mainly because the material properties are functions of other quantities rather than constants (e.g., time-dependent, frequency-dependent, and shear-rate-dependent properties). The potential benefit of using linear or nonlinear viscoelasticity in various engineered systems has been widely demonstrated [127, 155–158]. However, due to the difficulties described above, many design activities with these complex materials still rely on empirical observations and intuition rather than on rigorous processes of obtaining tailored optimal material designs.

Previous work performed by Corman et al. [12] has demonstrated a framework for incorporating linear viscoelastic (LVE) materials in early-stage engineering design. This work focused on a discrete Prony-series VE model (generalized Maxwell model) for designing vibration damping and isolating systems with linear viscoelasticity. Here, we extend our design representation of linear viscoelasticity with the stress relaxation spectrum, which imposes material formulation constraints that implicitly ensure more realistic and achievable material rheology targets, focusing the search on physically-realizable materials design targets.

In this study, we explain the characteristics of a material description enhances its value for design studies. Using these necessary characteristics, we present a design-appropriate material description, the continuous stress relaxation spectrum, for linear viscoelasticity. Using the multiobjective adaptive surrogate model-based optimization (MO-ASMO) algorithm presented in Chapter 4 and in Lee et al. [67], we solve a multiobjective optimization test problem involving the design of a quarter car suspension with a viscoelastic damper (VED) element, previously formulated as a benchmark problem of the MO-ASMO algorithm, but with the continuous stress relaxation spectra design representation. We also explain how these function-valued material properties could be characterized by simple and intuitive parameters. We use a reduced-dimensionality description for the LVE materials [132, 159]. Design solutions of LVE materials are plotted in an Ashby-style cross-property plot in this reduced-dimensionality framework, aiding interpretation and communication of the optimal materials design results in an intuitive and informative visualization.

6.3 Methods

6.3.1 Design-Appropriate Material Descriptions

Rheologically-complex materials can be described with various function-valued characteristic properties (denoted hereafter as a *material function*), which describe the material behaviors or

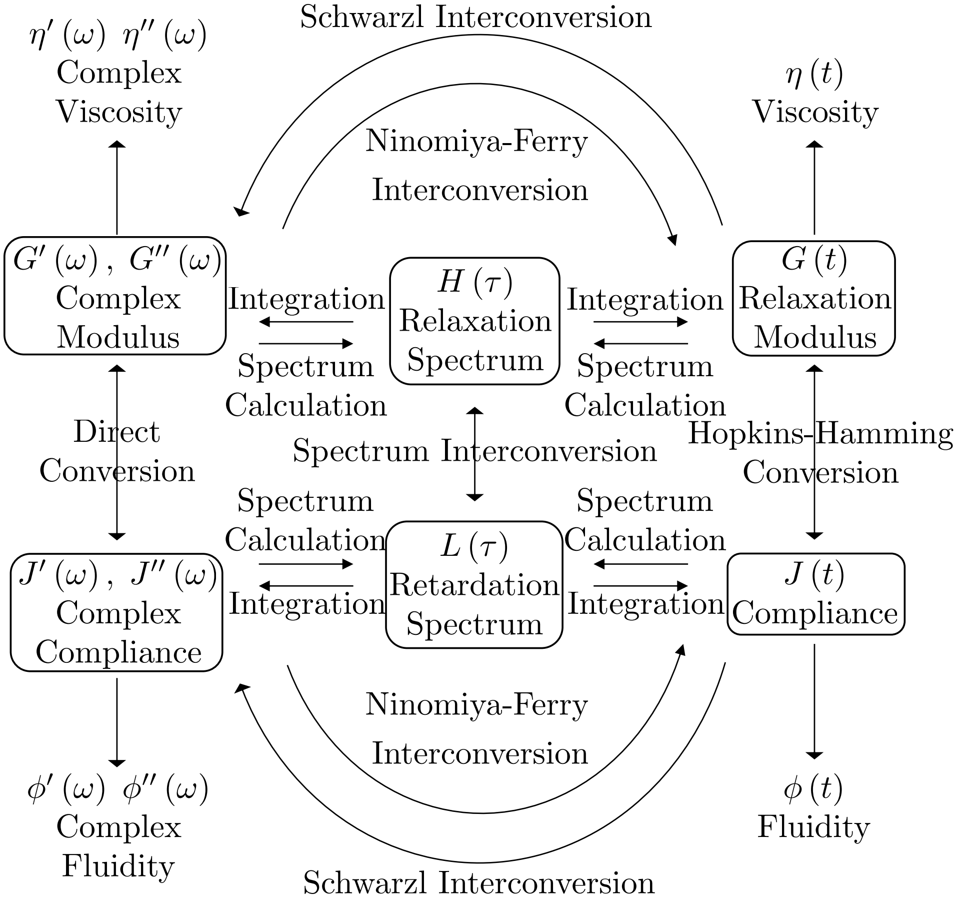

Figure 6.1: All LVE material functions are related to each other in the limit of LVE regime. The figure is adapted from Corman [159] and Ferry [160] and presented with modifications.

responses to the external input. Some quantities can be experimentally measured, and others can be derived from quantities measured from experiments. Material constitutive models describe how these material functions interact with the mechanical governing equations of materials or systems. For example, with simple linear elastic materials, Young's modulus is a constant-valued material property that can be used to describe the material's intrinsic characteristics. Hooke's law describes the connection between Young's modulus of the material and the stress-strain response. However, for the complex materials, this relationship is not obvious as Hooke's law or Navier-Stokes equation we see in simple elastic solids or Newtonian fluids. For incompressible LVE materials, various equivalent representations exist, including stress relaxation modulus $G(\tau)$, creep compliance $J(\tau)$, complex modulus $G', G''(\omega)$, and others (see Fig. 6.1) which are inter-related, and that convey all necessary information to describe the material behavior. Note, however, these representations are not equal and not all appropriate for use in design.

Corman et al. [12] outlined key criteria for parameters that are appropriate for designing materials. These key criteria are summarized as (1) the material properties used in design should be independently controllable; (2) the material properties should lead to mathematically tractable equations to model the motion response of the system; (3) the material properties should connect to physical microstructural mechanisms and information for use in the later stage of design.

First, material properties that are not independently controllable are not favorable for use as design variables. For example, the dynamic moduli G' and G'' are mathematically related to each other through Kramers-Kroenig relation [112], given as:

$$G'\left(\omega\right) = \frac{2\omega^2}{\pi}\int_0^\infty \frac{G''\left(s\right)/s}{\omega^2 - s^2}ds; \quad G''\left(\omega\right) = \frac{2\omega}{\pi}\int_0^\infty \frac{G'\left(s\right)}{s^2 - \omega^2}ds, \tag{6.1}$$

and cannot be independently designed. While the Kramers-Kroenig relation can be imposed as a nonlinear constraint for the design problem, this introduces an additional expensive design constraint that needs to be satisfied in addition to the already-expensive materials design problems. Although constraining Kramer-Kroenig relation is not a preferred method of designing systems with viscoelasticity, readers are referred to Booij and Thoone [161] for the approximations of transforms between VE quantities, including Kramers-Kroenig transform.

Second, the material function needs to be tractable with the responses of the system of interest. For example, problems with force, stress, or pressure-driven systems, the creep compliance $J(\tau)$ or the retardation spectrum $L(\tau)$ can be natural choices for describing the system governing equations. On the other hand, the deformation, deflection, or strain-driven systems, the relaxation modulus $G(\tau)$ or the relaxation spectrum $H(\tau)$ can be better choices, since these material functions lead to a simple, integral form of the system governing equations.

Third, the design-appropriate material function needs to connect its parametric quantities to the material architecture, microstructure mechanisms, and their information; thus, these quantities obtained by design processes can also be utilized for realizing the actual material in the later stage of design. For example, the area under a section of the stress relaxation spectrum $H(\tau)$ with respect to the $\ln(\tau)$ represents the intrinsic material rigidity associated with the relaxation time within the rage of timescale τ. The peak of the relaxation spectrum also corresponds to the concentrated relaxation timescale of the material. With these perspectives, the stress relaxation spectrum $H(\tau)$ is a design-appropriate material description.

Combining the three key criteria discussed above, a few material functions, including the stress relaxation modulus $G(\tau)$ and the stress relaxation spectrum $H(\tau)$ are both acceptable material descriptions for early-stage LVE design with displacement, deformation, or strain-controlled loading scenarios. Specifically, the spectrum $H(\tau)$ has advantages over the stress relaxation modulus $G(\tau)$, including the ability to provide information for the later design-stage material and the intrinsically constraining materials to physically-realizable options, we focus on the relaxation spectra design representation further in this study.

6.3.2 Relaxation Spectrum Representation

The relaxation modulus $G(\tau)$ is one of the most general and popular representations for describing a material's intrinsic stress relaxation characteristic in the time domain. In the spectrum domain, the material function represents multiple stress relaxation characteristics with a finite or an infinite range of timescale spectrum. The conversion between the stress relaxation modulus and spectrum can be given with the definition of commonly-used relaxation spectrum, given as:

$$G(t) = \int_0^\infty \frac{H(\tau)}{\tau} e^{-t/\tau} d\tau = \int_0^\infty H(\tau) e^{-t/\tau} d\ln\tau, \tag{6.2}$$

Table 6.1: Select list of continuous spectra model parameterizations, taken from Tschoegl [128], Martinetti et al. [129], Wiechert [130], Martinetti [162], Stankiewicz [163], Baumgaertel et al. [164], Baumgaertel and Winter [131], Winter [165], Winter and Chambon [166]. Shapes are shown in Fig. 6.2. Refer to Corman [159, p. 94] for extensive list of continuous relaxation spectrum models.

	Form	n_p	Refs.
Log-Normal Basis	$H(\tau) = H_\mathrm{max}\exp[-\frac{1}{2}\frac{\ln\tau}{\tau_\mathrm{max}\sigma}]$	3	[128–130]
Fractional Maxwell	$H(\tau) = \frac{G_\mathrm{FM}}{\pi}\tau^{-\alpha}\frac{\sin(\pi\alpha)+\tau^{\beta-\alpha}\sin(\pi\beta)}{1+2\tau^{\beta-\alpha}\cos(\pi(\beta-\alpha))+\tau^{2(\beta-\alpha)}}$	3	[162, 163]
BSW	$H(\tau) = \begin{cases} n_e G_N^0[(\frac{\tau}{\lambda_c})^{-n_g} + (\frac{\tau}{\lambda_\mathrm{max}})^{n_e}] & \text{if } \tau \leq \lambda_\mathrm{max} \\ 0 & \text{if } \tau > \lambda_\mathrm{max} \end{cases}$	5	[164]
Modified BSW	$H(\tau) = \left[H_g(\frac{\tau}{\lambda_c})^{-n_g} + n_e G_N^0(\frac{\tau}{\lambda_\mathrm{max}})^{n_e}\right]\exp[-(\frac{\tau}{\lambda_\mathrm{max}})^{\beta}]$ where $H_g = n_e G_N^0(\frac{\lambda_1}{\lambda_c})^{n_g}(\frac{\lambda_1}{\lambda_\mathrm{max}})^{n_e},\ \lambda_c < \lambda_1 < \lambda_\mathrm{max}$	6	[131]
Asymmetric Lorentz	$H(\tau) = H_\mathrm{max}\frac{r+r'}{r'(t_\mathrm{max}/t)^{\rho r}+r(t/t_\mathrm{max})^{\rho r'}}$ where $r = (n/n')^{1/(1+n/n')},\ r' = (n'/n)^{1/(1+n'/n)}$	5	[128]
Critical Gel	$H(\tau) = \frac{s}{\Gamma(n)}\tau^{-n},\ \lambda_0 < \tau < \infty$	2	[165, 166]

where $d\ln\tau$ is particularly convenient for interpreting the relaxation spectrum plotted on the log scale of τ. The relaxation spectrum can be either discrete or continuous. An example of converting the spectrum to the modulus is given in Fig. 6.3. A discrete spectrum can be described as a sum of multiple points in the viscosity-weighted spectrum domain, given as:

$$\hat{H}(\tau) = \sum_{i=1}^{N} \eta_i \cdot (\tau - \tau_i), \tag{6.3}$$

but this representation is equivalent to the M-mode Maxwell model, already explained in Section 4.4.2 of Chapter 4. Here, η_i is the viscosity magnitude, which is equivalent to $\tau_i G_i$ for i-th mode of Maxwell model parameters (G_i and τ_i). When the number of modes becomes infinite, the discrete relaxation spectrum becomes the viscosity-weighted continuous

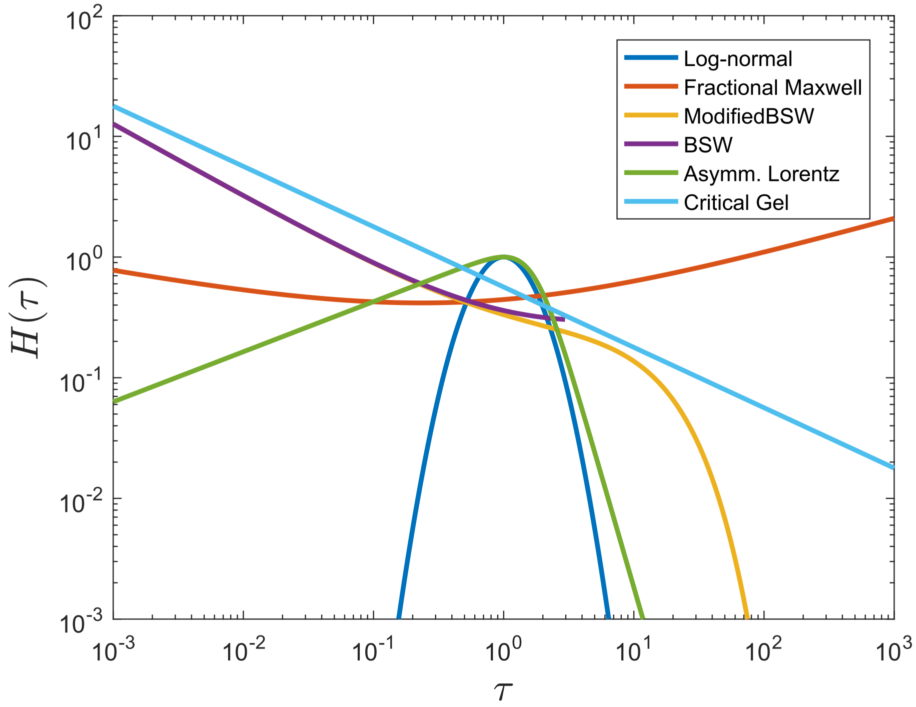

Figure 6.2: A selection of commonly used continuous spectra models (as given in Table 6.1). By using the continuous spectra representation, a whole variety of relaxation spectra can be modeled with a small number of parameters (ranging from 2 to 6 for models listed in Table 6.1).

relaxation spectrum, given as:

$$H(\tau) = \lim_{N\to\infty} \sum_{i=1}^{N} \eta_i \cdot \delta(\tau - \tau_i). \tag{6.4}$$

The shape of the continuous relaxation spectrum could theoretically be an arbitrary unconstrained continuous function. However, to limit our design space to practically realizable materials, we follow the common practice that uses certain parameterizations to represent typical behaviors of real materials [128–131, 162, 163, 167]. Examples of spectra parameterizations with their references are listed in Table 6.1. Also, select function shapes of the continuous relaxation spectra are shown in Fig. 6.2.

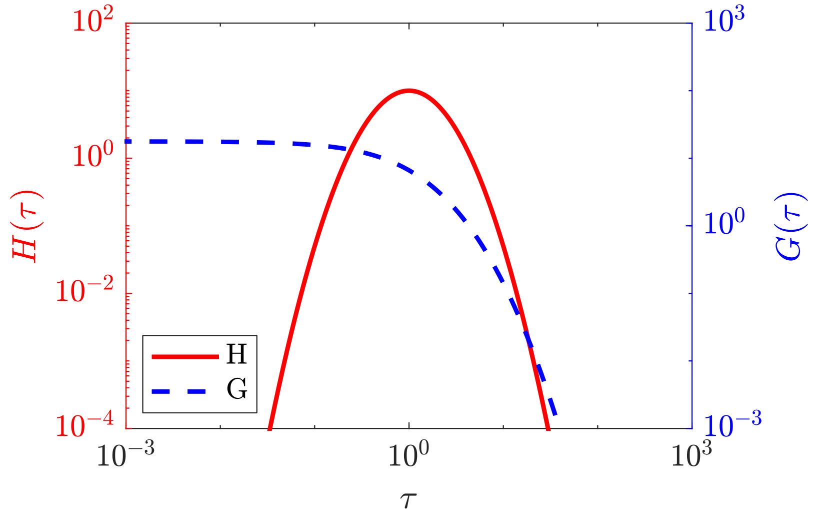

Figure 6.3: An arbitrary continuous relaxation spectrum function in log-normal distribution is converted to the corresponding relaxation modulus. See Eq. 6.2 for computing the relaxation modulus from the relaxation spectrum function.

6.3.3 Conversion Between Spectrum and Modulus

Conversion from the relaxation modulus to the relaxation spectrum is a mathematically ill-posed problem, while the opposite is straightforward [128, 168]. A small difference (error) in the relaxation modulus $G(\tau)$ results in a large difference or a deviation in the relaxation spectrum $H(\tau)$. It is natural to design with a material system with the relaxation spectrum material function or parameters, and convert the spectrum to the relaxation modulus if needed (e.g., in case the simulation demands the modulus function). However, designing with the relaxation modulus will create an added difficulty when the relaxation spectrum function or parameters need to be obtained. In addition to the perspectives described in the earlier section, the continuous relaxation spectra design representation is also favorable as a design-appropriate materials representation, because the conversion is only convenient in one way, i.e., converting from the spectrum to the modulus.

There are a few approximation methods that exist to convert from the modulus to the spectrum. First, several mathematical approximation formulations exist, including methods proposed by Alfrey and Doty [169] and by Schwarzl and Staverman [168]. Alfrey and Doty

[169] introduced an approximated conversion from the relaxation modulus function to the relaxation spectrum function, given as:

$$H(\tau) = -\left.\frac{dG(t)}{dt}\right|_{t=\tau}, \quad H(\ln\tau) = -\left.\frac{dG(t)}{d\ln\tau}\right|_{t=\tau}. \tag{6.5}$$

Schwarzl and Staverman [168] proposed utilization of direct inversion property of the Laplace transform, and the form of the approximation can be obtained, of order k, given as:

$$H(\tau) = \sum_k \left.\frac{(-1)^k}{(k-1)!}\frac{d^k G(t)}{d(\ln\tau)^k}\right|_{t=\tau}. \tag{6.6}$$

Second, an optimization algorithm can fit the relaxation spectrum function to approximate the relaxation modulus function. Since the conversion from the spectrum to the modulus is straightforward, the optimization algorithm can inversely fit the converted modulus from the spectrum to the target modulus. This process can be represented with the following optimization problem, given as:

$$\underset{H(\tau)}{\text{minimize}} \quad \int_0^\infty \left[\tilde{G}(t) - G(t)\right]^2 dt \tag{6.7a}$$

$$\text{subject to} \quad \tilde{G}(t) = \int_0^\infty H(\tau)\, e^{-t/\tau} d\ln\tau. \tag{6.7b}$$

Third, commercial software packages, such as TRIOS (TA Instrument), can aid computing approximated $H(\tau)$ from experimentally-measured complex modulus $G'(\omega)$ and $G''(\omega)$. In addition to the methods presented here, there are other approximation methods that can convert from the relaxation modulus to the relaxation spectrum, including the direct method presented by Schapery [170].

Figure 6.4 shows an example of the conversion between the relaxation modulus and the relaxation spectrum. First, a sample relaxation spectrum (denoted as the original H in Fig. 6.4a) is generated, computed the corresponding relaxation modulus using Eq. (6.2) (denoted as the original G in Fig. 6.4b). Using the computed G, several approximation

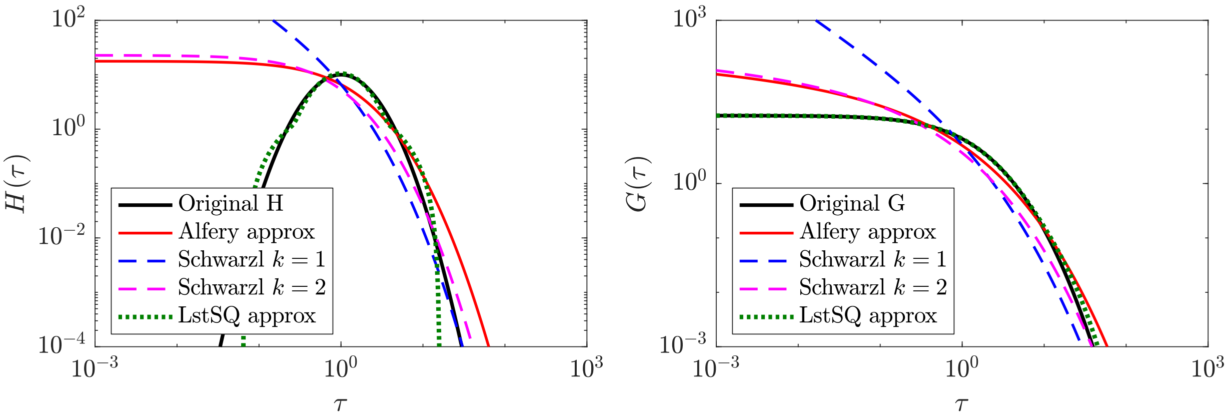

(a)

(b)

Figure 6.4: Various approximation methods for the relaxation spectrum using the relaxation modulus function is presented and compared. (a) The approximated relaxation spectra functions $H(\tau)$ are presented and compared to the reference spectrum denoted as Original H. (b) The approximated relaxation spectra functions are used to calculate the relaxation moduli functions $G(\tau)$ to compare how accurate the approximations represent the conversion.

methods are tested, including the Alfrey approximation and Schwarzl approximations with an order of 1 and 2, to obtain the relaxation spectra H in Fig. 6.4a. These approximated spectra are again tested with Eq. (6.2) to obtain the corresponding relaxation modulus G. These relaxation moduli G obtained from the approximated H are plotted in Fig. 6.4b to compare to the original G obtained with the reference H. All of the approximation methods show some deviations in the lower timescale spectra. When converted back to the relaxation modulus, these lower timescale deviations affect the lower timescale stiffness of the VE materials. However, the least squares approximation predicted the spectrum with a small error. The plot overlaps well, especially in the spectrum range where the viscous effect is significant (around $\tau \sim 10^0$). The computed response of the modulus G from the approximated H also fits well with the original G. However, due to the ill-posedness of the underlying mathematical problem, the least squares minimization algorithm is computationally expensive, rendering this conversion unfavorable for use with design optimization.

6.4 Reduced-Dimensionality Material Description

Corman and Ewoldt [132] introduced a reduced-dimensionality design representation that can present results of the VE materials design in a concise way, which can be presented in an Ashby-like cross-property plot. This reduced-dimensionality description of the VE materials is calculated directly from the integral moments of the continuous spectrum [127, 128]. The zeroth, the first, and the second-order integral moments are defined as:

$$M_0 = \int_0^\infty \frac{H(\tau)}{\tau} d\tau = G_0, \tag{6.8a}$$

$$M_1 = \int_0^\infty H(\tau)\, d\tau = \eta_0, \tag{6.8b}$$

$$M_2 = \int_0^\infty H(\tau)\, \tau d\tau = J_0 \eta_0^2, \tag{6.8c}$$

where G_0 is the plateau modulus, η_0 is the steady-state viscosity, and J_0 is the steady-state compliance. From these integral moments, additional low-dimensional descriptions of the characteristic relaxation times of the material can be calculated as:

$$\tau_1 = \frac{M_1}{M_0} = \frac{\eta_0}{G_0} = \tau_n \tag{6.9a}$$

$$\tau_2 = \frac{M_2}{M_1} = J_0 \eta_0 = \tau_\omega, \tag{6.9b}$$

where $\tau_1 = \tau_n$ is the mean relaxation time of the viscosity-weighted spectrum $H(\tau)$ and $\tau_2 = \tau_\omega$ is the mean relaxation time the modulus-weighted spectrum $Q(\tau)$ [127–129].

Here, the reduced-dimensionality descriptions of VE materials with calculated constants G_0, η_0, τ_1, and τ_2 can conveniently present key characteristics of the material relaxation behavior in a cross-property plot in an informative way, which is similar to those presented by Ashby [10, 171]. To include additional information that represents the spread of the VE relaxation times, both τ_1 and τ_2 needs to be represented on the plot, which is plotted as a line connecting two timescale points with a horizontal line. This difference in two different timescales in the logarithmic plot is directly related to the polydispersity index (PDI), given as:

$$\log(\text{PDI}) = \log(\tau_2) - \log(\tau_1) = \log\left(\frac{\tau_2}{\tau_1}\right). \tag{6.10}$$

Details of this reduced-dimensionality description are described in Corman [159] and Lee et al. [121]. The usage of this representation in the test problem can be found in Section 6.7.

6.5 Viscoelastic Material Functions

In this study, we use a few simple discrete and continuous relaxation spectra representation examples $H(\tau)$ using the (1) multimode Maxwell model, (2) Log-normal based continuous spectrum model, and the (3) modified Baumgaertel-Schausberger-Winter (BSW) continuous spectrum model. The first (multimode Maxwell) model represents the discrete spectrum-based VE representation, while the latter two (Log-normal and BSW) models represent the continuous spectra representations. A special case with $N_{\text{mode}} = 1$ for the multimode Maxwell model is distinctively called the single-mode Maxwell model, or Maxwell model, which can be mechanically represented by a single linear spring and a linear dashpot connected in series. This model has one primary relaxation time, defined as a ratio of the spring constant and viscosity, $\tau_0 = \eta_0/G_0$. The relaxation mode has viscous magnitude η_0 with units of [Pa s].

For the discrete spectrum models, many modes of strength η_i at each corresponding relaxation time τ_i can be linearly superposed. This allows complete freedom of the placement of material relaxation timescales and their respective relaxation strengths as material models from the design perspective. While some work to independently control multiple material timescales has been done [172], it is not clear how accurately many modes can be independently designed within a material, from a molecular and microstructural perspective.

On the other hand, the continuous relaxation spectra models may represent more realistic materials. Simply adding polydispersity about the prominent timescale to the Maxwell model allows the relaxation spectra representation counts for a more realistic material representation. The polydispersity spreads the relaxation characteristics over a range of timescales, making the material model follow the microstructural mechanisms that lead to the relaxation behavior (e.g., molecular weight of a polymer solution, bond energies for transient cross-links, droplet sizes for emulsions). This treatment, along with the log-normal function form for the modulus-weighted spectrum $Q(\tau)$, given as:

$$Q(\tau) = \frac{1}{\tau} H_{\max} \exp\left[-\frac{1}{2}\left(\frac{\ln \tau/\tau_{\max}}{\sigma}\right)^2\right] \tag{6.11}$$

naturally describes the relaxation behavior [128]. The viscosity-weighted equivalent is given as:

$$H(\tau) = H_{\max} \exp\left[-\frac{1}{2}\left(\frac{\ln \tau/\tau_{\max}}{\sigma}\right)^2\right]. \tag{6.12}$$

The primary timescale is represented by $\tau_{\max}$ with a viscous strength of $H_{\max}$. The smearing out of timescales around this value is given through the standard deviation, σ.

Many spectra models are proposed to impose molecular structures of the materials [173, 174] beyond simple statistical distributed spectra models, which are derived with the information of molecular geometry, length, and chain structures [175]. The BSW model [164] is one of the successful molecular structure-based models that impose the relaxation characteristics of long, linear, flexible molecules with uniform length [175].

The BSW model is a linear superposition of power laws of the glass transition and the entanglement behavior, expressed for up to certain cut off (maximum) characteristic timescale value, given as:

$$H(\tau) = \begin{cases} n_e G_N^0 [(\frac{\tau}{\lambda_c})^{-n_g} + (\frac{\tau}{\lambda_{\max}})^{n_e}] & \text{if } \tau \leq \lambda_{\max} \\ 0 & \text{if } \tau > \lambda_{\max} \end{cases}, \tag{6.13}$$

where G_N^0 is the plateau modulus, n_g and n_e are the relaxation exponents in the glass transition and entanglement regimes, respectively, λ_c is the characteristic timescale of crossover to the glass transition, and $\lambda_{\max}$ is the longest relaxation time, where the longest relaxation time is a function of the molecular weight M_w. The BSW model is valid for $M_w \gg M_c$, where M_c is the critical molecular weight.

The BSW model is then modified by Baumgaertel and Winter [131] to account for a broader range of polymers by adding an exponential cut off term at the longest relaxation time, in place of the abrupt conditional cut off. This enhanced model is called a modified BSW model, and is given as:

$$H(\tau) = \left[H_g \left(\frac{\tau}{\lambda_c} \right)^{-n_g} + n_e G_N^0 \left(\frac{\tau}{\lambda_{\max}} \right)^{n_e} \right] \exp \left[- \left(\frac{\tau}{\lambda_{\max}} \right)^{\beta} \right] \tag{6.14}$$

for $M_w \gg M_c$, where M_c is the critical molecular weight. Since the material function is continuous and differentiable for the entire range, the modified BSW model is more favorable for design, in addition to the model capability that handles the glass transition and the entanglement of long molecules, which is identical to the BSW model. Thus, we include the modified BSW model as one of our design target models for the test case presented in this chapter.

6.6 Design Problem With Linear Viscoelasticity

The quarter car suspension design problem with a VED formulated in Section 4.4.2 of Chapter 4 was expanded with more general material function descriptions, including the continuous relaxation spectra viscoelastic design representations. Figure 6.5a represents a standard quarter car suspension model with linear springs and dashpots. Using the same geometric architecture as the earlier problem with a VED, the linear dashpot between the sprung mass (m_1) and the unsprung mass (m_2) is replaced by an LVE element. Using this one-dimensional simple test problem, we can outline the mathematical framework necessary for solving the viscoelastic design problem with a relaxation spectrum description and draw

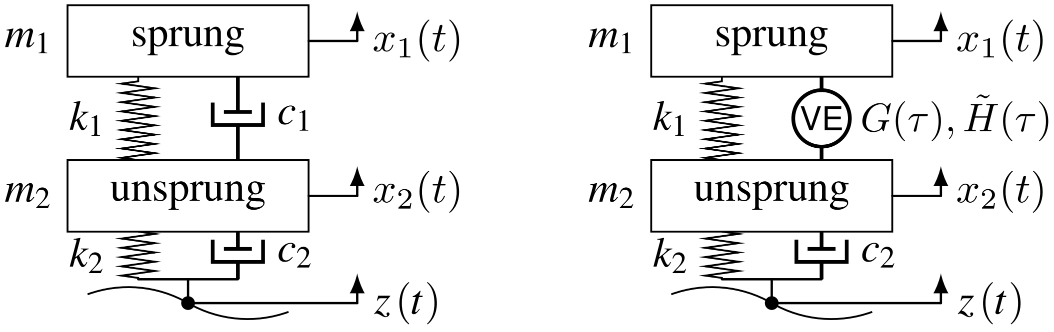

(a) (b)

Figure 6.5: The quarter car suspension model representing dynamic model of one-fourth of a car suspension design. Springs and dampers are used to control vibration transmission from the road profile $z(t)$ to the mass m_1. (a) Linear dashpot (viscous damper) is used for damping the quarter car suspension. (b) Viscoelastic element represented by continuous relaxation spectrum function $\tilde{H}$ is used in place of a linear viscous damper.

physical interpretations from the result to extract design knowledge that can be potentially extended to other design problems with viscoelasticity.

The VE element that uses a force connection (denoted as 'VE' in Fig. 6.5b) replaces the mechanical damper of the standard linear vehicle model. A detailed derivation of the VE force elements with a one-dimensional Maxwell model is described in Section 4.4.2 of Chapter 4. The time-dependent force through a one-dimensional VE element, F_{VE}, is given in Eq. (4.15). Here, we are extending the stress relaxation modulus $G(\tau)$ used in the previous chapter with the continuous relaxation spectra $H(\tau)$. Substituting Eq. (6.2) into Eq. (4.15) yields:

$$F = \int_0^\infty \left[\int_0^\infty \tilde{H}(\tau) \exp\left(-\frac{s}{\tau}\right) d(\ln \tau) \right] \dot{X}(t-s)\, ds, \tag{6.15}$$

where $\tilde{H}(\tau) = (\alpha_F/\alpha_X)H(\tau)$, α_F is a geometric mapping parameter between force and stress ($F = \alpha_F \varsigma$), α_X is a geometric mapping parameter between displacement and shear strain ($X = \alpha_X \gamma$), ς is the shear stress, and γ is the shear strain. The geometric parameters are used to formulate front factors in the governing equations to connect macroscopic system-level behaviors (e.g., force, displacement) to continuum-level behaviors (e.g., stress, strain). Details are explained in Corman [159].

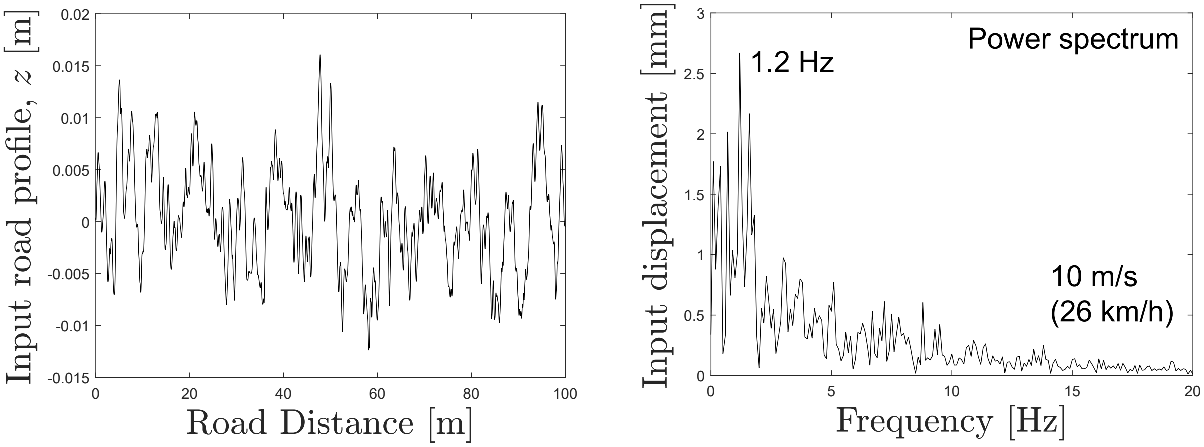

(a)

(b)

Figure 6.6: Sample input road profile used for designing the quarter car suspension. (a) Sample road profile from Allison [110], that is used to simulate road conditions for the quarter car suspension model. The vehicle model is simulated at a constant speed of 10 [m/s]. (b) The power spectrum calculated from the road profile with a vehicle speed of 10 [m/s] shows a dominant frequency at 1.2 Hz.

The dynamics of the quarter car suspension problem is also given as a matrix form of the state-space model in Eqs. (4.17)-(4.19) in Section 4.4.2 of Chapter 4. However, the matrix **C** in Eq. (4.18) contains expensive VE force elements, so the equation needs to be solved using a time-marching method. The objective functions are also described in Eqs. (4.13)-(4.14). The objective functions have the integral form of the squared quantities. The first objective function is a comfort metric, which integrates the squared quantity of the acceleration of the sprung mass. The second objective function is a handling metric, which integrates the squared difference between sprung mass displacement and road displacement. This metric tracks how much tire deflection has occurred in the entire road profile, which can be a proxy metric that represents how well the unsprung mass follows the road profile [115].

The model is subject to the following road profile adapted from Allison [110]. We used a single vehicle operating condition with velocity values of 10 [m/s] for simplicity (equivalent to 36 [kph] or 22.4 [mph]). The power spectrum presented in Fig. 6.6b illustrates that the road profile has a single dominant frequency for the given velocity value of the vehicle, which is 1.2 [Hz].

6.7 Results

The same design problem was solved with different VE material functions in the same form of the relaxation spectra formulation. Maxwell models are used in the design problem in the form of a discrete relaxation spectrum with one, two, and four modes. The log-normal and the BSW models are also used in the form of the same relaxation spectra formulation, but with continuous spectra.

The Pareto-optimal solutions, along with the evaluated points, are shown in Fig. 6.7 with linear (Figs. 6.7a and 6.7c) and log (Figs. 6.7b and 6.7d) scale plots. Figures 6.7a and 6.7b show views of the entire Pareto frontier, including achievable designs in the objective function space. Figures 6.7c and 6.7d show views of the magnified region near the anchor point that has the best values for the comfort metric. In the region near the compromise solution (a solution on the Pareto frontier that is closest to the utopia point), solutions obtained with different design representations are equivalent within a small tolerance. From this observation, all models we used in this study are representing a very similar design space, at least in the regions that optimal solutions are located. Also, we observed that there is no notable improvement by adding additional modes for the Maxwell model.

Among different design representations of the VE material functions, the BSW model exhibits difficulties in obtaining a set of smooth solutions in the region where the first objective function is minimized (obtained by giving up performance for the second objective function). Possible reasons might be due to either (1) higher design space dimension, (2) the optimization not fully converged to the true Pareto-optimal solutions, or (3) a restrictive design representation complicating an exploration of possible design candidates. However, considering that the BSW model provides rich information regarding molecular microstructure mechanisms for target material design, a choice of material function model needs to balance between numerical difficulties in design optimization and utility in the material realization stage.

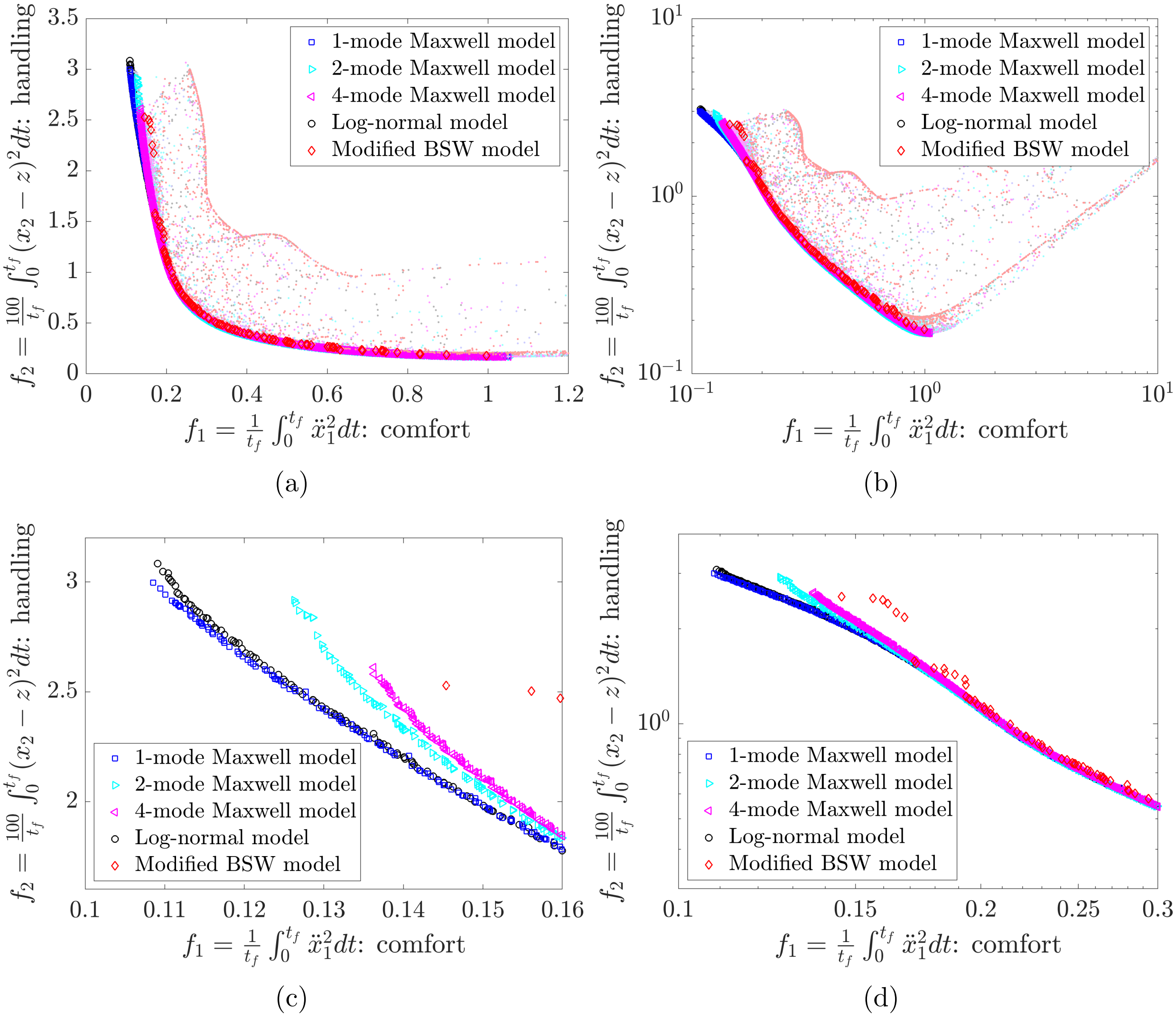

(a)

(b)

(c)

(d)

Figure 6.7: The objective function space for the quarter car suspension design problem with VED. The Pareto set (nondominated solutions) are shown as vivid color lines, while the dominated points evaluated during the design optimization process are shown as blurred, but matching, color dots. Each color represents a single material design, described by a different relaxation spectrum model. Additional modes do not improve system level performance. (a) Plotted in a linear scale plot. (b) Plotted in a log scale plot. (c) Magnified plot in a linear scale. (d) Magnified plot in a log scale.

Figure 6.8 shows the Pareto-optimal designs obtained from the multiobjective optimization performed with the multimode Maxwell model. Plot scales for different modes are equal, so the subplots except (b) can be directly compared with the locations of the markers. Characteristic VE relaxation modes are mainly located in the area where the relaxation timescale λ_i is at 10^{-3} [s] and the relaxation modulus G_i is within the range from 10^4 to

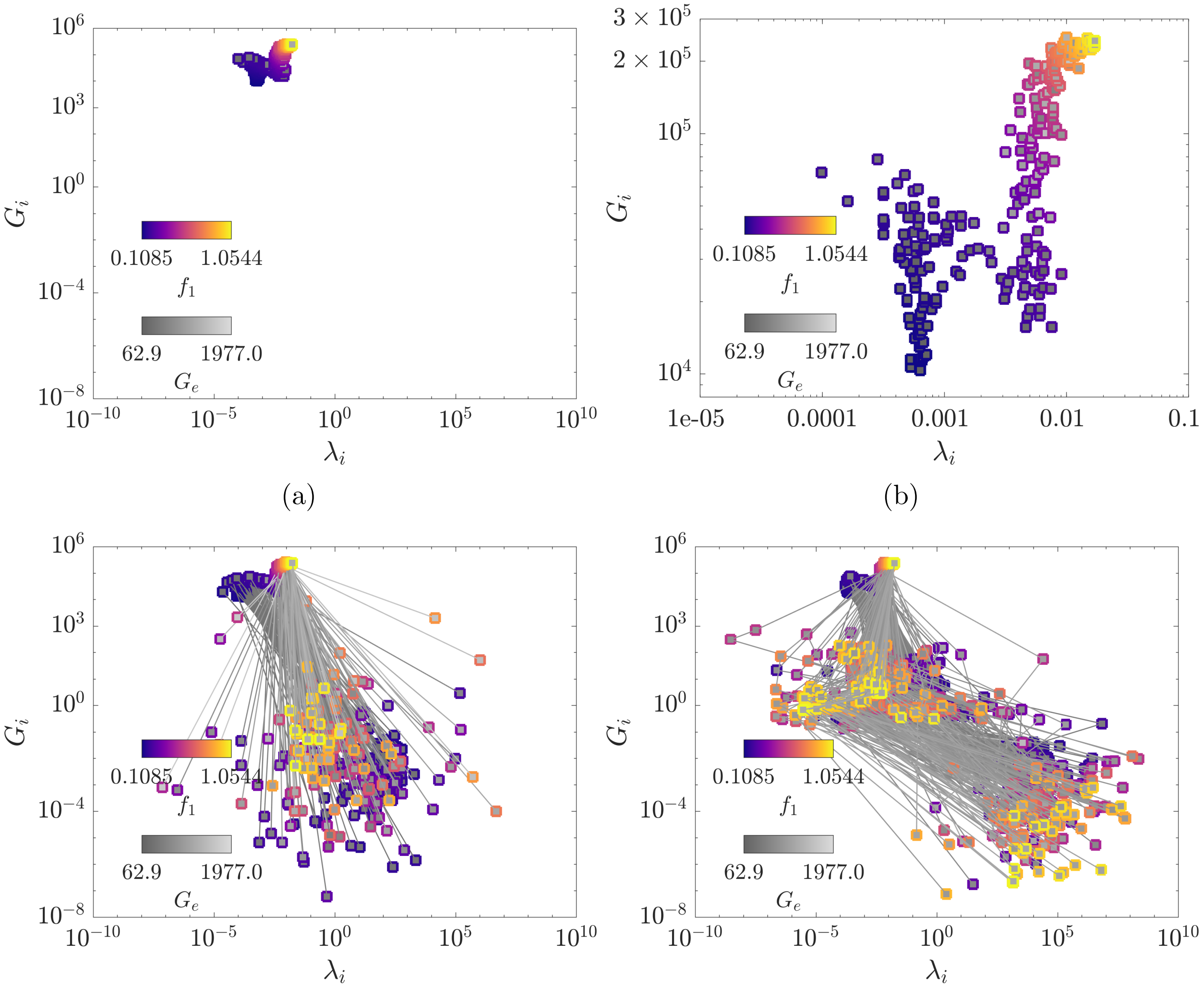

(a)

(b)

(c)

(d)

Figure 6.8: Optimal design results in the design space for the quarter car suspension with the multimode Maxwell models. Although the dimension of the design space for different numbers of modes differ, the number of variables for each mode are the same. Thus, the multimode Maxwell model can be visualized in a two-dimensional space, and the intensity of the gray scale represents the plateau relaxation modulus (G_e). (a) Design results using the single-mode Maxwell model. (b) Magnified view of the single-mode Maxwell model results. (c) Design results using the 2-mode Maxwell model. (d) Design results using the 4-mode Maxwell model.

10^6 [Pa]. The models with two and four modes do result in minor VE relaxation modes, but the values of these minor moduli are orders of magnitude less than the major moduli. However, as we see in Fig. 6.8d, the optimal designs mostly have a similar trend that the first mode is located within $G_1 \sim O\left(10^5\right)$ and $\lambda_1 \sim O\left(10^{-3}\right)$, the mid-range modes are

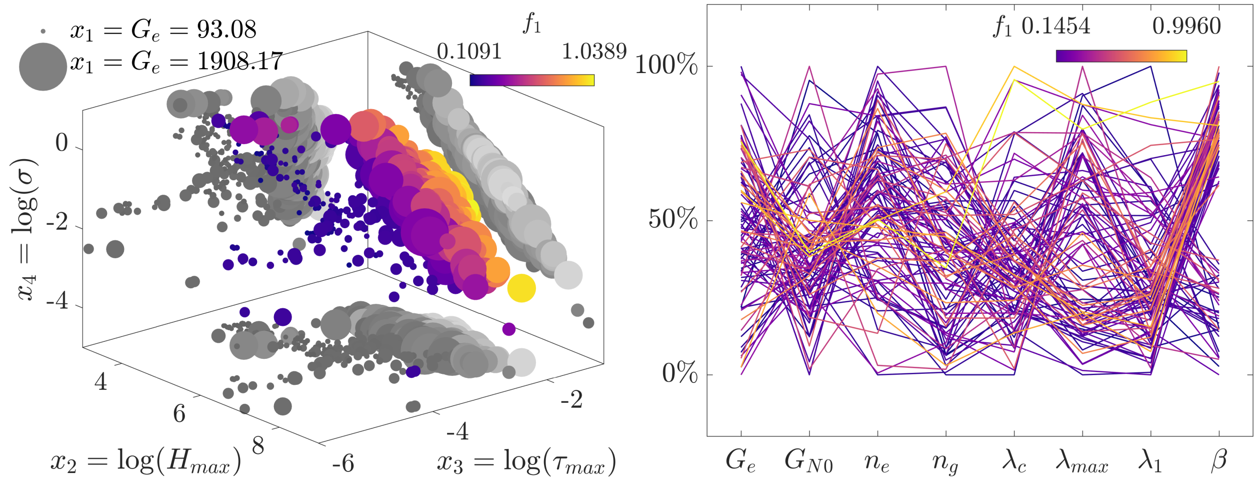

(a) (b)

Figure 6.9: Optimal design results in design space for the quarter car suspension with the log-normal and the BSW models. Both models have more than three design variables, which make it difficult to visualize the design candidates in an intuitive way. (a) Design results using the log-normal distribution model. (b) Design results using the BSW model with variable ranges: $213.8 \leq G_e \leq 1914.6[Pa]$, $0.289 \leq \log(G_{N0}) \leq 8.78$, $0.363 \leq n_e \leq 4.757$, $0.361 \leq n_g \leq 3.815$, $-8.130 \leq \log(\lambda_c) \leq 3.158$, $-4.439 \leq \log(\lambda_{\max}) \leq 10.000$, $-5.948 \leq \log(\lambda_1) \leq 5.309$, and $-1.925 \leq \log(\beta) \leq 0.946$.

located within $G_{2,3} \sim O(10^0)$ and $\lambda_{2,3} \sim O(10^{-7} - 10^3)$, and the last mode is located within $G_4 \sim O(10^{-2} - 10^{-7})$ and $\lambda_4 \sim O(10^2 - 10^6)$. This means that the problem's dynamic characteristics derives the most benefit from the first mode at around a timescale of 10^{-3} [s], while small supplementary damping at a wide range of timescales is also helpful to improve the system objectives. As a summary, it is clear that a single relaxation mode may be enough to achieve optimal system performance for this problem. However, in many cases, having single relaxation mode is unlikely achievable with real material systems. More likely, a material will exhibit some dispersity in relaxation time, which might be represented better with continuous relaxation spectra models, such as the log-normal or the BSW models.

Unlike multimode Maxwell models presented above, there exist some difficulties visualizing material functions with many parameters. Figure 6.9 shows the Pareto-optimal solutions obtained from the quarter car suspension design problem, with the log-normal distribution model (Fig. 6.9a) and the BSW model (Fig. 6.9b). The log-normal distribution model involves four design variables, including the plateau modulus (G_e), and BSW model involves eight design variables, with the plateau modulus and the cut off timescale β. Due to its high dimensionality, location of a design point in the design space hypercube requires visualization methods other than a Cartesian plot, such as a scatter plot with size and color markers for up to five dimensions, as shown in Fig. 6.9a, or parallel coordinates, as shown in Fig. 6.9b. We still see trends in these models as well. However, a preferred visualization of material design should represent the characteristics of the material design solution, rather than just showing optimal parameter values.

Figure 6.10 shows the Ashby-style reduced-dimensionality representation of the VE material proposed by Corman and Ewoldt [132]. This design representation transforms the continuous relaxation spectrum back into discrete data, which can be considered as a simplified version of the relaxation spectrum. Thus, this lower dimensionality representation cannot be restored to give full material information as is present with higher dimensionality continuous relaxation spectra representations. However, this plot conveys important material information that is critical to realize material design and synthesis. Also, this cross-property plot gives the designer resources intuitively obtain necessary information from the design solution to match the real material design.

Each plot shows the Pareto-optimal solutions obtained from the quarter car suspension design problem with a VED with different material function models. Here, we compare the results using the log-normal distribution (Fig. 6.10a), single-mode Maxwell model (Fig. 6.10b), and multimode Maxwell models (Figs. 6.10c, and 6.10d). The dotted vertical line shows the characteristic forcing frequency of the road profile used in the suspension dynamic simulation. All Pareto-optimal solutions have lower relaxation time from the perspective of the viscosity-weighted spectrum, which results in a small target Deborah number De for optimal behavior (De$<$ 1), allowing for a more viscous-like response of the VED element. The VED designs with better comfort performance (points with darker color saturation) have more fluid-like characteristics, while the designs with better handling performance (points

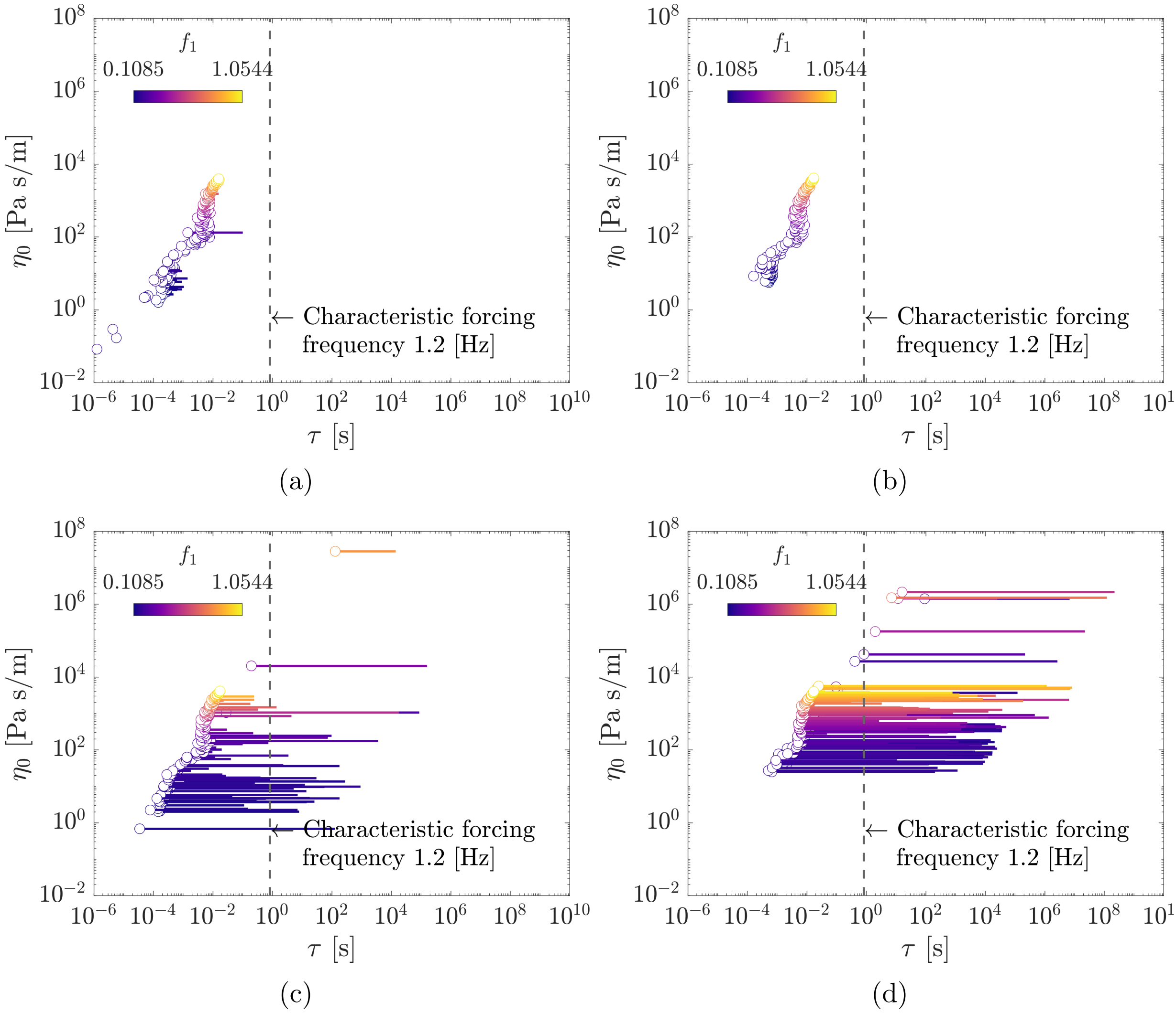

Figure 6.10: Viscoelastic material functions are reduced to three characteristic quantities: steady-state viscosity η_0, mean relaxation time of the viscosity-weighted spectrum τ_1, and mean relaxation time of the modulus-weighted spectrum τ_2, and are plotted in the Ashby-style cross-property plot. (a) Material design solutions using the log-normal distribution model. (b) Material design solutions using the single-mode Maxwell model. (c) Material design solutions using the two-mode Maxwell model. (d) Material design solutions using the four-mode Maxwell model.

with lighter color saturation) are closer to the characteristic forcing frequency, and have less fluid-like characteristics. These results align with standard vehicle design principles that harder suspensions perform better for handling with sacrifice in comfort.

6.8 Conclusion

In this work, our previous design study [67] with LVE with discrete relaxation modes is extended with continuous relaxation spectra design representations. The continuous relaxation spectra framework better represents real material systems for viscoelastic relaxation behavior, and provides various independently-controllable parameterizations that can connect with the molecular microstructure or information of the materials. Using these parameterizations, ranges of relaxation behavior can be captured and modeled without requiring a large number of design variables. Thus, the continuous relaxation spectra representation can be useful for material system design with viscoelasticity, as the model satisfies all three key criteria for design-appropriate models outlined by Corman et al. [12].

Also, we demonstrated the use of the continuous relaxation spectra using a simple quarter car suspension design problem with a VED element in place of a conventional linear dashpot. Using this demonstration problem, we obtained Pareto-optimal solutions with different material function models along with the continuous relaxation spectra representation. The objectives of this multiobjective optimization problem (MOP) are (1) enhancing comfort by minimizing sprung mass acceleration and (2) enhancing handling by minimizing the deviation of unsprung mass from the road profile. The optimal material design solutions are compared with the characteristic forcing frequency of the road profile and analyzed to interpret the physical meanings of the design solutions.

Using an Ashby-style reduced-dimensionality viscoelastic material design representation proposed by Corman and Ewoldt [132], the Pareto-optimal solutions are plotted in an intuitive cross-property plot space, and this visualization can aid in communicating the material information for design.

Most material models are designed for representing existing and synthesized materials that are already or to be characterized. However, not many material models are ready for use with materials design; we see many gaps in formulating design-appropriate material models.

Future work needs to be conducted in various areas to extend this study, including, but not limited to: (1) finding frameworks similar to the continuous relaxation spectra that can model realistic material behaviors, such as normal stress differences, thixotropy, shear thinning, and other nonlinear material responses; (2) how design methodologies can provide material design constraints to ensure material realizability, even if these constraints are difficult to formulate; and (3) handling and representing multiple spectrum peaks with the reduced-dimensionality material design representation.

Chapter 7

Simultaneous Design of Non-Newtonian Lubricant and Surface Texture Using Surrogate-Based Multiobjective Optimization[1]

7.1 Summary

Surface textures decrease friction in lubricated sliding with Newtonian fluids. Viscoelastic non-Newtonian lubricants can enhance frictional performance, but the optimal rheological material properties and their coupling to the texture design are non-obvious. In this study, we present a simultaneous design of both surface texture shape and non-Newtonian properties, which can be achieved by fluid additives that introduce viscoelasticity, shear-thinning, and normal stress differences. Two models with different fidelity and computational cost are used to model laminar non-Newtonian fluid flow between a rotating flat plate and a textured disk. At lower-fidelity, we use the Criminale-Ericksen-Filbey (CEF) constitutive model and a thin-film approximation for the conservation of momentum (Reynolds equation). At higher-fidelity, we use a fully nonlinear constitutive model typically applicable to polymer solutions (multi-mode Giesekus model) and the full 3-D momentum equations. Fluid additive design is parameterized by two relaxation modes, each having a timescale, added viscosity, and a nonlinear anisotropic drag parameter. To manage the computational complexity and constraints between design variables, we use our previously-developed multiobjective adaptive surrogate model-based optimization (MO-ASMO) method. A data-driven implicit constraint management technique, introduced in Chapter 4, is utilized to construct general boundaries to

---

[1] Reprinted by permission from Springer Nature Customer Service Centre GmbH: Springer Structural and Multidisciplinary Optimization (Lee, Schuh, Ewoldt, and Allison. Simultaneous design of non-Newtonian lubricant and surface texture using surrogate-based multiobjective optimization. *Struct. Multidiscipl. Optim.* 60(1):99-116), ©2019

prevent attempts to evaluate designs that would lead to simulation failure. We demonstrate the efficiency of our MO-ASMO method and provide insights into co-designing the lubricant and textured surface. The Pareto-optimal solutions include fluid designs with both high and low viscoelastic additive loading. We rationalize this trade-off and discuss how the optimal design targets can be physically realized.

7.2 Introduction

Surface textures decrease friction in lubricated sliding contact with Newtonian fluids [15, 16, 18]. In hydrodynamic lubrication applications, surface texturing helps generate hydrodynamic pressure to support loads [4, 36, 176], provide reservoirs for lubricant [15, 176–178], and trap debris to help prevent surface wear and damage [179, 180]. We previously have shown that this friction reduction can be enhanced further using more general surface topographies [4]; this recent work in freeform texture design was motivated by earlier studies that showed favorable surface shapes could enhance frictional characteristics [20]. For the study presented in [4], we developed surface parameterization techniques for generating an arbitrary texture profile subject to local slope (manufacturability) constraints. We modeled the flow of an incompressible Newtonian fluid over the textured surfaces using the Reynolds equation [36, 42], and used this model to determine the optimal texture profile for minimizing frictional loss (shear stress) and maximizing load capacity (normal force).

We have also studied friction reduction experimentally with surface textures and viscoelastic non-Newtonian lubricants [35, 181]. Viscoelastic non-Newtonian lubricants can decrease shear stress due to shear-thinning [182, 183] and increase the load capacity due to normal stress differences [184]. Combing these additional fluid properties with surface texturing results in greater friction reduction than when either strategy is used independently [35, 181]. However, optimization of these viscoelastic properties, or the combined optimization of both fluid and surface texture, has not been considered previously.

Based on these observations, we extend our design study to include viscoelastic non-Newtonian fluid effects in friction reduction. A key challenge is a paradigm of how to "design" the non-Newtonian fluid behavior. There is no single mathematical model to describe all possible non-Newtonian fluids in the nonlinear viscoelastic regime [185], although universal equations apply in some limited circumstances, such a very small deformation with linear viscoelastic design [12]. Nonlinear viscoelastic design is of interest here, and we consider two different constitutive models with different fidelities, though both are parameterized by the same fluid design parameters. Selecting the fluid design description is also non-trivial. Here, we focus on continuum-level descriptions that can be applicable to a range of possible fluid additives, rather than material-specific parameters such as polymer molecular weight or colloid size, which would depend on the specific material embodiment to achieve the desired rheology. Our results here serve as targets that can be achieved by a wide range of material classes (resulting in a rheological inverse problem [186]); however, we expect polymer solutions to be the most likely formulation.

Table 7.1: Fluid models used for design in this study and corresponding solver governing equations.

Case no.	Fluid model	Governing equation	Dimension
1	CEF model	Reynolds equation	2D (r, θ)
2	Giesekus model	Cauchy momentum equation	3D (r, θ, z)
0	Newtonian fluid	Cauchy momentum equation	3D (r, θ, z)

We include viscoelastic effects through two different models: the Criminale-Ericksen-Filbey (CEF) model, and a multi-mode Giesekus model. The flow fields with both models are three dimensional; however, the CEF model is less computationally expensive because it can be used in the thin-film limit [187] to derive a modified Reynolds equation (which we have done, see Appendix B and [188]) that includes viscoelastic effects, whereas the multi-mode Giesekus model is used with the full 3-D Cauchy Momentum equations. Combinations of the fluid models and governing equations are given in Table 7.1, and are discussed in more

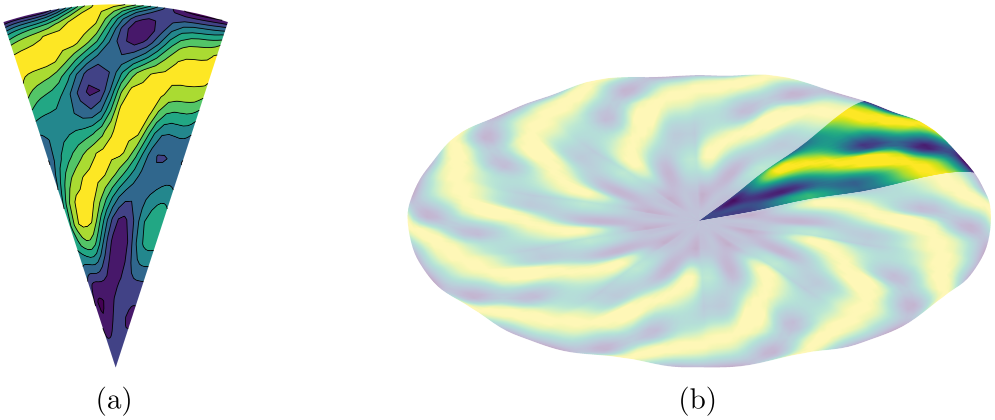
(a) (b)

Figure 7.1: A lubricated periodic surface texture design problem in a rotational tribo-rheometer setting. (a) Example of simulated periodic sector design. (b) Example of full disk design.

detail in Sections 7.3.1 and 7.4.1. We compare the results from the viscoelastic models to the Newtonian fluid reference case for the following reasons: first, the simplest models for including viscoelasticity are based on perturbations around the Newtonian fluid model (ordered fluid expansion [112]), and second, we are interested in comparing the system performance with viscoelasticity to the conventional Newtonian lubricants.

We have adapted our previous design optimization strategy [4, 36], which is illustrated in Fig. 2.1 in Chapter 2 and Fig. 7.1, to design both surface texture topography and non-Newtonian viscometric functions. Figures 2.1a (front view) and 2.1b (top view, a periodic sector) show the setup used previously in experiments [35] and the numerical texture design [4]. The fluid is confined between a flat plate that rotates at a constant angular velocity and a stationary textured surface. A sector shown in Figs. 2.1b, 2.1d, and 7.1a is an example design of the surface texture height profiles as a function of r and θ. Figure 7.1b shows an example of a fully-textured disk using ten periodic sectors.

As we extend our study to include nonlinear viscoelastic models, and move from 2-D to 3-D, the computational cost associated with the design problem increases significantly. In our previous study, where we modeled the fluid flow with the (Newtonian) Reynolds equation, the computational cost of the optimization was reduced by using a coarse design mesh that was mapped onto a finer analysis mesh [4]. The computational cost of the optimization can also be reduced by linearizing the Reynolds equation (with respect to the design variables) and iteratively solving using a sequential linear programming (SLP) strategy [41] or by adaptively constructing computationally-efficient surrogate models of expensive simulation responses [82]. Here, we solve the full nonlinear optimization problem using surrogate modeling. We have developed a multiobjective adaptive surrogate model-based optimization (MO-ASMO) strategy [67] that uses efficient sampling techniques to explore constrained design space and search for Pareto-optimal solutions. This algorithm is developed specifically for problems with narrow or geometrically-complex feasible design domains. We have imposed a local slope constraint on the gap height profile (manufacturability constraint), and have constrained the viscoelastic material functions using the analytical solution of the Giesekus model in steady, simple shear flow to represent realizable materials using a limited number of fluid parameters. It is demonstrated that the MO-ASMO algorithm is beneficial by reducing the overall computational cost of the combined fluid and texture design optimization problem.

Our contributions in this study are summarized here.

- We demonstrate that simultaneous co-design of texture (structural shape) and rheology (material properties) achieves better frictional system performance than design employing only texture shape optimization (as done previously). Our design is uniquely achieved by parameterizing the target viscometric functions, such as viscosity and first normal stress difference.

- We propose two unique non-Newtonian fluid solvers specifically for design applications involving surface texture shape design. We first suggest modeling the viscoelastic behavior with the CEF model, and use this constitutive relationship to derive a modified form of the Reynolds equation (CEF-Reynolds equation), which includes leading order viscoelasticity and inertia, in cylindrical coordinates. The solution of the CEF-Reynolds equation is obtained in nearly the same amount of time as the traditional Reynolds equation, but the solution also includes leading order viscoelastic and inertial effects that the Reynolds equation does not. The fidelity of the model can be improved by using the full 3-D Cauchy momentum equations in cylindrical coordinates, which we also use here, where the additional polymeric shear stress is included by a multi-mode Giesekus model. This representation also includes time-dependent fluid behavior (for example, relaxation) that is not included in the CEF-Reynolds equation. While this model increases design fidelity, it comes at the cost of longer simulation time. Both of these models are discretized using the pseudospectral method, which has many advantages over other discretization techniques for simulation-based optimization, as explained in Section 7.4.1.

- The design representation allows for determining physically realizable material functions, independent of the material formulation. The CEF model is material-independent, and the model parameters are the shear rate dependent viscosity and normal stress differences, which can be parameterized in any arbitrary way. Achieving these independent material properties with real materials requires the use of material-specific constitutive models (such as the Giesekus model, which applies for polymer solutions, polymer melts, worm-like micelles, etc.) where the material properties are related through parameters that have physical meanings, such as polymer relaxation time.

- Finally, we show that actively updated bounds that encapsulate the infeasible region using the support vector domain description (SVDD) method make possible the avoidance of design space regions that lead to numerical instabilities and simulation failure. SVDD accommodates very general boundaries, and this strategy improves overall computational efficiency.

This study is organized as follows. Section 7.3 presents the two non-Newtonian fluid models and the design problem formulation. Section 7.4 introduces solution procedures for fluid flow and surrogate-based design optimization. Section 7.5 presents the results and discusses the impact of using different fluid models on the design problem results. Section 7.6 then summarizes the results and concludes with the main findings from this study.

7.3 Formulation

We use models of two different fidelities, but both are governed by conservation of mass, momentum, and a constitutive equation for the fluid stress $\underline{\underline{\tau}}$. The different fidelities result from different simplifying assumptions of these governing equations. Conservation of mass (incompressible flow) and momentum are given by:

$$\nabla \cdot \underline{u} = 0 \tag{7.1a}$$

$$\rho \left(\frac{\partial \underline{u}}{\partial t} + \left[\underline{u} \cdot \nabla \right] \underline{u} \right) = -\nabla p + \nabla \cdot \underline{\underline{\tau}}, \tag{7.1b}$$

where $\underline{u}$ is the velocity field, ρ is fluid density, p is the isotropic pressure, and $\underline{\underline{\tau}}$ is the material stress. Fluid design parameters will appear in the material stress through the constitutive model for $\underline{\underline{\tau}}$.

We model this scenario at two different fidelities; one used the full 3-D conservation of momentum for the flow field with a high fidelity nonlinear viscoelastic constitutive equation for the stress tensor. The thin-film geometry and dynamic conditions motivate a lower-fidelity model that neglects complexities in both the governing momentum equation and the constitutive model. For this, we use a non-Newtonian fluid model that captures the nonlinear rheological behavior but only weak viscoelasticity and simplify the governing equations based on thin-film (lubrication approximation) concepts that neglect certain spacial derivatives in Eq. (7.1b). The governing constitutive equations for $\underline{\underline{\tau}}$, which involve the *fluid* design parameters, are described in the following subsections.

7.3.1 Non-Newtonian Fluid Models

Non-Newtonian fluids show different rheological behavior than Newtonian fluids; the behaviors most often studied are shear-thinning, viscoelasticity, generation of normal stresses in shear, and extensional thickening. These rheological behaviors can be described using different constitutive models. The two models we use are the CEF model and the multi-mode Giesekus model.

We select these two models because of their ability to predict shear-thinning, normal stress generation, and viscoelasticity (more details given below). The higher-fidelity Giesekus model is fully nonlinear and viscoelastic. It is derived in the context of polymeric systems (often used for polymer solutions and polymer melts), and is parameterized by $3k$ parameters, where k is the total number of relaxation modes. We limit ourselves here to $k = 2$ determined by the Bayesian Information Criterion (BIC), an approximation of the full Bayes factors [189]. Readers are referred to Appendix A.3 in Schuh [188] for the detailed procedure used to determine the parameter k. The CEF model is lower fidelity but is universally applicable to all non-Newtonian fluids in the limit of weak viscoelasticity. Thus, it can support a larger design space for achieving a given fluid behavior. The inputs to the CEF model are functions, which need to be parameterized; here, we choose to parameterize the rheological material functions for the CEF model using the steady shear material behavior for the Giesekus model, which allows us to have the proper interrelations between the viscosity and normal stress differences. Thus, both models have the same fluid design parameters consisting of two relaxation modes, each having a timescale, added viscosity, and a nonlinear anisotropic drag parameter: $(\lambda_k, \eta_k, \alpha_k)$.

Criminale-Ericksen-Filbey(CEF) Model

The CEF model [112, 190] is a constitutive model for the stress tensor $\underline{\underline{\tau}}$ that contains terms for the shear-rate dependent viscosity and the first and second normal stress differences, and is given as:

$$\underline{\underline{\tau}} = \eta\left(\dot{\gamma}\right)\underline{\underline{\gamma}}_{(1)} - \frac{1}{2}\Psi_1\left(\dot{\gamma}\right)\underline{\underline{\gamma}}_{(2)} + \Psi_2\left(\dot{\gamma}\right)\left(\underline{\underline{\gamma}}_{(1)} \cdot \underline{\underline{\gamma}}_{(1)}\right), \tag{7.2}$$

where the upper convected time derivative [191] of the shear rate $\underline{\underline{\dot{\gamma}}}$ is defined as:

$$\underline{\underline{\dot{\gamma}}} = \underline{\underline{\gamma}}_{(1)} = \underline{\nabla u} + \left(\underline{\nabla u}\right)^{\mathrm{T}}, \quad \text{and} \tag{7.3a}$$

$$\underline{\underline{\gamma}}_{(n+1)} = \frac{\partial \underline{\underline{\gamma}}_{(n)}}{\partial t} + \left(\underline{u} \cdot \underline{\nabla}\right) \underline{\underline{\gamma}}_{(n)} - \left(\left(\underline{\nabla}\, \underline{u}\right)^{\mathrm{T}} \cdot \underline{\underline{\gamma}}_{(n)} + \underline{\underline{\gamma}}_{(n)} \cdot \left(\underline{\nabla}\, \underline{u}\right) \right). \tag{7.3b}$$

The model parameters are the functions $\eta\left(\cdot\right)$, $\Psi_1\left(\cdot\right)$, and $\Psi_2\left(\cdot\right)$, which are equivalent to the viscometric functions in simple shear. For general flow fields, these functions depend on the instantaneous shear rate magnitude $\dot{\gamma}$, where $\dot{\gamma} = \sqrt{\frac{1}{2}\underline{\underline{\dot{\gamma}}} : \underline{\underline{\dot{\gamma}}}}$ (the operator ':' denotes the inner product of tensors). The first term in Eq. (7.2) models a generalized Newtonian fluid, and the remaining terms model the behavior of elastic effects from normal stress differences.

In steady, simple shear flow, where $\underline{u} = \dot{\gamma} y \hat{i}$, the CEF model gives the shear viscosity η, and the first and second normal stress difference coefficients Ψ_1 and Ψ_2 as $\eta = \eta\left(\dot{\gamma}\right)$, $\Psi_1 = \Psi_1\left(\dot{\gamma}\right)$, $\Psi_2 = \Psi_2\left(\dot{\gamma}\right)$, meaning that the inputs to the CEF model are the steady shear responses for a given fluid. It should be noted that for most polymeric systems, $\Psi_2\left(\dot{\gamma}\right) < 0$.

In small amplitude oscillatory shear, where $\underline{u} = \gamma_0 \omega \cos\left(\omega t\right) y \hat{i}$, γ_0 is the strain amplitude, and ω is the angular frequency, the CEF model gives the dynamic viscosity η' and the storage modulus G' as:

$$\eta' = \eta\left(\dot{\gamma} = 0\right), \tag{7.4a}$$

$$G' = \frac{1}{2}\Psi_1\left(\dot{\gamma} = 0\right)\omega^2, \tag{7.4b}$$

which is the same behavior as that predicted by the second-order fluid (SOF) model, which gives the first-order deviation from Newtonian fluid behavior, and is the same terminal regime (limit $\omega \to 0$) predicted by all fully nonlinear fluid models (including polymer systems) with a finite longest relaxation time.

The design inputs for this model are the rheological material functions $\eta\left(\dot{\gamma}\right)$, $\Psi_1\left(\dot{\gamma}\right)$, and $\Psi_2\left(\dot{\gamma}\right)$. There are infinitely many ways of representing the material functions; here, we choose to use the steady shear response from fully nonlinear models, which reduces the fluid design representation to the design inputs λ_k, η_{p_k}, and α_k, which are related to the steady-state behavior of $\eta\left(\dot{\gamma}\right)$, $\Psi_1\left(\dot{\gamma}\right)$, and $\Psi_2\left(\dot{\gamma}\right)$ for a multi-mode Giesekus model [112] as:

$$\eta = \eta_s + \sum_{k=1}^{n_{mode}} \eta_{p_k} \frac{\left(1 - f_k\right)^2}{1 + \left(1 - 2\alpha_k\right) f_k} \tag{7.5}$$

$$\Psi_1 = \sum_{k=1}^{n_{mode}} 2\eta_{p_k} \lambda_k \frac{f_k\left(1 - \alpha_k f_k\right)}{\left(\lambda_k \dot{\gamma}\right)^2 \alpha_k \left(1 - f_k\right)} \tag{7.6}$$

$$\Psi_2 = \sum_{k=1}^{n_{mode}} \eta_{p_k} \lambda_k \left(\frac{-f_k}{\left(\lambda_k \dot{\gamma}\right)^2}\right), \tag{7.7}$$

where:

$$f_k = \frac{1 - \chi_k}{1 + \left(1 - 2\alpha_k\right)\chi_k} \tag{7.8a}$$

$$\chi_k^2 = \frac{\sqrt{1 + 16\alpha_k\left(1 - \alpha_k\right)\left(\lambda_k \dot{\gamma}\right)^2} - 1}{8\alpha_k(1 - \alpha_k)\left(\lambda_k \dot{\gamma}\right)^2}. \tag{7.8b}$$

We use this model because of the predicted normal stress generation which is important in determining the thrust generation with polymer solutions. We limit the parameters $\eta_{p_k} \in \left[0, \frac{5}{2}\eta_s\right]$, $\lambda_k \in [10^{-5}, 10^{-2}]$, and $\alpha_k \in [0.01, 0.5]$. The bounds on η_{p_k} are determined by fitting the Huggins equation [192] to experimental data of zero shear viscosity as a function of polymer concentration, and noting the region where the Huggins equation is valid when compared to the experimental data. The bounds on λ_k are also determined from fitting the Giesekus model to experimental data at varying concentrations of polyisobutylene (PIB) [188], which are also within the range of concentrations tested here. The mobility factor α_k is bounded between 0.01 and 0.5 to ensure realistic material properties [193]. When α_k is less than 0.01, large Weissenberg numbers $Wi = \lambda\dot{\gamma}$ cause numerical instability, and numerical computation tends to fail [194]. The total number of fluid design variables is $3k$, where k is the number of relaxation modes in the parameterization.

Multi-Mode Giesekus Model

The CEF model only captures viscoelasticity in the limit of low frequency, close to steady-state. To capture the higher-order viscoelastic effects, we must use a higher fidelity model that captures the full range of a viscoelastic response. Here, we choose a multi-mode Giesekus model to simulate our polymeric stresses [112], given as:

$$\lambda_k \left(\frac{\partial \underline{\underline{\tau}}_{p_k}}{\partial t} + \left(\underline{u} \cdot \nabla\right) \underline{\underline{\tau}}_{p_k} - \left[\left(\nabla \underline{u}\right)^{\mathrm{T}} \cdot \underline{\underline{\tau}}_{p_k} + \underline{\underline{\tau}}_{p_k} \cdot \left(\nabla \underline{u}\right) \right] \right) \\ + \underline{\underline{\tau}}_{p_k} + \frac{\lambda_k \alpha_k}{\eta_{p_k}} \left(\underline{\underline{\tau}}_{p_k} \cdot \underline{\underline{\tau}}_{p_k} \right) = \eta_{p_k} \underline{\underline{\dot{\gamma}}}, \tag{7.9}$$

where λ_k is the relaxation time, η_{p_k} is the polymeric viscosity, and α_k is the mobility factor of the kth-mode, which can be physically related to the anisotropic drag of a polymer when deformed by the flow. Note that the entire first term in parentheses on the left-hand side is an upper convected time derivative of the polymeric stress $\underline{\underline{\tau}}_{p_k}$. The contributions from each mode are assumed to be additive such that the total polymeric stress $\underline{\underline{\tau}}_{p}$ is given as:

$$\underline{\underline{\tau}}_{p} = \sum_{k=1}^{n_{\mathrm{mode}}} \underline{\underline{\tau}}_{p_k}. \tag{7.10}$$

The steady shear viscosity and normal stress differences are the same as those given in Eqs. (7.5)-(7.7). Here the linear (small amplitude) viscoelastic behavior [112] is given as:

$$\eta' = \eta_s + \sum_{i=1}^{n_{\mathrm{mode}}} \frac{\eta_{p_k}}{1 + \left(\lambda_k \omega\right)^2} \tag{7.11a}$$

$$G' = \sum_{i=1}^{n_{\mathrm{mode}}} \frac{\eta_{p_k} \lambda_k \omega^2}{1 + \left(\lambda_k \omega\right)^2}, \tag{7.11b}$$

which applies for all frequencies in the linear regime.

We again use this model because of the predicted normal stress generation, which is important in determining the thrust generation with polymer solutions. We limit the parameter ranges to $\eta_{p_k} \in \left[0, \frac{5}{2}\eta_s\right]$, $\lambda_k \in [10^{-5}, 10^{-2}]$, and $\alpha_k \in [0.01, 0.5]$. The total number of design variables is $3k$, where k is the number of relaxation modes in the parameterization.

Parameters

Fluid properties, model parameters, computational mesh resolutions, operating conditions, and design constraint parameters for Cases 0, 1, and 2 in Table 7.1 are given in this section. The top and bottom disks (gap-controlled rotating disk and a fixed textured surface in Figs. 2.1a and 2.1d) have the same outer radius (r_o) of 20 mm. The minimum controlled gap height between the top and the bottom disks (h_0) is 269 μm; this value is used as the lower bound for the texture design gap height variable. The number of periodic sectors needed to construct a full disk (N_ϕ) is 10. The number of mesh nodes for each r-, θ-, and z-direction is $n_r = 6$, $n_\theta = 6$, and $n_z = 4$, respectively. Note that n_z does not apply to Case 1. The angular velocity of the flat plate (Ω), as shown in Fig. 2.1a, is 10 rad/s; solvent viscosity (η_s) and density (ρ_s) values are 9.624×10^{-3} Pa·s and 873.4 kg/m^3. The number of modes for the Giesekus fluid model is $n_{\text{mode}} = 2$ for Cases 1 and 2. For Case 0, this variable is not defined. The maximum angle for the texture inclination ($\theta_{\text{incl}} = 60°$) is explained in Section 7.3.2.

7.3.2 Design Problem Formulation

The design problem considered here is the simultaneous minimization of the input power to the rotating flat plate and maximization of the load-supporting normal force, while constraining the maximum texture inclination angle. This problem is formulated as a constrained nonlinear optimization problem:

$$\underset{\underline{x}_{\text{lb}} \leq \underline{x} \leq \underline{x}_{\text{ub}}}{\text{minimize}} \quad \underline{f}(\underline{x}) = [P,\ -F_N]^{\mathsf{T}} \tag{7.12a}$$

$$\text{subject to} \quad \underline{g}_1(\underline{x}) = \left[\left|\frac{h_{kj} - h_{(k-1)j}}{r_k - r_{(k-1)}}\right|, \left|\frac{h_{il} - h_{i(l-1)}}{r_i\theta_l - r_i\theta_{(l-1)}}\right|\right]^{\mathsf{T}} - \underline{\theta}_{\text{incl}} \leq \underline{0} \tag{7.12b}$$

$$\underline{g}_2(\underline{x}) = -h_{n_r 1} + h_{n_r l} \leq \underline{0} \tag{7.12c}$$

$$\underline{h}_3\left(\underline{x}\right) = h_{i1} - h_{in_\theta} = \underline{0}, \tag{7.12d}$$

$$\text{where} \quad P = M\Omega \tag{7.12e}$$

$$F_N = N_\phi \int_{-\varphi/2}^{\varphi/2} \int_{R_i}^{R_o} \left(p|_{z=0} - \tau_{zz}|_{z=0}\right) r dr d\theta \tag{7.12f}$$

$$M = N_\phi \int_{-\varphi/2}^{\varphi/2} \int_{R_i}^{R_o} \left(r\tau_{\theta z}|_{z=0}\right) r dr d\theta \tag{7.12g}$$

$$p_{ij},\ \underline{\underline{\tau}}_{ij} \leftarrow \text{flow-solver}\left(\underline{x}\right), \tag{7.12h}$$

for all $i = 1, \cdots, n_r$, $j = 1, \cdots, n_\theta$, $k = 2, \cdots, n_r$, and $l = 2, \cdots, n_\theta$. The design objectives are to minimize the power input $P = M\Omega$ and to maximize the normal force F_N simultaneously. Simultaneous optimization of the two objective functions (multiobjective optimization) results in a set of Pareto-optimal (nondominated) solutions. A manufacturability constraint applied in our previous study [4] is also implemented via the first vector-valued inequality constraint function $\underline{g}_1$. The maximum allowable local inclination angle between neighboring control points of the Lagrange polynomial interpolation over the texture geometry is limited to a predefined constant vector θ_{incl}. In addition, it is possible to have an infinite number of designs that are physically identical unless we set a reference point that is lower than any other location with the same radius, since the spatial design domain is rotationally periodic. To prevent this problem, we impose the inequality constraint $\underline{g}_2\left(\underline{x}\right)$. Also, the periodic boundary condition in the spatial design domain is specified using the constraint $\underline{h}_3\left(\underline{x}\right)$.

The design variable vector $\underline{x}$ is comprised of both surface height values at mesh nodes, h_{ij}, and fluid model parameters associated with each viscoelastic relaxation mode, k, given as $\underline{x} = \left[h_{ij}, \eta_{p_k}, \lambda_k, \alpha_k\right]^{\mathsf{T}}$ for all $i = 1, \cdots, n_r,\ \ j = 1, \cdots, n_\theta,\ \ k = 1, \cdots, n_{\text{mode}}$, and assuming we have a given fluid viscosity η, used as $\eta\left(\dot{\gamma}_1 \approx 0\right) = \eta$ and $\eta_s = \eta$ for the Giesekus model. The texture design is represented by a curvilinear mesh fitted to the cylindrical coordinate system and nodes spaced according to Gauss-Lobatto-Legendre (GLL) points [44] for each r and θ-direction. Gap heights h_{ij} are defined for each node of the mesh, where i and j are indices of the nodes in r and θ-directions. The texture design defined by h_{ij} is interpolated using Lagrange polynomials; the resulting texture surface used in this model is continuous and smooth. The viscoelastic material functions for the CEF model are described using analytical solutions of the material functions from the Giesekus model as described in Section 7.3.1. This representation strategy reduces the number of design variables significantly, which allows the same design variable set to be used for the two fluid constitutive models. Material functions used in the non-Newtonian fluid models are constrained to disallow certain combinations of values that are not numerically or physically realizable. This is implemented using the SVDD technique [97]. The SVDD method is discussed in Section 7.4.2 and Appendix D. Section 4.3.5 of Chapter 4 also describe this method with more information as an implicit constraint generation and management technique.

7.4 Methodology

7.4.1 Solution Procedures for Fluid Flow

Lower-Fidelity Model: Thin-Film Reynolds Equation With CEF Fluid

Previously we have developed code for solving the flow of an incompressible Newtonian fluid over general surface textures using the Reynolds equation [36], and have used that code for optimization of textured surfaces [4]. A previous study [187] showed that viscoelasticity could be included in the thin-film governing equations using the CEF model.

Here we derive a modified Reynolds equation with the CEF model for our design problem. Full details are provided in Appendix B. Briefly, we apply the following assumptions: (1) the gap height is small compared to the radius of the textured disk ($h\left(r,\theta\right)/R << 1$), (2) shear rate ($\dot{\gamma}\left(r,\theta\right) = r\Omega/h\left(r,\theta\right)$) is independent of z, (3) $\exists$ no second normal stress difference coefficient ($\Psi_2 = 0$), resulting in pressure that does not vary in the z-direction ($\partial p/\partial z = 0$), and (4) zero gradients in the z-direction are assumed for the other viscometric functions

$(\partial\eta/\partial z = 0,\ \partial\Psi_1/\partial z = 0)$. Splitting the pressure and velocity fields into $p = p_0 + p_1$ and $\underline{u} = \underline{u}_0 + \underline{u}_1$, and applying appropriate boundary conditions for the velocity fields results in two equations governing the flow of a CEF fluid over general surface textures; an equation similar to the steady-state Reynolds equation may be given as:

$$\frac{1}{r}\frac{\partial}{\partial r}\left(\frac{rh^3}{12\eta}\frac{\partial p_0}{\partial r}\right) + \frac{1}{r}\frac{\partial}{\partial \theta}\left(\frac{h^3}{12\eta r}\frac{\partial p_0}{\partial \theta}\right) = \frac{1}{r}\frac{\partial}{\partial \theta}\left(\frac{r\Omega h}{2}\right), \tag{7.13}$$

which includes shear-thinning, and another equation (where the right-hand side depends on the local Reynolds number and the local relationship between elasticity and viscosity), given as:

$$\frac{1}{r}\frac{\partial}{\partial r}\left(\frac{rh^3}{12\eta}\frac{\partial p_1}{\partial r}\right) + \frac{1}{r}\frac{\partial}{\partial \theta}\left(\frac{h^3}{12\eta r}\frac{\partial p_1}{\partial \theta}\right) = \frac{1}{r}\frac{\partial}{\partial r}\left(rG_r\right) + \frac{1}{r}\frac{\partial}{\partial \theta}\left(G_\theta\right), \tag{7.14}$$

where G_r and G_θ are functions of r, h, η, Ψ_1, $\frac{\partial p_0}{\partial r}$, and $\frac{\partial p_0}{\partial \theta}$. Detailed expressions for each term, and the full derivation of the modified CEF-Reynolds equations are given in Appendix B and in Schuh [188].

Higher-Fidelity Model: Full 3-D Momentum Equation With Giesekus Fluid

For the Giesekus model, the full Cauchy momentum equation is written in a tensorial form as:

$$\frac{\partial \underline{u}}{\partial t} + \left(\underline{u}\cdot\nabla\right)\underline{u} = -\frac{1}{\rho}\nabla p + \frac{\eta_s}{\rho}\nabla^2\underline{u} + \frac{1}{\rho}\nabla\cdot\underline{\underline{\tau}}_p, \tag{7.15}$$

where ρ is the fluid density, η_s is the solvent viscosity, and $\underline{\underline{\tau}}_p$ is the polymeric contribution to the shear stress. The contribution of the solvent has been pulled out of the stress tensor to improve numerical stability [195]. We assume that the solvent and polymeric stresses add to produce the total shear stress:

$$\underline{\underline{\tau}} = \underline{\underline{\tau}}_s + \underline{\underline{\tau}}_p, \quad \underline{\underline{\tau}}_s = \eta_s\underline{\underline{\dot{\gamma}}}. \tag{7.16}$$

The governing equations (conservation of momentum and incompressibility) provide four equations with ten unknowns; therefore, a constitutive equation must be used for $\underline{\underline{\tau}}_p$ to solve the fluid flow system. As stated above, we are using the multi-mode Giesekus model given in Eq. (7.9) with $n_{\text{mode}} = 2$.

We solve the transient governing equations in cylindrical coordinates to steady-state. The equations are solved on a periodic sector of a disk where $z \in [-h(r, \theta), 0]$; this is similar to our previous solution method with the Reynolds equation [4, 36]. The equations are discretized in space using a Galerkin pseudospectral method. We have mapped our 3-D periodic sector onto the $[-1, 1]$ cube using an invertible mapping [196, 197], where it was assumed that the gradient of the gap height profile $h(r, \theta)$ exists everywhere in the computational domain. We use GLL quadrature with optimally-chosen mesh points and quadrature weights so that the quadrature is exact for approximating polynomials of degree $2N - 1$, where $N + 1$ is the number of discretization points in a given direction [43, 44]. We use a third-order Adams Bashforth method with third-order extrapolation for the nonlinear terms in the time discretization. A velocity splitting technique is used for solving the pressure Poisson equation at each time step, and the diffusion terms are treated implicitly to aid stability [195].

Pseudospectral Method

We solve both governing equations presented in Section 7.4.1 and 7.4.1 using a Galerkin pseudospectral method for a periodic sector with $p_0|_{r=R_0} = p_1|_{r=R_0} = 0$, $\partial p_0/\partial r|_{r=R_i} = \partial p_1/\partial r|_{r=R_i} = 0$, and periodic boundary conditions in the θ-direction. The Dirichlet boundary condition $p|_{r=R_0} = 0$ is used to match the results described in Macosko [51] for flow between parallel disks. We use N_D-th order Lagrange polynomials for approximating quantities for each geometric dimension D. The texture design provided to the flow simulation is represented by the gap height h_{ij} for $i, j = 1, \cdots, n_r$, and the solution procedure associated with the pseudospectral method assumes that the entire computational domain is continuous and smooth in Lagrange polynomial form. Thus, this method obtains a very accurate fluid flow solution, even for coarse spatial meshes. Solutions for the design problem will also be smooth and continuous in the form of a Lagrange polynomial. Also, by maintaining the same mesh for the design representation and the simulation domain representation, we obtain very accurate design solutions without requiring a large number of design variables due to the characteristics of the interpolating polynomials used in the pseudospectral method. Increasing the mesh density, however, may introduce new practical design complexities, such as thinner texture features on the surface.

Experimental Validation of Numerical Model

The lower-fidelity model (thin-film Reynolds equation with CEF fluid) and the higher-fidelity model (full 3-D momentum equation with Giesekus fluid) are validated against steady shear experiments for varying concentrations of PIB in S6 base mineral oil using a cone-and-plate rheometer geometry of Θ=1.011° and R=20 mm, where Θ and R denote the cone angle and the radius, respectively. The comparison results show a good agreement between two models in a steady condition and between numerical and experimental results. The detailed comparisons of the raw torque and the raw normal thrust between experimental data and simulation results are provided in Section C.1 of Appendix C.

7.4.2 Design Procedures

Multiobjective Adaptive Surrogate Model-Based Optimization (MO-ASMO)

Efficient and effective sampling strategies for surrogate-based optimization (SBO) are well-studied in the context of finding a single optimum by balancing exploration and exploitation objectives in constructing surrogate models [82]. However, studies of sampling strategies for multiobjective optimization problems (MOPs) are largely limited to a global-level improvement of surrogate model accuracy as opposed to more efficient targeted accuracy improvements [198, 199]. Shan and Wang [200] developed the Pareto set pursuing (PSP) methodology that generates new training points toward regions where the predicted Pareto set is located, resulting in significant improvements in computational efficiency for the solution of MOPs using SBO.

The MO-ASMO code developed by Lee et al. [67] and presented in Chapter 4 is used here. The high-level process of the MO-ASMO framework is shown in Fig. 4.1 in Chapter 4. This code is a surrogate-based optimization framework that can manage multiple objective functions, tens or hundreds of design variables, and multiple linear and nonlinear constraints. Readers are referred to Fig. 4.1 in Chapter 4 for a high-level process description for the direct sampling-based [82] MO-ASMO algorithm. We have developed this method primarily for solving problems with complicated constraints that result in narrow or otherwise difficult to navigate feasible domains. It avoids infeasible samples to reduce the inefficient use of high-fidelity simulations, especially designs that are not physically meaningful or that result in numerical instability. The method aims to balance choosing samples that help improve surrogate model accuracy in the vicinity of the Pareto-optimal solution (a hypersurface in the design space), with choosing samples that aid exploration to improve the probability of finding global optima. The problem considered here is well-matched for this MO-ASMO method as it involves a large number of constraints that interrelate multiple design variables, and a computationally-expensive simulation. Readers are referred to [67] for a detailed description of this method, including sampling and validation, as well as openly-available source code.

Feasibility Management Using Support Vector Domain Description (SVDD)

When using simulations that use design variables as inputs, it is possible that certain combinations of design variable values correspond to a physically meaningless design that results in simulation failure. Some combinations that are physically meaningful may also result in numerical instabilities and simulation failure. In some cases, it may be possible to prevent consideration of designs that cause simulation failure via explicit algebraic constraints [67]. In other cases, it may not be known what variable combinations may cause failure until attempting simulation, preventing the definition of constraints a priori. In these circumstances, an alternative strategy is required.

In the studies presented here, it is not possible to define constraints a priori that prevent simulation failure. Certain numerical instabilities arise for a range of different designs. A strategy was developed to define arbitrary constraint boundaries (non-convex, disconnected infeasible domains) adaptively based on observed failed simulations. This strategy is based on the SVDD [96, 97]. In earlier work, the SVDD was used to define complex feasible regions. Here SVDD is used in the opposite manner to define regions of points that are infeasible in the sense that they lead to simulation failure. The availability of these constraints helps to avoid wasteful consideration of points that cannot be simulated.

At each MO-ASMO main iteration, the SVDD approximation of regions that cannot be simulated is improved by adding newly discovered infeasible points to the SVDD dataset. Using a strategy that defines the infeasible domain rather than the feasible domain avoids excessive limitations on design space exploration, all without a priori knowledge of the regions that cannot be simulated.

We constructed the Gaussian kernel-based SVDD [96] using a maximization problem given as:

$$\underset{\underline{0} \leq \underline{\beta} \leq \underline{C}}{\text{maximize}} \quad W\left(\underline{\beta}\right) = \sum_{i} \beta_i K_G\left(\underline{x}_i, \underline{x}_i\right) - \sum_{i,j} \beta_i \beta_j K_G\left(\underline{x}_i, \underline{x}_j\right), \tag{7.17}$$

where $\underline{C}$ is a vector of appropriate length where each element is the constant C. The Lagrange multipliers $\underline{\beta}$ are bounded above by $\underline{C}$. Varying C can help detect the outliers in the dataset that describes the domain. $K_G\left(\cdot, \cdot\right)$ is the Gaussian kernel function. After we construct the domain using the SVDD, an arbitrary point $\underline{z}$ is inside the described boundary if:

$$\begin{aligned} & R^2\left(\underline{x}\right) - R^2\left(\underline{z}\right) = \\ & K_G\left(\underline{x}, \underline{x}\right) - K_G\left(\underline{z}, \underline{z}\right) + 2\sum_{i} \beta_i \left(K_G\left(\underline{z}, \underline{x}_i\right) - K_G\left(\underline{x}_i, \underline{x}_i\right)\right) \geq 0, \end{aligned} \tag{7.18}$$

where $\underline{x}$ is a bounding point, which is called a support vector. A detailed explanation of SVDD is provided in Appendix D.

7.5 Results and Discussion

7.5.1 Case 1: Lower-Fidelity Model With CEF Fluid

Solutions of design problem Case 7.5.1 (CEF model with Reynolds equation) are illustrated in the objective function space in Fig. 7.2. Since the objective functions are (1) to minimize the power input and (2) to maximize the normal force, we desire points in this space to be close to the top-left corner. We used the Gaussian process surrogate modeling technique within the MO-ASMO framework for all numerical optimization studies presented here. Among the several stopping conditions available, we selected an average error criterion (less than 1%) evaluated during the validation stage in the MO-ASMO for terminating the optimization process. Optimal solutions (in the form of a Pareto frontier) are marked with colored circles, whereas all other design points evaluated during the course of optimization are marked with black and gray-scale dots. If a design point is displayed in a darker gray than another, this indicates that the former dominates the latter. Points having the same gray-scale intensity means they have the same rank according to a nondominated sorting strategy [46]. Optimal solutions have a range of input power values from 4.31×10^{-4} to 3.56×10^{-3} [W], and a range of normal force values from 6.16×10^{-4} to 1.50×10^{-1} [N]. The labels (a) through (f) that identify specific marked points in Fig. 7.2 corresponds to the texture and fluid designs given in Figs. 7.3a–7.3f and plot legends (a)–(f) of Figs. 7.4a and 7.4b. These representative solutions (a) through (f) were chosen subjectively based on the following criteria: (1) they should not be located in close proximity in the objective function space; (2) they should be among the best solutions in the Pareto frontier, i.e., they should be a point closer to the utopia point among solutions in close proximity; (3) and they should be evenly distributed in the objective function space.

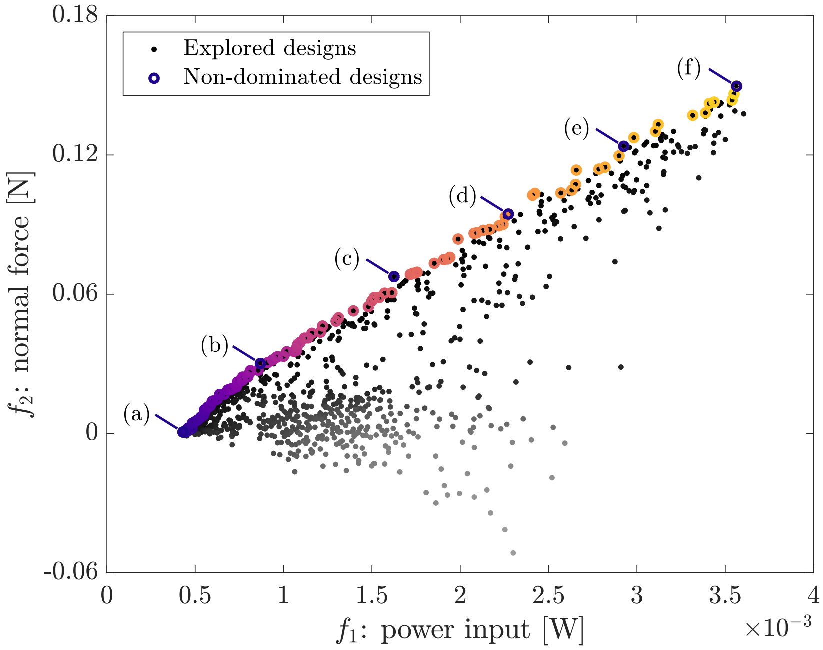

Figure 7.2: Explored designs and optimal solutions (nondominated designs) for the CEF model case displayed in the objective function space.

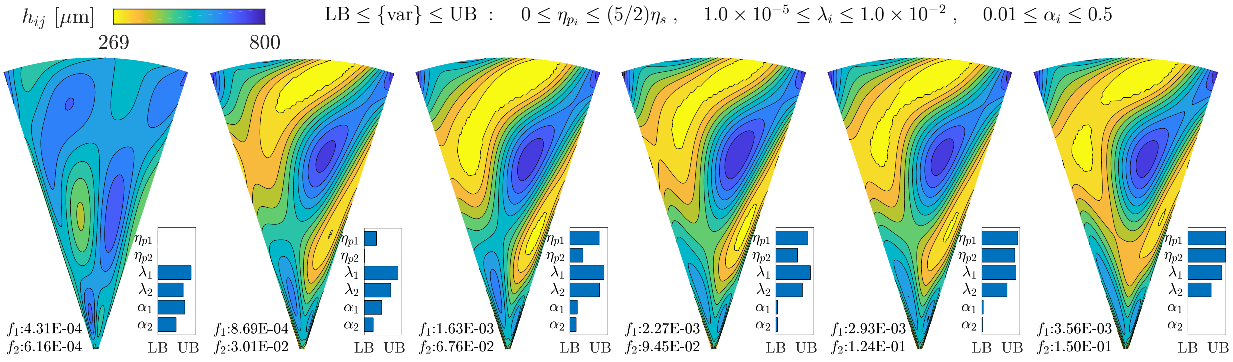

(a) (b) (c) (d) (e) (f)

Figure 7.3: Sample textured sector and fluid designs in the Pareto set from the CEF model case. f_1 represents the first objective function (power input [W]) and f_2 represents the second objective function (normal force [N]).

Design result (a) for Case 7.5.1 (refer to design point (a) in Figs. 7.2, 7.3a, and Line (a) in Fig. 7.4a) is an anchor point of the Pareto set; it has the minimum power value over all feasible designs. An anchor point is a nondominated point with one of the objective functions optimized, with all other objective functions ignored. Design point (a) results when power is minimized and normal force is not considered. This minimum-power design exhibits a

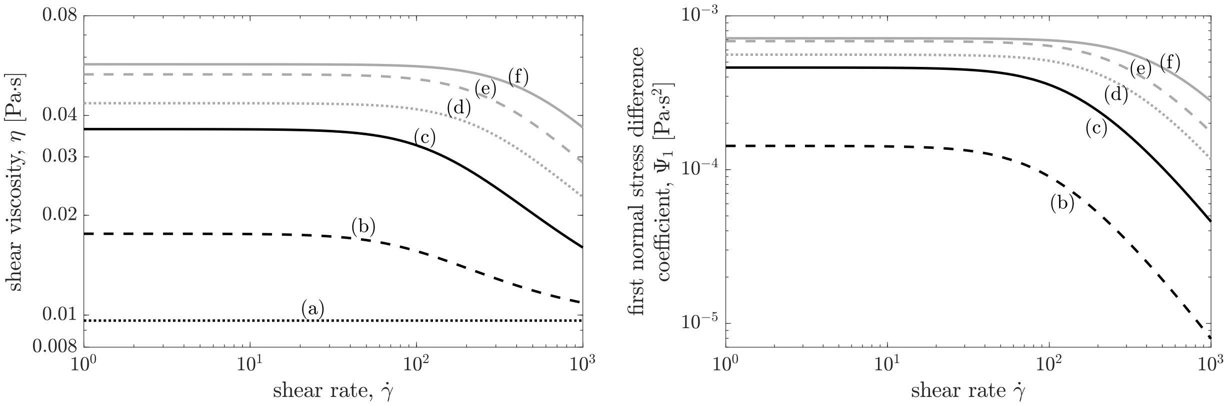

(a) (b)

Figure 7.4: Viscoelastic material functions of corresponding sample optimal designs from the CEF model case. (a) shear viscosity, (b) first normal stress difference coefficient. Curves (a)-(f) correspond to designs (a)-(f) in Figs. 7.2 and 7.3. Increased viscoelasticity (e.g. polymer additive) appears from design (a) to (f)

relatively flat texture surface with a small amount of asymmetry, and does not generate much normal force (4.31×10^{-4} [N]). This design solution is Newtonian (e.g., no polymer additive) and shows a flat shear viscosity in Line (a) of Fig. 7.4a, since the polymer viscosity values have converged to zero for all modes. Necessarily, no first normal stress difference appears.

Design result (f) (refer to design point (f) in Figs. 7.2, 7.3f, and Line (f) in Figs. 7.4a and 7.4b) is the other anchor point, which has a maximum normal force without consideration of power input. Unlike the former anchor point, this design has strong asymmetry with distinct elevation changes in the texture to form a spiral blade-like shape. As explained in our previous study, this spiral texture design directs the fluid pressure radially inward by acting as a converging channel, eventually generating the positive net normal force due to increased pressure near the disk center [4]. Also, this design solution includes non-Newtonian fluid properties with high polymer viscosity values for both modes (η_{p_1} and η_{p_2}). High polymer viscosity lifted the plateau of the overall shear viscosity, as shown in Line (f) of Fig. 7.4a and has the highest first normal stress difference values for the entire shear rate regime, as shown in Line (f) of Fig. 7.4b. These results are congruent with earlier studies based on Newtonian fluids where it was observed that: (1) a deeper surface reduces frictional loss, (2) symmetric surfaces do not generate any normal force due to geometric properties, and (3) stronger asymmetry generates larger normal forces [4, 36].

Other designs on the Pareto frontier between these two anchor points (refer to design points (b)–(e) in Figs. 7.2 and 7.3b–7.3e) have consistent trends. Specifically, we observe that: (1) the general shape of the surface texture designs does not change significantly, but steeper inclines in the texture are required to generate higher normal forces, and (2) an increased polymer viscosity and a decreased nonlinearity (anisotropy described by the mobility factor) help obtain higher normal forces.

These results show that the nonlinearity mainly plays a role when we optimize both objective functions simultaneously. An increased polymer viscosity tends to help increase load capacity, and increased nonlinearity helps reduce frictional losses. It should be noted that these responses are non-monotonic and have optimum values for achieving a certain balance between the two objectives.

To quantify the numerical solver uncertainty, solver parameter sensitivities were analyzed at the six selected solution points identified as (a)–(f) in Fig. 7.2. The solver parameter sensitivities are computed by obtaining deviations in the objective function values with predictable deviation possibilities in parameters, such as radius of the rotating disk (R_o), minimum controlled gap height between disks ($h_{\min}$), angular velocity of rotating disk (Ω), solvent viscosity (η_s), and solvent density (ρ_s), using the differential sensitivity analysis method. Deviations in parameters R_o and ρ_s affect less than 1% in both objective functions. Deviations in parameters Ω and η_s make changes between 1 to 3% in either or both objectives. Thus, this numerical solver is reliable for these four parameters. However, a deviation in $h_{\min}$ results in approximately 4% change in the first objective (power input) and about 11% change in the second objective (normal force). Thus, removing the offset in the gap height between disks is very important specifically for maintaining accuracy in normal force prediction. Detailed sensitivity analysis results are given in Table C.1 in Section C.2 of Appendix C.

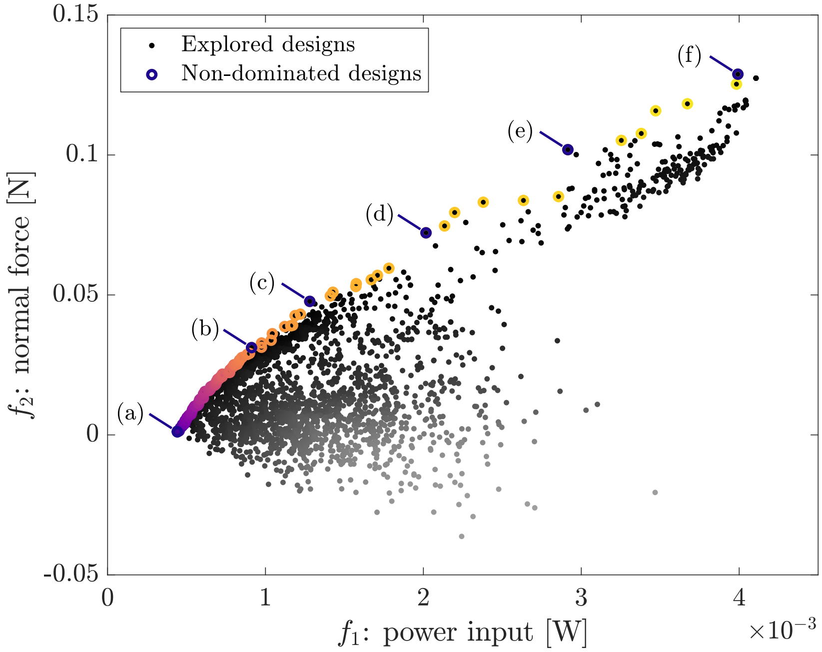

Figure 7.5: Explored designs and optimal solutions (nondominated designs) for the multi-mode Giesekus model case in the objective function space.

7.5.2 Case 2: Higher-Fidelity Model With Giesekus Fluid

Solutions of the design problem Case 2 (multi-mode Giesekus model with transient Cauchy momentum equation) are illustrated in the objective function space in Fig. 7.5. As with the CEF model (Fig. 7.2), the direction of the desired performance is toward the top-left corner, and the labeling strategy is kept consistent. Optimal solutions have a range of power input from 4.42×10^{-4} to 3.99×10^{-3} [W], and a normal force range of 1.11×10^{-3} to 1.29×10^{-1} [N]. The labels (a) through (f) indicate specific nondominated points in Fig. 7.5 that correspond to the texture and fluid designs shown in Figs. 7.6a–7.6f and plot legends (a)–(f) of Figs. 7.7a and 7.7b.

Design result (a) of Case 2 (refer to design point (a) in Figs. 7.5, 7.6a, and Line (a) in Fig. 7.7a) is the anchor point with minimum power input. This design shows a relatively flat texture surface with a small amount of asymmetry and Newtonian fluid properties, as was observed in Case 1. The maximum normal force anchor point is the design point (f) in Fig. 7.5 (also in Fig. 7.6f and Line (f) in Figs. 7.7a and 7.7b). This design has the most distinct

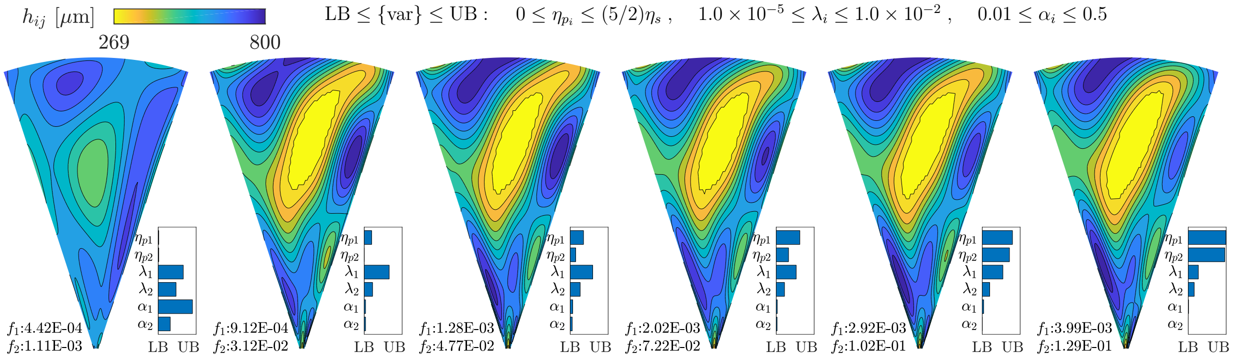

(a) (b) (c) (d) (e) (f)

Figure 7.6: Sample textured sector and fluid designs in the Pareto set from the multi-mode Giesekus model case. f_1 represents the first objective function (power input [W]) and f_2 represents the second objective function (normal force [N]).

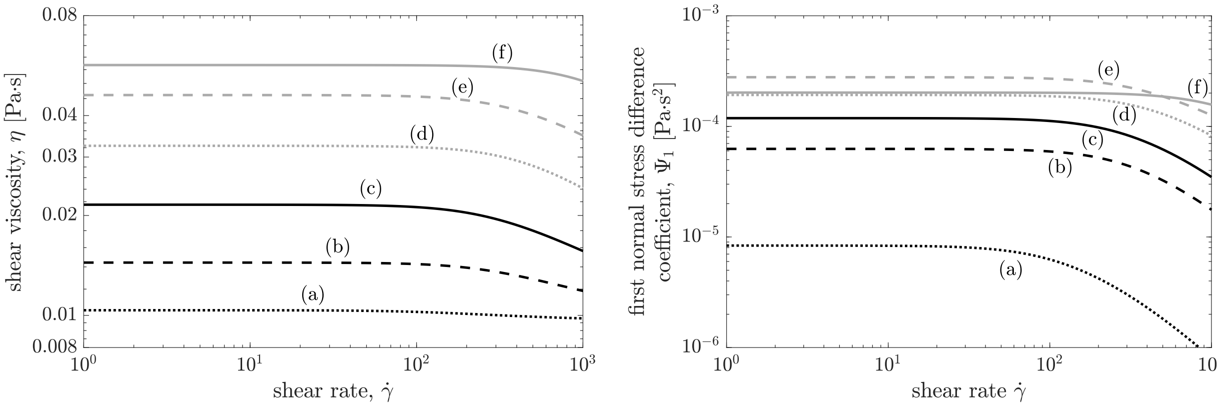

(a) (b)

Figure 7.7: Viscoelastic material functions of corresponding sample optimal designs from the Giesekus model case. (a) shear viscosity, (b) first normal stress difference coefficient. Curves (a)-(f) correspond to designs (a)-(f) in Figs. 7.5 and 7.6. Viscoelasticity (e.g. polymer additive) generally increases from design (a)-(f).

elevation changes in the texture, and, similar to the previous case, forms a spiral blade-like shape. As we see in Case 1, this design has the second-highest plateau value in shear viscosity as shown in Fig. 7.7a, and high first normal stress difference value as shown in Fig. 7.7b. As observed in these results, having a larger first normal stress difference at a higher shear rate has a more significant impact on generating and overall normal force than when operating in a lower shear rate regime. Although flow described by the Giesekus model can exhibit second normal stress difference (Ψ_2) effects, the results show that magnitudes of Ψ_2 are at least 1 to 2 orders of magnitude smaller than Ψ_1 and do not contribute a meaningful amount of normal force generation.

Other designs on the Pareto frontier between these two anchor points (refer to design points (b)–(e) in Fig. 7.5 and Figs. 7.6b–7.6e) also exhibit consistent trends: (1) the surface texture shapes do not change significantly, but larger elevation changes are needed to acquire higher normal forces, and (2) an increased polymer viscosity is associated with higher normal forces, and (3) the nonlinearity (mobility factor) is maintained with low (but non-zero) values for the entire range of designs.

Thus, for case 2, we can observe an increase in the normal force with a simultaneous increase in the power input as polymer viscosity values in modes 1 and 2 increase (from design (b) through (f)). However, all the optimal solutions converged to low mobility factor values, suggesting that shear-thinning is not desirable. Also, the optimal textures from Case 2 are, in general, deeper than those for Case 1. Design point (f) in Fig. 7.7b shows a different trend when comparing to other design points in Case 2 or Case 1. Even though Ψ_1 is lower in (f) than in (e), it produces a larger normal force. This is because the normal force is the integral of the normal stress difference times the squared shear rate over the entire textured domain. At the higher shear rate values, (f) is larger than (e), resulting in a larger contribution to the normal force. This is consistent with the notion that shear-thinning in the normal stress differences decreases the normal force. Therefore, other designs not considered here that keep the shear-thinning profile for the viscosity while having a nearly constant Ψ_1 across the desired shear rate range may produce better lubrication results.

To quantify the numerical solver uncertainty, solver parameter sensitivities were analyzed at the six selected solution points identified as (a)–(f) in Fig. 7.5. The solver parameter sensitivities are computed using the same procedure described in Section 7.4.1. Deviations in parameters R_o and ρ_s produce up to 1% differences in both objective functions. Deviations in parameters Ω and η_s make changes between 1 to 3% in either or both objectives. With these results, we can conclude that this numerical solver is reliable for these four parameters.

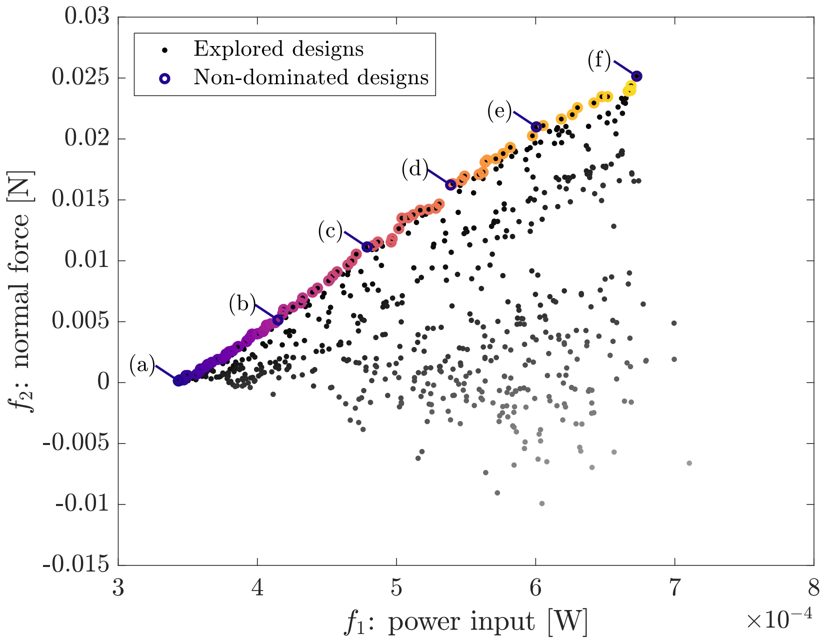

Figure 7.8: Explored designs and optimal solutions (nondominated designs) for the Newtonian fluid model case in the objective function space.

However, a deviation in $h_{\min}$ produces up to 5% change in the first objective (power input) and about 10% change in the second objective (normal force). Thus, as we concluded earlier, removing the offset in the gap height between disks is very important for maintaining accuracy in normal force prediction. Detailed sensitivity analysis results are given in Table C.2 in Section C.2 of Appendix C.

7.5.3 Case 0: Newtonian Fluid Model Case Result

An additional study is performed here using a Newtonian fluid model with a transient Cauchy momentum equation to provide a reference solution (Case 0). Solutions of this case are shown in Fig. 7.8. Optimal solutions have a range of power input from 3.43×10^{-4} to 6.73×10^{-4} [W], and a range of normal force values from 1.45×10^{-4} to 2.51×10^{-2} [N]. The labels (a) through (f) indicating specific marked points in Fig. 7.8 correspond to the texture and fluid designs given in Figs. 7.9a–7.9f.

Similar to the results obtained from the non-Newtonian fluid studies, we see analogous

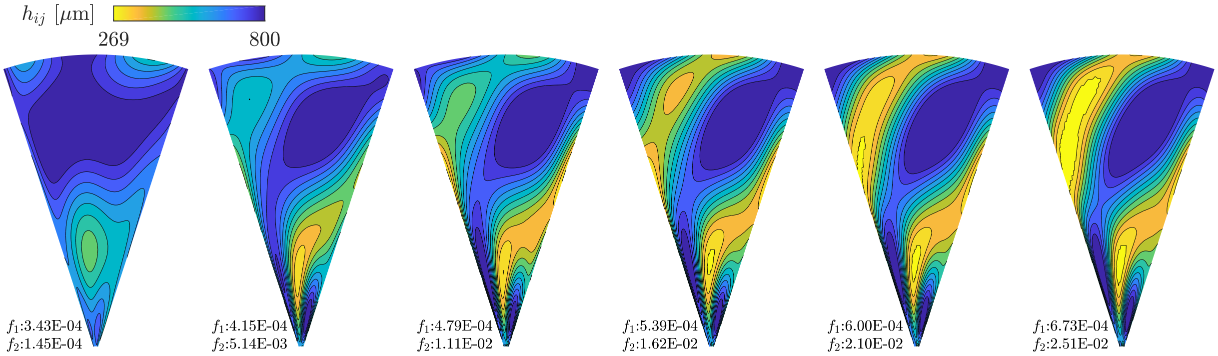

(a) (b) (c) (d) (e) (f)

Figure 7.9: Sample textured sector designs in the Pareto set from the Newtonian fluid model case. f_1 represents the first objective function (power input [W]) and f_2 represents the second objective function (normal force [N]).

trends in the shape of the surface textures. An anchor point with a minimum power input (shown as design point (a) of Case 0) has a deep and relatively planar textured surface. The maximum normal force anchor point, shown as design point (f), has a sharp and distinct asymmetric spiral blade-like texture shape, which directs the fluid pressure radially inward to generate a positive net normal force.

Other designs on the Pareto frontier between these two anchor points (refer to Points (b)–(e) in Fig. 7.8 and Figs. 7.9b–7.9e) have a consistent trend; unlike the other two non-Newtonian fluid cases, the texture designs are notably different from each other. The optimal designs on the Pareto frontier, in this case, show how changes in texture design only impact generated normal force values since all the designs have the same Newtonian fluid properties. Comparatively sudden elevation changes in the texture are observed for the entire set of design points that generate normal force (specifically see design points (b)–(f)).

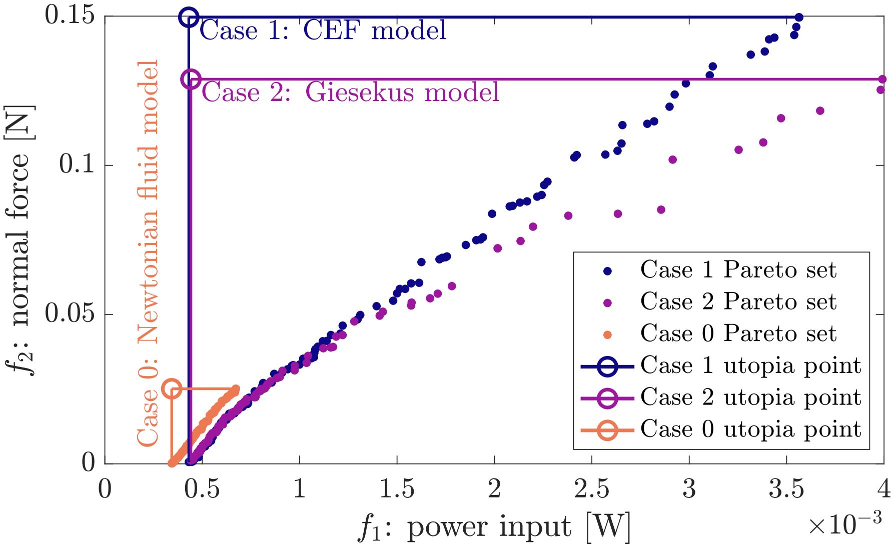

Figure 7.10: A comparison of the optimal solutions (Pareto set) of CEF, Giesekus, and Newtonian fluid models in the objective function space.

7.5.4 Comparisons and Discussion

Pareto Set Comparison

Figure 7.10 shows Pareto sets for three design studies simultaneously, including CEF (Case 1), Giesekus (Case 2), and Newtonian fluid model (Case 0) studies. Dots represent Pareto-optimal solutions (design points) in the objective function space, while circles represent the corresponding utopia points for each of the three design studies.

The study based on the Newtonian fluid model serves as a reference, illustrating how much normal force can be generated through improved texture design alone without tailoring non-Newtonian effects. For Newtonian fluids, Pareto-optimal designs span only a small range of power input levels (from 3.43×10^{-4} to 6.73×10^{-4} [W]). The maximum possible normal force generated without aid from viscoelastic effects is 2.51×10^{-2} [N].

When parameters that define fluid properties are added as design variables, the maximum possible normal force generated is increased by a factor of six. The CEF model case exhibits a maximum possible normal force of 1.50×10^{-1} [N], with a corresponding power input of 3.56×10^{-3} [W]. Using the multi-mode Giesekus model, we can obtain a maximum normal force of 1.29×10^{-1} [N], with a corresponding power input of 3.99×10^{-3} [W]. Although we used the same parameterizations for designing fluids in both non-Newtonian fluid cases, we see a significant difference in normal force generating capability. Design based on more simplified fluid simulations (i.e., modified Reynolds equation using a CEF fluid model) demonstrated the ability to identify designs that generate higher normal force values, at least as predicted by these simplified models.

Analysis of Friction Reduction and Load Supporting Normal Force

As we see in Figs. 7.2, 7.5, and 7.8, the two objectives of decreasing the input power and increasing the normal force are competing. When trying to minimize the input power, the optimal solutions indicate no added polymer (resulting in base solvent viscosity) and have the deepest texture profiles that result in the smallest shear stress. However, when aiming to maximize the normal force produced, the optimal solutions have polymer additives and exhibit a spiral-shaped texture profile. Designing the fluid parameters in this region is a non-trivial task, in part due to non-monotonic relationships between the normal force and the viscoelastic design parameters. This suggests that optimization of the viscometric functions plays a key role in performance enhancement.

Model Comparison

Based on the above results, the two fundamental problem types are (1) simultaneous design of texture and fluid properties, and (2) design of texture-only with fixed fluid properties. While the simultaneous texture and fluid design problem were solved using two distinct numerical fluid simulation models, they correspond to the same physical design problem. Both cases involve using a viscoelastic fluid (polymeric solution) as the lubricant, designing the fluid properties, and designing the texture shape. The only difference between these two cases is how the behavior was predicted, and the simplifying assumptions made. We highlight this point to clarify that the decision between methods can instead be made based on the following criteria: (1) computational efficiency, (2) prediction accuracy, (3) range of numerical limits, and (4) range of types of fluid behaviors that the model can predict. The models are compared here along these dimensions.

First, the CEF-Reynolds equation has a very efficient computational structure; the entire optimization using the MO-ASMO algorithm took only 21 minutes, whereas direct optimization using the NSGA-II algorithm required 85 minutes, both computed using a dual Xeon Gold 6130 workstation with 64 computing threads. The steady-state solution can be obtained directly without using a time marching transient solution procedure. Also, the CEF-Reynolds equation can predict the pressure and stress of the flow field efficiently within assumptions made during derivation. Since the CEF model can include shear-rate dependent viscosity and normal stress differences in calculating the velocity and pressure fields, the nonlinear viscoelasticity observed in our polymeric lubricant can be predicted well. However, because of the assumptions and limitations underlying the CEF-Reynolds equation (see Section 7.4.1 and [188]), prediction accuracy may be poor when certain flow conditions are present, such as recirculation or flow with non-trivial inertial effects. The CEF model maps material parameters to material properties in a less-constrained way compared to higher-fidelity options. This additional flexibility results in a wider exploration of designs in the material property space and higher normal force values, but may result in properties that are more difficult to realize physically. Within the design ranges of the other models (power input up to 2.5 [W] and normal force up to 0.1 [N]), this model produces a Pareto frontier that mostly overlaps with the Pareto frontiers generated using the other models.

Second, the Cauchy momentum equation with a multi-mode Giesekus model is the most computationally expensive choice, but it can predict the fluid flow very accurately, including inertial effects, recirculation, and other 3D effects. The Giesekus model can also include shear-rate dependent viscosity and normal stress difference effects on the velocity and pressure fields. Thus, this model is the most ideal for complex flow phenomena with nonlinear viscoelasticity. However, due to numerical instability under certain conditions, particular sets of input (shape and fluid) parameter values cannot be evaluated with this solver. Our MO-ASMO algorithm can handle these "unable-to-obtain-result" points by utilizing feasible region management functions based on the SVDD strategy. Thus, we improved computational solution efficiency by avoiding training samples that were incompatible with the model. After addressing this issue, the MO-ASMO algorithm produced improved solutions. However, even with the efficient MO-ASMO algorithm, the computation time for this optimization problem was significant (14 hours using the same machine). The Pareto frontier for this case overlaps with the CEF model results, but it could not produce designs with comparably high normal force generation.

It should be noted that the performance metric values reported in these results are based on distinct model types. One approach to providing a more fair comparison would be to evaluate Pareto-optimal designs generated by the lower-fidelity approaches via the higher-fidelity Giesekus model. This was attempted, and unfortunately, a number of nondominated solutions from Case 0 and 1 approaches resulted in numerical instabilities. Related ongoing work involves experimental testing of the associated designs to provide an accurate and fair design method comparison, but this experimental work is outside the scope of this study. When these ongoing studies are concluded, more complete statements can be made regarding the behavior and utility of the design methods presented, and whether modifications could be made to the Case 1 approach to focus design exploration on realizable high-performance designs.

Texture Shape Comparison

Sample texture shapes of full disks from our design solutions are compared in Fig. 7.11. Texture designs from the CEF model case are shown in subfigures (a), (d), and (g); texture designs from the Giesekus model case are shown in subfigures (b), (e), and (h); texture designs from the Newtonian fluid model case are shown in subfigures (c) and (f). Sample textures given here are selected to compare the resulting optimal textures between different

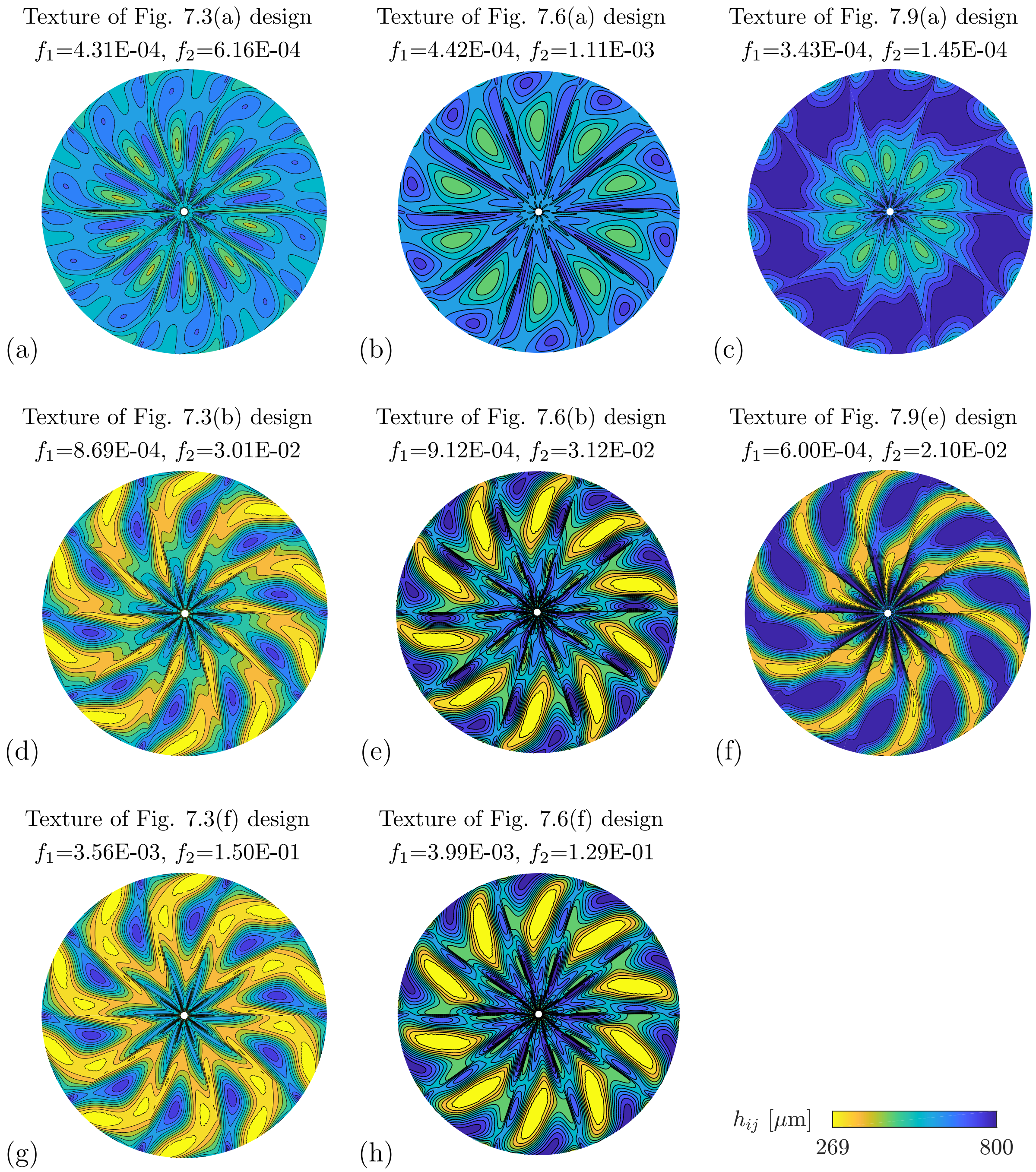

Figure 7.11: Sample textured disk designs in the Pareto set from all three fluid model (CEF, Giesekus, and Newtonian) cases. f_1 represents the first objective function (power input [W]) and f_2 represents the second objective function (normal force [N]). (a), (d), (g): results of CEF model case, (b), (e), (h): results of Giesekus model case, and (c), (f): results of Newtonian fluid model case. (a), (b), (c) generates nearly-zero normal force, (d), (e), (f) generates normal force of O(3E-02), and (g), (h) generates normal force over O(1E-01), which is not available with the Newtonian fluid.

fluid model cases.

Designs are arranged such that the normal forces generated by each design in a given row is similar. The first row designs ((a), (b), and (c)) are the textures that generate nearly-zero normal forces. These surface texture designs are relatively flat with a limited amount of asymmetry. The second-row designs ((d), (e), and (f)) are the textures that generate normal forces on the order of 3×10^{-2} [N]. These surface texture designs have very sharp and large elevation changes to create a spiral blade-like pattern, as discussed in Sections 7.4.1–7.5.3. For the Newtonian fluid model case, which relies on the texture to generate a normal force, the resulting design ((f)) generates a normal force value close to the highest possible without non-Newtonian fluid behavior. The third row ((g) and (h)) are the textures that generate normal force values over 1×10^{-1} [N], and are the highest normal force values for each of the respective design problems. Texture designs are not significantly different from the designs in the second row. This observation indicates that normal forces higher than what was purely achievable through only texture design depends solely on viscoelasticity. Further design studies using sequential design strategies (texture design optimization followed by fluid design, or vice versa) rather than simultaneous design may provide stronger evidence for the effects of viscoelasticity on normal force generation.

As described in Section 7.5.4, each simultaneous texture and fluid design study (Cases 1 and 2) used the same design objectives and variables. In other words, they involve the same design formulation, but use different numerical simulation approaches for prediction. Thus, unless two different solution sets provide the exact same objective function values, one of these two sets of solutions may dominate the other. However, it is possible that multiple solutions exhibit almost identical performance values. This issue is connected to the question of which fluid model or fluid solver can predict the behavior more accurately. Cross-validation of one solution with different fluid models, as well as an experimental validation of the solution, is needed and is a topic of ongoing work.

Problem Formulation Discussion

As we discussed earlier in Section 7.2, combined optimization of both fluid and surface texture in the lubricated sliding contact has not been considered previously. Thus, earlier efforts do not exist that could be used to build upon or compare to. The simultaneous problem formulation decisions were based on the discretion of the authors. In addition to the simultaneous approach used here, other problem formulations could be considered, such as sequential and nested approaches. It is known that the conventional sequential design process may not produce system-optimal solutions, while the nested and the simultaneous design approaches can identify system-optimal designs [201]. The nested design method generally demands more computational expenses for the simultaneous design method. However, the nested design may outperform the simultaneous design approach if the following conditions exist: (1) when the dimension of the design problem is not small and (2) when the inner-loop subproblem can be solved efficiently [202]. In this study, on the other hand, two different design targets (fluid and texture) are solved in a single simulation routine (one of the solvers presented in Section 7.4.1). Consequently, separating these two design targets into inner and outer loops is computationally inefficient, although formulating the design problem as a single optimization problem results in a large number of design variables.

While selecting a simultaneous formulation had clear benefits, determining an effective design representation for the fluid material functions was less straightforward. Using the Giesekus fluid parameterization for designing the material functions limits the solution within certain types of complex fluids. Using the Giesekus fluid parameterization does not mean that the solution fluid is only achieved by the polymeric additives; the same solution may be achieved via multiple different chemical and molecular formulation strategies. However, using a different class of fluids may result in fluid properties that cannot be realized by the Giesekus fluid parameterization. Investigating a variety of fluid parameterizations is beyond the scope of this study, but is an important open research question, and foundational work has been performed recently in areas including organizing different models for design [185], model selection studies [136], and database descriptions of complex rheological properties [186].

7.6 Conclusion

In this study, we designed non-Newtonian lubricant properties and surface texture simultaneously for lubricated sliding contact using the MO-ASMO algorithm and two non-Newtonian fluid models. The Giesekus fluid parameterization used for both constitutive models provides practical and physically-achievable material function shapes, but it is acknowledged that this parameterization strategy may limit fluid system design performance. Different models and design representations would be required to explore such an expanded design space, but would likely come at the cost of increased solution complexity and computational expense. We obtained nondominated optimal design solutions (i.e., Pareto sets), and compared a set of sample texture and fluid design results. We identified trends in texture shapes, which agreed with trends from our previous studies, observed fluid parameter trends, and identified how fluid design influences objective function values.

The MO-ASMO algorithm was applied successfully to solve this simultaneous fluid and texture design problem with two objectives. A direct optimization (using either nonlinear program (NLP) or genetic algorithm (GA)) was impractical given our computational resources (specifically for Case 2). The MO-ASMO algorithm enables accurate solutions without requiring access to exceptionally high-performance computing resources. A specific challenge arises when attempting to use general-purpose NLP algorithms due to the Giesekus model stability properties. Certain combinations of texture shape and fluid parameter values cause model divergence. An explicit and precise description of the boundary between compatible and incompatible parameter values is not available, making direct application of standard NLP solvers impractical. The MO-ASMO algorithm mitigates these issues effectively using the SVDD strategy for adaptively constructing an explicit boundary between regions with acceptable input values and those that lead to divergence. Our use of the SVDD strategy is differentiated from others by encapsulating observed invalid input regions to avoid during the exploration stage, which ensures a comprehensive exploration of the entire computable design space.

We observe that added viscoelasticity to the Newtonian solvent significantly increases normal force generation from the numerical optimization results in this study. All the optimal texture designs are qualitatively similar in shape to our earlier studies based on a Newtonian lubricant, but viscoelasticity plays a vital role in increasing normal force generation by up to a factor of five without a significant change in texture design. We see that optimal textures obtained with Newtonian and non-Newtonian fluids resulted in different shapes and elevation changes. This shows that the simultaneous design of the non-Newtonian lubricant and surface texture is necessary to achieve overall higher system performance.

A comprehensive set of physical experiments to compare performance indices (power input and normal force) for a carefully-selected set of numerically-optimized texture and fluid designs is a topic of ongoing work. Preparation for the experimental measurement requires a micro-fabrication of textured disks and a formulation of viscoelastic lubricants. Observing that all the design solutions on the Pareto frontier have different fluid properties, a set of representative sample designs will need to be selected carefully for comparison with simulation results. Experimental texture fabrication, fluid formulation, and testing are outside the scope of this investigation, which is focused on simulation-based optimization studies. Such future work will build upon the targets identified in our work here, which combine the simultaneous and coupled effects of both texture and viscoelastic fluid properties.

Chapter 8

Conclusions and Outlook

8.1 Summary of Contributions

This dissertation presented methods for the integrated design of viscoelastic (VE) materials and structural geometry. The studies in this dissertation proposed a new way of designing with VE materials by combining system design considerations with integrated materials and structural geometry design. Unlike other materials studies driven by specifically intended material behaviors or characteristics, the performance-driven approach presented in this dissertation is distinct in the overall objective that aims to agnostically find optimal material characteristics specifically tailored for the overall system design problem.

The studies presented in this dissertation provide clear answers to the research questions raised in each chapter. Answering these research questions demanded novel findings that ultimately resulted in novel design principles for performance enhancement and solution efficiency. Surface textures were limited to predefined shapes in the previous literature, but these predefined shapes unnecessarily constrain the design space. The fore-aft asymmetry profile, under this relaxation, transforms into a spiral blade shape, which directs pressure toward the center. Relaxing these unnecessary geometric design constraints allowed performance enhancement of more than order of magnitude. The studies also showed that the normal stress differences generate load-carrying normal force regardless of the shear direction through the profile of the fore-aft asymmetry. Finally, the study showed the effectiveness of the integrated design approach using VE lubricant and structural geometry.

The chapters included in this dissertation are classified into two parts—Part I: Methodologies for surface texture design, and Part II: Integrated design with viscoelasticity. The chapters illustrate methodologies for and demonstrations of system-level performance-driven simultaneous material and structural design. As a whole, the dissertation studies present the exploitation of design spaces that are often unexplored by established design strategies; this is accomplished through (1) general and unrestrictive texture parameterizations, (2) design strategies and formulations that enable solving high-dimensional design problems, (3) use of design-appropriate models and representations for viscoelasticity, and (4) efficient numerical design algorithms and structures that help to solve challenging design problems, specifically with VE material systems. The obtained design results were analyzed to provide insights that connect design solutions with the mechanisms of governing physics and physical implications.

Chapter 2 presented a study that focuses on the improvement of frictional performance—minimizing frictional loss and maximizing load-carrying capacity—in systems with full-film lubricated sliding contact and textured surfaces. Previous studies used predefined texture shapes, such as cylindrical dimples or other polygonal dimple arrays, to achieve a better frictional performance of the lubricated sliding contact [17, 21, 22, 27]. By eliminating unnecessary predefined texture shape assumptions and allowing general texture topography, both performance indices were improved in exceptional ways. The study presented incremental transitions from the conventional dimple textures to more sophisticated texture design parameterizations, and revealed that having less restrictive design representations can achieve system performance improvement by over an order of magnitude. The study also offered insights into the underlying mechanisms leveraged by these designs to improve performance. The free-form optimal texture profiles consist of asymmetric expansion-contraction channels, following the trends that the previous study [30] already suggested. In addition to the asymmetry, the optimal texture contours result in spiral texture geometries. The spiral blade-like texture profile acts as a converging channel directing flow radially inward, and this concentrated pressure near the disk center generates a positive net normal force, helping to achieve increased load-carrying capacity and reduced leakage at the outer boundaries.

Chapter 3 presented a development of the texture design optimization model to capitalize on problem structure to support increased design fidelity. Specifically, a mathematically-equivalent reformulation of the fluid mechanics model was discovered that was amenable to linearization, which then enabled the formulation of a sequential linear programming (SLP) strategy that supported simultaneous improvement in design representation fidelity and computational efficiency. The study presented in Chapter 2 achieved an efficient solution by reducing the design dimension using the spline texture representation and solving the nonlinear program (NLP), treating the simulation as a black-box. However, in this study, the fluid flow simulation and the design optimization formulations are integrated within the same system of equations, by introducing a new optimization variable involving both the pressure gradient and the cube of gap height at each mesh node location. In this way, the flow simulation and the optimal texture design problems could be solved simultaneously. This transformation supports the linearization of the governing equations and design objectives, and the SLP is used with a trust-region method and the ε-constraint method to obtain Pareto-optimal texture designs with a high-dimension texture design resolution. The results showed that the SLP solution with higher design resolution is at least an order of magnitude faster than the lower-resolution black-box optimization. In addition, a well-selected starting point was discovered to be sufficient for identifying all Pareto-optimal solutions, in contrast to the NLP solutions, where a multi-start strategy was required for each solution point. However, the SLP method exhibits several clear limitations. Since the trust-region is the only bound for the monotonic linear problem formulation, the solution relies on the convergence of the trust-region steps, and cannot explore outside the trust-region at each trial. Several SLP method improvements are suggested for future research, including the ability to explore from an arbitrary design point as a starting point and implementation of a sophisticated stepping method to enhance solution performance further.

Chapter 4 presented novel efficient sampling strategies and implicit constraint management strategies included with a new framework, termed here as multiobjective adaptive surrogate model-based optimization (MO-ASMO), for efficient solution of surrogate-based multiobjective optimization problems (SB-MOPs). Many efforts in the adaptive surrogate modeling (ASM) have successfully resolved challenges for single-objective optimization problems (SOPs). However, there exist additional challenges that have not been addressed for solving multiobjective optimization problems (MOPs) using surrogate-based optimization (SBO). One of the issues we observed from the previous literature is that a possible coupling between the nature of MOPs and sampling strategies has not been thoroughly investigated. Adaptive sampling strategies typically place additional samples near the predicted design solution, which for single-objective problems takes the form of a single point in the design space, frequently with a higher concentration in descending directions. However, MOPs generally have multiple points as a set of design solutions (a predicted Pareto set) with distances between neighboring points that can vary significantly. Locating new sample points using general-purpose sampling methods for each design point in the Pareto set could be possible. However, this strategy will likely require more samples to achieve a given level of MOP solution accuracy, and cannot take the samples generated by the neighboring solutions into consideration. Thus, the new sampling strategies specifically developed for SB-MOPs is required. Future work should include comparative studies between standard adaptive sampling strategies applied to MOPs, and simultaneous sampling strategies that account for all intermediate Pareto-set solutions to provide quantitative insight into the overall effectiveness of candidate sampling methods.

New strategies presented in this chapter are driven by demands in solving challenging high-dimensional, expensive, and black-box (HEB) MOPs with tight and narrow feasible regions. The strategy involved partitioning of expensive and inexpensive function evaluations, and selectively evaluate them at different adaptive refinement stages. The developed sampling strategies are especially effective in avoiding regions in the design space where additional information is not valuable, or the simulation is likely to fail. Also, the sampling strategy for the exploitation of predicted solution regions was developed specifically for MOPs, where the obtained solution is a set of Pareto-optimal points rather than a single design point. Also, for problems with frequent simulation failures, an implicit boundary generation method using the support vector domain description (SVDD) is proposed. With this method, a significant improvement over the Pareto frontier is observed, while limiting the number of full model evaluations to a reasonable level. Using the developed MO-ASMO framework, we expect to explore challenging MOPs previously not exploited well. However, there are gaps that need to be addressed in future studies, including mathematical formulations that can overcome the *curse of dimensionality*, robust sampling and convergence schemes and hybrid methods that do not rely on stochastic elements, and a deeper investigation of balancing exploitation and exploration, to achieve better performance of robustly identifying globally-optimal solutions for challenging HEB MOPs.

Chapter 5 presented a survey of existing numerical design strategies and efficient techniques that can be applied for solving expensive VE relaxation stress-strain relations. A one-dimensional stress relaxation equation for linear viscoelastic (LVE) materials is discussed and analyzed with respect to challenges regarding the convolution integral terms. Several different numerical approaches for integrating the convolution term were discussed, in both frequency- and time-domains. Improving upon computationally-expensive direct integration, several techniques that can mitigate the computational effort are introduced. Especially, the linear time-invariant state-space (LTISS) system approximation [148, 154] opens a large possibility that many other efficient single-step algorithms can be applied to design LVE materials. Possible applicability of the derivative function surrogate modeling (DFSM) [153] is also discussed for dynamic systems that have expensive derivative functions. The chapter summarized different design methodologies that can be applied for solving integro-differential equations (IDEs) that involve convolution integrals. The study also suggested a future research topic focusing on how design parameters can be formulated and manipulated independently to constrain the design solutions within the design regions where the material design solutions are guaranteed to be physically-realizable options.

Chapter 6 specifically presented continuous relaxation spectra design representations for LVE materials. With a view of criteria for the design-appropriate material models established in Corman et al. [12], the LVE material representations were analyzed, and a rationale for selecting the continuous relaxation spectra design representation was presented. The study included transformations between the VE relaxation modulus function and continuous relaxation spectrum, where one transformation direction is straightforward, whereas the other direction is a mathematically ill-posed problem. A demonstration of two-way transformations is presented with several different approximation methods, including the Alfrey and Doty [169], Schwarzl and Staverman [168], and least square approximation methods. A quarter-car automotive suspension test problem with a viscoelastic damper (VED), presented in Chapter 4, is again solved using several LVE material design representations, and the results are visualized in an Ashby-style reduced-dimensionality representation space, introduced by Corman and Ewoldt [132] for delivering intuitive optimal material characteristics. Possible future works are identified for extending the impact of this work. Expected future topics include finding mathematical frameworks for other rheological quantities (e.g., thixotropy, shear-thinning, and other nonlinear material responses), handling material design constraints that will potentially lead physically-realizable materials, and the enhanced reduced-dimensionality design representations that can exhibit multiple peaks in the relaxation spectrum.

Chapter 7 presented an integrated design of non-Newtonian lubricant material properties and surface texture geometrical structure to achieve improved performance beyond what is available only through surface texture design changes with Newtonian fluids. The design problem was solved with two different VE material models (the Criminale-Ericksen-Filbey (CEF) and multimode Giesekus models), and compared to the design solutions with Newtonian fluid as a lubricant. The MO-ASMO framework presented in Chapter 4 was applied to solve this simultaneous fluid and texture design problem with two objective functions. Specifically, MO-ASMO made solution possible with reasonable computational effort, with the capability to efficiently place training samples with separately-evaluated inexpensive constraints, and to adaptively manage implicit constraint boundaries where excessive simulation failures were observed. This capability is specifically needed for the Giesekus fluid model due to its stability properties. Certain combinations of texture shape and fluid parameter values cause model divergence, and the explicit and precise a priori description of boundaries around these input regions is not available. The solution suggests that added viscosity significantly increases normal force generation because the normal force differences (coefficients: Ψ_1 and Ψ_2) create stress elements perpendicular to the shear direction. After a certain level of normal force is achieved, the texture shape mostly remains identical, and the fluid property changes to obtain increased normal force levels. An important observation is that the design solutions are different depending on the material models we used for the optimization, although these cases involve the same physical design problem. This issue is connected to the question of which fluid model or fluid solver can predict the behavior more realistically. Cross-validation of solutions with multiple solvers, as well as an experimental validation of the solution, is needed and suggested as a future research topic.

8.2 Extension of Dissertation Research

Throughout the dissertation research, the studies have been carefully conducted with validated numerical methods and solvers. The Reynolds equation solver for Newtonian fluid and texture used in Chapters 2 and 3 was rigorously validated with experimental data in Schuh et al. [36], and numerical limits in nominal depth were identified in Lee et al. [4]. The non-Newtonian fluid and texture solvers used in Chapter 7 were validated using experimental data from tests using cone-and-plate geometry for a range of concentrations of polyisobutylene (PIB) solution in a Newtonian mineral base oil, given in the supplementary material of Lee et al. [13] and in Appendix C.1. The CEF model and the Giesekus model fluid and texture solvers are further validated with dimple-shaped textures in Schuh [188] and Schuh and Ewoldt [203], respectively. However, these fluid and texture solvers are experimentally validated with a limit of predefined texture shapes of symmetric and asymmetric cylindrical dimples and inclined planes. Design solutions of the studies conducted in this dissertation have following characteristics: (1) texture designs span a full range of disk area, (2) texture designs have arbitrary continuous height profiles over the two-dimensional coordinate system, (3) non-Newtonian fluid design parameters define the polymeric contribution, relaxation time, and nonlinearity of the fluid properties, and (4) the Giesekus fluid design parameterization is selected for polymeric solutions in the fabrication of the non-Newtonian fluids for experiments. Planned extensions of this dissertation research will include experimental validation studies for the texture designs presented here.

The objectives of this planned experimental research are (1) to validate the numerical fluid and texture solvers with the optimal design solutions, (2) to validate the optimality of the design solutions to evaluate design methods utilized in the previous chapters, and (3) to provide methodologies for the integrated design of VE materials and structural geometry with an experiment-in-the-loop optimization process. The numerical design solutions suggest that the spiral blade-like periodic grooves that direct flow inward generates net positive normal force. Possible simplification of this general shape could be a combination of depth of the groove, spiral angle-to-radius (θ/R_o), expanding slope, and contracting slope. This simplification enables the exploration of a wide range of texture shapes in the experimental study, but while maintaining the characteristic shape of the optimal texture design solutions. The textures will be fabricated using the stereolithography (SLA) process, with the geometric dimensions of $R_o = 20$ mm and $h_0 = 269$ μm. The fluids will be fabricated using a PIB with $M_n = 600$ kg/mol, $M_W = 1,000$ kg/mol, and $M_v = 1,200$ kg/mol, as listed by Sigma-Aldrich, dissolved in the Cannon Instrument general-purpose viscosity standard S6 mineral oil at various concentrations. The VE material functions at these various concentrations will be obtained by cone-and-plate rheometric material characterizations, and will be fitted with the steady-state Giesekus model parameters. These fluid model fitting data will be provided to construct a simple surrogate model representing the PIB concentration with respect to the fluid parameter values. This way, it will be possible to continuously estimate the optimal concentration of the PIB with the design solution with material function parameters. Possible outcomes of this planned experimental study are (1) a comparison between the numerical solution and the experimental measurement of optimal free-form height profiles of the texture spanning a full area of the disk, (2) optimality and sensitivity analyses of fluid and geometry parameters using parameter sweeps, and (3) a model that connects the PIB solution concentration to the Giesekus fluid model parameters.

8.3 Outlook

Design representations play a key role in the success of engineering design problems. Different texture design parameterizations resulted in different ranges of performance levels. Depending on the material model representations, the level of freedom in design space could vary, and increased freedom enhances the possibility of discovering fundamentally novel material system designs. On the other hand, the freedom given by certain material models leads the solution to reach an impractical design region due to unknown physical constraints. Thus, selecting and formulating appropriate design representations is very important in problems with complex natures.

Figure 8.1 shows a conceptual three-axis coordinate system of metrics indicating characteristics of models for design. Here, greater distance from the origin indicates improvement. In this figure, as an example, two different models used in Chapters 2 and 3 are compared. As we discussed in Chapter 3, different design models and representations have different characteristics, although the design problem remains the same. The SLP method exhibited higher design dimensionality, supporting enhance design freedom, and resulted in an order-of-magnitude faster solution time compared to the NLP reference model. Thus, the SLP model can be indicated with larger axis values for design representation fidelity and computational efficiency in Fig. 8.1, indicating improvement along both dimensions. However, the analysis

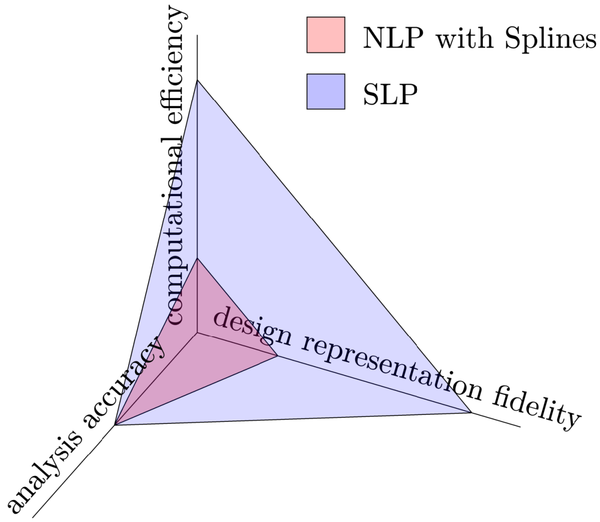

Figure 8.1: Models used in design optimization can be conceptually presented in three-axis coordinate system of (1) design representation fidelity, (2) analysis accuracy, and (3) computational efficiency. Outward direction is superior for all three axes.

result was not different depending on the solver formulations. The SLP method provided analysis accuracy that is comparable to the accuracy of the solution with the black-box model (used with NLP). Thus, both models have the same coordinate location for the analysis accuracy axis in this conceptual model.

With this or similar model comparison frameworks, the material models may be compared in visually-intuitive ways. Pipkin [124] space maps material models with De and Wi number space, and these two metrics characterize different rheological material responses well. Combining the concepts presented in Figure 8.1 and the Pipkin space, rheological material models can also be classified and mapped not only by rheological characteristics, but also by design-appropriateness as well, and this work is left for a topic of future research.

This dissertation focused on the system-level performance-driven integrated design of materials and structural geometry. This approach is particularly useful when these designed materials are used directly for practical applications for which the design problem is being solved. However, designing materials have more difficulties beyond those addressed in this dissertation. When optimal rheology is obtained, these rheological characteristics need to be realized with available material systems. Thus, the resulting rheological design needs to

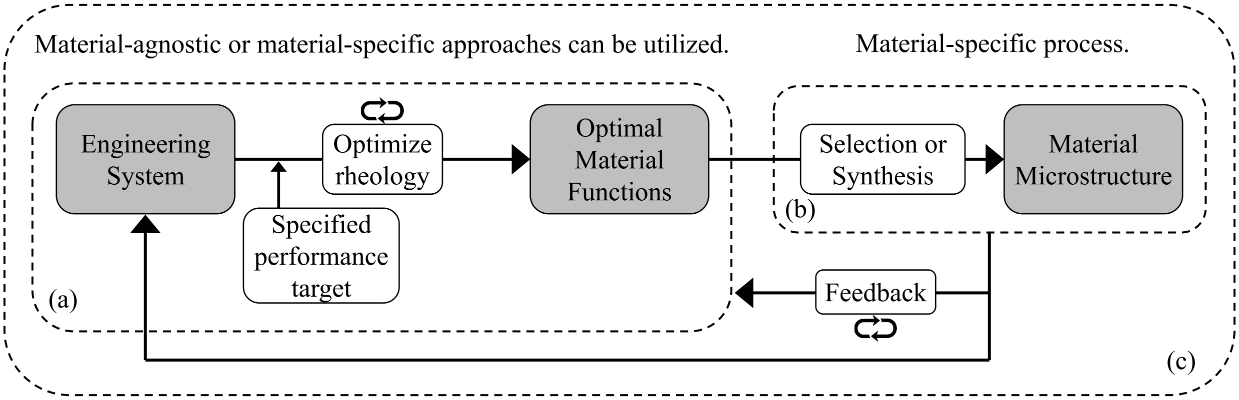

Figure 8.2: A comprehensive design framework that combines higher system-level design and lower microscopic mechanics of material-level design processes. (a) System-level performance-driven integrated design process presented in this dissertation. (b) Material-specific microstructural level design process. (c) Comprehensive design approach that combines both (a) and (b) processes.

connect to the molecular microstructures, microscopic material systems, and submicroscopic mechanisms of the materials. There is a possibility that multidisciplinary design optimization (MDO) architectures and strategies can play a role in solving such problems. From the system-level to submicroscopic levels, multidisciplinary models need to be holistically solved to obtain realizable material design solutions, and MDO strategies can help solve these problems.

Figure 8.2 shows a high-level structure of the larger integrated design framework, combining the current system-to-rheology design effort presented in this dissertation (given in Fig. 8.2a) with material-specific design processes (given in Fig. 8.2b). Importantly, combining these two processes will provide information coming from the mechanics of the material systems (e.g., microscopic material characteristics and limits) fed back to the rheology- and system-level design process, enabling the realization of designed materials in a comprehensive framework.

8.4 Concluding Remarks

This dissertation presented integrated design methodologies, numerical techniques, and solution procedures and insights obtained from solving practical engineering design problems.

Integrated design approaches provided significant design enhancement, mostly at least an order of magnitude better along more than one objective function index. Design methodologies and texture design representations presented in Part I were effective in achieving the dissertation's goals. Material design representations, and practical integrated material and structural geometry designs presented in Part II, successfully demonstrated the advantages of using the proposed integrated design approach and numerical design methodologies.

The methodologies and design practices presented in this dissertation will impact new, unprecedented engineering design opportunities with the paradigm of designing VE materials simultaneously with other system design elements. This new paradigm opens up more expansive possibilities for better designs by exploiting material systems in a holistic approach. Also, the developed design optimization tools (such as the trust-region-assisted SLP method for high-dimensional design problem coupled with simulation, and the MO-ASMOs framework developed for solving challenging SB-MOPs) can be utilized to open up more unexploited design spaces in various domains of engineering design. Suggested topics of future work, including design model comparison framework and multilevel, multiscale, multidisciplinary optimization frameworks, may also have an impact that potentially enables the use of novel materials and discovery of new materials designed based on rational design processes and information. These wide-open possibilities will benefit design engineers by enabling the use of complex materials in their design processes, which was previously not easily-accessible, and will expand impact toward our larger society with more efficient and sustainable ways of development, driven by the utilization of efficiently-designed materials.

Appendices

Appendix A

Viscoelastic Materials and Pipkin Space

A.1 Dimensionless Groups for Viscoelasticity

Many rheologically-complex materials, including linear and nonlinear viscoelastic materials, have characteristic timescales. With material relaxation timescale λ and other extrinsic quantities, such as shear rate $\dot{\lambda}$, frequency $\dot{\omega}$, and observation time t_{char}, two dimensionless numbers can be defined as

$$\text{Deborah number: } \mathrm{De} = \frac{\lambda}{t_{\text{char}}} \text{ or } \lambda\omega\text{, and} \tag{A.1a}$$

$$\text{Weissenberg number: } \mathrm{Wi} = \lambda\dot{\gamma}. \tag{A.1b}$$

The Deborah number defines a ratio of the material's relaxation timescale to the observation time, representing relatively how fast stress relaxation is occurring to the observation time or characteristic time [123]. When the relaxation time is relatively smaller than the observation time ($\mathrm{De} \ll 1$), the material exhibits fluid-like behavior. The Newtonian fluid is the limiting case with $\mathrm{De} \to 0$. When the relaxation time is larger than the observation time ($\mathrm{De} \gg 1$), the material exhibits solid-like behavior. The elastic solid is the other limiting case with $\mathrm{De} \to \infty$.

The Weissenberg number defines a dimensionless shear rate, that can be interpreted as a ratio of elastic to viscous force, or a ratio between two different timescales [112]. Linear viscoelastic (LVE) materials exhibit linear relationship between stress and strain at any given time, which allows linear superposition, in addition to the memory effect that Boltzmann proposed for the LVE. The LVE assumption is only valid in the region with low Wi numbers. Also, in many cases, the materials exhibit only one timescale, and in this case we use De as the choice of dimensionless number [112].

A.2 Pipkin Space

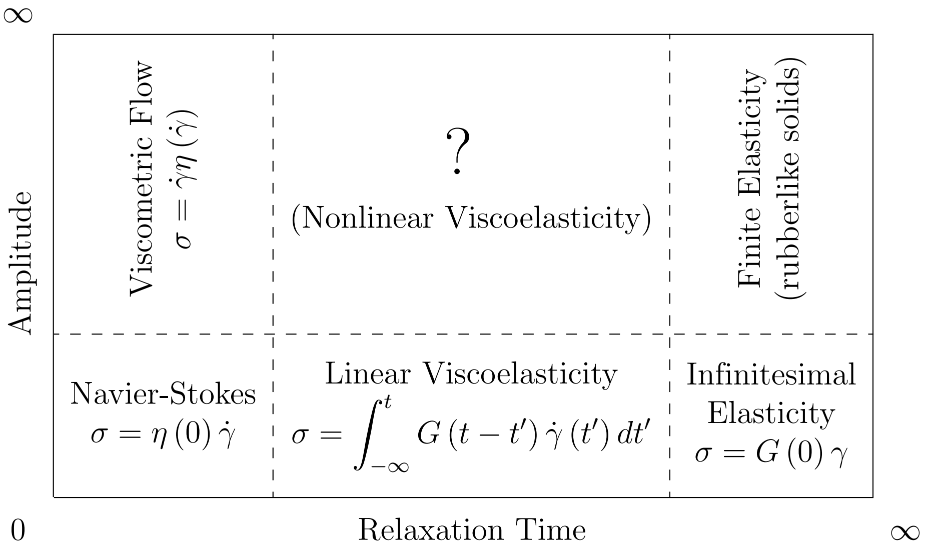

Figure A.1: Pipkin Space [124]

Pipkin space in Fig. A.1 (adapted from Pipkin [124, p. 133]) describes classes of rheological materials in a distorted two-dimensional map of the Deborah number (relaxation time) and the Weissenberg number (amplitude) space. The LVE is located in the region that has small amplitude, but all ranges of the relaxation time. Beyond the small amplitude region, the largest space that has the '?' symbol can be described as a region for nonlinear viscoelasticity. This region can include wide range of material classes with different characteristics, and cannot be represented by a single or a few constitutive equations.

Appendix B

Derivation of CEF-Reynolds Equation

We use the Criminale-Ericksen-Filbey (CEF) model in the incompressible Cauchy-Momentum equations [112, 195],

$$\nabla \cdot \underline{u} = 0 \tag{B.1a}$$

$$\rho \left(\frac{\partial \underline{u}}{\partial t} + \left[\underline{u} \cdot \nabla \right] \underline{u} \right) = -\nabla p + \nabla \cdot \underline{\underline{\tau}} \tag{B.1b}$$

$$\underline{\underline{\tau}} = \eta \left(\dot{\gamma} \right) \underline{\underline{\gamma}}_{(1)} - \frac{1}{2} \Psi_1 \left(\dot{\gamma} \right) \underline{\underline{\gamma}}_{(2)} + \Psi_2 \left(\dot{\gamma} \right) \left[\underline{\underline{\gamma}}_{(1)} \cdot \underline{\underline{\gamma}}_{(1)} \right], \tag{B.1c}$$

where the $\underline{u}$ is the velocity vector, p is the pressure, and ρ is the fluid density, the gradient and divergence operators are appropriate for cylindrical coordinates, and the coordinate system is defined in Fig. B.1.

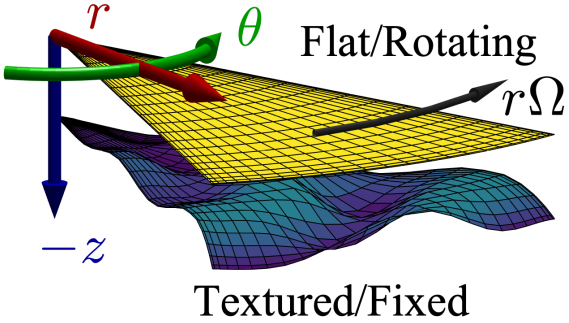

Figure B.1: Periodic cell of textured surface in cylindrical coordinates. The coordinate system and directions of motion are defined as shown.

We can simplify the governing equations in the thin film limit by assuming:

1. $h(r, \theta)/R \to 0$; thin film approximation to neglect velocity gradients in the flow direction.

2. The shear rate is

$$\dot{\gamma}\left(r,\theta\right) \equiv \sqrt{\frac{1}{2}\underline{\underline{\gamma}}_{1} : \underline{\underline{\gamma}}_{1}} \approx \frac{r\Omega}{h\left(r,\theta\right)}, \tag{B.2}$$

   which is independent of z, where Ω is the angular velocity of the flat plate.

3. $\Psi_2 = 0$, so that $\tau_{zz} = 0$.

Under these assumptions, the incompressible Cauchy momentum equations simplify to

$$\frac{1}{r}\frac{\partial}{\partial r}\left(ru_r\right) + \frac{1}{r}\frac{\partial u_\theta}{\partial \theta} + \frac{\partial u_z}{\partial z} = 0 \tag{B.3a}$$

$$-\frac{\partial p}{\partial r} + \eta\left(\dot{\gamma}\right)\frac{\partial^2 u_r}{\partial z^2} + \frac{\Psi_1\left(\dot{\gamma}\right)}{r}\left[\left(\frac{\partial u_r}{\partial z}\right)^2 - \left(\frac{\partial u_\theta}{\partial z}\right)^2\right] + \rho\frac{u_\theta^2}{r} = 0 \tag{B.3b}$$

$$-\frac{1}{r}\frac{\partial p}{\partial \theta} + \eta\left(\dot{\gamma}\right)\frac{\partial^2 u_\theta}{\partial z^2} + \frac{2\Psi_1\left(\dot{\gamma}\right)}{r}\left[\left(\frac{\partial u_r}{\partial z}\right)\left(\frac{\partial u_\theta}{\partial z}\right)\right] - \rho\frac{u_r u_\theta}{r} = 0 \tag{B.3c}$$

$$-\frac{\partial p}{\partial z} = 0, \tag{B.3d}$$

with boundary conditions on the velocity field

$$u_r\left(z = -h\left(r,\theta\right)\right) = u_r\left(z = 0\right) = 0 \tag{B.4a}$$

$$u_\theta\left(z = -h\left(r,\theta\right)\right) = 0, \;\; u_\theta\left(z = 0\right) = r\Omega \tag{B.4b}$$

$$u_z\left(z = -h\left(r,\theta\right)\right) = u_z\left(z = 0\right) = 0 \tag{B.4c}$$

to satisfy the no slip and no penetration conditions, where u_r, u_θ, and u_z are the velocities in the r, θ, and z directions respectively. The resulting simplified Cauchy momentum equations are a set of coupled, non-linear, second order partial differential equations (PDEs) for the velocity.

B.1 Perturbation Solution

Because the governing equations are a set of coupled, non-linear PDEs, we choose to solve for the velocity and pressure fields using a regular perturbation expansion in both the Re_h and De for both the velocity and the pressure [204–206]. We use the non-dimensional variables

$$r^* = \frac{r}{R} \tag{B.5a}$$

$$z^* = \frac{z}{h_0} \tag{B.5b}$$

$$u_r^* = \frac{u_r}{R\Omega} \tag{B.5c}$$

$$u_\theta^* = \frac{u_\theta}{R\Omega} \tag{B.5d}$$

$$u_z^* = \frac{u_z}{R\Omega\left(\frac{h_0}{R}\right)} \tag{B.5e}$$

$$\eta^* = \frac{\eta\left(\dot{\gamma}\right)}{\eta_0} \tag{B.5f}$$

$$\Psi_1^* = \frac{\Psi_1\left(\dot{\gamma}\right)}{\Psi_{10}} \tag{B.5g}$$

$$p^* = \frac{p}{\eta_0\Omega\left(\frac{R}{h_0}\right)^2} \tag{B.5h}$$

where R is the outer radius of the textured disk, h_0 is the maximum gap height, η_0 is the shear shear viscosity, and Ψ_{10} is the zero shear normal stress difference coefficient.

Substituting the non-dimensional variables into the governing equations gives

$$\frac{1}{r^*}\frac{\partial}{\partial r}\left(r^* u_r^*\right) + \frac{1}{r^*}\frac{\partial u_\theta^*}{\partial \theta} + \frac{\partial u_z^*}{\partial z^*} = 0 \tag{B.6a}$$

$$-\frac{\partial p^*}{\partial r^*} + \eta^*\frac{\partial^2 u_r^*}{\partial {z^*}^2} + \mathrm{De}\frac{\Psi_1^*}{r^*}\left[\left(\frac{\partial u_r^*}{\partial z^*}\right)^2 - \left(\frac{\partial u_\theta^*}{\partial z^*}\right)^2\right] + \mathrm{Re}_h\frac{{u_\theta^*}^2}{r^*} = 0 \tag{B.6b}$$

$$-\frac{1}{r^*}\frac{\partial p^*}{\partial \theta} + \eta^*\frac{\partial^2 u_\theta^*}{\partial {z^*}^2} + \mathrm{De}\frac{2\Psi_1^*}{r^*}\left[\left(\frac{\partial u_r^*}{\partial z^*}\right)\left(\frac{\partial u_\theta^*}{\partial z^*}\right)\right] - \mathrm{Re}_h\frac{u_r^* u_\theta^*}{r^*} = 0 \tag{B.6c}$$

$$-\frac{\partial p^*}{\partial z^*} = 0 \tag{B.6d}$$

where we have defined the Reynolds number as $\mathrm{Re}_h \equiv \frac{\rho\Omega h_0^2}{\eta_0}$ and the Deborah number as $\mathrm{De} \equiv \frac{\Psi_{10}\Omega}{\eta_0}$.

We expand the velocity and pressure fields using a regular perturbation expansion in both the Re_h and De [204–206],

$$u_r^* = u_{r_0}^* + \mathrm{Re}_h u_{r_I}^* + \mathrm{De} u_{r_E}^* + O\left(\mathrm{Re}_h^2, \mathrm{De}^2\right) \tag{B.7a}$$

$$u_\theta^* = u_{\theta_0}^* + \mathrm{Re}_h u_{\theta_I}^* + \mathrm{De} u_{\theta_E}^* + O\left(\mathrm{Re}_h^2, \mathrm{De}^2\right) \tag{B.7b}$$

$$u_z^* = u_{z_0}^* + \mathrm{Re}_h u_{z_I}^* + \mathrm{De} u_{z_E}^* + O\left(\mathrm{Re}_h^2, \mathrm{De}^2\right) \tag{B.7c}$$

$$p^* = p_0^* + \mathrm{Re}_h p_I^* + \mathrm{De} p_E^* + O\left(\mathrm{Re}_h^2, \mathrm{De}^2\right). \tag{B.7d}$$

We expand in this manner because in the limit that both the Re_h and De tend to 0, we should recover the governing equations for the traditional Reynolds equation [36, 42].

After substituting the expansions into the governing equations and collecting the same order terms, we obtain the following non-dimensional equations:

0th Order Terms

$$\frac{1}{r^*}\frac{\partial}{\partial r}\left(r^* u_{r_0}^*\right) + \frac{1}{r^*}\frac{\partial u_{\theta_0}^*}{\partial \theta} + \frac{\partial u_{z_0}^*}{\partial z^*} = 0 \tag{B.8a}$$

$$\eta^* \frac{\partial^2 u_{r_0}^*}{\partial {z^*}^2} - \frac{\partial p_0^*}{\partial r^*} = 0 \tag{B.8b}$$

$$\eta^* \frac{\partial^2 u_{\theta_0}^*}{\partial {z^*}^2} - \frac{1}{r^*}\frac{\partial p_0^*}{\partial \theta} = 0 \tag{B.8c}$$

$$\frac{\partial p_0^*}{\partial z^*} = 0 \tag{B.8d}$$

Order Re$_h$ Terms

$$\frac{1}{r^*}\frac{\partial}{\partial r}\left(r^* u_{r_I}^*\right) + \frac{1}{r^*}\frac{\partial u_{\theta_I}^*}{\partial \theta} + \frac{\partial u_{z_I}^*}{\partial z^*} = 0 \tag{B.9a}$$

$$\eta^* \frac{\partial^2 u_{r_I}^*}{\partial {z^*}^2} - \frac{\partial p_I^*}{\partial r^*} + \frac{{u_{\theta_0}^*}^2}{r^*} = 0 \tag{B.9b}$$

$$\eta^* \frac{\partial^2 u^*_{\theta_I}}{\partial z^{*2}} - \frac{1}{r^*}\frac{\partial p^*_I}{\partial \theta} - \frac{u^*_{r_0} u^*_{\theta_0}}{r^*} = 0 \tag{B.9c}$$

$$\frac{\partial p^*_I}{\partial z^*} = 0 \tag{B.9d}$$

Order De Terms

$$\frac{1}{r^*}\frac{\partial}{\partial r}\left(r^* u^*_{r_E}\right) + \frac{1}{r^*}\frac{\partial u^*_{\theta_E}}{\partial \theta} + \frac{\partial u^*_{z_E}}{\partial z^*} = 0 \tag{B.10a}$$

$$\eta^* \frac{\partial^2 u^*_{r_E}}{\partial z^{*2}} - \frac{\partial p^*_E}{\partial r^*} + \frac{\Psi^*_1}{r^*}\left[\left(\frac{\partial u^*_{r_0}}{\partial z^*}\right)^2 - \left(\frac{\partial u^*_{\theta_0}}{\partial z^*}\right)^2\right] = 0 \tag{B.10b}$$

$$\eta^* \frac{\partial^2 u^*_{\theta_E}}{\partial z^{*2}} - \frac{1}{r^*}\frac{\partial p^*_E}{\partial \theta} + \frac{2\Psi^*_1}{r^*}\left[\left(\frac{\partial u^*_{r_0}}{\partial z^*}\right)\left(\frac{\partial u^*_{\theta_0}}{\partial z^*}\right)\right] = 0 \tag{B.10c}$$

$$\frac{\partial p^*_E}{\partial z^*} = 0 \tag{B.10d}$$

To simplify the total number of governing equations, we combine the corresponding equations for the order Re_h and order De terms, since both equations are linear in the variables of interest and both must satisfy the incompressibility constraint. After performing the superposition, we introduce new variables, defined as

$$u^*_{r_1} = u^*_{r_I} + u^*_{r_E} \tag{B.11a}$$

$$u^*_{\theta_1} = u^*_{\theta_I} + u^*_{\theta_E} \tag{B.11b}$$

$$u^*_{z_1} = u^*_{z_I} + u^*_{z_E} \tag{B.11c}$$

$$p^*_1 = p^*_I + p^*_E \tag{B.11d}$$

so that the resulting equations are

$$\frac{1}{r^*}\frac{\partial}{\partial r}\left(r^* u^*_{r_1}\right) + \frac{1}{r^*}\frac{\partial u^*_{\theta_1}}{\partial \theta} + \frac{\partial u^*_{z_1}}{\partial z^*} = 0 \tag{B.12a}$$

$$\eta^* \frac{\partial^2 u^*_{r_1}}{\partial z^{*2}} - \frac{\partial p^*_1}{\partial r^*} + \frac{\Psi^*_1}{r^*}\left[\left(\frac{\partial u^*_{r_0}}{\partial z^*}\right)^2 - \left(\frac{\partial u^*_{\theta_0}}{\partial z^*}\right)^2\right] + \frac{{u^*_{\theta_0}}^2}{r^*} = 0 \tag{B.12b}$$

$$\eta^* \frac{\partial^2 u^*_{\theta_1}}{\partial z^{*2}} - \frac{1}{r^*}\frac{\partial p^*_1}{\partial \theta} + \frac{2\Psi^*_1}{r^*}\left[\left(\frac{\partial u^*_{r_0}}{\partial z^*}\right)\left(\frac{\partial u^*_{\theta_0}}{\partial z^*}\right)\right] - \frac{u^*_{r_0} u^*_{\theta_0}}{r^*} = 0 \tag{B.12c}$$

$$\frac{\partial p_1}{\partial z^*} = 0. \tag{B.12d}$$

In dimensional form, this gives us the final set of governing equations with appropriate boundary conditions. Once the 0th order terms are known, the 1st order terms can be obtained.

0th Order

$$\frac{1}{r}\frac{\partial}{\partial r}\left(r u_{r_0}\right) + \frac{1}{r}\frac{\partial u_{\theta_0}}{\partial \theta} + \frac{\partial u_{z_0}}{\partial z} = 0 \tag{B.13a}$$

$$\eta\left(\dot{\gamma}\right)\frac{\partial^2 u_{r_0}}{\partial z^2} - \frac{\partial p_0}{\partial r} = 0 \tag{B.13b}$$

$$\eta\left(\dot{\gamma}\right)\frac{\partial^2 u_{\theta_0}}{\partial z^2} - \frac{1}{r}\frac{\partial p_0}{\partial \theta} = 0 \tag{B.13c}$$

$$\frac{\partial p_0}{\partial z} = 0 \tag{B.13d}$$

$$u_{r_0}\left(z = -h\left(r,\theta\right)\right) = u_{r_0}\left(z = 0\right) = 0 \tag{B.13e}$$

$$u_{\theta_0}\left(z = -h\left(r,\theta\right)\right) = 0,\ u_{\theta_0}\left(z = 0\right) = r\Omega \tag{B.13f}$$

$$u_{z_0}\left(z = -h\left(r,\theta\right)\right) = u_{z_0}\left(z = 0\right) = 0 \tag{B.13g}$$

1st Order

$$\frac{1}{r}\frac{\partial}{\partial r}\left(r u_{r_1}\right) + \frac{1}{r}\frac{\partial u_{\theta_1}}{\partial \theta} + \frac{\partial u_{z_1}}{\partial z} = 0 \tag{B.14a}$$

$$\eta\left(\dot{\gamma}\right)\frac{\partial^2 u_{r_1}}{\partial z^2} - \frac{\partial p_1}{\partial r} + \frac{\Psi_1\left(\dot{\gamma}\right)}{r}\left[\left(\frac{\partial u_{r_0}}{\partial z}\right)^2 - \left(\frac{\partial u_{\theta_0}}{\partial z}\right)^2\right] + \rho\frac{u^2_{\theta_0}}{r} = 0 \tag{B.14b}$$

$$\eta\left(\dot{\gamma}\right)\frac{\partial^2 u_{\theta_1}}{\partial z^2} - \frac{1}{r}\frac{\partial p_1}{\partial \theta} + \frac{2\Psi_1\left(\dot{\gamma}\right)}{r}\left[\left(\frac{\partial u_{r_0}}{\partial z}\right)\left(\frac{\partial u_{\theta_0}}{\partial z}\right)\right] - \rho\frac{u_{r_0}u_{\theta_0}}{r} = 0 \tag{B.14c}$$

$$\frac{\partial p_1}{\partial z} = 0 \tag{B.14d}$$

$$u_{r_1}\left(z = -h\left(r,\theta\right)\right) = u_{r_1}\left(z = 0\right) = 0 \tag{B.14e}$$

$$u_{\theta_1}\left(z=-h\left(r,\theta\right)\right)=u_{\theta_1}\left(z=0\right)=0 \tag{B.14f}$$

$$u_{z_1}\left(z=-h\left(r,\theta\right)\right)=u_{z_1}\left(z=0\right)=0 \tag{B.14g}$$

B.2 CEF-Reynolds Equation

We solve the governing equations given in the boxes above in the same manner as the tradition Reynolds equation [36, 42]. The steps are:

1. Obtain the velocities in the r and θ direction in terms of the unknown pressure field and the boundary conditions.
2. Substitute the obtained velocities into the incompressibility equation.
3. Integrate over the z direction and use Leibniz's rule for integrating the derivatives in the r and θ direction.

Using these steps, we eventually obtain two equations for the unknown pressure fields p_0 and p_1, given as

0th Order

$$\frac{1}{r}\frac{\partial}{\partial r}\left(\frac{rh^3}{12\eta}\frac{\partial p_0}{\partial r}\right)+\frac{1}{r}\frac{\partial}{\partial\theta}\left(\frac{h^3}{12\eta r}\frac{\partial p_0}{\partial\theta}\right)=\frac{1}{r}\frac{\partial}{\partial\theta}\left(\frac{r\Omega h}{2}\right) \tag{B.15}$$

1st Order

$$\frac{1}{r}\frac{\partial}{\partial r}\left(\frac{rh^3}{12\eta}\frac{\partial p_1}{\partial r}\right)+\frac{1}{r}\frac{\partial}{\partial\theta}\left(\frac{h^3}{12\eta r}\frac{\partial p_1}{\partial\theta}\right)=\frac{1}{r}\frac{\partial}{\partial r}\left(rG_r\right)+\frac{1}{r}\frac{\partial}{\partial\theta}\left(G_\theta\right) \tag{B.16a}$$

$$G_r=\frac{r\Omega h}{40}\left(\frac{\rho\Omega h^2}{\eta}\right)B_r+\frac{r\Omega h}{12}\left(\frac{\Psi_1\Omega}{\eta}\right)A_r \tag{B.16b}$$

$$B_r=1-\frac{1}{3}\left(\frac{1}{\eta\Omega}\frac{\partial p_0}{\partial\theta}\left(\frac{h}{r}\right)^2\right)+\frac{1}{28}\left(\frac{1}{\eta\Omega}\frac{\partial p_0}{\partial\theta}\left(\frac{h}{r}\right)^2\right)^2 \tag{B.16c}$$

$$A_r=-1-\frac{1}{20}\left(\frac{1}{\eta\Omega}\frac{\partial p_0}{\partial\theta}\left(\frac{h}{r}\right)^2\right)^2+\frac{1}{20}\left(\frac{1}{\eta\Omega}r\frac{\partial p_0}{\partial r}\left(\frac{h}{r}\right)^2\right)^2 \tag{B.16d}$$

$$G_\theta = \frac{r\Omega h}{240}\left(\frac{\rho\Omega h^2}{\eta}\right)B_\theta + \frac{r\Omega h}{120}\left(\frac{\Psi_1\Omega}{\eta}\right)A_\theta \tag{B.16e}$$

$$B_\theta = \left(\frac{1}{\eta\Omega}r\frac{\partial p_0}{\partial r}\left(\frac{h}{r}\right)^2\right) - \frac{3}{14}\left(\frac{1}{(\eta\Omega)^2}r\frac{\partial p_0}{\partial r}\frac{\partial p_0}{\partial \theta}\left(\frac{h}{r}\right)^4\right) \tag{B.16f}$$

$$A_\theta = \left(\frac{1}{(\eta\Omega)^2}r\frac{\partial p_0}{\partial r}\frac{\partial p_0}{\partial \theta}\left(\frac{h}{r}\right)^4\right) \tag{B.16g}$$

Equation B.15 resembles the traditional form of the Reynolds equation in cylindrical coordinates [36, 207], and includes shear thinning. Equation B.16a also resembles the traditional Reynolds equation, and the right hand side depends on the local Reynolds number Re_h and the local relation of elasticity to viscosity, which can be interpreted as a local Deborah number, De.

Once Equations B.15 and B.16a are solved (with suitable boundary conditions), the velocity field can be obtained. The obtained pressure and velocity fields can then be used to calculate the normal force and torque on the moving flat plate.

Appendix C

Experimental Validation and Sensitivity Analysis of Fluid and Texture Solvers

C.1 Experimental Validation Using Cone-and-Plate Rheometer

The thin-film Reynolds equation with Criminale-Ericksen-Filbey (CEF) fluid (CEF-Reynolds) and the full 3-D momentum equation with Giesekus fluid (Giesekus-3D) solvers are validated against steady shear experiments for varying concentrations of polyisobutylene (PIB) in S6 base mineral oil using a cone-and-plate rheometer geometry of Θ=1.011° and R=0.02 m, where Θ and R denote the cone angle and the radius, respectively. Since we use the same parameterizations for CEF and Giesekus fluids, we performed a least-square fitting for the two-mode Giesekus fluid using the experimental data for six different concentrations: 0.05, 0.1, 0.18, 0.357, 0.5, and 0.76 wt% of PIB solution in a Newtonian mineral base oil (trade name: S6 Newtonian viscosity standard, Cannon Instrument Company, η_s=9.624 mPa-s at 20°C). Using fitted parameters, the cone-and-plate geometry is numerically modeled for both CEF-Reynolds and Giesekus-3D solvers and simulated for the six fluid concentrations and the entire angular velocity range that covers the shear rate range of obtained experimental data.

The comparison of the raw torque T and the raw normal force (thrust) F_N experimental data (circles) to simulation results (dotted line: CEF-Reynolds, solid line: Giesekus-3D) is shown in Fig. C.1. Good agreement is seen between the experiments and the simulations for the cone-and-plate rheometer geometry with a steady shear condition.

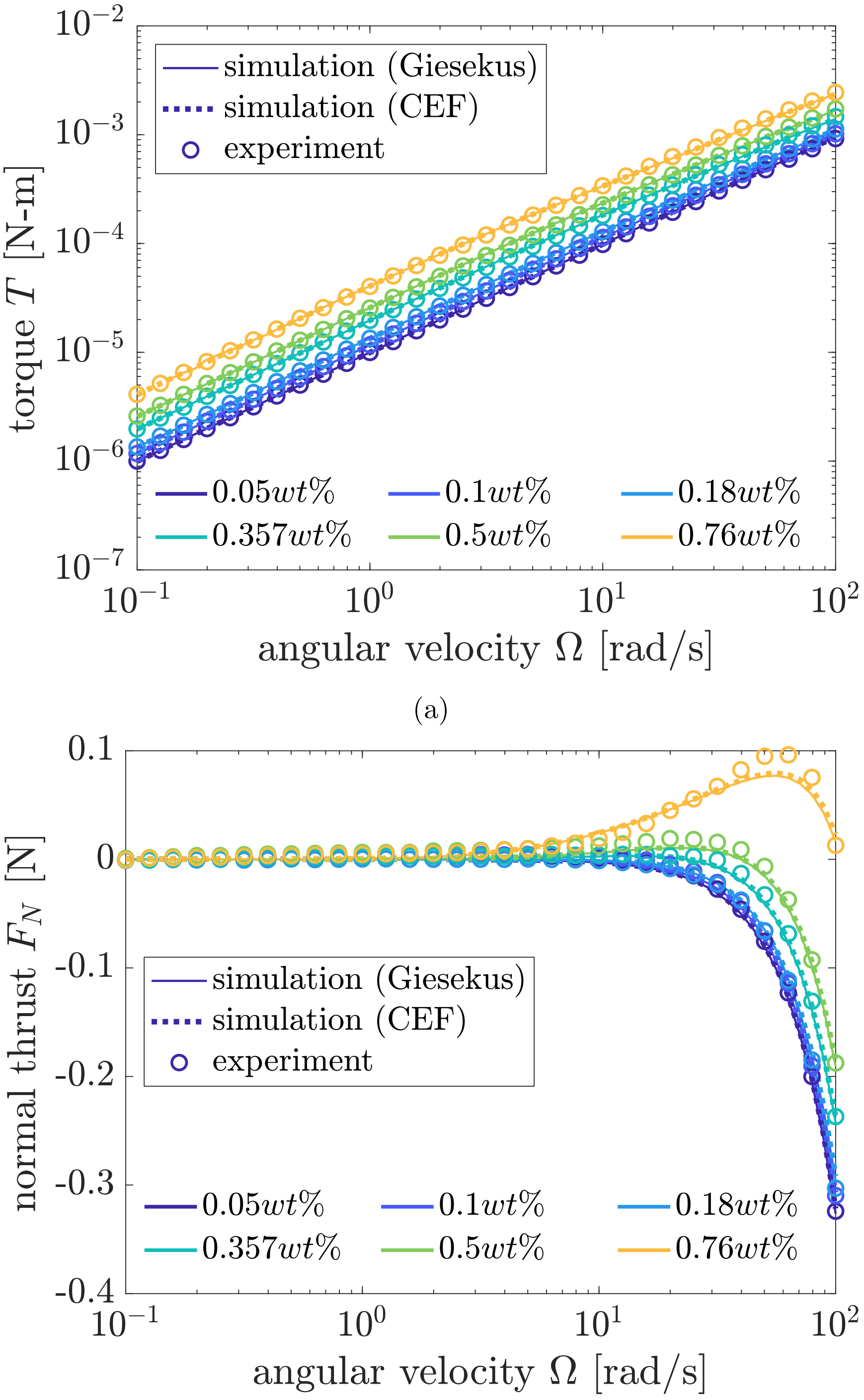

(a)

(b)

Figure C.1: Comparison of raw torque T and raw normal force F_N data from experiments using a cone-and-plate rheometer geometry and simulations using CEF-Reynolds and Giesekus-3D solvers. (a) Torque T. (b) Normal force F_N.

C.2 Solver Parameter Sensitivity Analysis

We analyzed ranges of solutions affected by mechanical and fluid parameter uncertainties for our numerical solvers using a differential sensitivity analysis method. Mechanical parameters include geometrical and operating parameters, including the radius of the parallel discs, minimum controlled gap height between discs, and angular velocity of the rotating disc. Fluid parameters include operating temperature, which affects solvent viscosity. Design variables in the fluid parameters, such as polymeric viscosity, relaxation time, and the mobility factor of design target viscoelastic fluid, are not assessed here because they are design targets rather than measured properties in this study.

The radius of the discs (R_o) as well as the textured disc can be very precisely manufactured for the tribo-rheometric experiments. However, to see the effect of radius changes, we set a deviation of ± 50 μm. The nominal gap height ($h_{\min}$), which serves as a minimum gap height between the discs in this study, can affect the apparent viscosity of the system directly. According to Schuh and Ewoldt [30], the maximum gap offset between true and apparent gap values is 19 μm during the gap zeroing procedure in the experiment. Thus, we set a deviation of $+19$ μm for the minimum gap height. The measured value of the solvent viscosity (η_s) is 9.624 mPa-s, which is less than 5% lower than the specification value of 10 mPa-s; thus, we set a deviation of $\pm 5\%$ for the solvent viscosity. The measured density of the solvent (ρ_s) is 873.4 kg/m^3, which is 0.5% lower than the specification value of 878 kg/m^3; thus, we set a deviation of $\pm 1\%$ for the solvent density that covers this difference with enough margin.

Tables C.1 and C.2 show changes in the objective functions (f_1: power input, f_2: normal force) when each parameter variable deviates specified amount for CEF-Reynolds and Giesekus-3D solvers respectively. We performed this differential sensitivity analysis on 6 select designs for each case; thus, the deviations in the objective functions have mean values and standard deviation values (with ± sign) in their table entries.

Table C.1: Result of differential sensitivity analysis for the CEF-Reynolds solver parameters

variable	deviation	deviations in f_1 [%]	deviations in f_2 [%]
$R_o = 20$ mm	-50 μm	-0.941 ± 0.031	-0.924 ± 0.035
	$+50$ μm	$+0.948\pm0.032$	$+0.931\pm0.035$
$h_{\min} = 269$ μm	$+19$ μm	-4.164 ± 0.492	-11.398 ± 0.390
$\Omega = 10$ rad/s	-1%	-1.772 ± 0.125	-0.927 ± 0.159
	$+1\%$	$+1.785\pm0.129$	$+0.928\pm0.160$
$\eta_s = 9.624$ mPa-s	-5%	-2.481 ± 1.619	-2.024 ± 1.368
	$+5\%$	$+2.481\pm1.619$	$+2.023\pm1.368$
$\rho_s = 873.4$ kg/m^3	-1%	+7.6e-6±5.8e-6	-0.048 ± 0.083
	$+1\%$	−7.6e-6±5.8e-6	$+0.048\pm0.083$

Table C.2: Result of differential sensitivity analysis for the Giesekus-3D solver parameters

variable	deviation	deviations in f_1 [%]	deviations in f_2 [%]
$R_o = 20$ mm	-50 μm	-0.860 ± 0.265	-0.458 ± 1.314
	$+50$ μm	$+0.978\pm0.018$	$+1.005\pm0.020$
$h_{\min} = 269$ μm	$+19$ μm	-4.599 ± 0.855	-10.100 ± 1.574
$\Omega = 10$ rad/s	-1%	-1.787 ± 0.270	-0.501 ± 1.329
	$+1\%$	$+1.912\pm0.059$	$+1.047\pm0.077$
$\eta_s = 9.624$ mPa-s	-5%	-2.770 ± 1.662	-1.869 ± 0.887
	$+5\%$	$+2.570\pm1.684$	$+2.479\pm2.178$
$\rho_s = 873.4$ kg/m^3	-1%	$+0.106\pm0.271$	$+0.442\pm1.343$
	$+1\%$	-0.052 ± 0.128	$+0.316\pm0.474$

Appendix D

Support Vector Domain Description

We constructed the Gaussian kernel-based support vector domain description (SVDD) [96] using a maximization problem given as

$$\underset{\underline{0}\leq\underline{\beta}\leq\underline{C}}{\text{maximize}} \quad W\left(\underline{\beta}\right) = \sum_i \beta_i K_G\left(\underline{x}_i, \underline{x}_i\right) - \sum_{i,j} \beta_i \beta_j K_G\left(\underline{x}_i, \underline{x}_j\right) \tag{D.1}$$

where $\underline{C}$ is a vector of constant C, which is a parameter value that constrains the Lagrange multiplier $\underline{\beta}$ and is used to detect the outliers of the described domain. Using the Gaussian kernel function (or any other kernel function that satisfies Mercer's theorem [208]) allows the implicit mapping of objects $\underline{x}$ to some feature space, which allows the encapsulating hypersphere to tightly describe the region of the clouds of objects. The Gaussian kernel is defined as

$$K_G\left(\underline{x}_i, \underline{x}_j\right) = \exp\left(-q\left|\left|\underline{x}_i - \underline{x}_j\right|\right|^2\right), \tag{D.2}$$

where $q \geq 0$ is the width parameter, which quantifies how tightly-encapsulate the boundaries of the point clouds will be. Testing if any arbitrary point $\underline{z}$ is inside the encapsulated domain can be performed using the computation of distance from the center of the featured space constructed from Eq. D.1 given as

$$R^2\left(\underline{z}\right) = K_G\left(\underline{z}, \underline{z}\right) - 2\sum_i \beta_i K_G\left(\underline{z}, \underline{x}_i\right) + \sum_{i,j} \beta_i \beta_j K_G\left(\underline{x}_i, \underline{x}_j\right) \tag{D.3}$$

and the arbitrary point $\underline{z}$ is inside the described boundary if

$$R^2(\underline{x}) - R^2(\underline{z}) = K_G(\underline{x},\underline{x}) - K_G(\underline{z},\underline{z}) + 2\sum_i \beta_i \left(K_G(\underline{z},\underline{x}_i) - K_G(\underline{x}_i,\underline{x}_i)\right) \geq 0 \qquad \text{(D.4)}$$

where $\underline{x}$ is a bounding point, which is called a support vector.

When training the constraint boundaries using the SVDD technique, getting the exact 'radius' of the boundary encapsulating training points can be practically obtained by the maximum value of the radii of all the training points. This radius value exactly confine all the training points with zero tolerance.

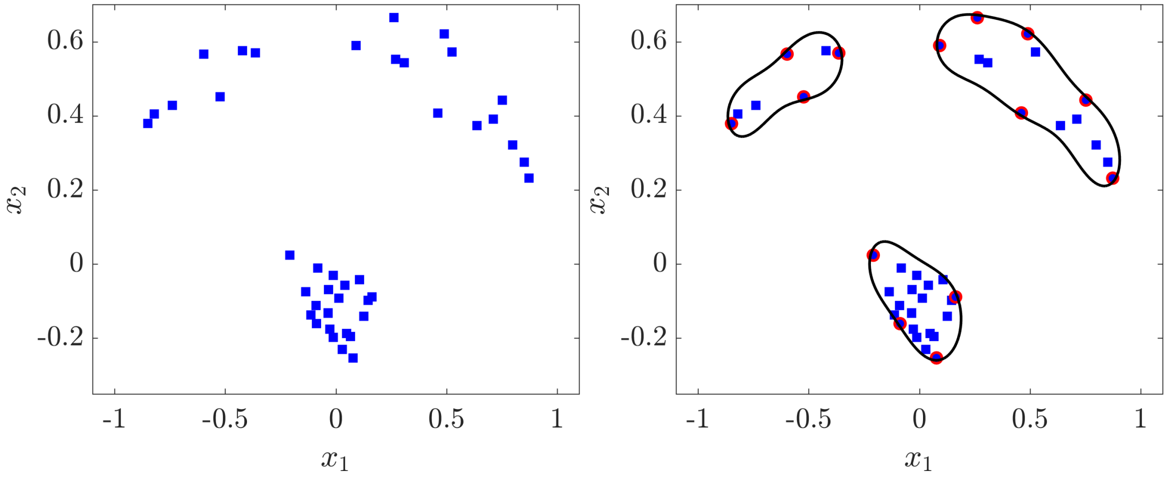

(a) (b)

Figure D.1: A test case showing how the SVDD algorithm describes boundaries of the data point clouds. (a) Artificial data set in 2D space. (b) The support vectors (data points with red circles) and the domain encapsulating the data point clouds (black curved lines).

Fig. D.1 shows a test case with an artificial data set in two-dimensional space. A detailed description of the SVDD derivation can be found in Tax and Duin [96], and more test cases using the SVDD based on the Gaussian kernel are demonstrated in Malak and Paredis [97].

References

[1] Raphael T. Haftka. Simultaneous analysis and design. *AIAA Journal*, 23(7):1099–1103, July 1985. doi: 10.2514/3.9043.

[2] Evin J. Cramer, J. E. Dennis Jr., Paul D. Frank, Robert Michael Lewis, and Gregory R. Shubin. Problem formulation for multidisciplinary optimization. *SIAM Journal on Optimization*, 4(4):754–776, November 1994. doi: 10.1137/0804044.

[3] Daiyu Zhang, Baowei Song, Peng Wang, and Yanru He. Performance evaluation of MDO architectures within a variable complexity problem. *Mathematical Problems in Engineering*, 2017:2759762, February 2017. doi: 10.1155/2017/2759762.

[4] Yong Hoon Lee, Jonathon K. Schuh, Randy H. Ewoldt, and James T. Allison. Enhancing full-film lubrication performance via arbitrary surface texture design. *Journal of Mechanical Design*, 139(5):053401, March 2017. doi: 10.1115/1.4036133.

[5] Ronghu Chi, Zhongsheng Hou, Biao Huang, and Shangtai Jin. A unified data-driven design framework of optimality-based generalized iterative learning control. *Computers & Chemical Engineering*, 77(9):10–23, June 2015. doi: 10.1016/j.compchemeng.2015.03.003.

[6] Albert E. Patterson, Yong Hoon Lee, and James T. Allison. Overview of the development and enforcement of process-driven manufacturability constraints in product design. In *Proceedings of the ASME 2019 International Design Engineering Technical Conferences, Volume 4: 24th Design for Manufacturing and the Life Cycle Conference*, number DETC2019-97384, page V004T05A001, Anaheim CA, August 2019. ASME. doi: 10.1115/DETC2019-97384.

[7] Miguel Seabra, José Azevedo, Aurélio Araújo, Luís Reis, Elodie Pinto, Nuno Alves, Rui Santos, and João Pedro Mortágua. Selective laser melting (SLM) and topology optimization for lighter aerospace componentes. *Procedia Structural Integrity*, 1:289–296, April 2016. doi: 10.1016/j.prostr.2016.02.039.

[8] Daniel R. Herber and James T. Allison. A problem class with combined architecture, plant, and control design applied to vehicle suspensions. *Journal of Mechanical Design*, 141(10):101401, October 2019. doi: 10.1115/1.4043312.

[9] James T. Allison, Tinghao Guo, and Zhi Han. Co-design of an active suspension using simultaneous dynamic optimization. *Journal of Mechanical Design*, 136(8):081003, August 2014. doi: 10.1115/1.4027335.

[10] Michael F. Ashby, Hugh Shercliff, and David Cebon. *Materials: Engineering, Science, Processing and Design*. Butterworth-Heinemann, Oxford, 3rd edition, 2013. isbn: 978-0-08-099434-5.

[11] Michael F. Ashby. *Materials Selection in Mechanical Design*. Butterworth-Heinemann, Oxford, UK, 5th edition, 2016. isbn: 978-0-08-100599-6.

[12] R. E. Corman, Lakshmi Rao, N. Ashwin Bharadwaj, James T. Allison, and Randy H. Ewoldt. Setting material function design targets for linear viscoelastic materials and structures. *Journal of Mechanical Design*, 138(5):051402, March 2016. doi: 10.1115/1.4032698.

[13] Yong Hoon Lee, Jonathon K. Schuh, Randy H. Ewoldt, and James T. Allison. Simultaneous design of non-Newtonian lubricant and surface texture using surrogate-based multiobjective optimization. *Structural and Multidisciplinary Optimization*, 60(1): 99–116, January 2019. doi: 10.1007/s00158-019-02201-1.

[14] Yong Hoon Lee, Vedant, Randy H. Ewoldt, and James T. Allison. Strain-actuated solar arrays for spacecraft attitude control assisted by viscoelastic damping. In *Advances in Structural and Multidisciplinary Optimization: Proceedings of the 13th World Congress of Structural and Multidisciplinary Optimization*, pages 149–155, Beijing, China, May 2019. Dalian University of Technology Electronic & Audio-Visual Press. isbn: 978-7-89437-207-9.

[15] Y. Wakuda, M.and Yamauchi, S. Kanzaki, and Y. Yasuda. Effect of surface texturing on friction reduction between ceramic and steel materials under lubricated sliding contact. *Wear*, 254(3-4):356–363, February 2003. doi: 10.1016/S0043-1648(03)00004-8.

[16] Izhak Etsion. Improving tribological performance of mechanical components by laser surface texturing. *Tribology Letters*, 17:733–737, November 2004. doi: 10.1007/s11249-004-8081-1.

[17] Ashwin Ramesh, Wasim Akram, Surya P. Mishra, Andrew H. Cannon, Andreas A. Polycarpou, and William P. King. Friction characteristics of microtextured surfaces under mixed and hydrodynamic lubrication. *Tribology International*, 57:170–176, January 2013. doi: 10.1016/j.triboint.2012.07.020.

[18] Michael T. Johnston, William P. King, and Randy H. Ewoldt. Shear stress characteristics of microtextured surfaces in gap-controlled hydrodynamic lubrication. *Tribology International*, 82(Part A):123–132, February 2015. doi: 10.1016/j.triboint.2014.10.005.

[19] Lakshmi Gururaja Rao, Jonathon K. Schuh, Randy H. Ewoldt, and James T. Allison. On using adaptive surrogate modeling in design for efficient fluid power. In *Proceedings of the*

ASME 2015 International Design Engineering Technical Conferences and Computers and Information in Engineering Conference. Volume 2B: 41st Design Automation Conference, number DETC2015-46832, page V02BT03A024, Boston, MA, August 2015. ASME. doi: 10.1115/DETC2015-46832.

[20] Haiwu Yu, Xiaolei Wang, and Fei Zhou. Geometric shape effects of surface texture on the generation of hydrodynamic pressure between conformal contacting surfaces. *Tribology Letters*, 37:123–130, February 2010. doi: 10.1007/s11249-009-9497-4.

[21] S. M. Hsu, Y. Jing, D. Hua, , and H. Zhang. Friction reduction using discrete surface textures: principle and design. *Journal of Physics D: Applied Physics*, 47(33):335307, July 2014. doi: 10.1088/0022-3727/47/33/335307.

[22] M. Fesanghary and M. M. Khonsari. On the optimum groove shapes for load-carrying capacity enhancement in parallel flat surface bearings: Theory and experiment. *Tribology International*, 67:254–262, November 2013. doi: 10.1016/j.triboint.2013.08.001.

[23] C. Shen and M. M. Khonsari. Effect of dimple's internal structure on hydrodynamic lubrication. *Tribology Letters*, 52:415–430, December 2013. doi: 10.1007/s11249-013-0225-8.

[24] S. Kango, D. Singh, and R.K. Sharma. Numerical investigation on the influence of surface texture on the performance of hydrodynamic journal bearing. *Meccanica*, 47: 469–482, February 2012. doi: 10.1007/s11012-011-9460-y.

[25] M. B. Dobrica, M. Fillon, M. D. Pascovici, and T. Cicone. Optimizing surface texture for hydrodynamic lubricated contacts using a mass-conserving numerical approach. *Proceedings of the Institution of Mechanical Engineers, Part J: Journal of Engineering Tribology*, 224(8):737–750, August 2010. doi: 10.1243/13506501JET673.

[26] Toshikazu Nanbu, Ning Ren, Yoshiteru Yasuda, Dong Zhu, and Q. Jane Wang. Micro-textures in concentrated conformal-contact lubrication: effects of texture bottom shape and surface relative motion. *Tribology Letters*, 29(3):241–252, March 2008. doi: 10.1007/s11249-008-9302-9.

[27] Jing Han, Liang Fang, Jiapeng Sun, Yanqing Wang, Shirong Ge, and Hua Zhu. Hydrodynamic lubrication of surfaces with asymmetric microdimple. *Tribology Transactions*, 54(4):607–615, 2011. doi: 10.1080/10402004.2011.584364.

[28] R. A. Burton. Effects of two-dimensional, sinusoidal roughness on the load support characteristics of a lubricant film. *ASME Journal of Basic Engineering*, 85(2):258–262, June 1963. doi: 10.1115/1.3656572.

[29] S. T. Tzeng and Edward Saibel. Surface roughness effect on slider bearing lubrication. *ASLE Transactions*, 10(3):334–348, 1967. doi: 10.1080/05698196708972191.

[30] Jonathon K. Schuh and Randy H. Ewoldt. Asymmetric surface textures decrease friction with newtonian fluids in full film lubricated sliding contact. *Tribology International*, 97:490–498, May 2016. doi: 10.1016/j.triboint.2016.01.016.

[31] Hod Lipson. Frontiers in additive manufacturing. *The Bridge*, 42(1):5–12, March 2012.

[32] Xiuqing Hao, Shiyuan Pei, Li Wang, Hua Xu, Ning He, and Bingheng Lu. Microtexture fabrication on cylindrical metallic surfaces and its application to a rotor-bearing system. *The International Journal of Advanced Manufacturing Technology*, 78(5):1021–1029, May 2015. doi: 10.1007/s00170-014-6648-z.

[33] Mihai Arghir, Nicolas Roucou, Mathieu Helene, and Jean Frene. Theoretical analysis of the incompressible laminar flow in a macro-roughness cell. *Journal of Tribology*, 125 (2):309–318, April 2003. doi: 10.1115/1.1506328.

[34] Gwidon W. Stachowiak and Andrew W. Bachelor. *Engineering Tribology*. Butterworth-Heinemann, Oxford, 4th edition, 2014. doi: 10.1016/C2011-0-07515-4, isbn: 978-0-12-397047-3.

[35] Jonathon K. Schuh. Surface textures and non-newtonian fluids for decreased friction in full film lubrication. Master's thesis, University of Illinois at Urbana-Champaign, Urbana, IL, USA, 2015. http://hdl.handle.net/2142/78561.

[36] Jonathon K. Schuh, Yong Hoon Lee, James T. Allison, and Randy H. Ewoldt. Design-driven modeling of surface-textured full-film lubricated sliding: validation and rationale of nonstandard thrust observations. *Tribology Letters*, 65(2):35 (17pp), June 2017. doi: 10.1007/s11249-017-0818-8.

[37] Jamshid A. Samareh. Survey of shape parameterization techniques for high-fidelity multidisciplinary shape optimization. *AIAA Journal*, 39(5):877–884, May 2001. doi: 10.2514/2.1391.

[38] Dengsheng Zhang and Guojun Lu. Review of shape representation and description techniques. *Pattern Recognition*, 37(1):1–19, January 2004. doi: 10.1016 /j.patcog.2003.07.008.

[39] Vidya Ganapati, Owen D. Miller, and Eli Yablonovitch. Light trapping textures designed by electromagnetic optimization for sub-wavelength thick solar cells. *IEEE Journal of Photovoltaics*, 4(1):175–182, January 2014. doi: 10.1109/JPHOTOV.2013.2280340.

[40] Cong Shen and M. M. Khonsari. Numerical optimization of texture shape for parallel surfaces under unidirectional and bidirectional sliding. *Tribology International*, 82(A): 1–11, February 2015. doi: 10.1016/j.triboint.2014.09.022.

[41] Chendi Lin, Yong Hoon Lee, Jonathon K. Schuh, Randy H. Ewoldt, and James T. Allison. Efficient optimal surface texture design using linearization. In Schumacher et al., editor, *Advances in Structural and Multidisciplinary Optimization: Proceedings of the 12th World Congress of Structural and Multidisciplinary Optimization*, pages 632–647, Cham, 2018. Springer. doi: 10.1007/978-3-319-67988-4_48.

[42] Osborne Reynolds. On the theory of lubrication and its application to mr. beauchamp tower's experiments, including an experimental determination of the viscosity of olive oil. *Philosophical Transactions of the Royal Society of London*, 177:157–234, January 1886. doi: 10.1098/rstl.1886.0005.

[43] Michael T. Heath. *Scientific Computing: An Introductory Survey*. McGraw-Hill, New York, 2nd edition, 2002. doi: 10.1137/1.9781611975581, isbn: 978-1-611975-57-4.

[44] Bengt Fornberg. *A Practical Guide to Pseudospectral Methods*. Cambridge University Press, Cambridge, 2009. doi: 10.1017/CBO9780511626357, isbn: 978-0-521-64564-5.

[45] Yoshikazu Sawaragi, Hirotaka Nakayama, and Tetsuzo Tanino, editors. *Theory of Multiobjective Optimization*. Academic Press, Orlando, FL, 1st edition, 1985. isbn: 978-0-12-620370-7.

[46] Kalyanmoy Deb, Amrit Pratap, Sameer Agarwal, and T. Meyarivan. A fast and elitist multiobjective genetic algorithm: NSGA-II. *IEEE Transactions on Evolutionary Computation*, 6(2):182–197, August 2002. doi: 10.1109/4235.996017.

[47] Kalyanmoy Deb. Multi-objective genetic algorithms: problem difficulties and construction of test problems. *Evolutionary Computation*, 7(3):205–230, 1999. doi: 10.1162 /evco.1999.7.3.205.

[48] Matthias Ehrgott. *Multicriteria Optimization*. Springer-Verlag, Berlin, Germany, 2005. doi: 10.1007/3-540-27659-9, isbn: 978-3-540-27659-3.

[49] Yacov Y. Haimes, Leon S. Lasdon, and David A. Wismer. On a bicriterion formulation of the problems of integrated system identification and system optimization. *IEEE Transactions on Systems, Man, and Cybernetics*, SMC-1(3):296–297, July 1971. doi: 10.1109/TSMC.1971.4308298.

[50] Wolfgang Bauer. *Hydropneumatic Suspension Systems*. Springer-Verlag, Berlin, Germany, 2011. doi: 10.1007/978-3-642-15147-7, isbn: 978-3-642-15147-7.

[51] Macosko, Christopher W. *Rheology: Principles, Measurements, and Applications*. Wiley-VCH, Weinheim, 1994. doi: 10.1002/cite.330671126, isbn: 978-0-471-18575-8.

[52] Anders Forsgren, Philip E. Gill, and Margaret H. Wright. Interior methods for nonlinear optimization. *SIAM Review*, 44(4):525–597, 2002. doi: 10.1137/S0036144502414942.

[53] Y. Qiu and M. M. Khonsari. On the prediction of cavitation in dimples using a mass-conservative algorithm. *Journal of Tribology*, 131(4):041702, October 2009. doi: 10.1115/1.3176994.

[54] Danny J. Lohan, Ercan M. Dede, and James T. Allison. Topology optimization for heat conduction using generative design algorithms. *Structural and Multidisciplinary Optimization*, 55(3):1063–1077, March 2017. doi: 10.1007/s00158-016-1563-6.

[55] C. A. Glasbey and K. V. Mardia. A review of image-warping methods. *Journal of Applied Statistics*, 25(2):155–171, 1998. doi: 10.1080/02664769823151.

[56] M. J. Alexander, J. T. Allison, and P. Y. Papalambros. Reduced representations of vector-valued coupling variables in decomposition-based design optimization. *Structural and Multidisciplinary Optimization*, 44(3):379–391, September 2011. doi: 10.1007/s00158-011-0636-9.

[57] Christian Kanzow, Christian Nagel, Hirokazu Kato, and Masao Fukushima. Successive linearization methods for nonlinear semidefinite programs. *Computational Optimization and Applications*, 31(3):251–273, July 2005. doi: 10.1007/s10589-005-3231-4.

[58] Grigory Ryk, Yuri Kligerman, and Izhak Etsion. Experimental investigation of laser surface texturing for reciprocating automotive components. *Tribology Transactions*, 45 (4):444–449, 2002. doi: 10.1080/10402000208982572.

[59] Jafar Takabi and M. M. Khonsari. On the dynamic performance of roller bearings operating under low rotational speeds with consideration of surface roughness. *Tribology International*, 86:62–71, June 2015. doi: 10.1016/j.triboint.2015.01.011.

[60] Conglin Dong, Chengqing Yuan, Lei Wang, Wei Liu, Xiuqin Bai, and Xinping Yan. Tribological properties of water-lubricated rubber materials after modification by MoS2 nanoparticles. *Scientific Reports*, 6:35023, October 2016. doi: 10.1038/srep35023.

[61] Cong Shen and M. M. Khonsari. Effect of dimple's internal structure on hydrodynamic lubrication. *Tribology Letters*, 52(3):415–430, December 2013. doi: 10.1007/s11249-013-0225-8.

[62] Yong Hoon Lee, Jonathon K. Schuh, Randy H. Ewoldt, and James T. Allison. Shape parameterization comparison for full-film lubrication texture design. In *Proceedings of the ASME 2016 International Design Engineering Technical Conferences and Computers and Information in Engineering Conference. Volume 2B: 42nd Design Automation Conference*, number DETC2016-60168, page V02BT03A037, Charlotte, NC, August 2016. ASME. doi: 10.1115/DETC2016-60168.

[63] Aviram Ronen, Izhak Etsion, and Yuri Kligerman. Friction-reducing surface-texturing in reciprocating automotive components. *Tribology Transactions*, 44(3):359–366, 2001. doi: 10.1080/10402000108982468.

[64] Ravinder B. Siripuram and Lyndon S. Stephens. Effect of deterministic asperity geometry on hydrodynamic lubrication. *Journal of Tribology*, 126(3):527–534, July 2004. doi: 10.1115/1.1715104.

[65] Wenyu Sun and Ya-Xiang Yuan. *Optimization Theory and Methods*. Springer, Boston, MA, 2006. doi: 10.1007/b106451, isbn: 978-0-387-24975-9.

[66] K. V. John, C. V. Ramakrishnan, and K. G. Sharma. Minimum weight design of trusses using improved move limit method of sequential linear programming. *Computers & Structures*, 27(5):583–591, 1987. doi: 10.1016/0045-7949(87)90073-3.

[67] Yong Hoon Lee, R. E. Corman, Randy H. Ewoldt, and James T. Allison. A multi-objective adaptive surrogate modeling-based optimization (MO-ASMO) framework using efficient sampling strategies. In *Proceedings of the ASME 2017 International Design Engineering Technical Conferences*, number DETC2017-67541 in Volume 2B: 43rd Design Automation Conference, page V02BT03A023, Cleveland, OH, August 2017. ASME. doi: 10.1115/DETC2017-67541.

[68] Vira Chakong and Yacov Y. Haimes. *Multiobjective Decision Making: Theory and Methodology.* North-Holland, Amsterdam, Netherlands, 1983. isbn: 978-0-444-00710-0.

[69] Eckart Zitzler and Lothar Thiele. Multiobjective evolutionary algorithms: a comparative case study and the strength pareto approach. *IEEE Transactions on Evolutionary Computation*, 3(4):257–271, March 1999. doi: 10.1109/4235.797969.

[70] Kalyanmoy Deb and Himanshu Jain. An evolutionary many-objective optimization algorithm using reference-point-based nondominated sorting approach, part i: solving problems with box constraints. *IEEE Transactions on Evolutionary Computation*, 18 (4):577–601, 2014. doi: 10.1109/TEVC.2013.2281535.

[71] Gabriele Eichfelder. *Adaptive Scalarization Methods in Multiobjective Optimization.* Springer-Verlag, Berlin, Heidelberg, 2008. doi: 10.1007/978-3-540-79159-1.

[72] Thomas Saaty and Saul Gass. Parametric objective function (part 1). *Journal of the Operations Research Society of America*, 2(3):316–319, August 1954. doi: 10.1287/opre.2.3.316.

[73] A. Pascoletti and P. Serafini. Scalarizing vector optimization problems. *Journal of Optimization Theory and Applications*, 42(4):499–524, April 1984. doi: 10.1007/BF00934564.

[74] Hao Wang, André Deutz, Thomas Bäck, and Michael Emmerich. Hypervolume indicator gradient ascent multi-objective optimization. In Trautmann et al., editor, *Evolutionary Multi-Criterion Optimization: 9th International Conference EMO 2017*, volume 10173 of *Lecture Notes in Computer Science*, pages 654–669, Münster, Germany, February 2017. Springer. doi: 10.1007/978-3-319-54157-0_44.

[75] Donald R. Jones, Matthias Schonlau, and William J. Welch. Efficient global optimization of expensive black-box functions. *Journal of Global Optimization*, 13(4):455–492, August 1998. doi: 10.1023/A:1008306431147.

[76] Nestor V. Queipo, Raphael T. Haftka, Wei Shyy, Tushar Goel, Rajkumar Vaidyanathan, and P. Kevin Tucker. Surrogate-based analysis and optimization. *Progress in Aerospace Sciences*, 41(1):1–28, January 2005. doi: 10.1016/j.paerosci.2005.02.001.

[77] Saman Razavi, Bryan A. Tolson, and Donald H. Burn. Review of surrogate modeling in water resources. *Water Resources Research*, 48(7):W07401, July 2012. doi: 10.1029/2011WR011527.

[78] G. E. P. Box and K. B. Wilson. On the experimental attainment of optimum conditions. *Journal of the Royal Statistical Society, Series B*, 13(1):1–45, 1951. doi: 10.1007/978-1-4612-4380-9_23.

[79] Georges Matheron. *Estimating and Choosing*. Springer, Berlin, 1989. doi: 10.1007/978-3-642-48817-7, isbn: 978-3-642-48817-72.

[80] Corinna Cortes and Vladimir Vapnik. Support-vector networks. *Machine Learning*, 20 (3):273–297, September 1995. doi: 10.1007/BF00994018.

[81] Michael J. D. Powell. Radial basis function for multivariable interpolation: a review. In *Algorithms for Approximation*, pages 143–167. Clarendon Press, Oxford, UK, January 1987. doi: 10.5555/48424.48433.

[82] G. Gary Wang and S. Shan. Review of metamodeling techniques in support of engineering design optimization. *Journal of Mechanical Design*, 129(4):370–380, May 2006. doi: 10.1115/1.2429697.

[83] Timothy W. Simpson, Vasilli Toropov, Vladimir Balabanov, and Felipe A. C. Viana. Design and analysis of computer experiments in multidisciplinary design optimization: a review of how far we have come - or not. In *12th AIAA/ISSMO Multidisciplinary Analysis and Optimization Conference*, number AIAA 2008-5802, Victoria, British Columbia, Canada, September 2008. AIAA. doi: 10.2514/6.2008-5802.

[84] Alexander I. J. Forrester and Andy J. Keane. Recent advances in surrogate-based optimization. *Progress in Aerospace Sciences*, 45(1):50–79, 2009. doi: 10.1016/j.paerosci.2008.11.001.

[85] V. Roshan Joseph. Space-filling designs for computer experiments: A review. *Quality Engineering*, 28(1):28–35, August 2016. doi: 10.1080/08982112.2015.1100447.

[86] Sushant Garud, Iftekhar A. Karimi, and Markus Kraft. Design of computer experiments: a review. *Computers & Chemical Engineering*, 106:71–95, August 2017. doi: 10.1016/j.compchemeng.2017.05.010.

[87] J. E. Dennis and Virginia Torczon. Managing approximation models in optimization. In Natalia M. Alexandrov and M. Y. Hussaini, editors, *Multidisciplinary Design Optimization: State of the Art*, number 80, pages 330–347. Society for Industrial and Applied Mathematics, Philadelphia, Pennsylvania, USA, June 1997.

[88] Ignacio G. Osio and Cristina H. Amon. An engineering design methodology with multistage bayesian surrogates and optimal sampling. *Research in Engineering Design*, 8(4):189–206, December 1996. doi: 10.1007/BF01597226.

[89] Matthias Schonlau, William J. Welch, and Donald R. Jones. Global versus local search in constrained optimization of computer models. In Flournoy et al., editor, *New Developments and Applications in Experimental Design*, pages 11–25. Institute of Mathematical Statistics, Hayward, CA, 1998. doi: 10.1214/lnms/1215456182.

[90] Lei Peng, Li Liu, Teng Long, and Wu Yang. An efficient truss structure optimization framework based on CAD/CAE integration and sequential radial basis function metamodel. *Structural and Multidisciplinary Optimization*, 50(2):329–346, August 2014. doi: 10.1007/s00158-014-1050-x.

[91] George H. Cheng, Adel Younis, Kambiz Haji Hajikolaei, and G. Gary Wang. Trust region based mode pursuing sampling method for global optimization of high dimensional design problems. *Journal of Mechanical Design*, 137(2):021407, February 2015. doi: 10.1115/1.4029219.

[92] Parviz Mohammad Zadeh, Mohsen Sayadi, and Amirreza Kosari. An efficient metamodel-based multi-objective multidisciplinary design optimization framework. *Applied Soft Computing*, 74:760–782, January 2019. doi: 10.1016/j.asoc.2018.09.014.

[93] Cheng Lin, Fengling Gao, and Yingchun Bai. An intelligent sampling approach for metamodel-based multi-objective optimization with guidance of the adaptive weighted-sum method. *Structural and Multidisciplinary Optimization*, 57(3):1047–1060, March 2018. doi: 10.1007/s00158-017-1793-2.

[94] M. S. Eldred and D. M. Dunlavy. Formulations for surrogate-based optimization with data fit, multifidelity, and reduced-order models. In *Proceedings of the 11th AIAA/ISSMO Multidisciplinary Analysis and Optimization Conference*, number AIAA 2006-2117, page 20pp, Portsmouth, VA, 2006. American Institute of Aeronautics and Astronautics. doi: 10.2514/6.2006-7117.

[95] Rayan Hussein and Kalyanmoy Deb. A generative Kriging surrogate model for constrained and unconstrained multi-objective optimization. In *Proceedings of the Genetic and Evolutionary Computation Conference 2016*, pages 573–580, New York, NY, 2016. Association for Computing Machinery. doi: 10.1145/2908812.2908866.

[96] David M. J. Tax and Robert P. W. Duin. Support vector domain description. *Pattern Recognition Letters*, 20(11-13):1191–1199, 1999. doi: 10.1016/S0167-8655(99)00087-2.

[97] Richard J. Malak, Jr. and Christiaan J. J. Paredis. Using support vector machines to formalize the valid input domain of predictive models in systems design problems. *Journal of Mechanical Design*, 132(10):101001, October 2010. doi: 10.1115/1.4002151.

[98] Karel Crombecq, Dirk Gorissen, Dirk Deschrijver, and Tom Dhaene. A novel hybrid sequential design strategy for global surrogate modeling of computer experiments. *SIAM Journal on Scientific Computing*, 33(4):1948–1974, 2011. doi: 10.1137/090761811.

[99] Ping Jiang, Leshi Shu, Qi Zhou, Hui Zhou, Xinyu Shao, and Junnan Xu. A novel sequential exploration-exploitation sampling strategy for global metamodeling. *17th IFAC Symposium on System Identification*, 48(28):532–537, 2015. doi: 10.1016/j.ifacol.2015.12.183.

[100] Ali Ajdari and Hashem Mahlooji. An adaptive exploration-exploitation algorithm for constructing metamodels in random simulation using a novel sequential experimental design. *Communications in Statistics - Simulation and Computation*, 43(5):947–968, October 2014. doi: 10.1080/03610918.2012.720743.

[101] Peter Eades. A heuristic for graph drawing. *Congressus Numerantium*, 42:149–160, 1984. MathSciNet: 0753497.

[102] Thomas M. J. Fruchterman and Edward M. Reingold. Graph drawing by force-directed placement. *Software: Practice and Experience*, 21(11):91129–1164, November 1991. doi: 10.1002/spe.4380211102.

[103] Yong Hoon Lee. Multiobjective adaptive surrogate modeling-based optimization toolbox I. `https://github.com/yonghoonlee/MO-ASMO-I`, 2017.

[104] Yong Hoon Lee. Multiobjective adaptive surrogate modeling-based optimization toolbox II. `https://github.com/yonghoonlee/MO-ASMO-II`, 2018.

[105] Jörg Bremer and Michael Sonnenschein. Constraint-handling for optimization with support vector surrogate models - a novel decoder approach. In *11th International Conference on Agents and Artificial Intelligence (ICAART)*, Barcelona, Spain, February 2013. doi: 10.5220/0004241100910100.

[106] A. Osyczka and S. Kundu. A new method to solve generalized multicriteria optimization problems using the simple genetic algorithm. *Structural Optimization*, 10(2):94–99, November 1995. doi: 10.1007/BF01743536.

[107] Kalyanmoy Deb, Lothar Thiele, Marco Laumanns, and Eckart Zitzler. Scalable test problems for evolutionary multi-objective optimization. In A. Abraham, L. Jain, and R. Goldberg, editors, *Evolutionary Multiobjective Optimization*, Advanced Information and Knowledge Processing, pages 105–145. Springer, London, UK, 2005. doi: 10.1007/1-84628-137-7_6, isbn: 978-1-84628-137-2.

[108] Yong Hoon Lee. A multiobjective optimization test problem. `https://www.mathworks.com/matlabcentral/fileexchange/61800`, 2017.

[109] H. H. Rosenbrock. An automatic method for finding the greatest or least value of a function. *The Computer Journal*, 3(3):175–184, January 1960. doi: 10.1093/comjnl/3.3.175.

[110] James T. Allison. *Optimal Partitioning and Coordination Decisions in Decomposition-based Design Optimization.* PhD thesis, University of Michigan, Ann Arbor, MI, 2008. http://hdl.handle.net/2027.42/58449.

[111] Reza N. Jazar. *Vehicle Dynamics: Theory and Application, 3rd Ed.* Springer, New York, NY, 2017. doi: 10.1007/978-3-319-53441-1, isbn: 9783319534404.

[112] R. Byron Bird, Robert C. Armstrong, and Ole Hassager. *Dynamics of Polymeric Liquids, Volume 1: Fluid Mechanics.* Wiley, New York, 2nd edition, 1987. isbn: 978-0-471-80245-7.

[113] James T. Allison. Simulation and animation of a quarter-car automotive suspension model. `https://www.mathworks.com/matlabcentral/fileexchange/35478`, 2012.

[114] C. C. Smith, D. Y. McGehee, and A. J. Healey. The prediction of passenger riding comfort from acceleration data. *Journal of Dynamic Systems, Measurement, and Control*, 100(1):34–41, March 1978. doi: 10.1115/1.3426338.

[115] Jianbo Lu and M. DePoyster. Multiobjective optimal suspension control to achieve integrated ride and handling performance. *IEEE Transactions on Control Systems Technology*, 10(6):807–821, December 2002. doi: 10.1109/TCST.2002.804121.

[116] Songqing Shan and G. Gary Wang. Metamodeling for high dimensional simulation-based design problems. *Journal of Mechanical Design*, 132(5):051009, May 2010. doi: 10.1115/1.4001597.

[117] Mohan D. Rao. Recent applications of viscoelastic damping for noise control in automobiles and commercial airplanes. *Journal of Sound and Vibration*, 262(3):457–474, May 2003. doi: 10.1016/S0022-460X(03)00106-8.

[118] Amir Rashid and Cornel Mihai Nicolescu. Design and implementation of tuned viscoelastic dampers for vibration control in milling. *International Journal of Machine Tools and Manufacture*, 48(9):1036–1053, July 2008. doi: 10.1016/j.ijmachtools.2007.12.013.

[119] G. D. Dean, L. N. McCartney, R. Mera, and J. M. Urquhart. Modeling nonlinear viscoelasticity in polymers for design using finite element analysis. *Polymer Engineering and Science*, 51(11):2210–2219, November 2011. doi: 10.1002/pen.21993.

[120] Kai A. James and Haim Waisman. On the importance of viscoelastic response consideration in structural design optimization. *Optimization and Engineering*, 17(4):631–650, December 2016. doi: 10.1007/s11081-016-9327-0.

[121] Yong Hoon Lee, R. E. Corman, Randy H. Ewoldt, and James T. Allison. Continuous relaxation spectra and its reduced-dimensionality descriptions for engineering design with linear viscoelasticity. In *ASME 2019 International Mechanical Engineering Congress and Exposition, 26th Symposium on Fluid Mechanics and Rheology of Nonlinear Materials and Complex Fluids*, number IMECE2019-13370, Salt Lake City, UT, 2019. ASME. http://hdl.handle.net/2142/106123.

[122] Lakshmi Gururaja Rao and James T. Allison. Generalized viscoelastic material design with integro-differential equations and direct optimal control. In *Proceedings of the ASME 2015 International Design Engineering Technical Conferences and Computers and Information in Engineering Conference. Volume 2B: 41st Design Automation Conference*, number DETC2015-46768, page V02BT03A008, Boston, MA, August 2015. ASME. doi: 10.1115/DETC2015-46768.

[123] Nhan Phan-Thien. *Understanding Viscoelasticity: An Introduction to Rheology*. Springer, Berlin, 2nd edition, 2013. doi: 10.1007/978-3-642-32958-6, isbn: 978-3-642-32958-6.

[124] A. C. Pipkin. *Lectures on Viscoelasticity Theory.* Springer, New York, 1972. doi: 10.1007/978-1-4615-9970-8, isbn: 978-1-4615-9970-8.

[125] Ludwig Boltzmann. Zur theorie der elastischen nachwirkung. *Wiedemann's Annalen der Physik und Chemie*, 241(11):430–432, 1878. doi: 10.1002/andp.18782411107.

[126] S. Breuer and E. T. Onat. On uniqueness in linear viscoelasticity. *Quarterly of Applied Mathematics*, 19(4):355–359, January 1962. doi: 10.1090/qam/136170.

[127] Randy H. Ewoldt, Anette E. Hosoi, and Gareth H. McKinley. Rheological fingerprinting of complex fluids using large amplitude oscillatory shear (LAOS) flow. *Annual Transactions of the Nordic Rheology Society*, 15, 2007.

[128] Nicholas W. Tschoegl. *The Phenomenological Theory of Linear Viscoelastic Behavior.* Springer-Verlag Berlin Heidelberg, Berlin, Germany, 3rd edition, 1989. isbn: 978-3-642-73602-5, doi: 10.1007/978-3-642-73602-5.

[129] Luca Martinetti, C. L. Torre, Olivia, Kenneth. S. Schweizer, and Randy H. Ewoldt. Inferring the nonlinear mechanisms of a reversible network. *Macromolecules*, 51(21): 8772–8789, October 2018. doi: 10.1021/acs.macromol.8b01295.

[130] E. Wiechert. Gesetze der elastischen nachwirkung f ur constante temperatur. *Annalen der Physik*, 286(10):335–348, 1893. doi: 10.1002/andp.18932861011.

[131] M. Baumgaertel and H. H. Winter. Interrelation between continuous and discrete relaxation time spectra. *Journal of Non-Newtonian Fluid Mechanics*, 44:15–36, 1992. doi: 10.1016/0377-0257(92)80043-W.

[132] R. E. Corman and Randy H. Ewoldt. Mapping linear viscoelasticity for design and tactile intuition. *Applied Rheology*, 29(1):141–161, December 2019. doi: 10.1515/arh-2019-0013.

[133] Nihar Deodhar, Joseph Deese, and Christopher Vermillion. Experimentally infused plant and controller optimization using iterative design of experiments - theoretical framework and airborne wind energy case study. *Journal of Dynamic Systems, Measurement, and Control*, 140(1):011004, January 2017. doi: 10.1115/1.4037014.

[134] K. M. B. Jansen. *Thermomechanical Modelling and Characterisation of Polymers.* Delft University of Technology, Delft, 2007.

[135] Stephen Makau Kimanzi. A simple approach to viscoelastic material selection for impact absorption. Master's thesis, The University of British Columbia, Okanagan, BC, Canada, 2019. doi: 10.14288/1.0376038.

[136] Jonathan B. Freund and Randy H. Ewoldt. Quantitative rheological model selection: Good fits versus credible models using bayesian inference. *Journal of Rheology*, 59(3): 667–701, 2015. doi: 10.1122/1.4915299.

[137] F. Mastroddi, F. Martarelli, M. Eugeni, and C. Riso. Time- and frequency-domain linear viscoelastic modeling of highly damped aerospace structures. *Mechanical Systems and Signal Processing*, 122:42–55, May 2019. doi: 10.1016/j.ymssp.2018.12.023.

[138] Yuji Tasaka, Taiki Yoshida, Richard Rapberger, and Yuichi Murai. Linear viscoelastic analysis using frequency-domain algorithm on oscillating circular shear flows for bubble suspensions. *Rheologica Acta*, 57(3):229–240, March 2018. doi: 10.1007/s00397-018-1074-z.

[139] Michael Sipser. *Introduction to the Theory of Computation*. Cengage Learning, Boston, 3rd edition, 2013. isbn: 978-1-133-18779-0.

[140] Nicole L. Ramo, Christian M. Puttlitz, and Kevin L. Troyer. The development and validation of a numerical integration method for non-linear viscoelastic modeling. *PLoS One*, 13(1):e0190137, January 2018. doi: 10.1371/journal.pone.0190137.

[141] Adailton S. Borges, Adriano S. Borges, Albert W. Faria, Domingos A. Rade, and Thiago P. Sales. Time domain modeling and simulation of nonlinear slender viscoelastic beams associating Cosserat theory and a fractional derivative model. *Latin American Journal of Solids and Structures*, 14(1):153–173, January 2017. doi: 10.1590/1679-78252928.

[142] Jordan Yankov Hristov. Linear viscoelastic responses: the Prony decomposition naturally leads into the Caputo-Fabrizio fractional operator. *Frontiers in Physics*, 6: 135, December 2018. doi: 10.3389/fphy.2018.00135.

[143] K. Diethelm and A. D. Freed. An efficient algorithm for the evaluation of convolution integrals. *Computers & Mathematics with Applications*, 51(1):51–72, January 2006. doi: 10.1016/j.camwa.2005.07.010.

[144] Alan D. Freed. *Soft Solids*. Cengage Learning, Boston, 2013. doi: 10.1007/978-3-319-03551-2, isbn: 978-3-319-03551-2.

[145] Lawrence F. Shampine and Mark W. Reichelt. The MATLAB ODE suite. *SIAM Journal on Scientific Computing*, 18(1):1–22, January 1997. doi: 10.1137/S1064827594276424.

[146] Daniel R. Herber, Yong Hoon Lee, and James T. Allison. Unified framework for solving general linear-quadratic dynamic optimization problems utilizing direct transcription and quadratic programming. in preparation.

[147] Yong Hoon Lee, Daniel R. Herber, and James T. Allison. Simulation and optimization of linear viscoelasticity in the time domain using approximate linear time-invariant state-space models. In *25th International Congress of Theoretical and Applied Mechanics*, Milano, Italy, August 2021. accepted.

[148] Daniel R. Herber and James T. Allison. Approximating arbitrary impulse response functions with Prony basis functions. Technical Report UIUC-ESDL-2019-01, Engineering System Design Laboratory, Urbana, IL, USA, 2019. http://hdl.handle.net/2142/106010.

[149] Elbert Hendricks, Ole Jannerup, and Paul Haase Sørensen. *Linear Systems Control*. Springer, Berlin, 2008. doi: 10.1007/978-3-540-78486-9, isbn: 978-3-540-78486-9.

[150] Michael E. McCormick. *Ocean Wave Energy Conversion*. Dover, Mineola, NY, 2nd edition, 2007. isbn: 978-0-486-46245-5.

[151] W. E. Cummins. The impulse response function and ship motions. Technical report, David Taylor Model Basin, Navy Department, Washington, DC, USA, 1962. http://hdl.handle.net/1721.3/49049.

[152] A. F. Rodríguez, L. de Santiago Rodrigo, E. L. Guillén, J. M. R. Ascariz, J. M. M. Jiménez, and L. Boquete. Coding Prony's method in MATLAB and applying it to biomedical signal filtering. *BMC Bioinformatics*, 19(451), November 2018. doi: 10.1186/s12859-018-2473-y.

[153] Anand P. Deshmukh and James T. Allison. Design of dynamic systems using surrogate models of derivative functions. *Journal of Mechanical Design*, 139(10):101402, October 2017. doi: 10.1115/1.4037407.

[154] Frank Lemmer, Steffen Raach, David Schlipf, and Po Wen Cheng. Parametric wave excitation model for floating wind turbines. *Energy Procedia*, 94:290–305, September 2016. doi: 10.1016/j.egypro.2016.09.186.

[155] Robert E. Shadwick. Mechanical design in arteries. *The Journal of Experimental Biology*, 202:3305–3313, December 1999.

[156] Mark Denny. The role of gastropod pedal mucus in locomotion. *Nature*, 285:160–161, May 1980. doi: 10.1038/285160a0.

[157] D. B. Caldwell. Vibration damping in world trade center using viscoelastic material. Technical report, The 3M Company, New York, 1972.

[158] P. G. De Gennes. Soft adhesives. *Langmuir*, 12(19):4497–4500, September 1996. doi: 10.1021/la950886y.

[159] Rebecca E. Corman. *Design tools for linear viscoelastic fluids*. PhD thesis, University of Illinois at Urbana-Champaign, Urbana, IL, USA, 2019. http://hdl.handle.net/2142/105817.

[160] John D. Ferry. *Viscoelastic Properties of Polymers*. John Wiley & Sons, Inc, New York, 3rd edition, 1980. isbn: 978-0-471-04894-7.

[161] H. C. Booij and G. P. J. M. Thoone. Generalization of Kramers-Kronig transforms and some approximations of relations between viscoelastic quantities. *Rheologica Acta*, 21(1):15–24, January 1982. doi: 10.1007/BF01520701.

[162] Luca Martinetti. *Uniaxial Extensional Behavior of A–B–A Thermoplastic Elastomers: Structure-Properties Relationship and Modeling*. PhD thesis, University of Minnesota, 2015. http://hdl.handle.net/11299/181776.

[163] Anna Stankiewicz. On the monotonicity of the relaxation spectrum of fractional maxwell model of viscoelastic materials. *ECONTECHMOD*, 7(1):117–125, 2018.

[164] M. Baumgaertel, A. Schausberger, and H. H. Winter. The relaxation of polymers with linear flexible chains of uniform length. *Rheologica Acta*, 29(5):400–408, September 1990. doi: 10.1007/BF01376790.

[165] H. H. Winter. Analysis of dynamic mechanical data: inversion into a relaxation time spectrum and consistency check. *Journal of Non-Newtonian Fluid Mechanics*, 68(2-3): 225–239, 1997. doi: 10.1016/S0377-0257(96)01512-1.

[166] H. H. Winter and F. Chambon. Analysis of linear viscoelasticity of a crosslinking polymer at the gel point. *Journal of Rheology*, 30(2):367–382, 1986. doi: 10.1122/1.549853.

[167] M. E. De Rosa and H. H. Winter. The effect of entanglements on the rheological behavior of polybutadiene critical gels. *Rheologica Acta*, 33:220–237, May 1994. doi: 10.1007/BF00437307.

[168] F. Schwarzl and A. J. Staverman. Higher approximations of relaxation spectra. *Physica*, 18(10):791–798, October 1952. doi: 10.1016/S0031-8914(52)80267-8.

[169] Turner Alfrey and Paul Doty. The methods of specifying the properties of viscoelastic materials. *Journal of Applied Physics*, 16(11):700, November 1945. doi: 10.1063/1.1707524.

[170] Richard Allan Schapery. Approximate method of transform inversion for viscoelastic stress analysis. In *Proceedings of the fourth U.S. National Congress of Applied Mechanics*, pages 1075–1084, Berkeley, CA, 1962. ASME. doi: 10.1063/1.1707524.

[171] Michael F. Ashby. Material and process charts. Technical report, Granta Design, Ltd., Cambridge, UK, 2009.

[172] Scott C. Grindy, Robert Learsch, Davoud Mozhdehi, Jing Cheng, Devin G. Barrett, Zhibin Guan, Phillip B. Messersmith, and Niels Holten-Andersen. Control of hierarchical polymer mechanics with bioinspired metal-coordination dynamics. *Nature Materials*, 14:1210–1216, December 2015. doi: 10.1038/nmat4401.

[173] Prince E. Rouse Jr. A theory of the linear viscoelastic properties of dilute solutions of coiling polymers. *Journal of Chemical Physics*, 21(7):1272–1280, July 1953. doi: 10.1063/1.1699180.

[174] P. G. de Gennes. Reptation of a polymer chain in the presence of fixed obstacles. *Journal of Chemical Physics*, 55(2):572, July 1971. doi: 10.1063/1.1675789.

[175] Toyoichi Tanaka. *Experimental Methods in Polymer Science*. Academic Press, San Diego, 2010. doi: 10.1016/C2009-0-22460-3, isbn: 978-0-08-050612-8.

[176] D. B. Hamilton, J. A. Walowit, and Allen C. M. A theory of lubrication by microirregularities. *Journal of Basic Engineering*, 88(1):177–185, March 1966. doi: 10.1115/1.3645799.

[177] Ulrika Pettersson and Staffan Jacobson. Influence of surface texture on boundary lubricated sliding contacts. *Tribology International*, 36(11):857–864, November 2003. doi: 10.1016/S0301-679X(03)00104-X.

[178] Daniel Gropper, Ling Wang, and Terry J. Harvey. Hydrodynamic lubrication of textured surfaces: A review of modeling techniques and key findings. *Tribology International*, 94:509–529, February 2016. doi: 10.1016/j.triboint.2015.10.009.

[179] Nam P. Suh, Mohsen Mosleh, and Phillip S. Howard. Control of friction. *Wear*, 175 (1-2):151–158, June 1994. doi: 10.1016/0043-1648(94)90178-3.

[180] M. Varenberg, G. Halperin, and I. Etsion. Different aspects of the role of wear debris in fretting wear. *Wear*, 252(11-12):902–910, July 202. doi: 10.1016/S0043-1648(02)00044-3.

[181] Jonathon K. Schuh, Yong Hoon Lee, James T. Allison, and Randy H. Ewoldt. Surface textures and non-Newtonian fluids for decreasing friction in lubricated sliding contact. In *2015 Fluid Power Innovation and Research Conference*, Minneapolis, MN, 2015.

[182] R. L. Batra and V. Mohan. Roller bearing lubrication with shear thinning lubricants. *Wear*, 51(2):213–225, December 1978. doi: 10.1016/0043-1648(78)90261-2.

[183] H. Hirani, K. Athre, and S. Biswas. Lubricant shear thinning analysis of engine journal bearings. *Tribology Transactions*, 44(1):125–131, 2001. doi: 10.1080/10402000108982435.

[184] Li Xiaodi, Chen Haosheng, Chen Darong, and Wang Jiadao. Normal stress effects in journal bearing lubrication with maxwell fluid. In Luo et al., editor, *Advanced Tribology*, pages 231–234, Berlin, Heidelberg, 2009. Springer. doi: 10.1007/978-3-642-03653-8_73.

[185] Randy H. Ewoldt. Extremely soft: Design with rheologically-complex fluids. *Soft Robotics*, 1(1):12–20, March 2014. doi: 10.1089/soro.2013.1508.

[186] Arif Z. Nelson and Randy H. Ewoldt. Design of yield-stress fluids: a rheology-to-structure inverse problem. *Soft Matter*, 13(41):7578–7594, 2017. doi: 10.1039/C7SM00758B.

[187] J. Ashmore, A. Q. Shen, H. P. Kavehpour, H. A. Stone, and G. H. McKinley. Coating flows of non-Newtonian fluids: Weakly and strongly elastic limits. *Jurnal of Engineering Math*, 60(1):17–41, January 2008. doi: 10.1007/s10665-007-9152-8.

[188] Jonathon K. Schuh. *Co-design of surface textures and non-Newtonian fluids for decreased friction*. PhD thesis, University of Illinois at Urbana-Champaign, Urbana, IL, USA, 2018. http://hdl.handle.net/2142/100988.

[189] Gideon Schwarz. Estimating the dimension of a model. *The Annals of Statistics*, 6(2): 461–464, March 1978. doi: 10.1214/aos/1176344136.

[190] William O. Criminale, Jr., J. L. Ericksen, and G. L. Filbey, Jr. Steady shear flow of non-Newtonian fluids. *Archive for Rational Mechanics and Analysis*, 1(1):410–417, January 1957. doi: 10.1007/BF00298018.

[191] James Gardner Oldroyd. On the formulation of rheological equations of state. *Proceedings of the Royal Society of London, Series A, Mathematical and Physical Sciences*, 200(1063):523–541, February 1950. doi: 10.1098/rspa.1950.0035.

[192] Maurice L. Huggins. The viscosity of dilute solutions of long-chain molecules. IV. dependence on concentration. *Journal of the American Chemical Society*, 64(11): 2716–2718, November 1942. doi: 10.1021/ja01263a056.

[193] Kunt Atalık and Roland Keunings. On the occurrence of even harmonics in the shear stress response of viscoelastic fluids in large amplitude oscillatory shear. *Journal of Non-Newtonian Fluid Mechanics*, 122(1):107–116, September 2004. doi: 10.1016/j.jnnfm.2003.11.012.

[194] Roland Keunings. A survey of computational rheology. In *Proceedings of the XIIIth International Congress on Rheology*, pages 7–14, Cambridge, UK, August 2000. British Society of Rheology. doi: 10.1.1.505.1793.

[195] R. G. Owens and T. N. Phillips. *Computational Rheology.* Imperial College Press, London, UK, 2002. isbn: 978-1-86094-186-3.

[196] M. O. Deville, P. F. Fischer, and E. H. Mund. *High-Order Methods for Incompressible Fluid Flow.* Cambridge University Press, Cambridge, UK, 2002. isbn: 978-0-521-45309-7.

[197] David A. Kopriva. *Implementing Spectral Methods for Partial Differential Equations.* Springer, Berlin, 2009. doi: 10.1007/978-90-481-2261-5, isbn: 978-90-481-2261-5.

[198] Benjamin Wilson, David Cappelleri, Timothy W. Simpson, and Mary Frecker. Efficient Pareto frontier exploration using surrogate approximations. *Optimization and Engineering*, 2(1):31–50, March 2001. doi: 10.1023/A:1011818803494.

[199] Ingrida Steponavičė, Mojdeh Shirazi-Manesh, Rob J. Hyndman, Kate Smith-Miles, and Laura Villanova. On sampling methods for costly multi-objective black-box optimization. In Pardalos et al., editor, *Advances in Stochastic and Deterministic Global Optimization*, volume 107 of *Springer Optimization and Its Applications*, pages 273–296. Springer, Cham, 2016. doi: 10.1007/978-3-319-29975-4_15.

[200] Songqing Shan and G. Gary Wang. An efficient pareto set identification approach for multiobjective optimization on black-box functions. *Journal of Mechanical Design*, 127 (5):866–874, September 2005. doi: 10.1115/1.1904639.

[201] Anand P. Deshmukh and James T. Allison. Multidisciplinary dynamic optimization of horizontal axis wind turbine design. *Structural and Multidisciplinary Optimization*, 53 (1):15–27, January 2016. doi: 10.1007/s00158-015-1308-y.

[202] Daniel R. Herber and James T. Allison. Nested and simultaneous solution strategies for general combined plant and control design problems. *Journal of Mechanical Design*, 141(1):011402, October 2018. doi: 10.1115/1.4040705.

[203] Jonathon K. Schuh and Randy H. Ewoldt. Low Reynolds number friction reduction with polymers and textures. *Journal of Non-Newtonian Fluid Mechanics*, 273:104167, November 2019. doi: 10.1016/j.jnnfm.2019.104167.

[204] J. A. Tichy and S.-H. Chen. Plane slider bearing load due to fluid inertia–experiment and theory. *Journal of Tribology*, 107(1):32–38, January 1985. doi: 10.1115/1.3260999.

[205] Oscar Pinkus and Beno Sternlicht. *Theory of Hydrodynamic Lubrication*. McGraw-Hill, New York, NY, 1961.

[206] J. A. Tichy. Non-Newtonian lubrication with the convected Maxwell model. *Journal of Tribology*, 118(2):344–348, January 1996. doi: 10.1115/1.2831307.

[207] K.E. Beschorner, C.F. Higgs III, and M.R. Lovell. Derivation of Reynolds equation in cylindrical coordinates applicable to pin-on-disk and CMP. In *Proceedings of the STLE/ASME International Joint Tribology Conference*, number IJTC2008-71245, pages 399–401, Miami, FL, October 2008. ASME. doi: 10.1115/IJTC2008-71245.

[208] James Mercer. Functions of positive and negative type, and their connection the theory of integral equations. *Philosophical Transactions of the Royal Society of London A: Mathematical, Physical and Engineering Sciences*, 209(441-458):415–446, 1909. doi: 10.1098/rsta.1909.0016.